Absorption, Diffusion, and Reaction of Plasma Species in Aqueous Media

Tijin Hanno Geo Saji

Preparation. LaTeX documentation system in OverLeaf.
Printing. 24-drukwerk.nl

ISBN: 978-90-386-6769-0
NUR: 928
A catalogue record is available from the Eindhoven University of Technology Library.

Financial support.
The work presented in this thesis was funded by the Institute for Complex Molecular Systems (ICMS). The research was conducted at Eindhoven University of Technology in the Materials Simulation & Modelling (MSM) research group in the Department of Applied Physics and Science Education.

Absorption, Diffusion, and Reaction of Plasma Species in Aqueous Media

PROEFSCHRIFT

ter verkrijging van de graad van doctor aan de Technische Universiteit Eindhoven,
op gezag van de rector magnificus prof.dr. S.K. Lenaerts,
voor een commissie aangewezen door het College voor Promoties,
in het openbaar te verdedigen op donderdag 8 oktober 2026 om 16:00 uur

door

Tijin Hanno Geo Saji

geboren te Kozhencherry, Kerala, India

Dit proefschrift is goedgekeurd door de promotoren en de samenstelling van de promotiecommissie is als volgt:

voorzitter:	prof.dr. B. Koopmans
1e promotor:	prof.dr. S. Calero
2e promotor:	prof.dr.ir. T.J.H. Vlugt (Technische Universiteit Delft)
co-promotor:	dr. B. Bagheri
leden:	prof.dr. P.A. Bobbert
	prof.dr. A. Lyulin
	dr. P. Dey (Technische Universiteit Delft)
	dr. D. Dubbeldam (Universiteit van Amsterdam)
	prof.dr. S.M. Verduyn Lunel (Universiteit Utrecht)

Het onderzoek dat in dit proefschrift wordt beschreven is uitgevoerd in overeenstemming met de TU/e Gedragscode Wetenschapsbeoefening.

I will go before you and make the crooked places straight;
I will break in pieces the gates of bronze and cut the bars of iron.
I will give you the treasures of darkness and hidden riches of secret places
Isaiah 45:2-3a, NKJV

Contents

Chapter 1

Introduction

Humankind has long been captivated by lightning - the cascading white streak that runs across the dark sky. From ancient beliefs that cast it as a divine instrument [1] to Benjamin Franklin's kite experiment [2], lightning has played a defining role in mankind's development. Fundamentally, lightning is a powerful electric discharge that ionizes the air around to create plasma. Just as the mastery of fire once reshaped the trajectory of human advancement, progress in plasma science is enabling scientists to leverage its power in ways that could transform modern society.

1.1 What is Plasma?

Plasma is described as the fourth state of matter, with other states of matter being solid, liquid, and gas. It is generated when energy is applied to the gas phase, inducing ionization of the gas phase (see Figure 1.1). The electrons produced during the ionization process can collide with neutral gas molecules, initiating a cascade of chemical reactions, including ionizations, dissociations, and excitations. These collisions generate free electrons, ions, neutral species, radicals, excited species, electromagnetic fields, radiation (E(UV)/VIS), and heat [4, 5]. In this thesis, the electromagnetic fields, radiation and heat are referred to as physical properties of plasma and the chemical species that are generated are referred to as chemical properties of plasma. Plasma occurs naturally in phenomena such as the Sun [6], lightning [7], and auroras [8], and is widely utilized in technological applications such as materials processing (such as etching, deposition, and surface modification) [9], fluorescent lighting [10], high-voltage switchgear [11], and various

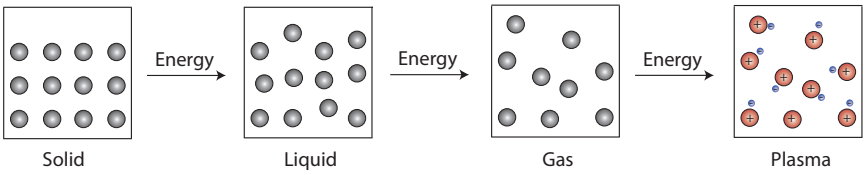

Figure 1.1: Representation of the different states of matter. In this figure, a solid is transformed into a liquid upon the addition of energy, and with further energy addition, the liquid transforms into a gas. Plasma is produced by supplying energy (thermal or electrical) to the gas phase to form an ionized gas phase consisting of charged and neutral species, radicals, and excited species. In the figure, the grey spheres represent the charge-neutral particles that constitute the solid, liquid and gas phases. The red and blue spheres represent the cations and electrons, respectively, produced upon the addition of energy to the gas phase. This figure is adapted from Ref. [3].

life-science applications such as wound healing [12], cancer treatment [13], and the promotion of plant growth [14].

1.2 Non-Thermal Plasma

Plasma contains electrons, ions and neutral gas particles. Considering a Maxwellian distribution for the velocities of electrons, ions, and neutrals, each of these components can have different corresponding temperatures, T_e (for electrons), T_i (for ions), and T_g (for neutral gas particles). Plasmas can be broadly categorized into Thermal Plasma (TP) and Non-Thermal Plasma (NTP) based on the temperatures of the components (T_e, T_i, T_g) [15] (see Figure 1.2). In thermal plasmas, the applied external energy ionizes the gas phase so that $T_i \approx T_e \approx T_g > 10^3$ K [16]. This is also called an equilibrium plasma, as the different components have approximately the same temperature. In contrast, in NTP, electrons are selectively excited and accelerated, while momentum transfer to ions and neutral species is minimized. For NTP, $T_i \approx T_g \approx 300$ K - 1000 K and $T_e > 10^4$ K [3, 16]. Because the different components have temperatures that are not equal, NTP is also referred to as non-equilibrium plasmas. It is also called cold plasma, as the ions and neutral gas particles, which are the dominant components in terms of number densities compared to electrons, are close to ambient temperature [17]. Since the temperatures of the heavy species (ions and neutral gas particles) in NTP are closer to ambient temperature compared to TP, NTP allows for lower thermal impact on the interacting matter (for example, silicon wafers for plasma

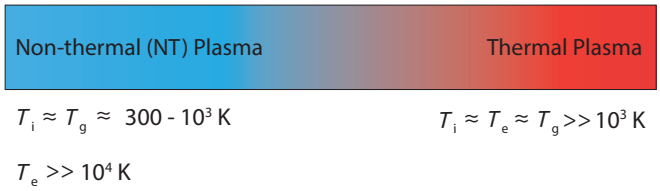

Figure 1.2: Two categories of plasma, thermal plasma and non-thermal plasma. In thermal plasma, the temperatures of electrons (T_e), ions (T_i), and neutral gas particles (T_g) are approximately the same, typically of the order of 10^3 K. In sharp contrast, non-thermal plasma is characterized by an electron temperature (T_e) of the order of 10^4 K, while the ion and gas temperatures (T_i and T_g) are much lower and approximately equal (300 - 1000 K). In this figure, the color transitions from blue to red as T_i and T_g increase. This figure is adapted from Ref. [3].

etching [18, 19], organic matter for plasma medicine applications [20]) compared to TP, while maintaining high reactivity (due to both the physical and chemical properties of plasma) [3]. Due to the minimal thermal impact of NTP on the interacting matter, NTP has applications ranging from materials processing [21] to biomedicine [20] and environmental remediation [22]. Historically, prior to the 1990s, the use of NTP in the commercial sector was largely confined to industries focused on integrated circuit development and polymer surface treatment [23]. The emergence of clinically oriented plasma technologies, such as kINPen®MED for chronic wound treatment [24], Canady Helios Cold Plasma [25] system for cancer therapy, and Prism Plasma for dermatological treatments [26], ushered in the broad integration of non-thermal plasma (NTP) into the field of biomedicine.

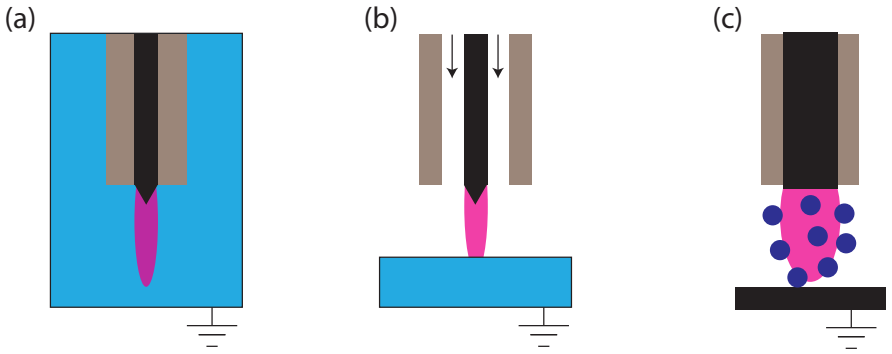

Figure 1.3: Representation of different types of plasma-liquid systems. (a) Example of direct discharge in liquid, where the plasma is initiated and sustained within the liquid medium, (b) gas phase plasma with liquid electrode, where the physical and chemical components of plasma produced in the gas phase are transferred into the liquid phase after passing through the gas–liquid interface, (c) gas phase plasma with dispersed liquid phase, which is an example of multiphase plasmas. Due to the large surface-to-volume ratio of dispersed liquid droplets, the mass transfer of reactive plasma species into the droplets is significantly enhanced. In this figure, the liquid is shown in blue, the plasma in pink, the dielectric in brown, and the metal electrodes in black. This figure is adapted from Ref. [4].

1.3 Plasma interactions with liquid

Typically, for the life science applications of NTP, plasma comes into contact with a liquid layer [27, 28]. At the reactor level, there are several configurations in which the plasma comes in contact with the liquid medium. These configurations can be broadly categorized as follows (see also Figure 1.3) [4]:

1. Direct liquid phase discharges
2. Gas phase plasmas producing reactivity in the liquid
3. Multiphase plasmas

These plasma-liquid reactors, as a whole, come in different configurations and voltage sources. While some sources are nanosecond-pulsed and use DC voltages for generating plasma, other sources could be AC excitation at 50–60 Hz, up to GHz-range microwave excitation [4]. Additionally, there can be different types of feed gas (the gas that is to be ionized). Noble gases such as He or Ar, ambient air,

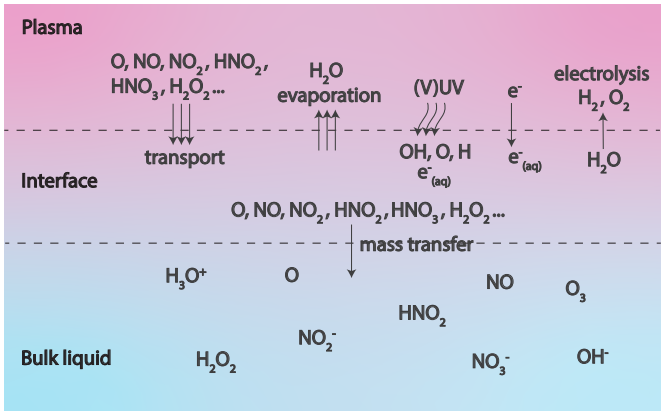

Figure 1.4: Schematic representation of the various mechanisms and reactive species present in the plasma gas phase, the liquid phase, and at the gas–liquid interface. The physical and chemical components of plasma come into contact with the liquid phase through the interface separating the plasma and liquid phases. This figure is adapted from Ref. [4].

and O_2 and N_2 containing gas mixtures are a few of the examples of feed gases. In this thesis, we focus on the gas-phase plasmas producing reactivity in the liquid reactor type. However, the results could also be useful for the multiphase plasma reactor type, as mass transfer of plasma species into the liquid droplets is involved in this reactor type. Upon contact with the liquid, the plasma delivers all of its components to the liquid medium (both the physical and chemical components of plasma) (see Figure 1.4). To understand how plasma impacts the surface under treatment, it is important to investigate the magnitude of the electromagnetic field delivered to the liquid, which species are generated, and their flux as a function of time and space in both the gas and liquid phases.

1.4 Plasma-liquid interactions for life science applications

Plasma-liquid interactions can play a major role in life science applications such as wound healing [29], dentistry [30], wastewater treatment [31, 32], and promoting plant growth and health [33]. In such applications, plasmas are created in O_2-N_2 gas mixtures, ambient air, O_2-N_2 gas mixtures with inert gases. The plasma created in the above-mentioned feed gas can create reactive oxygen and nitrogen species (RONS) in the gas phase, including, but not limited to, H_2O_2, NO, NO_2, HNO_2, HNO_3 and OH [3] (see Figure 1.5). RONS exhibit both antimicrobial

1

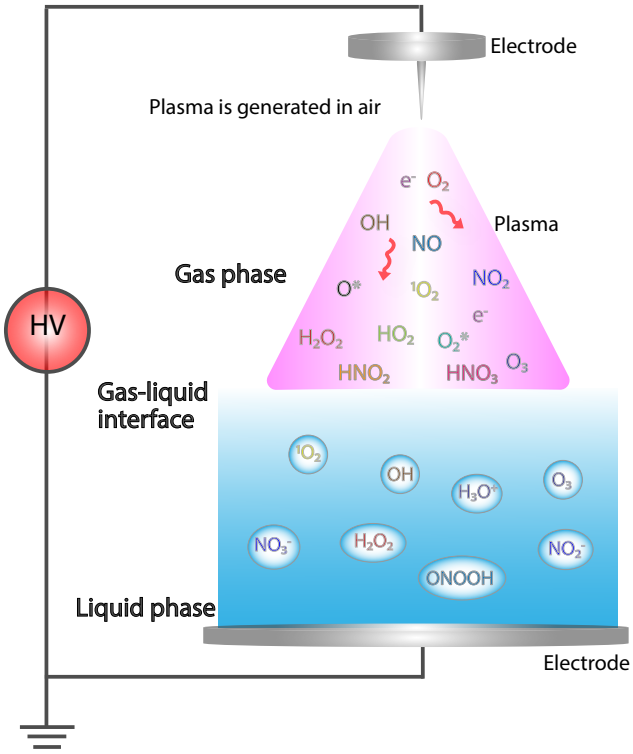

Figure 1.5: Illustration of a gas phase plasma injecting physical and chemical components of plasma (reactive oxygen and nitrogen species (RONS) along with the electrons and electromagnetic radiation) into the liquid phase. In this example, plasma is generated in air using a high voltage source (labelled as 'HV' in the figure).

properties (H_2O_2, O_3, OH) [33] and nutritional properties (NO_2^-, NO_3^-, NO) [34] that make RONS vital for the life science applications of NTP. For such life science applications, non-thermal plasmas are operated at ambient conditions (atmospheric pressure and room temperature). In these life science applications, RONS, together with plasma physics, interact (oxidation reactions) with biological matter, such as microorganisms and mammalian cells [35]. However, it is widely recognized that plasma chemistry plays a more dominant role in biological effects (cell apoptosis, wound healing) than plasma physics [36]. Consequently, a detailed understanding of the plasma chemistry (species generated in the gas and liquid phases, the concentration of species in both phases, the chemical reactions the species undergo in both phases, and the interaction of the species with organic matter) is essential [37–39].

1.5 Computational approaches to study plasma-liquid interactions

Experimental techniques can be used to characterize electromagnetic fields and species fluxes in both the gas and liquid phases. However, the investigation of plasma–liquid systems presents several inherent challenges. First, the plasma and liquid phases are strongly coupled, such that changes in one phase alter the state of the other phase. For example, when the pH of the liquid changes (due to aqueous phase chemical reactions), the electrical conductivity of the liquid changes, which in turn affects the electromagnetic field in the system [40]. Second, even at fixed operating conditions, such as fixed feed gas, voltage source, and reactor configuration, the properties of both the plasma and liquid phases (e.g., pH, electrical conductivity) evolve constantly over time [4]. Third, continuous plasma exposure induces temporal modifications of the surface and bulk liquid properties (such as electrical conductivity) [4, 41].

Computational approaches provide a complementary framework to experiments by providing information on the physical and chemical properties of plasma. Continuum level (fluid) and particle models are used to describe the gas phase (properties such as densities of plasma species, charge distribution, and electric field). These models provide properties such as particle velocity, fields, and chemical properties (concentration of species) as a function of time and space, which can be used to determine the flux and dosage of species delivered to the target substrate [42]. State-of-the-art models, which consider the entire gas and liquid phases, are fluid-type to the best of our knowledge [43–48]. These models are referred to as plasma-fluid models. In these models, a series of nonlinear partial differential equations that account for the conservation of mass, momentum, and energy coupled to the Poisson equation is considered [49]. Such models provide information about the physical and chemical properties of plasma, either only as

a function of time (0D) [50], or as a function of time and space (1D [43, 44], 2D [45–47], and 3D [48, 51]). In continuum models of plasma-liquid reactors, the Henry coefficient is an essential parameter for predicting the mass transfer of the species from the gas phase to the liquid phase. Henry coefficient is the proportionality constant in Henry's law, which states that the amount of gas dissolved in the liquid phase at equilibrium is proportional to the partial pressure of the gas [52]. The Henry coefficient and diffusion coefficients are used to incorporate the transport of species from the gas phase to the liquid phase.

1.6 Transport of reactive species to the liquid phase

Plasma fluid models are used to study the plasma-liquid systems at the reactor level [46]. In these models, mass transfer of the species from the gas phase to the liquid phase is quantified with Henry coefficients, and the spatial distribution of the species is determined using diffusion coefficients. However, experimental Henry coefficients for RONS are scarce. A few reasons for the data scarcity include chemical reactions of the species, low solubility leading to concentrations below the detection limits of measurement sensors, and the sensitivity of Henry coefficients to properties such as the salt concentration of the liquid and temperature [52]. Existing experimental measurements are also subject to uncertainties that can affect the predictive power of plasma fluid models [53]. In this work, we focussed on providing the Henry coefficients and diffusion coefficients for RONS. We also provide models of RONS that can later be used to study their interactions or their impact on biological molecules. In this thesis, the liquid considered is water, as in most life science applications, the liquid phase consists predominantly of water. Nevertheless, this procedure can be extended to other types of liquids (such as saline solutions, which we have investigated in Chapter 7 of this thesis). The transport properties of RONS in water were computed using molecular simulation techniques.

1.6.1 Molecular Simulations

Molecular simulation is a computational technique that allows for the computation of properties of a system by simulating the behaviour of constituent atoms and molecules using physics-based principles, such as Newtonian mechanics and Boltzmann statistics [54, 55]. It serves as a bridge between the microscopic length and time scales and the system-level properties. Molecular simulations typically operate on length scales on the order of nanometers and time scales on the order of nanoseconds [54]. To access larger spatial and temporal regimes, higher-level computational approaches, such as continuum or plasma fluid models, should be used [42]. Molecular simulations are a natural choice for computing the coefficients

describing the mass transport and diffusion. This is because diffusion is inherently a molecular-scale ($\sim$ nm, $\sim$ ns) phenomenon [56], and determining the Henry coefficient requires extrapolation to the limit of infinite dilution [52], both of which can be accurately addressed using molecular simulation methods [54]. The molecular simulations in this work use classical force fields to characterize the interaction between the constituent molecules.

Classical force fields are a collection of analytical functions and the associated parameters that describe the intramolecular and intermolecular interactions of the molecules [57]. These force fields are termed "classical" as the functional forms in these force fields are predefined and do not change during simulations. The choice of classical force fields is motivated by their ability to provide an optimal balance between statistical reliability, accessible system sizes, and computational efficiency, particularly in comparison with *ab initio* methods or machine-learned force field approaches [58, 59]. These characteristics make the classical force fields well-suited for evaluating thermodynamic and transport properties of the species considered in this work. In the rest of the thesis, the term "force fields" will be used to refer to classical force fields. To investigate the properties (solubility and diffusion) of RONS, we need interaction potentials that describe the interaction of RONS with other molecules of the same type, for RONS with water, and water-water interactions. For water-water interactions, there are water force fields available in the literature, such as the TIP3P [60], TIP4P/2005 [61], and TIP5P-E [62, 63] models [64]. These models are well-validated and tested. However, this is not the case for the RONS, as we do not have accurate force fields for all RONS to accurately characterize the RONS-RONS or RONS-water interactions. These force fields are important because the Henry coefficients and diffusion coefficients are severely impacted by the quality of the force field used to describe the RONS. To determine the suitability of the force field, it is verified whether the force field has been previously validated against relevant experimental data. If such validation exists, the force field is used to compute relevant thermodynamic and transport properties, such as the Henry and diffusion coefficients. In the absence of prior validation, a systematic validation of the force field is performed, in which selected properties are computed and compared to corresponding experimental data. In this work, experimental thermodynamic properties, such as liquid phase densities and the vapor-liquid equilibrium (where vapor and liquid phases of species are in thermodynamic equilibrium) properties, were used to compare with the computed properties. In the absence of any experimental data for the species, *ab initio* quantum mechanical calculations are performed, and the interaction potential is fitted to the energy surfaces obtained from the quantum mechanical calculations (see Figure 1.6).

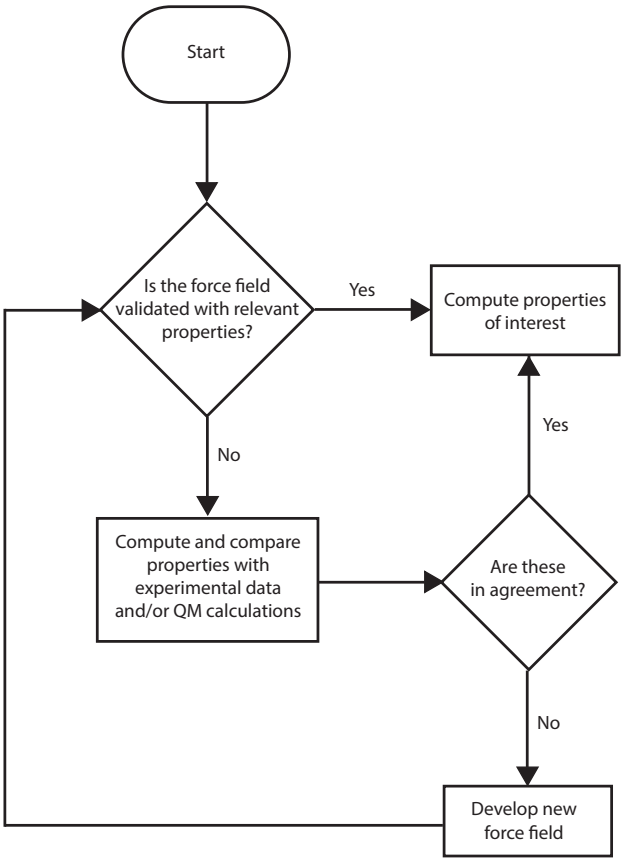

Figure 1.6: Workflow for the validation and development of force fields for reactive oxygen and nitrogen species. The procedure begins by determining whether the available force field for the species in the literature has been validated with respect to relevant experimental properties. If validation exists, the force field can be used to compute the properties of interest. If the validation does not exist, key thermodynamic properties, such as densities, are computed and compared with corresponding experimental data. Results obtained from quantum mechanical calculations can also be used to validate the force field. This comparison determines whether the force field can be used for further computations or whether the development and parametrization of a new force field are required.

1.6.2 Computing the equilibrium of chemical reactions

Classical force field-based molecular simulations are not without challenges. Chemical reactions, which also play a crucial role in life science applications, cannot be adequately described using a classical force field alone, as bond dissociations are not explicitly represented within such frameworks. The equilibrium of chemical reactions can be investigated in the reaction ensemble [65–67]. The reaction ensemble is used to determine the chemical reaction equilibrium by integrating ideal gas behaviour with changes arising from interactions of the reactants with a disruptive medium (in this case, the liquid). In addition to the force fields, the reaction ensemble requires the isolated molecule partition functions of the species (q_{total}) involved [68]. q_{total} is the sum over all energy states of an isolated molecule, and its logarithm is proportional to the Gibbs energy of formation [54, 69]. It is important to note that the isolated molecule partition functions are assumed not to depend on the medium, an assumption that is generally valid in most cases [70]. Given the isolated molecule partition functions of the species and the force fields that describe the interactions of the species, one can compute the equilibrium constants (K) of the reactions in which the species are involved. It should be noted that the methodology used in this thesis enables the investigation of chemical reaction equilibrium, but not the kinetics of the chemical reaction. Investigating reaction kinetics requires the resolution of reaction pathways and the computation of associated energy barriers, which can be achieved with *ab initio* quantum mechanical calculations.

1.7 What is investigated in this thesis?

In general, reactive oxygen and nitrogen species (RONS) can be classified according to the occupancy of their outer electron shell (whether it is complete or incomplete) and their net charge, as molecules (HNO_2, H_2O_2, and N_2O_4), radicals (NO_2, NO and O), or ions (NO_2^-, NO_3^-, and H_3O^+). In this thesis, a selection of species from each category was investigated (see Figure 1.7). In addition, the electronic spin states (which depend on the arrangement of electrons in the energy levels) of the species play a major role in determining their interactions with water (diffusion and solubility). We investigated the differences in the interaction for atomic oxygen, O, in its triplet state, O(^{3}P) (has two unpaired electrons that are parallel in its outer shell) and in its singlet state, O(^{1}D) (all the electrons in the outer shell are paired) and quantified the differences in the diffusion and Henry coefficients.

The RONS were further classified based on whether the species undergoes hydrolysis or not. For species, such as H_2O_2 and NO that do not react with water, the Henry coefficients (H_s^{cp}) and self-diffusion coefficients (D) are computed using molecular simulations (see Figure 1.8). For H_2O_2, two different force fields were available in the literature to represent the species. We computed the interaction

1

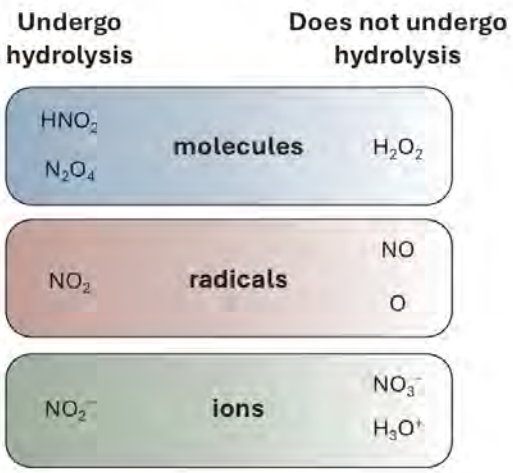

Figure 1.7: List of species investigated in this work, categorized according to whether the species undergo hydrolysis. The species that undergo hydrolysis includes, HNO_2 ($HNO_2 + H_2O \rightleftharpoons {NO_2}^- + H_3O^+$), N_2O_4 ($N_2O_4 + 2\,H_2O \rightleftharpoons HNO_2 + {NO_3}^- + H_3O^+$), NO_2 ($2\,NO_2 + 2\,H_2O \rightleftharpoons HNO_2 + {NO_3}^- + H_3O^+$) and NO_2^-. Note that the hydrolysis reaction of NO_2^- ($NO_2^- + H_2O \rightleftharpoons HNO_2 + OH^-$) is not included in this work as it is not a thermodynamically favourable reaction at ambient conditions ($\sim$ 298 K and 1 bar) studied in this work [69]. The species are further classified as molecules (closed-shell, charge-neutral species), radicals (charge-neutral species containing an unpaired electron) and ions (closed-shell charged species). Plasma generates atomic oxygen (O) in different spin states, the ground ($O(^3P)$) and excited states ($O(^1D)$), which were also investigated in this work.

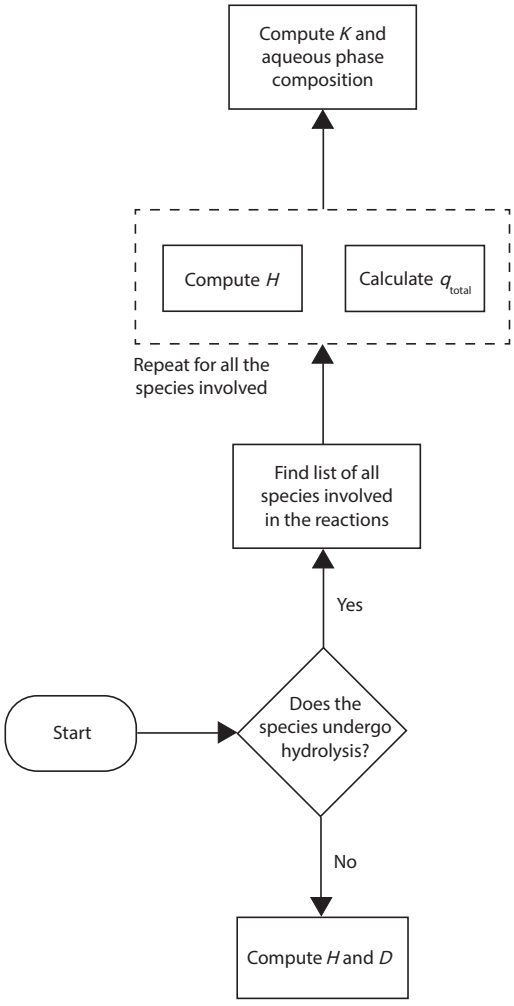

Figure 1.8: Workflow for computing thermodynamic and transport properties of a species. If the species does not undergo hydrolysis to form reaction products, the Henry coefficients (H_s^{cp}) and self-diffusion coefficients (D) are computed using molecular simulation techniques. If the species undergoes hydrolysis, all the species that are involved in the reactions are identified, the Henry coefficients are computed, and the isolated molecular partition functions (q_{total}) of each species are calculated using analytical functions which are described in Chapter 2. These quantities are used to determine the equilibrium constants of the reaction (K) and the aqueous phase compositions.

of H_2O_2 with different water models and investigated which combination of force fields predicts transport and thermodynamic properties in better agreement with the experiments. In the case of NO, for which no sufficiently accurate force field was available, we developed a new force field validated with the experimental vapor-liquid-equilibrium (VLE) properties of NO. We needed to take into account the chemical dimerization of NO at the VLE temperatures [71, 72]. To represent the dimerization reaction in the vapor and liquid phases, we used the reaction ensemble with the isolated molecule partition function of NO and its dimer, $(NO)_2$. The newly developed force field was used to predict the interaction behaviour of NO in water. Plasma generates atomic oxygen in the ground and excited states. Since electronic spin states are not explicitly considered in a classical force field, state-specific force fields were developed for atomic oxygen based on *ab initio* quantum mechanical calculations. Using these newly developed force fields, values of H_s^{cp} and D for atomic oxygen in water are computed.

For species that undergo hydrolysis reactions, all species involved in the hydrolysis process and subsequent reactions are first identified. For each of these species, the Henry constant and isolated molecule particle function (q_{total}) are computed. Upon completion of this procedure for all the relevant species in the reactions, the equilibrium constants of the reactions (K) and the resulting aqueous phase composition are determined (see Figure 1.8). We considered NO_2 as an example of a species that undergoes hydrolysis. We provide a model that considers NO_2 and its dimer N_2O_4 in the gas phase. The gas-phase composition is evaluated as a function of temperature and pressure. The aqueous-phase composition for a given gas-phase composition was computed. To determine the aqueous speciation resulting from NO_2 hydrolysis, all relevant reactions associated with its hydrolysis were considered. For each species of the reaction, a force field is required, using which the solubility of each species is computed. We also required the isolated molecule partition function of each of the species involved in the reaction. We combined these data and built a model to compute the equilibrium constants of the reaction and the composition of the liquid phase as a function of temperature and pressure.

1.8 Scope and outline of this thesis

This thesis is organized as follows. The methodologies used to compute the thermodynamic properties and parameters of the reactive oxygen and nitrogen species are explained in Chapter 2. A brief discussion of the algorithms, ensembles and molecular simulation methods is presented in this chapter.

In Chapter 3, existing force fields for H_2O_2 in the literature, those developed by Cordeiro [73] and Orabi & English [74], were validated by reproducing the experimental anhydrous H_2O_2 densities. The pure densities of H_2O_2 computed

using the Orabi force field were in excellent agreement with the experimental densities for a temperature range of 253 K to 353 K. The thermodynamic and transport properties (densities, viscosities, and self-diffusion coefficients) of aqueous solutions of H_2O_2 were computed for the entire composition range (H_2O_2 mole fractions of 0–1.0) at 298 K and 1 bar. Four different water models were used, namely, TIP3P [60], mTIP3P [75], TIP4P/2005 [61], and TIP5P-E [62, 63], in combination with the force fields for H_2O_2. Among the combinations, the Orabi FF - TIP4P/2005 combination predicted the aqueous densities, viscosities and self-diffusion coefficients of aqueous H_2O_2 solutions in good agreement with the corresponding experimental values. However, due to the anomalous attraction between the water molecules and the H_2O_2 molecules, as confirmed by the radial distribution functions, the viscosities of the H_2O_2 - TIP5P-E systems were much higher than the experimental values. This led to very small values for the self-diffusion coefficients of H_2O_2 and water molecules. Additionally, we computed the excess chemical potentials of H_2O_2 in water and thereby the Henry coefficients of H_2O_2. The Cordeiro force field, in combination with the TIP3P and mTIP3P water force fields, was observed to predict Henry coefficients within the range of experimental values.

In Chapter 4, a new force field was developed for the reactive NO-$(NO)_2$ system. The new force field accurately reproduces the vapor-liquid equilibrium (VLE) properties of the NO-$(NO)_2$ system, including, coexistence vapor-liquid densities, dimer mole fractions in liquid phase, saturated vapor pressures, and heats of vaporization, in excellent agreement with the experimental values for the temperature range 120 K - 170 K. The VLE properties of the pure NO and $(NO)_2$ system were compared with the properties predicted using existing force fields for NO, those developed by Lachet *et al.* [76] and Zhou *et al.* [77]. For the pure NO system, the VLE properties predicted using the new force field were in good agreement with those predicted using the Lachet FF. However, there was a large deviation between the predictions with the newly developed force field and the Zhou FF. This discrepancy can be attributed to the omission of dimer formation at the boiling point of NO in the work of Zhou and co-workers, which corresponds to the temperature at which the Zhou FF was validated with respect to the experimental values of density and heat of vaporization. For pure $(NO)_2$, deviations of the predicted VLE properties using the new force field with those computed with the Lachet FF were quantified. We also performed a sensitivity analysis to investigate the effects of L-J parameters (σ and ϵ/k_B of NO and $(NO)_2$) as well as the atomization energy of $(NO)_2$, $D_{0,(NO)_2}$, on the VLE properties of the reactive NO-$(NO)_2$ system. The results indicate that the VLE properties are affected by both the L-J parameters as well as the atomization energy, which is in sharp contrast with the NO_2-N_2O_4 system, where the VLE is dominated by q_{total}. This difference could be attributed to the higher atomization energy of N_2O_4 compared to $(NO)_2$.

In Chapter 5, thermodynamic and transport properties of NO in water are presented. The Saji FF, which was developed in Chapter 4, was used to model NO. The self-diffusion coefficients of NO in water for three different concentrations of the solute for temperatures ranging from 273 - 333 K were computed and were found to be in good agreement with the experimental values. The Henry coefficient of NO was also computed for the same temperature range and was compared with the experimental data at 298 K. The predicted values were found to be in agreement with experiments. Nitrous and nitric acids are formed upon the hydrolysis of NO_2. Nitrous acid can further undergo ionization reaction to form nitrate and hydronium ions, and it may also disproportionate to form nitric acid, nitric oxide and water. To analyze the chemical equilibrium of the above reactions, the CASpy solver [68], a chemical reaction equilibrium solver, was modified to handle arbitrary constraints in chemical reaction equilibria. NO_2 dimerizes to form N_2O_4, and therefore, the gas phase composition at different pressures and temperatures is calculated using the gas phase equilibrium constant. The calculations show that the dimer concentration in the gas phase increases with increasing pressure and decreasing temperature. The hydrolysis reaction of NO_2 was found to be an exothermic reaction as the equilibrium of the reaction shifts to the reactant side with an increase in temperature. Consequently, the pH of the system decreases with increasing pressure and increases with increasing temperature. A brief discussion on the importance of accurate data for parameters such as the atomization energy for determining the reaction equilibrium is also provided in this chapter.

In Chapter 6, state-specific force fields were parameterized to describe the interaction between atomic oxygen and water on the triplet and singlet energy surfaces. Using the newly developed force fields, the self-diffusion coefficients and Henry coefficients of the atomic oxygen were computed for the temperature range of 273 - 333 K. On the triplet energy surfaces, the ground state exhibit the highest values of D and H_s^{cp}, while on the singlet energy surfaces, the first excited state, showed the highest values. We also performed a systematic analysis to identify the influence of individual L-J parameters (σ and ϵ/k_{B}) on D and H_s^{cp}. This was performed by varying the values of σ and ϵ/k_{B} for a charge-neutral particle in water at temperatures in the range 300 - 350 K. The results indicate that the self-diffusion coefficients are more sensitive to the particle size (σ), while the Henry coefficients are more sensitive to the strength of the interaction with water (ϵ/k_{B}). Additionally, it was observed that the dissolution process changes from endothermic to exothermic once the solute-solvent interactions become stronger than the solvent-solvent interactions.

In Chapter 7, a systematic analysis was performed to identify the influence of salt concentrations on D and H_s^{cp} of RONS in water. The D and H_s^{cp} were computed for charge-neutral particle in water, parameterized by varying values of σ and ϵ/k_{B} at a temperature of 300 K and a pressure of 1 bar. The results

indicate that D decreases with increasing salt concentrations (a ca. 12% decrease on average was observed for an increase in molality of 1.00 m). An increase in salt concentrations leads to a decrease in the values of H_s^{cp} (ca. 22% decrease for a 1.00 m increase in salt concentration). This indicates a salting-out effect for the charge-neutral particles. Key conclusions and outlook are also presented in the thesis.

The methodologies used in this work allow modeling of the plasma–water system by incorporating diffusion coefficients, Henry coefficients, and chemical reaction equilibrium constants.

1

Chapter 2

Theoretical Framework

In this chapter, the fundamental principles underlying molecular simulation techniques, such as Monte Carlo and Molecular Dynamics, are introduced, followed by a description of the algorithms used. This chapter also provides a concise overview of the force fields and the statistical ensembles used in the simulations. Finally, the thermodynamic and transport properties computed using these techniques are outlined. For more information on the simulation techniques, we would like to refer the reader to Refs. [54, 55, 78].

2.1 Force Fields

To compute the properties of a molecular system, it is necessary to characterize the interactions between the molecules within the system. While quantum mechanical methods can provide highly accurate interaction potentials, these methods are computationally expensive for large systems (> 100 atoms). For these large systems, the interactions are typically represented using functional forms. A force field consists of a set of functions together with associated parameters that describe both the bonded and non-bonded interactions of the molecules in the system.

The potential energy functions that describe the bonded interactions (i.e interactions formed by a chemical bond) within a molecule (U_{bonded}) consist, for example, of functions that define the bond stretching (U_{bond}), angle bending (U_{bend}), and dihedral torsion (U_{dihedral}) potentials. Additional potential energy functions can also be incorporated within a force field. A comprehensive review of such terms can be found in Ref. [79]. Figure 2.1 shows an illustration of these bonded interactions.

2

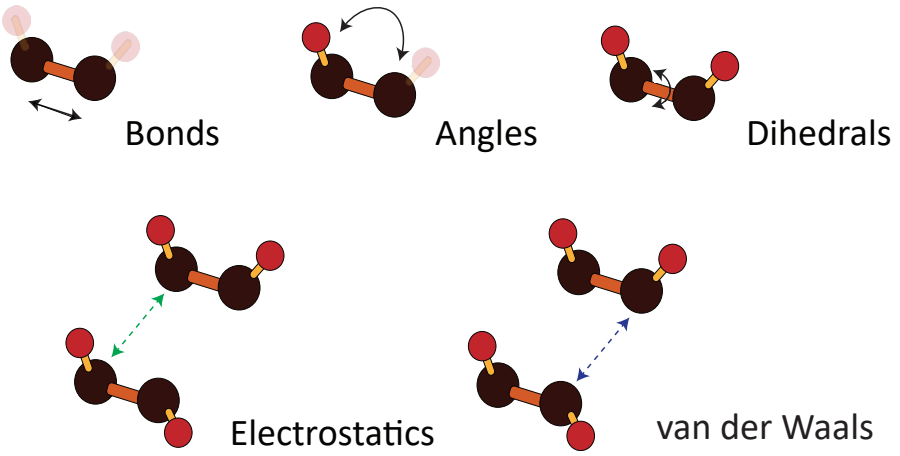

Figure 2.1: Bonded and non-bonded interactions of a molecule that together constitute its force field. In this figure, the bonded interactions include bond stretching, angle bending, and dihedral torsion, while the non-bonded interactions comprise electrostatics and van der Waals interactions. These interactions can also be categorized as intramolecular or intermolecular interactions. Bonded interactions are always intramolecular, whereas non-bonded interactions can be either intermolecular or intramolecular.

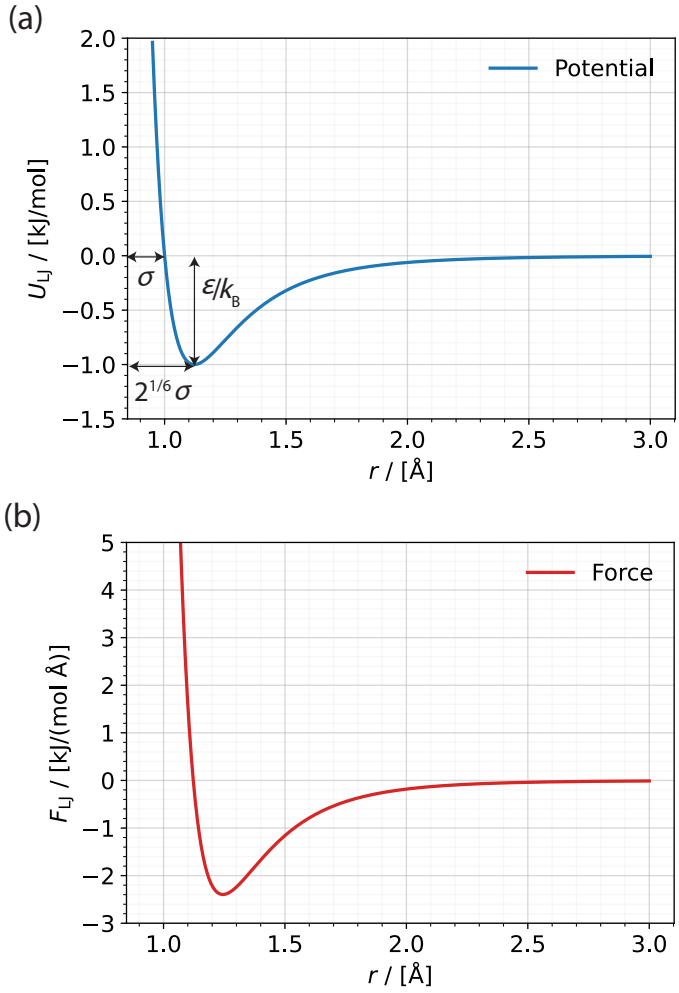

Figure 2.2: (a) The Lennard-Jones potential (U_{LJ}) and (b) the corresponding force ($F_{\mathrm{LJ}} = -\nabla U_{\mathrm{LJ}}$) for two identical single-site particles characterized by σ = 1 Å and ϵ/k_{B} = 120 K ($\sim$ 1 kJ/mol), as a function of the intermolecular separation (r) as the particles approach one another.

Non-bonded interactions are interactions of atoms that are not formed by a chemical bond but interact via van der Waals or electrostatic interactions. The Lennard-Jones (L-J) potential is a commonly used potential energy function that is used to model the van der Waals interactions between atoms.

$$E_{\mathrm{LJ}} = 4\epsilon_{ij}\left[\left(\frac{\sigma_{ij}}{r_{ij}}\right)^{12} - \left(\frac{\sigma_{ij}}{r_{ij}}\right)^{6}\right]. \tag{2.1}$$

Here, ϵ represents the depth of the potential well, σ represents the distance at which the particle-particle interaction energy equals zero and r_{ij} is the distance between atoms i and j. The L-J potential consists of both attractive and repulsive terms. While the attractive part (where $F_{\mathrm{LJ}} > 0$) represents the van der Waals interactions, the repulsive part ($F_{\mathrm{LJ}} < 0$) is an empirical approximation that denotes the repulsive force arising from Pauli's exclusion principle [80]. The mixing rules for the L-J parameters for two dissimilar non-bonded atoms are given by either Lorentz-Berthelot mixing rules [81]

$$\sigma_{ij} = \frac{\sigma_i + \sigma_j}{2} \tag{2.2}$$

$$\epsilon_{ij} = \sqrt{\epsilon_i \epsilon_j} \tag{2.3}$$

or by the geometric average [55]

$$\sigma_{ij} = \sqrt{\sigma_i \sigma_j} \tag{2.4}$$

$$\epsilon_{ij} = \sqrt{\epsilon_i \epsilon_j}. \tag{2.5}$$

As computing the non-bonded interactions is a computationally expensive task, the non-bonded interaction potentials are truncated at a cutoff distance. Thus, the non-bonded interactions are calculated only for atoms that lie within the cutoff radius. The energy contribution of particles outside the cutoff radius can be approximated by analytic tail corrections of the form [54]

$$E_{\mathrm{LJ}}^{\text{tail correction}} = \frac{1}{2}\sum_{i,j}\frac{16\pi N_i N_j \epsilon_{ij}}{V}\left(\frac{\sigma_{ij}^{12}}{9R_c^9} - \frac{\sigma_{ij}^{6}}{3R_c^3}\right) \tag{2.6}$$

where, N_i, N_j is the number of atoms of type i and j, respectively, $\epsilon_{i,j}$ and $\sigma_{i,j}$ are the L-J parameters for the interaction between atoms of type i and j, V is the volume of the simulation box, and R_{c} is the cutoff radius. The energy correction term in Equation 2.6 is specific to the Lennard–Jones potential. Alternative interaction potentials require different functional forms for the corresponding tail correction.

The electrostatic interactions are modelled by the Coulombic potential energy function

$$E_{\text{electrostatic}} = \frac{1}{4\pi\epsilon_o}\frac{q_i q_j}{r_{ij}}, \tag{2.7}$$

where ϵ_o is the permittivity in vacuum, q represents the atomic partial charges and r_{ij} is the distance between atoms i and j. The Coulombic potential converges as $\frac{1}{r}$. A potential that decays as $1/r^n$ in a d-dimensional space is conditionally convergent if $n < d$ [55]. Conditional convergent implies that the result of the summation depends on the order of summation. Since the Coulombic potential converges as $\frac{1}{r}$, it is conditionally convergent in two and three-dimensional systems. In contrast, the Lennard–Jones potential decays with an attractive term proportional to r^{-6}, for which the exponent of r exceeds the spatial dimensionality in a 3D system ($n = 6 > d = 3$), and therefore is absolutely convergent [55]. Note that the L-J potential also has a repulsive term with $n = 12$, which is much larger than the value of d for a 3D system. Therefore, unlike the Lennard-Jones potential, the Coloumbic potential has a range larger than the common cutoff radius used in simulations ($\sim 9 - 12$ Å) and therefore would miss part of the interactions if only the interactions within the cutoff were computed [54]. Moreover, truncating Coloumbic interactions would lead to spurious dipole moments and non-physical rearrangement of molecules, which leads to artificial peaks in the radial distribution functions [82, 83].

2.1.1 Ewald summation

To overcome the problem of conditional convergence of Coloumbic interactions, Ewald summations can be used in molecular simulation techniques. Ewald summation overcomes the issue of conditional convergence by subtracting and adding a diffuse charge distribution (ρ^G) around a point charge [54]. The point charges in the system can be described using Dirac delta functions, that is centered on an atom site

$$\rho_i(\mathbf{r}) = \sum_{i=1}^{n} q_i \delta(\mathbf{r} - \mathbf{r}_i). \tag{2.8}$$

The diffuse charge distribution, ρ^G, is given by

$$\rho_i^G(\mathbf{r}) = \sum_{i=1}^{n} q_i \left(\frac{\alpha}{\pi}\right)^{\frac{3}{2}} e^{-\alpha(\mathbf{r}-\mathbf{r}_i)^2} \tag{2.9}$$

where q_i is the point charge on the atom on site i and α is the width of the Gaussian distribution. The subtraction and addition of ρ^G from the point charges leads to

$$\rho_i(\mathbf{r}) = (\rho_i(\mathbf{r}) - \rho_i^G(\mathbf{r})) + \rho_i^G(\mathbf{r}). \tag{2.10}$$

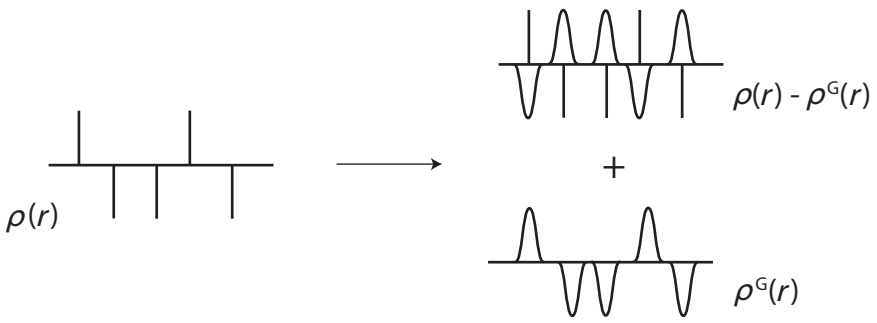

Figure 2.3: Schematic representation of the Ewald method in which a diffuse charge distribution, ρ^G, is subtracted from and added to the point charges (described by Dirac delta functions), ρ (see Equation 2.10). The electrostatic potential experienced by a particle is decomposed into three contributions, *(1)* potential due to diffuse charge distribution (computed in reciprocal space), *(2)* potential due to a set of point charges, each paired with a neutralizing counter-charge distribution (computed in real space), and *(3)* the self-correction term which is to correct the over-counting of the interaction of a particle with its own neutralizing counter-charge distribution. This figure is adapted from Ref. [54].

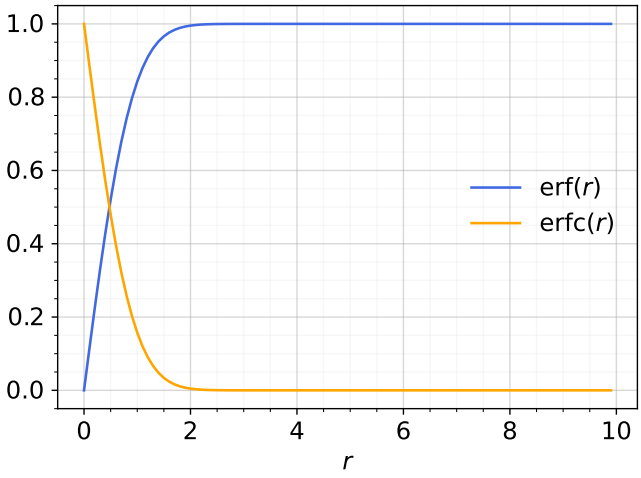

Figure 2.4: Plot of the error function and the complementary error function.

The total Coulombic potential energy U_e from the charge density given in Equation 2.10 can be written as [54, 57]

$$U_{\mathrm{e}} = U_{\mathrm{e,\ real}} + U_{\mathrm{e,\ reciprocal}} - U_{\mathrm{e,\ self}}. \tag{2.11}$$

Here, $U_{\mathrm{e,\ real}}$ and $U_{\mathrm{e,\ reciprocal}}$ are the Coulombic potential energies due to $(\rho_i(\mathbf{r}) - \rho_i^G(\mathbf{r}))$ and $\rho_i^G(\mathbf{r})$, respectively. $U_{\mathrm{e,\ self}}$ is the term for the correction of self-interaction between the charge distribution centred at a point charge q_i and the point charge q_i. $U_{\mathrm{e,\ real}}$ is computed in the real space within the cutoff radius and is given by

$$U_{e,\mathrm{real}} = \frac{1}{4\pi\epsilon_o} \sum_{i<j}^{n} \frac{q_i q_j \mathrm{erfc}(\sqrt{\alpha} r_{ij})}{r_{ij}}. \tag{2.12}$$

where $\mathrm{erfc}(x)$ is the complement of $\mathrm{erf}(x)$, i.e.,

$$\mathrm{erfc}(x) = 1 - \mathrm{erf}(x). \tag{2.13}$$

$\mathrm{erf}(x)$ is the error function and is defined as

$$\mathrm{erf}(x) = \frac{2}{\sqrt{\pi}} \int_0^x \mathrm{e}^{-t^2}\, \mathrm{d}t. \tag{2.14}$$

A plot of the error function and the complementary error function is shown in Figure 2.4. Unlike $\frac{1}{r}$, $U_{e,\mathrm{real}}$ in Equation 2.12 can be easily truncated at 9 - 12 Å,

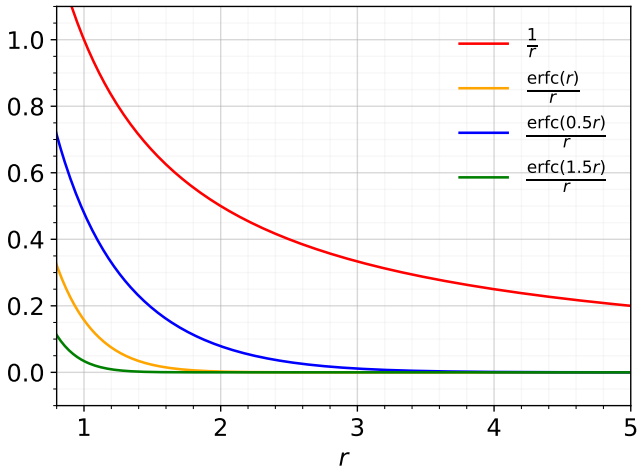

Figure 2.5: $\frac{\text{erfc}(r)}{r}$ as a function of r. This figure also contains plots for $\frac{1}{r}$, $\frac{\text{erfc}(0.5r)}{r}$, and $\frac{\text{erfc}(1.5r)}{r}$ as a function of r. This figure illustrates that $\frac{\text{erfc}(r)}{r}$ decays to zero at large values of r.

provided that α is chosen wisely. This can be seen from Figure 2.5. $U_{\text{e, reciprocal}}$ is computed in the reciprocal space and is given by

$$U_{e,\text{reciprocal}} = \frac{1}{4\pi\epsilon_o}\left(\frac{2\pi}{V}\sum_{k\neq 0}\frac{1}{k^2}|\rho(\mathbf{k})|^2 e^{-k^2/4\alpha}\right), \tag{2.15}$$

where $\mathbf{k} = (2\pi/L)\mathbf{l}$, L being the length of the cubic box, and $\mathbf{l} = (l_x, l_y, l_z)$ are the lattice vectors in the reciprocal space. The correction term, $U_{\text{e, self}}$, is given by

$$U_{e,\text{self}} = \frac{1}{4\pi\epsilon_o}\left(\left(\frac{\alpha}{\pi}\right)^{\frac{1}{2}}\sum_{i=1}^{n} q_i^2\right). \tag{2.16}$$

Substituting Equations 2.12, 2.15 and 2.16 in Equation 2.11, one obtains

$$U_e = \frac{1}{4\pi\epsilon_o}\left(\sum_{i<j}^{n}\frac{q_i q_j \text{erfc}(\sqrt{\alpha}r_{ij})}{r_{ij}} + \frac{2\pi}{V}\sum_{k\neq 0}\frac{1}{k^2}|\rho(\mathbf{k})|^2 e^{-k^2/4\alpha} - \left(\frac{\alpha}{\pi}\right)^{\frac{1}{2}}\sum_{i=1}^{n} q_i^2\right). \tag{2.17}$$

From Equation 2.9 it is evident that a higher value of α would lead to a narrower Gaussian charge distribution. This would lead to a more efficient screening of the point charge and faster convergence in real space. However, in the reciprocal space,

a narrower Gaussian distribution (due to high values of α) would require more number of k-vectors (N_k) for the computation of the reciprocal space component of the Coloumbic potential. In contrast, a lower α, means a lower N_k in the reciprocal space, but lead to slower convergence in real space. Therefore, there exists a trade-off between α and N_k [55]. As a first guess one can choose $\alpha = \frac{3.2}{R_\mathrm{c}}$ and $k = 8$ [79].

2.1.2 Periodic Boundary Conditions

Molecular simulations are used to predict the bulk behaviour of the systems. However, the finite number of molecules contained within a simulation cell is, in general, insufficient to fully represent macroscopic bulk conditions. In a three-dimensional system, the fraction of molecules at or near the surface scales as $N^{-1/3}$ (where N is the total number of molecules) [54], implying that surface effects are disproportionately large for small systems. However, it is not computationally feasible to use large simulation cells as the computational time would be prohibitive. Therefore, to simulate bulk phase behaviour, one needs periodic boundary conditions (PBC). In this approach, the finite simulation cell containing the system of interest is replicated in all spatial directions to form an infinite periodic lattice of identical cells. When a particle moves in the central cell, all its replicas also move identically in their respective cells. When a particle moves out of a cell, its replica will move into the cell, keeping the number of particles constant. In this setup, the particles in the simulation cell can also interact with particles in the other replica simulation cells. To avoid multiple interactions between a pair of particles (for computational efficiency), the minimum image convention is adopted, where only the interaction is considered for which the interatomic distance is minimum (see Figure 2.6) [54, 57].

However, using PBC can create artificial correlations between the simulation cell and its replicas, which are not present in the macroscopic bulk system. Such artifacts can be minimized by using a sufficiently large simulation cell. The adequacy of a given system size is commonly assessed through validation studies. Although densities and viscosities exhibit limited finite-size effects, self-diffusion coefficients are influenced by the size of the simulation box and are corrected for their finite-size effects [84, 85]. Only at very low densities, computed values of η depend on the system size [86].

2.2 Ensembles

In a classical formulation, the dynamic state of a particle is described by its position and momentum coordinates. Therefore, a total of 6 coordinates are needed to describe the state of a particle, 3 each for position and momentum. For

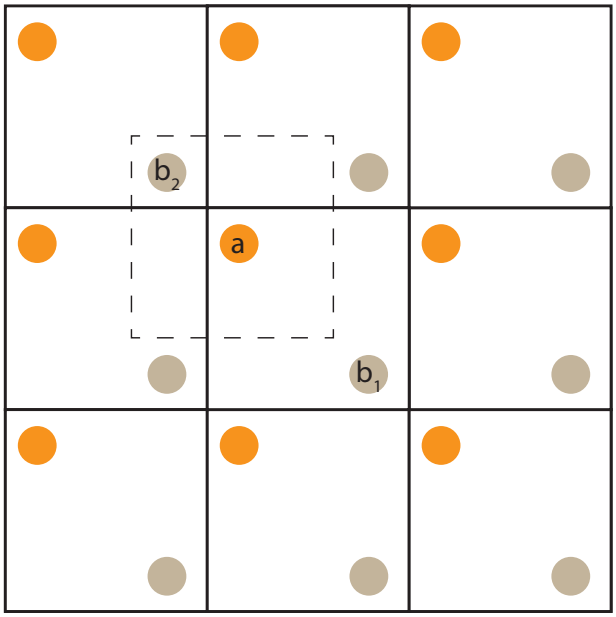

Figure 2.6: A two-dimensional representation of the periodic boundary conditions in which the central simulation cell is replicated in all directions to generate an infinite periodic lattice. The dashed box illustrates the minimum image convention applied to a particle 'a' in the central simulation cell. The minimum image convention is used to avoid multiple interactions between a pair of particles. The minimum image convention implies that the cutoff (R_c) must be smaller than half the box size in each direction. In this figure, particle 'a' interacts with 'b_2' instead of 'b_1' as 'b_2' is the nearest (in terms of distance) image to 'a'.

a system of N particles, $6N$ coordinates are needed to describe the system. This $6N$ dimensional space is called the phase space. A point in this phase space is called a microstate. A macrostate describes the macroscopic properties of the system such as the internal energy, temperature, pressure, etc. These macroscopic properties can be achieved by different combinations of the microstates. The collection of the microstates that obey the macroscopic constraints of the system is defined as an ensemble. The statistical averages of the ensemble are used to calculate observable thermodynamic quantities such as temperature, pressure, etc. A brief description of the ensembles used in this work is provided in the subsections below. For more detailed information, the reader is referred to Refs. [54, 55].

2.2.1 Statistical Ensembles

Canonical Ensemble

In the canonical ensemble, the number of molecules (N), the volume (V), and the temperature (T) are fixed. The partition function Q for the NVT ensemble is written as

$$Q = \frac{1}{N!\ h^{3N}} \int \int \exp\left[-\beta H(\mathbf{r}^N, \mathbf{p}^N)\right]\ \mathrm{d}\mathbf{r}^N\ \mathrm{d}\mathbf{p}^N, \tag{2.18}$$

where H is the Hamiltonian of the system and N is the number of particles. h is Planck's constant and h^{3N} is the volume of a microstate. For a N particle system, $\mathbf{r}^N$ is defined as $\{\mathbf{r}^N = \mathbf{r}_1, \mathbf{r}_2,...\mathbf{r}_N\}$ and $\mathbf{p}^N$ is defined as $\{\mathbf{p}^N = \mathbf{p}_1, \mathbf{p}_2,...\mathbf{p}_N\}$. The classical limit is defined when $\Lambda << d$. Here, Λ is the de Broglie wavelength given by $\Lambda = \frac{h}{\sqrt{2\pi M k_\mathrm{B} T}}$ and d is the average interatomic distance between the particles. M is the sum of the masses of all atoms in the molecule, and T is the temperature. In the classical limit, one can separate the integrals over momenta and space and evaluate the integrals separately. It can be shown that once the integration over momenta is calculated, Equation 2.18 simplifies to [54]

$$Q = \frac{1}{N!\ \Lambda^{3N}} \int \exp\left[-\beta U(\mathbf{r}^N)\right]\ \mathrm{d}\mathbf{r}^N, \tag{2.19}$$

where U is the potential energy of the system that does not depend on the momenta. Using a coordinate vector of the atoms in the system scaled by the inverse length of the simulation box, $\mathbf{s}$ ($\mathbf{s} = \mathbf{r}/L$), one can write the partition function for the NVT ensemble as [54]

$$Q_\mathrm{NVT} = \frac{V^N}{\Lambda^{3N} N!} \int \mathrm{d}\mathbf{s}^N \exp\left[-\beta U(\mathbf{s}^N\right]), \tag{2.20}$$

where V is the volume of the simulation box, N is the number of molecules, U is the potential energy of the configuration $\mathbf{s}^N$. Note that due to the rescaling of the coordinate vector with the inverse of the length of the simulation box, L, the

potential energy of the system, U, is also a function of the volume of the simulation box, V, along with the scaled coordinate vectors ($\mathbf{s}$). However, for convenience, U is written as a function of $\mathbf{s}$ only and V is omitted as an argument for U. $\mathscr{N}$ is defined as the probability density of finding a microstate in the phase space. $\mathscr{N}$ is required to obtain the ensemble average of a quantity A which is given by

$$<A> = \frac{\int \mathrm{d}\mathbf{s}^N \mathscr{N}(\mathbf{s}^N) A(\mathbf{s}^N)}{\int \mathrm{d}\mathbf{s}^N \mathscr{N}(\mathbf{s}^N)} = \frac{\int \mathrm{d}\mathbf{s}^N \mathscr{N}(\mathbf{s}^N) A(\mathbf{s}^N)}{Q}. \tag{2.21}$$

For the NVT ensemble:

$$\mathscr{N}(\mathbf{s}^N, T) \propto \exp\left[-\beta U(\mathbf{s}^N)\right]. \tag{2.22}$$

In the NVT ensemble, the fluctuating property is the potential energy of the system, U.

Isobaric-Isothermal Ensemble

In the isobaric-isothermal ensemble, the number of molecules (N), the external pressure (P), and the temperature (T) are fixed. The partition function for the NPT ensemble is given by [54]

$$Q_{\mathrm{NPT}} = \frac{\beta P}{\Lambda^{3N} N!} \int \mathrm{d}V\, V^N \exp\left[-\beta P V\right] \int \mathrm{d}\mathbf{s}^N \exp\left[-\beta U(\mathbf{s}^N)\right]), \tag{2.23}$$

where P is the external pressure on the system. All other variables have the same definition as in the NVT ensemble partition function. For the NPT ensemble,

$$\mathscr{N}(\mathbf{s}^N, N, V, T) \propto V^N \exp\left[-\beta P V\right]\ \exp\left[-\beta U(\mathbf{s}^N\right]. \tag{2.24}$$

In the NPT ensemble, the fluctuating properties are U (potential energy of the system) and V (volume of the simulation box). One can also treat the logarithm of the volume ($\ln(V)$) as the fluctuating property instead of V. The partition function then becomes [54]

$$Q_{\mathrm{NPT}} = \frac{\beta P}{\Lambda^{3N} N!} \int \mathrm{d}(\ln V)\, V^{N+1} \exp\left[-\beta P V\right] \int \mathrm{d}\mathbf{s}^N \exp\left[-\beta U(\mathbf{s}^N)\right]), \tag{2.25}$$

and the corresponding probability density is

$$\mathscr{N}(\mathbf{s}^N, N, \ln V, T) \propto V^{N+1} \exp\left[-\beta P V\right]\ \exp\left[-\beta U(\mathbf{s}^N\right]. \tag{2.26}$$

Gibbs Ensemble

The Gibbs ensemble describes two phases (vapor and liquid) that are in equilibrium with each other [87]. In this ensemble, the system contains two simulation boxes

that represent the vapor and liquid phases. These boxes can exchange molecules with the condition that the total number of molecules (N) in the two boxes remains fixed. For the NVT version of the Gibbs ensemble, the total volume (V) of two boxes is also fixed. As in the earlier ensembles, the temperature T is also fixed. In this work, the NVT version of the Gibbs ensemble is used. The partition function of a single-component NVT version of the Gibbs ensemble is given by [54]

$$Q_{\mathrm{GE,NVT}} = \sum_{n_1=0}^{N} \frac{1}{V\Lambda^{3N} n_1!(N-n_1)!} \int \mathrm{d}V_1 V_1^{n_1} (V-V_1)^{N-n_1} \times \int \mathrm{d}\mathbf{s}^{n_1} \exp[-\beta U_1(\mathbf{s}^{n_1})] \int \mathrm{d}\mathbf{s}^{N-n_1} \exp[-\beta U_2(\mathbf{s}^{(N-n_1)})]. \tag{2.27}$$

Here, n_1 and $N-n_1$ are the number of molecules in simulation boxes 1 and 2, respectively. Similarly, V_1 and $V-V_1$ are the volumes of simulation boxes 1 and 2, respectively. U_1 and U_2 are the total potential energies in boxes 1 and 2, respectively. The probability density for the Gibbs ensemble is given by

$$\mathscr{N}(\mathbf{s}^{n_1}, \mathbf{s}^{N-n_1}, N, n_1, V, V_1, T) \propto \frac{V_1^{n_1}(V-V_1)^{N-n_1}}{n_1!(N-n_1)!} \times \exp\left[-\beta(U(\mathbf{s}^{n_1}) + U(\mathbf{s}^{N-n_1}))\right]. \tag{2.28}$$

The fluctuating properties in the NVT version of the Gibbs ensemble are the number of molecules (n) of each box, the volume (V) of each box and the potential energies (U) of each box.

Reaction Ensemble

The reaction ensemble allows for the calculation of thermodynamic properties of a chemically reactive system. In this ensemble, the total number of atoms is conserved. The partition function of the reaction ensemble in the constant volume version is given by [54]

$$Q_{\mathrm{RxMC,NVT}} = \sum_{N_1=0}^{\infty} \cdots \sum_{N_S=0}^{\infty} \exp\left[\sum_{i=1}^{S} (\beta\mu_i N_i + N_i \ln \frac{V q_i}{\Lambda_i^3} - \ln N_i!)\right] \times \int \mathrm{d}\mathbf{s}^N \exp[-\beta U(\mathbf{s}^N)]. \tag{2.29}$$

where, $\frac{V q_i}{\Lambda_i^3}$ is the ideal gas partition function of species i. Note that q_i is the isolated molecule partition function of species i excluding the translation partition function ($\frac{V}{\Lambda_i^3}$) of the species. μ_i and N_i are the chemical potential and number

of molecules of species i, and S is the total number of species. The probability density for the reaction ensemble (NVT version) is given by

$$\mathscr{N}(\mathbf{s}^N, N, T) \propto \exp\left[\sum_{i=1}^{S}(\beta\mu_i N_i + N_i \ln\frac{V q_i}{\Lambda_i^3} - \ln N_i!) - \beta U(\mathbf{s}^N)\right]. \tag{2.30}$$

In the NVT version reaction ensemble, U and the number of molecules of each species are the fluctuating properties. It should be noted that this ensemble allows for the investigation of the thermodynamic equilibrium of the system and not the kinetics of the reaction involved.

2.3 Monte Carlo Method

In the previous section, the partition function Q of different ensembles were discussed. In principle, one can calculate thermodynamic properties if Q is known using Equation 2.21. However, Q contains multidimensional integrals with the number of independent coordinates equal to $N \times d$, where N is the number of molecules and d is the dimension of the system. Such evaluations are computationally intractable using the numerical methods available. For example, consider evaluating the $N \times d$ dimensional integrand numerically on a mesh of points containing m equidistant points along a coordinate axis. For a 3-dimensional (d) system with 100 molecules (N) evaluated at a modest resolution of 10 (m) equidistant points along each axis, it would require evaluating the integrand at m^{Nd} points. This corresponds to 10^{300} points, rendering numerical integration infeasible [54].

Monte Carlo is a stochastic method to compute multidimensional integrals. For example, in Figure 2.7, the area of the circle is computed by generating random points within a square and observing what fraction of the points fall within the boundary of the circle. However, as seen in Equation 2.19, Q is dependent on the Boltzmann factor, $\exp[-\beta U]$, and is non-negligible only in small regions of the phase space. This is due to numerous configurations in phase space in which atoms are in close proximity, resulting in $U >> 0$. Consequently, the corresponding Boltzmann factor, $\exp[-\beta U]$, becomes very small. Therefore, it would be inefficient and challenging to evaluate the partition function by direct numerical integration.

The Metropolis algorithm provides a systematic procedure for sampling configurations with non-negligible Boltzmann weights. Such a sampling is called *importance sampling* [54]. Rather than exploring configuration space uniformly, the algorithm preferentially visits states that contribute significantly to equilibrium averages, i.e., microstates where $\exp[-\beta U]$ is not vanishing. The Metropolis Monte Carlo technique creates a series of configurations that converges to the desired equilibrium probability distribution, which depends on the thermodynamic

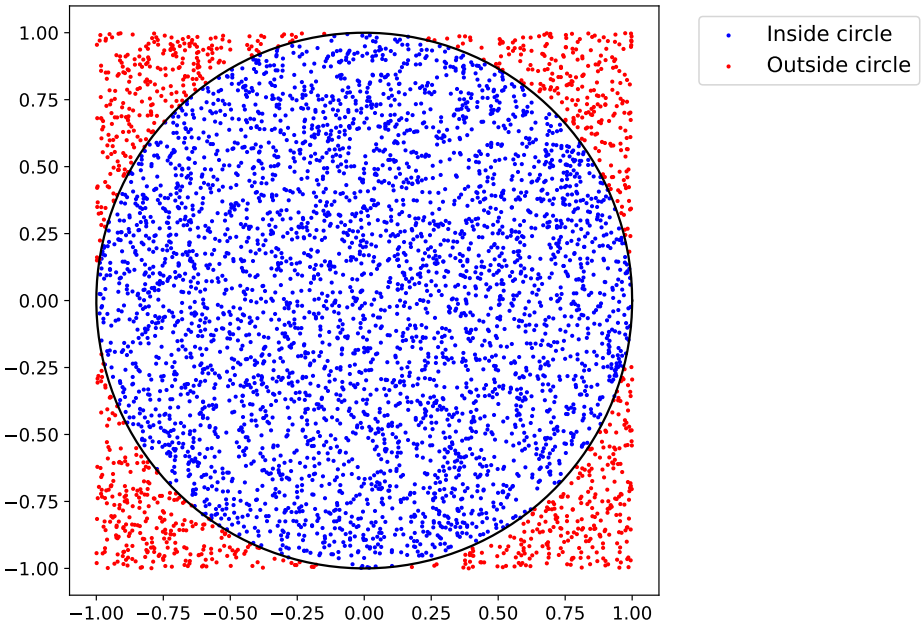

Figure 2.7: Computing area of a circle with unit radius using Monte Carlo method. The area of the circle is computed by generating N random points within a square centred at (0,0) and with a side length of 2 units. All the random points that have an Euclidean distance from the origin less than unity are considered to be within a circle. In this figure, the blue dots and red dots represent the random points inside and outside the circle, respectively. The ratio of the area of the circle to that of the square is then approximated by the ratio of the number of points falling inside the circle to the total number of sampled points, N. This probabilistic estimate converges to the exact value as N becomes large. In this figure, 5000 random points are used to compute the area of the unit circle. A total of 3926 points out of the 5000 points lie inside the circle, resulting in a computed area of 3.1408 for the circle with unit radius. Note that this approach will fail if the circle is much smaller than the square.

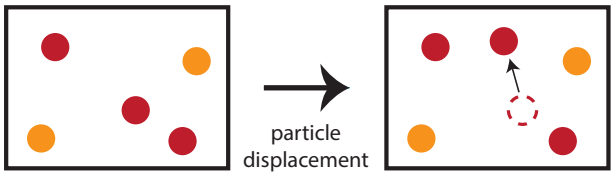

Figure 2.8: Illustration of the trial moves in the canonical ensemble, where the number of particles (N), volume of the simulation box (V) and the temperature (T) of the system remain constant, and the fluctuating quantity is the potential energy (U) of the system. The particle displacement is the trial move that samples the fluctuating quantity U in the system. In the figure, the dotted circle represents the position of the particle prior to the particle displacement trial move.

ensemble. For example, in the canonical (NVT) ensemble, the target distribution is the Boltzmann distribution. The sequence of configurations (or states) generated forms a Markov chain. The defining property of a Markov chain is that the probability of generating a new state depends only on the current state and is independent of the prior history. Therefore, it is termed memory-less. To create the series of configurations, a set of trial moves that sample the fluctuating properties in the ensemble is needed.

For the NVT ensemble, which has the potential energy of the system as the fluctuating quantity, particle displacement trial moves sample the configurational energy. The particle displacement trial moves include translational and rotational trial moves. For the NPT ensemble, which has volume along with the potential energy as the fluctuating quantities, both the particle displacement and volume change trial moves are included. For the NVT version of the Gibbs ensemble, the trial moves include particle displacements, volume exchanges, and particle exchanges between boxes 1 and 2 to sample the fluctuating quantities associated with this ensemble. Similarly, for the reaction ensemble, trial moves that convert reactants to reaction products and vice versa, along with the particle displacement trial moves are included, thereby incorporating both configurational and compositional changes.

The acceptance criterion for trial moves is constructed so that the ensemble of sampled configurations converges to the desired equilibrium probability distribution, which depends on the thermodynamic ensemble employed. This means that system states are visited with a probability proportional to $\mathcal{N}$. One of the requirements for trial moves is that the transition probability from the old state 'o' to the new state 'n' ($\pi(\mathrm{o} \rightarrow \mathrm{n})$) should be such that once equilibrium is established, the underlying probability to be in a certain system state is not destroyed. This requires $\pi(\mathrm{o} \rightarrow \mathrm{n})$ to obey global balance. Global balance condition requires the

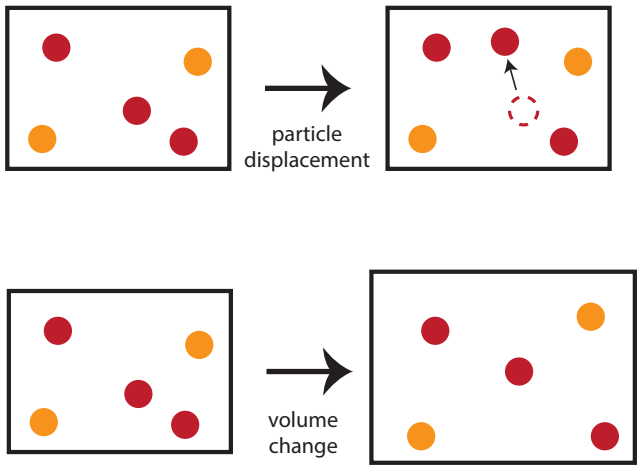

Figure 2.9: Illustration of the trial moves in an isobaric-isothermal ensemble, where the number of particles (N), pressure (P) and the temperature (T) of the system remain constant. The particle displacements and volume change trial moves sample the fluctuating quantities U and V of the system, respectively. Note that even though the volume of the simulation box changes, $\mathbf{s}^N$ remains constant during volume changes. In the figure, the dotted circle represents the position of the particle prior to the particle displacement trial move.

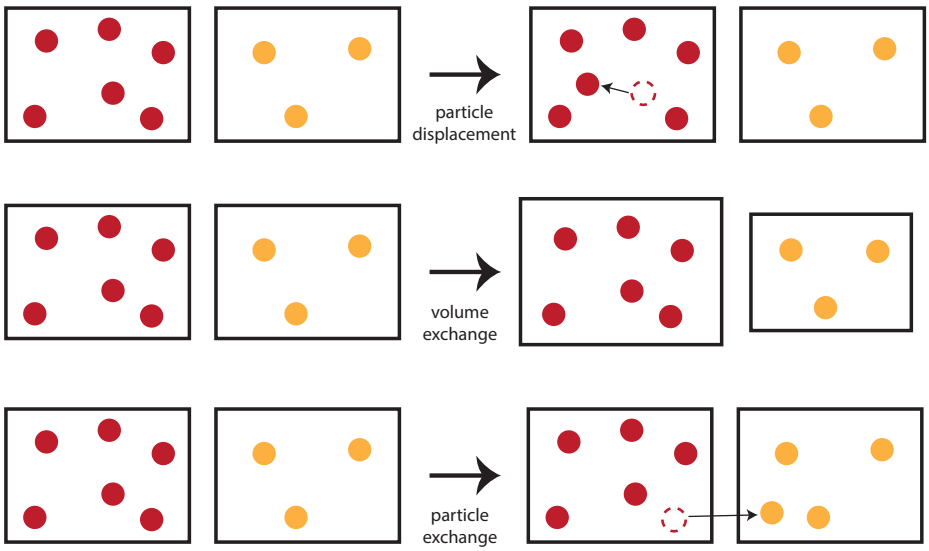

Figure 2.10: Illustration of the trial moves in the NVT version of the Gibbs ensemble, where the total number of particles in both simulation boxes (N_t), the sum of the volumes of the simulation boxes (V) and the temperature (T) of the system remain constant. The fluctuating quantities, U_1, U_2, V_1, V_2, and the number of particles in each box (n_1 and n_2) are sampled by the corresponding trial moves, that is, particle displacements, volume exchanges, and particle exchanges, respectively. In the figure, the dotted circles represent the position of the particles prior to the particle displacement trial move.

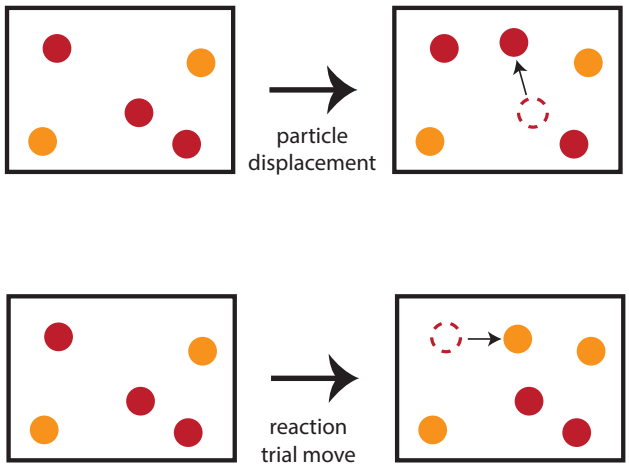

Figure 2.11: Illustration of the trial moves in the constant volume version of the reaction ensemble, where the number of atoms (N_a), volume of the simulation box (V) and the temperature of the system remain constant. The fluctuating properties are the potential energy of the system, U, and the stoichiometric composition, which are sampled by the particle displacement trial moves and reaction trial moves (reactants to reaction products and vice versa), respectively. In the figure, the dotted circles represent the position of the particles prior to the particle displacement trial move.

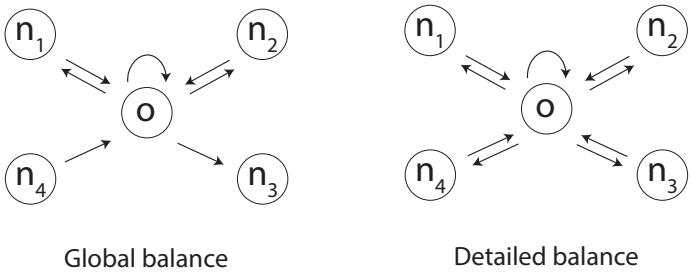

Figure 2.12: Illustration of global balance and detailed balance. In the global balance condition (Equations 2.31 and 2.32), the probability flux out of the old state 'o' to other new states 'n' should be equal to the total probability flux from all other 'n' states to 'o'. In contrast, the detailed balance condition (Equation 2.33) requires that the probability flux between any pair of states be equal.

probability flux out of the old state 'o' to other new states 'n' to be equal to the total probability flux from all other 'n' states to 'o'. That is

$$\mathscr{N}(\mathrm{o}) \times \sum_{i=1}^{m} \pi(\mathrm{o} \to \mathrm{n}_i) = \sum_{i=1}^{m} \mathscr{N}(\mathrm{n}_i) \times \pi(\mathrm{n}_i \to \mathrm{o}). \tag{2.31}$$

Here $\mathscr{N}(i)$ is the *a priori* probability density of finding the system in state i and m is the number of new states 'n' in the system (see Figure 2.12). Note that for simplicity, we consider discrete states.

$\pi(\mathrm{o} \to \mathrm{n})$ can be written as $\alpha(\mathrm{o} \to \mathrm{n}) \times \mathrm{acc}(\mathrm{o} \to \mathrm{n})$, where $\alpha(\mathrm{o} \to \mathrm{n})$ is the probability of attempting a trial move from state 'o' to state 'n', and $\mathrm{acc}(\mathrm{o} \to \mathrm{n})$ is the probability of accepting the trial move from state 'o' to 'n'. Equation 2.31 can therefore be written as.

$$\mathscr{N}(\mathrm{o}) \times \sum_{i=1}^{m} \alpha(\mathrm{o} \to \mathrm{n}_i) \times \mathrm{acc}(\mathrm{o} \to \mathrm{n}_i) = \sum_{\mathrm{i}=1}^{m} \mathscr{N}(\mathrm{n}_i) \times \alpha(\mathrm{n}_i \to \mathrm{o}) \times \mathrm{acc}(\mathrm{n}_i \to \mathrm{o}). \tag{2.32}$$

It is convenient to impose a stricter condition called detailed balance. Detailed balance requires the probability flux between any pair of states to be equal. This

condition guarantees that, at equilibrium, the probability flux between any pair of states is equal. The detailed balance condition is given by

$$\mathscr{N}(\mathrm{o}) \times \alpha(\mathrm{o} \to \mathrm{n}) \times \mathrm{acc}(\mathrm{o} \to \mathrm{n}) = \mathscr{N}(\mathrm{n}) \times \alpha(\mathrm{n} \to \mathrm{o}) \times \mathrm{acc}(\mathrm{n} \to \mathrm{o}). \tag{2.33}$$

If Equation 2.33 is satisfied, then Equation 2.31 necessary follows. Note that the strict detailed balance is not necessary in MC simulation, but it simplifies the computation [88]. Another condition $\pi(\mathrm{o} \to \mathrm{n})$ must obey is to be ergodic. This requires every accessible part in the configuration space to be reached from a given point in the configuration space using a finite number of Monte Carlo trial moves. However, the presence of high energy barriers may cause the simulation to be quasi-ergodic, thereby hindering adequate sampling of configurational space. Such cases would require the introduction of techniques to facilitate accessibility to the high-energy states (low probability to visit) in the configurational space (for example, see Section 2.3.1).

In the Metropolis scheme of Ref. [54], $\alpha(i \to j)$ is taken to be symmetric. Equation 2.33 can then be written as

$$\frac{\mathscr{N}(\mathrm{n})}{\mathscr{N}(\mathrm{o})} = \frac{\mathrm{acc}(\mathrm{o} \to \mathrm{n})}{\mathrm{acc}(\mathrm{n} \to \mathrm{o})}. \tag{2.34}$$

The choice of the acceptance rule by Metropolis *et al.* [54] was

$$\begin{aligned} \mathrm{acc}(\mathrm{o} \to \mathrm{n}) &= \frac{\mathscr{N}(n)}{\mathscr{N}(o)} \qquad \text{if } \mathscr{N}(n) < \mathscr{N}(o) \\ &= 1 \qquad\qquad\quad \text{if } \mathscr{N}(n) \geq \mathscr{N}(o). \end{aligned} \tag{2.35}$$

which can be written in compact form as

$$\mathrm{acc}(\mathrm{o} \to \mathrm{n}) = \min\left(1, \frac{\mathscr{N}(\mathrm{n})}{\mathscr{N}(\mathrm{o})}\right). \tag{2.36}$$

Sampling using the above criteria creates a list of configurations that obey the desired probability distribution.

Equation 2.21 shows how to find the ensemble average of a property. Since importance sampling of the Metropolis algorithm generates states that follow the probability distribution ($\mathscr{N}$) corresponding to the ensemble, the ensemble average of a property A (such as density) can be computed using an unweighted average

$$\langle A \rangle = \lim_{m \to \infty} \frac{1}{m} \sum_{i=1}^{m} A(i) = \frac{\int d\mathbf{s}^N \mathscr{N}(\mathbf{s}^N) A(\mathbf{s}^N)}{Q}. \tag{2.37}$$

Here, m is the number of states in the Markov chain generated by the Metropolis algorithm, and $A(i)$ is the value of quantity A for state i. The average of the

property A computed using the Metropolis algorithm is equal to the ensemble average of A computed using Equation 2.21. This procedure enables the computation of thermodynamic properties, including densities [89, 90], excess chemical potentials [91], heat capacities [92, 93], and other related thermodynamic properties.

2.3.1 Continuous Fractional Component Monte Carlo method

The computation of properties (such as excess chemical potentials) in the different ensembles discussed in Section 2.2.1 involves particle insertion and deletion trial moves. In highly dense systems, particle insertion attempts frequently fail due to overlaps with neighbouring particles, resulting in very low acceptance probabilities. The Continuous Fractional Component (CFC) Monte Carlo method [94–97] addresses this limitation by enabling the gradual insertion of molecules into the system, thereby significantly improving sampling efficiency in high-density regimes. These particle transfers are performed using "fractional molecules". Each fractional molecule is assigned a continuous fractional parameter, λ ($\lambda \in [0, 1]$). $\lambda = 0$ indicates no interactions between the fractional molecule and the rest of the system (i.e., fractional molecules act as ideal gas molecules). $\lambda = 1$ represents "whole molecules" and full interactions between fractional molecules and other molecules in the system. A collection of one or more fractional molecules is called a fractional group [68, 98]. In the Brick-CFCMC software [97–99], fractional groups must be charge neutral to maintain the overall charge neutrality of the system.

In the CFCMC ensembles, an additional fluctuating quantity (λ of a fractional molecule) is introduced along with the fluctuating quantities described in Section 2.2.1. Therefore, one should include the trial moves to sample the "λ space". The expanded ensembles (referred to as CFC Ensembles) and the probability density ($\mathscr{N}$) required for acceptance criteria of the new trial moves are discussed in the following section.

2.3.2 CFC Ensembles

Canonical Ensemble

For a CFC NVT ensemble, the partition function is given by [99]

$$Q_{\mathrm{NVT,CFC}} = \frac{V^{N+1}}{\Lambda^{3(N+1)} N!} \int_0^1 \mathrm{d}\lambda \int \mathrm{d}\mathbf{s}^N \exp\left[-\beta U\left(\mathbf{s}^N\right)\right] \times \int \mathrm{d}\mathbf{s}_{\mathrm{frac}} \exp\left[-\beta U_{\mathrm{frac}}\left(\mathbf{s}_{\mathrm{frac}}, \mathbf{s}^N, \lambda\right)\right] \tag{2.38}$$

where U_{frac} is the potential energy of the fractional molecule, U is the total potential energy minus U_{frac}, $\mathbf{s}_{\mathrm{frac}}$ is the scaled coordinate vector of the fractional molecule

and λ is the continuous coupling parameter. The corresponding probability density is

$$\mathscr{N}(\mathbf{s}^N, \mathbf{s}_{\text{frac}}, \lambda, T) \propto \exp\left[-\beta(U(\mathbf{s}^N) + U_{\text{frac}}(\mathbf{s}^N, \mathbf{s}_{\text{frac}}, \lambda))\right]. \tag{2.39}$$

Isobaric-Isothermal Ensemble

The partition function for CFC NPT ensemble is given by [99]

$$\begin{aligned} Q_{\text{NPT,CFC}} = \frac{\beta P}{\Lambda^{3(N+1)} N!} \int_0^1 \mathrm{d}\lambda \int \mathrm{d}V V^{N+1} \exp\left[-\beta P V\right] \\ \times \int \mathrm{d}\mathbf{s}^N \exp\left[-\beta U\left(\mathbf{s}^N\right)\right] \int \mathrm{d}\mathbf{s}_{\text{frac}} \exp\left[-\beta U_{\text{frac}}\left(\mathbf{s}_{\text{frac}}, \mathbf{s}^N, \lambda\right)\right] \end{aligned} \tag{2.40}$$

where P is the imposed external pressure. All other variables have the same definition as in 2.3.2. $\mathscr{N}$ for the NPT ensemble is given by

$$\begin{aligned} \mathscr{N}(\mathbf{s}^N, \mathbf{s}_{\text{frac}}, \lambda, N, V, T) \propto \\ V^{N+1} \exp\left[-\beta P V\right] \ \exp\left[-\beta U(\mathbf{s}^N)\right] \exp\left[-\beta U_{\text{frac}}(\mathbf{s}^N, \mathbf{s}_{\text{frac}}, \lambda)\right]. \end{aligned} \tag{2.41}$$

Gibbs Ensemble

The partition function of a CFC Gibbs Ensemble in the NVT version is by [99, 100]

$$\begin{aligned} Q_{\text{GE,NVT,CFC}} = \frac{1}{\Lambda^{3(N+1)} N!} \sum_{i=1}^{2} \sum_{n_1=0}^{N} \frac{N!}{n_1!\,(N-n_1)!} \int_0^1 \mathrm{d}\lambda \\ \times \int_0^V \mathrm{d}V_1 V_1^{n_1+\delta_{i1}} \left(V - V_1\right)^{N-n_1+\delta_{i2}} \\ \times \int \mathrm{d}\mathbf{s}^{n_1} \exp\left[-\beta U_1\left(\mathbf{s}^{n_1}\right)\right] \\ \times \int \mathrm{d}\mathbf{s}^{N-n_1} \exp\left[-\beta U_2\left(\mathbf{s}^{N-n_1}\right)\right] \\ \times \left(\delta_{i1} \int \mathrm{d}\mathbf{s}_{\text{frac}} \exp\left[-\beta U_{\text{frac},1}\left(\ \mathbf{s}_{\text{frac}},\ \mathbf{s}^{n_1}, \lambda\right)\right] \right. \\ \left. + \delta_{i2} \int \mathrm{d}\mathbf{s}_{\text{frac}} \exp\left[-\beta U_{\text{frac},2}\left(\mathbf{s}_{\text{frac}}, \mathbf{s}^{N-n_1}, \lambda\right)\right]\right). \end{aligned} \tag{2.42}$$

Here, δ_{ij} is used to indicate if the fractional molecule is in box 1 (if $i = j = 1$) or in box 2 (if $i = j = 2$). All other variables have the same definitions as those used in Sections 2.2.1 and 2.3.2. $\mathscr{N}$ for the NVT Gibbs ensemble is given by

$$\mathscr{N}(\mathbf{s}^{n_1}, \mathbf{s}^{N-n_1}, \mathbf{s}^{i}_{\text{frac}}, \lambda, N, n_1, V, V_1, T, i) \propto$$
$$\frac{V_1^{n_1+\delta_{i1}}(V-V_1)^{N-n_1+\delta_{i2}}}{n_1!(N-n_1)!} \times \exp\left[-\beta(U_1(\mathbf{s}^{n_1}) + U_2(\mathbf{s}^{N-n_1}))\right]$$
$$\times(\delta_{i1}\ \exp\left[-\beta(U_{\text{frac},1}(\mathbf{s}_{\text{frac}}, \mathbf{s}^{n_1}, \lambda)\right] + \delta_{i2}\ \exp\left[-\beta(U_{\text{frac},2}(\mathbf{s}_{\text{frac}}, \mathbf{s}^{N-n_1}, \lambda)\right]). \tag{2.43}$$

2

Reaction Ensemble

The partition function of a CFC Reactive Ensemble in the NVT version is given by [99]

$$Q_{\text{RxMC},V,\text{CFC}} = \sum_{N_1=0}^{\infty} \cdots \sum_{N_S=0}^{\infty} \sum_{\delta=0}^{1} \int_0^1 \mathrm{d}\lambda$$
$$\times \exp\left[\sum_{i=1}^{R} \beta\mu_i\left(N_i + \delta\nu_i\right) + \left(N_i + \delta\nu_i\right)\ln\left(\frac{Vq_i}{\Lambda_i^3}\right) - \ln N_i!\right]$$
$$\times \exp\left[\sum_{i=R+1}^{S} \beta\mu_i\left(N_i + (1-\delta)\nu_i\right) + \left(N_i + (1-\delta)\nu_i\right)\ln\left(\frac{Vq_i}{\Lambda_i^3}\right) - \ln N_i!\right] \tag{2.44}$$
$$\times \int \mathrm{d}\mathbf{s}^N \exp\left[-\beta U\left(\mathbf{s}^N\right)\right] \int \mathrm{d}\mathbf{s}_{\text{frac}}^{N_{\text{frac}}}\ \exp\left[-\beta U_{\text{frac}}\ \left(\mathbf{s}_{\text{frac}}^{N_{\text{frac}}}, \mathbf{s}^N, \lambda, \delta\right)\right].$$

Here, components 1 to R are considered reactants, and components $R+1$ to S are reaction products. δ value is 1 for fractional molecules of reactant products and 0 for fractional molecules of reactants. All other variables have the same definitions as used in Sections 2.2.1 and 2.3.2. The corresponding probability density is given by

$$\mathscr{N}(\mathbf{s}^N, \mathbf{s}_{\text{frac}}^{N_{\text{frac}}}, N, N_{\text{frac}}, \lambda, \delta, T) \propto$$
$$\exp\left[\sum_{i=1}^{R}(\beta\mu_i(N_i + \delta\nu_i) + (N_i + \delta\nu_i)\ln\frac{Vq_i}{\Lambda_i^3} - \ln N_i!)\right]$$
$$\times\ \exp\left[\sum_{i=R+1}^{S}(\beta\mu_i(N_i + (1-\delta)\nu_i) + (N_i + (1-\delta)\nu_i)\ln\frac{Vq_i}{\Lambda_i^3} - \ln N_i!)\right] \tag{2.45}$$
$$\times\ \exp\left[-\beta U(\mathbf{s}^N)\right] \exp\left[-\beta U_{\text{frac}}\left(\mathbf{s}_{\text{frac}}^{N_{\text{frac}}}, \mathbf{s}^N, \lambda, \delta\right)\right].$$

Using the newly defined probability densities ($\mathscr{N}$) for each expanded CFC ensemble and Equation 2.36, the acceptance criteria for trial moves in the respective CFC ensembles can be derived.

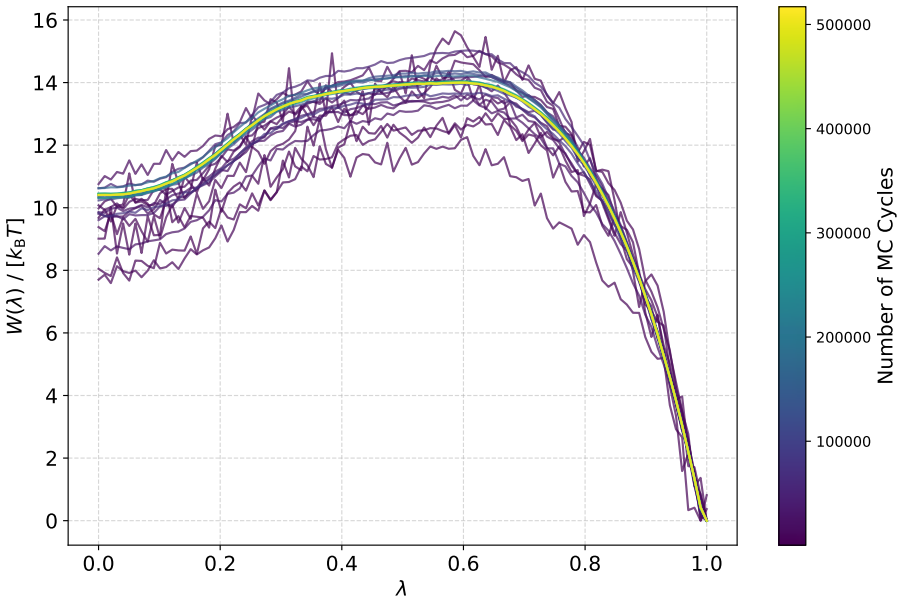

Figure 2.13: Weightfunction, W, as a function of coupling parameter, λ, for a fractional molecule of water in TIP3P water system is shown. The evolution of $W(\lambda)$ with the successive Monte Carlo cycles is illustrated. Here, a total of 100 bins are used.

Wang-Landau algorithm

To increase the efficiency of particle transfers, λ is biased with a weight function ($W(\lambda)$) using the Wang-Landau algorithm [101]. This ensures a smooth observed probability distribution of λ. The Boltzmann average of any property (A) is then computed using [100]

$$\langle A \rangle = \frac{\langle\ A\ \exp[-W(\lambda)]\rangle_{\text{biased}}}{\langle \exp[-W(\lambda)]\rangle_{\text{biased}}}. \tag{2.46}$$

To implement the Wang-Landau algorithm, a histogram (W) is constructed with a series of bins (usually 100) to store the values of the weight function corresponding to a value of λ. A second histogram (H), with an identical binning scheme, is used to store the number of visits to a particular bin. In the absence of a pre-defined weight function, both W and H are initialized to zero. If an initial weight function is provided, it is used to initialize W. When a trial move proposes a change to a particular value of λ, the W of the bin corresponding to the λ is

updated according to

$$W(\lambda) = W(\lambda) - F_{\text{mod}}, \tag{2.47}$$

where F_{mod} is a user-defined input that updates the values of W. Simultaneously, H is updated according to

$$H(\lambda) = H(\lambda) + 1. \tag{2.48}$$

The histogram (H) is considered flat when the difference between its maximum and minimum bin counts falls below the product of the flatness criterion (F_{c}) (specified as "Flatc" in Brick-CFCMC) and the average number of visits per bin. Upon satisfying this flatness condition, H is reset to zero, F_{mod} is reduced by a factor of F_{red} (user-defined input) and W is shifted by subtracting its minimum value to prevent numerical overflow. This iterative procedure is repeated until F_{mod} falls below a given threshold (usually 10^{-6}) [99].

2.4 Isolated Molecule Partition Function

The isolated molecular partition (q_{total}) is the sum over all possible energy levels of an isolated molecule. It provides a bridging link between the molecular level and macroscopic level properties. q_{total} is required to compute the chemical potentials and reaction equilibrium constants. The isolated molecular partition function is given by [99]

$$q_{\text{total}}(V,T) = q_{\text{trans}}(V,T)q_{\text{vib}}(T)q_{\text{rot}}(T)q_{\text{elec}}(T). \tag{2.49}$$

The translational partition function, q_{trans}, is given by [99]

$$q_{\text{trans}}(V,T) = \frac{V}{\Lambda^3}, \tag{2.50}$$

wherein Λ is the thermal de Broglie wavelength of the molecule, $\Lambda = \frac{h}{\sqrt{2\pi M k_{\text{B}} T}}$. Here, h is the Planck constant, M is the sum of the masses of all atoms in the molecule, T is the temperature, and V is the volume. In Brick-CFCMC, a reference state of $V = V_0 = 1$ Å^3 is used for q_{trans} [68, 99].

The vibrational partition function, q_{vib}, considering the vibrational ground state energy as the zero of the vibrational energy, is calculated using [99]

$$q_{\text{vib}}(T) = \prod_{i=1}^{\alpha} \frac{1}{1 - \exp\left[\frac{-\Theta_{\text{vib},i}}{T}\right]}, \tag{2.51}$$

in which i runs from 1 to α, where α is the number of vibrational degrees of freedom. For a linear molecule, $\alpha = 3n - 5$ and for a non-linear molecule, α

$= 3n - 6$, where n is the number of atoms in the molecule. $\Theta_{\text{vib},i} = \frac{h\nu_i}{k_\text{B}}$ is the characteristic vibrational temperature corresponding to the i^{th} normal mode with vibrational frequency, ν_i.

The energy levels (ϵ_J) of a diatomic molecule, under the rigid-rotor approximation is given by [99]

$$\epsilon_J = \frac{h^2 J(J+1)}{8\pi^2 I}, \tag{2.52}$$

where J is the rotational quantum number, I is the principal moment of inertia. The energy level corresponding to $J = 0$ is chosen as the zero of the rotational energy for the calculation of the rotational partition function, q_rot. The rotational constant of an axis, X, is related to the moment of inertia of that axis, I, by $I = \frac{h}{8\pi^2 X}$. For a diatomic molecule, q_rot is given by [99]

$$q_\text{rot}(T) = \frac{T}{\sigma_\text{rot}\Theta_\text{rot}}, \tag{2.53}$$

where $\Theta_\text{rot} = \frac{h^2}{8\pi^2 I k_\text{B}}$ is the characteristic rotational temperature. σ_rot is the rotational symmetry number of the molecule, which is the number of indistinguishable configurations the molecule can be brought into by rotation about its centre of mass [102]. The rotational partition function, q_rot, for non-linear polyatomic species, is calculated using [99]

$$q_\text{rot}(T) = \frac{\sqrt{\pi}}{\sigma_\text{rot}} \left(\frac{T^3}{\Theta_{\text{rot,A}}\Theta_{\text{rot,B}}\Theta_{\text{rot,C}}} \right)^{1/2}, \tag{2.54}$$

where, σ_rot is the rotational symmetry number, $\Theta_{\text{rot,A}}$, $\Theta_{\text{rot,B}}$ and $\Theta_{\text{rot,C}}$ are the characteristic rotational temperatures corresponding to the principal moments of inertia, I_A, I_B and I_C, respectively.

Finally, the electronic partition function, q_elec, is calculated using [99]

$$q_\text{elec}(T) = g_\text{e1} \exp\left[\frac{D_0}{k_\text{B}T}\right] \tag{2.55}$$

where g_e1 is the degeneracy of the electronic ground state. D_0 is the atomization energy of the molecule which is defined as the difference between the enthalpy of formation of the molecule and the sum of the enthalpies of formation of the dissociated atoms which constituted the molecule [99]. The energy of the infinitely dissociated atoms at the ground electronic state is taken as the zero of the electronic energy.

2.5 Molecular Dynamics

The ergodicity hypothesis states that for an ergodic system, the time average of a property is equal to the ensemble average [54]. That is

$$\langle A \rangle_{\text{time}} = \frac{\int_0^t A(\tau) d\tau}{t} = \langle A \rangle \tag{2.56}$$

where t is the total simulation time and $A(\tau)$ is the value of property A at time τ. This allows the computation of a property by generating a single trajectory through the phase space that visits the relevant states (for example, those states with non-negligible Boltzmann factors in NVT ensemble) for an ensemble.

Molecular Dynamics is a simulation technique that is used to study the time evolution of a system by generating such trajectories. In sharp contrast to Monte Carlo methods, where the system evolves through stochastic trial moves, Molecular Dynamics determines the system trajectory by numerically integrating Newton's equations of motion as a function of time. In this approach, the force acting on each particle in the system is computed, and the positions and velocities of the particles are propagated in time accordingly. One of the algorithms used to integrate the equations of motion is the Velocity-Verlet algorithm [103], which is given by the following equations

$$\mathbf{r}(t + \Delta t) = \mathbf{r}(t) + \mathbf{v}(t)\Delta t + \frac{\mathbf{f}(t)}{m}\Delta t^2 \tag{2.57}$$

$$\mathbf{v}(t + \Delta t) = \mathbf{v}(t) + \frac{\mathbf{f}(t + \Delta t) + \mathbf{f}(t)}{2m}\Delta t. \tag{2.58}$$

Here $\mathbf{r}$ and $\mathbf{v}$ are the position and velocity vectors of the particle, respectively. $\mathbf{f}$ is the force acting on the particle and Δt is the time step. Another algorithm used in this work is the Leap-Frog algorithm. The positions and velocities are updated by

$$\mathbf{r}(t + \Delta t) = \mathbf{r}(t) + \mathbf{v}\left(t + \frac{\Delta t}{2}\right)\Delta t \tag{2.59}$$

$$\mathbf{v}\left(t + \frac{\Delta t}{2}\right) = \mathbf{v}\left(t - \frac{\Delta t}{2}\right) + \frac{\mathbf{f}(t)}{m}\Delta t. \tag{2.60}$$

The integration time step, Δt must be sufficiently small to accurately resolve the changes in interparticle interaction between each time step. Otherwise, numerical instability might appear [104]. Therefore, Δt is determined by the steepness of the interaction potential. Additionally, Δt must be able to resolve the fastest vibrations in the system.

Note that the trajectories of the system through the phase space are highly sensitive to the initial conditions. Trajectories that are initially infinitesimally

close diverge exponentially with time. This sensitivity of the trajectories to initial conditions, which causes the trajectories to diverge, is the Lyapunov instability [54]. The source of divergence could be integration errors and rounding errors associated with finite computer precision. Therefore, in MD simulations, one is not interested in individual trajectories but in generating states representative of the desired ensemble and computing statistical averages of the corresponding properties. In this regard, MD simulations are different from predicting the trajectory of a rocket or satellite in space, where accurate determination of a specific trajectory is essential, despite both systems being governed by Newton's equations of motion [54].

Molecular dynamics simulations enable the computation of both thermodynamic properties, such as densities, as well as transport properties, including viscosities and self-diffusion coefficients. The natural ensemble of a Molecular Dynamics simulation is the microcanonical ensemble (constant N, V, and E). For the NVT and NPT ensembles, thermostats and barostats are required to ensure that the states visited in the trajectories reflect the probability distribution ($\mathscr{N}$) corresponding to these ensembles.

2.5.1 Thermostats and Barostats

The systems studied in this work are investigated at constant temperatures. To maintain a system at a constant temperature, thermostats are required. The role of the thermostat is not only limited to maintaining a constant temperature, but also in ensuring that the time-averaged properties of the system are in accordance with the canonical ensemble average defined by the Boltzmann distribution. For example, the specific heat at constant volume is obtained from the fluctuations of energy of the system. Thus, if a thermostat does not reproduce the statistical variance of the energy of the system, thermodynamic properties such as the specific heat at constant volume cannot be reproduced, even if the simulation is maintained at the desired temperature.

The Nosé-Hoover thermostat couples the system to an artificial heat bath using a fictitious degree of freedom, s. With the addition of the new coordinate, s, the Hamiltonian of the system is modified by adding the following terms to the existing Hamiltonian, $Lk_{\mathrm{B}}T\ \ln(s) + \frac{\mathscr{M}}{2}\dot{s}^2$. Here L is an adjustable parameter and $\mathscr{M}$ is an effective mass associated with the variable s. Nosé showed that with the correct choice of parameter L, the ensemble averages reduces to the canonical averages [54].

To maintain a constant pressure, the volume of the system is considered as a dynamic variable. The Parinello-Rahman and Nosé-Hoover barostats were used in this thesis, the details of which can be found in Ref. [54].

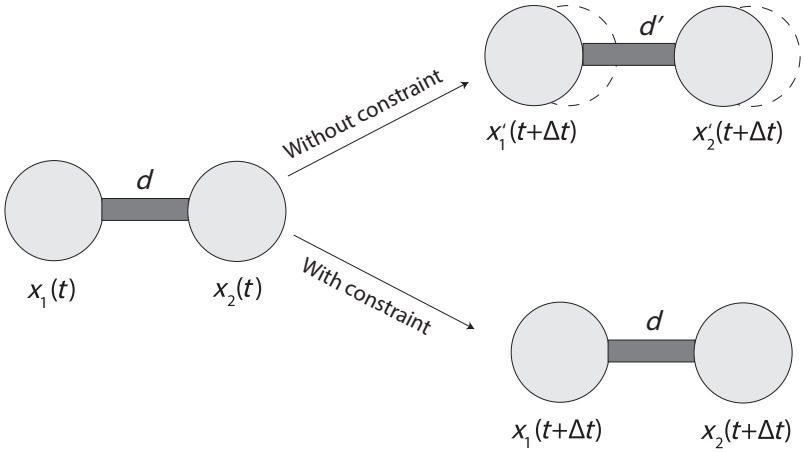

Figure 2.14: Constraining the bond length d of a diatomic molecule. At time t, the bond length of the molecule is d. Without applying constraints, numerical integration of the equations of motion would result in an updated bond length d' at time $t + \Delta t$. Upon applying constraints, the bond length at time $t + \Delta t$ is restored to d. Adapted from Ref. [57].

2.5.2 Constraints

The fast vibrations in a system are usually constrained so that larger time steps (Δt) can be used during an MD simulation run. Consider a diatomic molecule whose bond length is to be constrained to a length d. Without any constraining forces, the numerical integration of the equations of motion would result in the distance between the two atoms of the diatomic molecule being d'. A potential energy function ($\sigma = \lambda(d^2 - (x_2 - x_1)^2)$) can be defined, which goes to zero when the distance between the two atoms in the molecule is equal to the equilibrium bond length, d. Note that λ is a variable. The corresponding force of σ can be taken as the constraining force $\mathbf{G}$ ($\mathbf{G} = -\frac{1}{2}\nabla\sigma$). With the constraint force $\mathbf{G}$, the equations of motion would lead to the new positions of the atoms of the diatomic molecule. Constraining the new distance between the atoms would lead to a quadratic equation in λ. Solving the quadratic equation for λ yields the value of λ required to constrain the bond length to d. However, solving for multiple constraints (which is usually the case of an MD simulation) entails matrix inversions, which are computationally expensive. This issue can be avoided by using an iterative procedure (such as the one used by the SHAKE [105] or LINCS [106] algorithms) to determine the constraint coefficients [57].

2.6 Computed Properties

This section provides a brief overview of the properties evaluated in this thesis. These properties are broadly classified into thermodynamic and transport properties. Thermodynamic properties are state properties that depend on the macroscopic state variables such as temperature, pressure, and composition. These properties are time-independent. Density and excess chemical potential are examples of thermodynamic properties. In contrast, transport properties characterize the time-dependent mass or momentum flux within a system, such as the diffusion coefficient and viscosity.

2.6.1 Excess chemical potential

The excess chemical potential can be computed from the Boltzmann sampled probability distribution of λ by the following equation in CFCMC [99]

$$\mu_i^{\text{ex}} = -k_{\text{B}}T \ln\left[\frac{p(\lambda=1)}{p(\lambda=0)}\right], \tag{2.61}$$

where $p(\lambda{=}1)$ and $p(\lambda{=}0)$ are the Boltzmann sampled probability distributions of λ at 1 and 0, respectively, k_{B} is the Boltzmann constant, and T is the absolute temperature. For large and/or strongly polar molecules, μ^{ex} is computed using

thermodynamic integration. In this method, values of $\left\langle \frac{\partial U}{\partial \lambda} \right\rangle$ are computed from a series of independent simulations at different fixed values of λ for $\lambda \in [0, 1]$. Here, U is the total potential energy of the system. μ^{ex} is then computed by integrating $\left\langle \frac{\partial U}{\partial \lambda} \right\rangle$

$$\mu_i^{\text{ex}} = \int_0^1 \left\langle \frac{\partial U}{\partial \lambda} \right\rangle \mathrm{d}\lambda. \tag{2.62}$$

2.6.2 Henry Coefficients

The excess chemical potential at infinite dilution ($\mu^{\text{ex},\infty}$) can be used to determine the Henry volatility coefficient (K_v^{px}) by [107].

$$K_v^{\text{px}} = \rho \; k_{\text{B}} T \exp\left[\left(\frac{\mu^{\text{ex},\infty}}{k_{\text{B}} T}\right)\right], \tag{2.63}$$

where ρ is the number density of the solvent. K_v^{px} is in units of [Pa]. The definition of the Henry law constants is according to Sander [52]. The Henry coefficient (H_s^{cp}) in units of [mol/m^3 Pa] can be obtained using the following conversion:

$$H_s^{\text{cp}} \approx \frac{\rho_{\text{H}_2\text{O}}}{M_{\text{H}_2\text{O}} K_v^{\text{px}}}, \tag{2.64}$$

in which $\rho_{\text{H}_2\text{O}}$ is the density of the solvent (water), and $M_{\text{H}_2\text{O}}$ is the molar mass of water [52]. The Henry coefficient (H_s^{cp}) will have the SI units only if ρ, k_{B}, T, and M are in SI units.

2.6.3 Self-diffusion Coefficients and Viscosities

Self-diffusion coefficient ($D_{\text{MD},i}$) of a species i is calculated from the mean-squared displacements of all the molecules of species i.

$$D_{\text{MD},i} = \lim_{t\to\infty} \frac{1}{2t} \frac{1}{3N_i} \left\langle \sum_{j=1}^{N_i} (\mathbf{r}_{j,i}(t) - \mathbf{r}_{j,i}(0))^2 \right\rangle. \tag{2.65}$$

Here, t is the correlation time, N_i is the number of molecules of species i, and $\mathbf{r}_{j,i}$ is the position vector of j^{th} molecule of species i. The self-diffusion coefficient of a particle can be influenced by the hydrodynamic interaction with its periodic images, and these interactions are system-size dependent [85]. In this thesis, the self-diffusion coefficients were corrected for finite-size effects with the Yeh-Hummer equation [85, 108]

$$D = D_{\text{MD}} + \frac{k_{\text{B}} T \xi}{6\pi\eta L}, \tag{2.66}$$

where D is the self-diffusion coefficient calculated with the finite-size effects corrections. k_{B} is the Boltzmann constant, T is the absolute temperature (in

Kelvin), ξ is a dimensionless number which is equal to 2.837 for a cubic simulation box, L is the length of the cubic simulation box, and η is the viscosity of the system.

The viscosities are calculated from the auto-correlation function of all the components of the traceless stress tensor ($P^{os}_{\alpha\beta}$) [109]

$$\eta = \lim_{t\to\infty} \frac{1}{20\,t} \frac{V}{k_B T} \left\langle \sum_{\alpha\beta} \left(\int_0^t P^{os}_{\alpha\beta}(t')\mathrm{dt}' \right)^2 \right\rangle, \tag{2.67}$$

where V is the volume of the system. In Equation 2.67, $P^{os}_{\alpha\beta}$ is given by

$$P^{os}_{\alpha\beta} = \frac{P_{\alpha\beta} + P_{\beta\alpha}}{2} - \delta_{\alpha\beta} \left(\frac{1}{3} \sum_k P_{kk} \right), \tag{2.68}$$

where $\delta_{\alpha\beta}$ is the Kronecker delta. Viscosities usually do not depend on the system size, unless the density is very low [85, 86].

2

Chapter 3

Computing solubility and thermodynamic properties of H_2O_2 in water

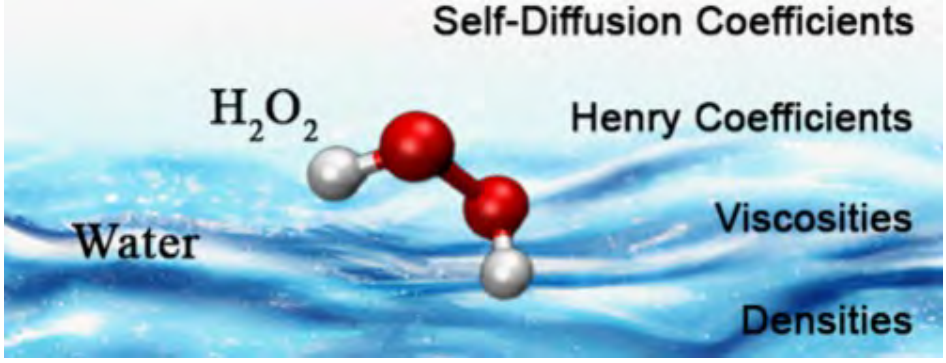

This chapter is based on the following publication: T. H. G. Saji, J. M. Vicent-Luna, T. J. H. Vlugt, S. Calero and B. Bagheri, *Computing solubility and thermodynamic properties of H_2O_2 in water*, Journal of Molecular Liquids, **401**, 124530 (2024).

Overview

Hydrogen peroxide plays a key role in many environmental and industrial chemical processes. We performed classical Molecular Dynamics and Continuous Fractional Component Monte Carlo simulations to calculate thermodynamic properties of H_2O_2 in aqueous solutions. The quality of the available force fields for H_2O_2 developed by Orabi & English (Journal of Chemical Theory and Computation, 2018, 14, 2808-2821), and by Cordeiro (Biochimica et Biophysica Acta (BBA) - Biomembranes, 2014, 1838, 438-444) was systematically evaluated. To assess which water force field is suitable for predicting properties of H_2O_2 in aqueous solutions, four widely used water force fields were used, namely the TIP3P, TIP4P/2005, TIP5P-E, and a modified TIP3P force field. While the computed densities of pure H_2O_2 in the temperature range of 253 - 353 K using the force field by Orabi & English are in excellent agreement with experimental results, the densities using the force field by Cordeiro are underestimated by 3%. The TIP4P/2005 force field in combination with the H_2O_2 force field developed by Orabi & English can predict the densities of H_2O_2 aqueous solution for the whole range of H_2O_2 mole fractions in very good agreement with experimental results. The TIP4P/2005 force field in combination with either of the H_2O_2 force fields can predict the viscosities of H_2O_2 aqueous solutions for the whole range of H_2O_2 mole fractions in reasonably good agreement with experimental results. The computed diffusion coefficients for H_2O_2 and water molecules using the TIP4P/2005 force field with either of the H_2O_2 force fields are almost constant for the whole range of H_2O_2 mole fractions. Hydrogen bond analysis showed a steady increase in the number of hydrogen bonds with the solute concentrations in H_2O_2 aqueous solutions for all combinations except for the Cordeiro-TIP5P-E and Orabi-TIP5P-E systems, which showed a minimum at intermediate concentrations. The Cordeiro force field for H_2O_2 in combination with either of the water force fields can predict the Henry coefficients of H_2O_2 in water in better agreement with experimental values than the force field by Orabi & English.

3.1 Introduction

Hydrogen peroxide, H_2O_2, has attracted considerable interest as it plays a key role in the oxidative chemistry of the troposphere. It can be found both in the gas and in the aqueous phase [110, 111], and has several industrial [112], environmental [113], and biological [114] applications. The recombination of hydroperoxyl (HO_2) radicals is the most important chemical pathway leading to the production of H_2O_2 in the troposphere [115–117]. Subsequently, H_2O_2 can lead to the acidification of clouds, rain, and fog by oxidizing SO_2 and converting it into H_2SO_4 (and to a less extent oxidizing NO_2 and converting it into HNO_3) [118–122]. H_2O_2 also serves as a reservoir of HO_x radicals that are key oxidants in controlling the self-cleaning of the atmosphere [123–125].

H_2O_2 was first synthesized by Thenard [126] by the reaction of barium peroxide with nitric acids in 1818 and is now considered an important reagent of green chemistry since it decomposes to water and oxygen as the only reaction products. This feature makes H_2O_2 an environmentally friendly oxidizing agent for a wide range of applications such as pulp and paper bleaching, textile applications, detergent applications, disinfectant applications, wastewater treatment, and chemical oxidation processes [127, 128]. It could also serve as a liquid fuel, an alternative to H_2 and O_2, in a fuel cell [129–131].

H_2O_2 is currently produced on an industrial scale with the anthraquinone oxidation (AO) process in which hydrogen, atmospheric oxygen, and an anthraquinone derivative (typically 2-alkyl-anthraquinone) are used with the latter acting as a reaction carrier [127, 128]. The ubiquitous AO process involves multiple steps which require significant energy input and generates waste. In addition, the transport, storage, and handling of bulk H_2O_2 involve hazards as it is irritating to nose and eyes, and high concentration of H_2O_2 is explosive [132]. Other methods for large-scale production of H_2O_2 include partial oxidation of primary or secondary alcohols, and electrochemical methods [133]. Novel alternatives are under investigation such as direct synthesis of H_2O_2 from O_2 and H_2 using a variety of catalysts like alumina, silica, carbon, solvents (e.g., water) [134, 135], photocatalytic reactions over semiconductors where reactive oxygen-based species (e.g., $OH^{\bullet}$, O^{2-}, and H_2O_2) are formed at the surface of semiconductor oxides under UV irradiation [136]. An alternative technology to produce H_2O_2 is to use low temperature (or non-thermal) plasmas [137, 138] which allows H_2O_2 production at ambient temperatures and pressures [139–143]. This enables direct delivery of H_2O_2 to different substrates; even to heat sensitive substrates such as living tissues. The latter has led to biomedical applications of low temperature plasmas [4]. For such applications, it is important to know which mechanisms determine the uptake of plasma products (e.g., H_2O_2) in the liquid around the cells and what is the concentration of plasma products in the aqueous phase. For this, information on the solubility and thermodynamic properties of

the molecule are necessary so that this can be leveraged into macroscopic plasma fluid models [47] to predict the final concentration of H_2O_2 in the liquid phase. Little information is available on the solubility and thermodynamic properties of H_2O_2 in aqueous solutions. The scarcity of this data is especially relevant when temperature and/or pressure changes. The motivation of this work is to provide such data for H_2O_2 using molecular simulations.

Due to the pivotal role of H_2O_2 in many chemical processes, many experimental and computational studies have been conducted to investigate its properties. The crystal structure of H_2O_2 was investigated using diffraction methods or Raman spectroscopy in Refs. [144–148]. Other experimental studies have investigated its densities [149], viscosities [150], vibrational spectra [145, 151–154], vapor pressures [155] and other thermodynamic properties [156]. In addition, densities, freezing points, and vapor pressures of aqueous H_2O_2 solutions were investigated experimentally in Refs. [149, 157–159].

Various computational studies have been carried out which shed light on structural properties of H_2O_2 monomers as well as its clusters, torsional barrier energies, and vibrational-rotational energy levels [160–164] using quantum mechanical approaches. Structure and dynamics of H_2O_2 in water were also investigated using quantum mechanical methods in Refs. [165–167].

In this work, we use force field based Molecular Dynamics (MD) and Continuous Fractional Component Monte Carlo (CFCMC) simulations with the purpose of obtaining solubilities and thermodynamic properties of H_2O_2 in water, for the first time, in a systematic manner such that the quality of the available force fields for H_2O_2 are assessed. Given the complete miscibility of H_2O_2 in water at all concentrations, it is both practical and insightful to explore the properties of H_2O_2 aqueous solutions at varying mole fractions. This allows for a comprehensive understanding of the behaviour of the solution at different concentrations.

Although several force fields are available for H_2O_2 [168–171], only a few of these have been parameterized with respect to the interactions between both H_2O_2 - H_2O_2 and H_2O_2 - H_2O. One is the ABEEM/MM, the atom-bond electronegativity equalization fluctuating charge molecular force field [172, 173], which is computationally very expensive due to its complex potential energy functional form [172, 173]. A simple additive potential model for H_2O_2 was proposed by Orabi & English [74] which was parameterized to account for interactions of H_2O_2 with itself and with water. The model was calibrated with regard to the experimental density and heat of vaporization of pure liquid H_2O_2 at 0° C, and it was able to reproduce the experimental diffusion coefficient at 0° C and the heat capacity at 25° C of liquid H_2O_2. With a combination of the modified TIP3P water force field [75], the H_2O_2 force field could predict the experimental hydration free energies and densities of aqueous H_2O_2 solutions [74]. Another force field parametrization is from the work of Cordeiro [73], wherein the bonded interactions were obtained from *ab initio* quantum calculations [161, 174],

and the Lennard-Jones parameters and partial charges were modified to reproduce the properties of pure liquid H_2O_2 and its hydration free energy. This force field was used to study the distribution, mobility and residence times of H_2O_2 at the interface of water and phospholipid biomembranes. In addition, there is another parametrization in the paper by Vácha *et al.* [171] in which the behaviour of H_2O_2 at the air-water interface was investigated. The force field by Vácha *et al.* [171] only includes electrostatic and van der Waals interactions which were calibrated against the experimental hydration energies of H_2O_2. H_2O_2 exhibits internal cis-trans rotation with an energy barrier of about 4.6 kJ/mol [175, 176]. This is about 2 k_BT (k_B is the Boltzmann constant and T is the temperature) at room temperature. A realistic model of hydrogen peroxide should incorporate the energy barrier for the internal cis-trans rotation of the molecule. This is the case for the force field by Orabi & English [74] and the force field by Cordeiro [73]. The force field by Vácha *et al.* [171] does not allow this rotation to occur.

In this chapter, we evaluate the quality of the force fields which were developed by Cordeiro [73], and Orabi & English [74] for predicting the thermodynamic properties of H_2O_2 in aqueous solutions. We exclude the force field by Vácha *et al.* [171] from our study as it is unable to capture the internal rotation that takes place in H_2O_2 at ambient conditions. We compute the densities of pure H_2O_2 for a range of temperatures (253 K to 353 K), and compare the results with experimental values. In addition, we compute densities, viscosities, and self-diffusion coefficients of H_2O_2 and water in aqueous solutions of H_2O_2 for the whole range of H_2O_2 mole fractions at ambient temperatures and pressures.

To evaluate which water force field is suitable for predicting properties of aqueous solutions of H_2O_2, we use four different widely used water force fields: TIP3P [60, 75], TIP5P-E [177], TIP4P/2005 [61], and a modified version of TIP3P (mTIP3P) [75] that was used in the original work by Orabi & English [74]. The TIP3P [60, 75] force field is able to predict the densities and heats of vaporization of water at ambient conditions, it performs better in calculating the specific heats of water [177], and it also predicts the excess chemical potential of water in better agreement with the experimental values compared to TIP4P/2005 and TIP5P-E [178]. TIP5P-E can capture the thermal conductivities of water [177] and its maximum density near 4°C [62]. TIP4P/2005 [61, 179] can predict the densities and self-diffusion coefficients of water with commendable accuracy [61]. The results are compared with experimental values. Finally, we compute the Henry coefficients of H_2O_2 in water at 300 K and 1 bar.

The rest of this chapter is organized as follows. In Section 3.2, details of the force fields which were developed by Cordeiro [73], and Orabi & English [74] are provided, and the MD and CFCMC simulations are described. The results are presented and discussed in Section 3.3. Finally, concluding remarks are presented in Section 3.4.

Table 3.1: Potential energy functions for force fields developed by Cordeiro [73], and Orabi & English [74]. E_{bonds}, E_{angles}, $E_{\text{dihedrals}}$, E_{vdW}, and $E_{\text{electrostatic}}$ represent the stretching, bending, torsional, van der Waals and electrostatic energies, respectively. The definition of parameters is explained in the text (see section 3.2.1). The parameters are provided in Tables A.1 and A.2 of Appendix A.

Force field	Cordeiro [73]	Orabi & English [74]
E_{bonds}	$\frac{1}{4}k_b(b^2 - {b_0}^2)^2$	$\frac{1}{2}k_b(b - b_0)^2$
E_{angle}	$\frac{1}{2}k_\theta(\cos\theta - \cos\theta_0)^2$	$\frac{1}{2}k_\theta(\theta - \theta_0)^2$
$E_{\text{dihedrals}}$	$\sum_{n=0}^{5} C_n(\cos\psi)^n$	$k_\phi(1 + \cos 2\phi - \delta)$
E_{vdW}	$4\epsilon_{ij}[(\frac{\sigma_{ij}}{r_{ij}})^{12} - (\frac{\sigma_{ij}}{r_{ij}})^6]$	$4\epsilon_{ij}[(\frac{\sigma_{ij}}{r_{ij}})^{12} - (\frac{\sigma_{ij}}{r_{ij}})^6]$
$E_{\text{electrostatic}}$	$\frac{1}{4\pi\epsilon_o}\frac{q_i q_j}{r_{ij}}$	$\frac{1}{4\pi\epsilon_o}\frac{q_i q_j}{r_{ij}}$

3.2 Methodology

3.2.1 Force Fields

The force fields developed by Cordeiro [73] and Orabi & English [74] for H_2O_2 both use potential energy functions for bonded interactions (i.e., bonds, angles, and dihedrals) as well as non-bonded interactions, including van der Waals (vdW) and electrostatic interactions. The total potential energy (E_{total}) is given by

$$E_{\text{total}} = E_{\text{bonds}} + E_{\text{angles}} + E_{\text{dihedrals}} + E_{\text{vdW}} + E_{\text{electrostatic}}, \tag{3.1}$$

where E_{bonds}, E_{angles}, $E_{\text{dihedrals}}$, E_{vdW}, and $E_{\text{electrostatic}}$ are presented in Table 3.1 for both force fields. The bonded interaction parameters (E_{bonds}, E_{angles}, and $E_{\text{dihedrals}}$) listed in Table 3.1 have the following definitions: b is the bond distance, θ is the bond angle, ϕ is the dihedral angle, δ is the multiplicity factor, and ψ is the supplementary angle of ϕ. k_b, k_θ, k_ϕ are the force constants of the bond stretching, angle vibration, and dihedral potentials. b_0 and θ_0 represent the bond distance and bond angle, respectively, at which the corresponding potential functions equal zero. C_n with n ranging from 0 to 5 represents the coefficients for the Ryckaert-Bellemans dihedral potential [180]. q represents the atomic partial charges of the electrostatic energy ($E_{\text{electrostatic}}$) term. A Lennard-Jones (L-J) potential is used for the long-range van der Waals interactions, in which σ represents the distance at which the particle-particle interaction energy is zero, and ϵ represents the depth of the potential well. The mixing rules for the L-J parameters for two dissimilar non-bonded atoms are given by Lorentz-Berthelot (see Equations 2.2 and 2.3) for

the force field by Orabi & English and geometric average (see Equations 2.4 and 2.5) for the force field by Cordeiro. The values of these parameters are provided (using the GROMACS convention) in Table A.1 and Table A.2 of Appendix A for both force fields. The cutoff radius for Lennard-Jones and Coulombic interactions was set to 9 Å. The Particle-Mesh-Ewald [181, 182] method was used to treat long-range electrostatic interactions. Long-range tail corrections were applied to both energies and pressures [54].

We use three different rigid water force fields in this chapter, namely TIP3P [60, 75], TIP4P/2005 [61], and TIP5P-E [62, 63]. We also use a modified TIP3P water force field (mTIP3P) [75] which was used in the work by Orabi & English [74]. In the remainder of this chapter, the force field developed by Cordeiro [73] is referred to as "Cordeiro" and the force field developed by Orabi & English [74] is referred to as "Orabi".

3.2.2 MD simulations

All-atom Molecular Dynamics (MD) simulation of anhydrous H_2O_2 for a range of temperatures from 253 K to 353 K, and H_2O_2 aqueous solutions for various mole fractions of H_2O_2 in the range from 0 to 1.0 at 298 K, were performed using the GROningen MAchine for Chemical Simulations (GROMACS) version 2022.4 [183–187]. Each system was prepared in a simulation box with an initial length of 27.6 Å, containing 500 molecules. A snapshot of a simulation box containing 250 H_2O_2 molecules and 250 H_2O molecules is shown in Figure 3.1.

After energy minimization using the steepest descent algorithm followed by a conjugate gradient algorithm, the MD simulations were run for 100 ps in the constant number of atoms/molecules, volume and temperature (NVT) ensemble. The simulations were then continued in the constant number of atoms/molecules, pressure and temperature (NPT) ensemble for 25 ns. For calculating the viscosities and self-diffusivities, the simulations were continued in the NVT ensemble for another 20 ns. The temperature was kept fixed by the Nosé-Hoover thermostat [188]. The Parinello-Rahman barostat [189] with a time constant of 1 ps and compressibility of 4.5×10^{-5} bar^{-1} was used to keep the pressure at 1 bar. In all simulations, Newton's equations of motion were integrated with a leap-frog algorithm [190] with a time step of 2 fs. Periodic boundary conditions were applied in all Cartesian directions. The parallel linear constraint solver (P-LINCS) [106, 191] was used to constrain the O−H bonds in the H_2O_2 molecule. In this way, the fastest degree of freedom in H_2O_2 (O−H vibrations), is removed which allows to safely use 2 fs time step in our MD simulations.

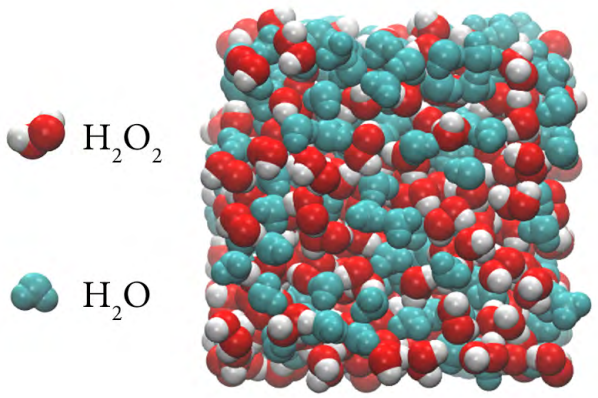

Figure 3.1: A snapshot of a simulation box containing 250 H_2O_2 (red and white spheres represent oxygen and hydrogen atoms, respectively) and 250 H_2O molecules (green spheres), generated by the Visual Molecular Dynamic (VMD) software [192].

3.2.3 MC simulations

Continuous Fractional Component Monte Carlo (CFCMC) simulations [95–97] using the open-source Brick-CFCMC software [97–99] were performed in the isothermal-isobaric (NPT) ensemble to compute the excess chemical potentials (μ^{ex}) from which the Henry coefficients (H_s^{cp}) were calculated. CFCMC simulations contained 300 water molecules in a cubic simulation box with initial dimensions of 21 Å. A single fractional molecule of H_2O_2 was introduced to calculate its excess chemical potential. The cutoff radius for the intermolecular L-J and Coulombic interactions was set to 9 Å. The Ewald summation [193] method was used for calculating electrostatic interactions. Long-range tail corrections were applied to the L-J potential. Periodic boundary conditions were applied in all directions.

For CFCMC simulations, 1,000 initialization cycles were carried out followed by 5×10^6 equilibration cycles and 5×10^6 production cycles. One cycle refers to N number of trial moves, where N is the total number of molecules. Trial moves were selected with the following probabilities: 32% translation trial moves, 22% rotation trial moves, 1% volume changes, 5% each of bending and torsion trial moves, 25% λ changes, and 10% hybrid trial moves that combined swap and identity change trial moves [99]. Three independent simulations were performed for each combination of water force field and H_2O_2 force field to obtain an average value and the standard deviation for the Henry coefficients.

3.3 Results and Discussion

3.3.1 Densities

The densities of anhydrous H_2O_2 for a temperature range of 253 K to 353 K (in steps of 20 K) for both the Orabi and Cordeiro force fields are plotted in Figure 3.2. We used the *gmx density* tool to compute the average density of each system. The experimental values are shown in black circles [149]. The melting point and boiling point of H_2O_2 are reported as 272.74 K and 423.15 K, respectively [194]. While the Cordeiro force field underestimates the densities of anhydrous H_2O_2 by about 3% compared to the experimental values, the densities of anhydrous H_2O_2 using the Orabi force field are in excellent agreement with the experimental values.

Next, we evaluate which water force field is suitable for predicting the densities of H_2O_2 aqueous solutions. To this end, we modelled systems of H_2O_2 aqueous solutions for the whole range of H_2O_2 mole fractions (0 to 1.0) at $T = 298$ K and 1 bar using the Orabi or Cordeiro force fields in combination with four different water force fields: TIP3P, TIP4P/2005, TIP5P-E, and the modified TIP3P water force field (mTIP3P) which was used in the work by Orabi & English [74]. The choice of temperature at 298 K and pressure at 1 bar was motivated by the availability of experimental results by which we could validate our models. The results as a function of the H_2O_2 mole fraction are shown in Figure 3.3. The experimental values [157] are added for comparison.

The densities of pure water (i.e., a mole fraction of zero), using the four water force fields are in good agreement with the reported data at 298 K and 1 bar [61, 195]. The Orabi force field for H_2O_2 in combination with the TIP4P/2005 water force field or mTIP3P water force field predicts the densities of the aqueous solutions in good agreement (ca. 0.6%) with the experimental values [157]. The predicted values for densities of solutions using the TIP5P-E water force field in combination with the Orabi or Cordeiro force fields at low and high concentrations of H_2O_2 are in good agreement with the experimental values. At intermediate concentrations (0.4 - 0.6 mole fractions), however, the TIP5P-E in combination with the Orabi or Cordeiro force fields overestimates the densities of solutions by 2% and 5%, respectively. The TIP3P water force field in combination with the Orabi force field underestimates the densities of the solutions by 2%. The Cordeiro-TIP3P and Cordeiro-mTIP3P models underestimate the densities by 3% at intermediate concentrations. The Cordeiro force field in combination with the TIP4P/2005 water force field also underestimates the densities of the solution with a more pronounced effect at higher mole fractions of H_2O_2 (≥ 0.5, by 3%).

We conclude that the Orabi force field is a better force field than the Cordeiro force field for predicting the densities of pure H_2O_2 in the temperature range of 253 - 353 K. In addition, the TIP4P/2005 or the mTIP3P force field in combination with the Orabi force field predicts the densities of H_2O_2 aqueous solutions for

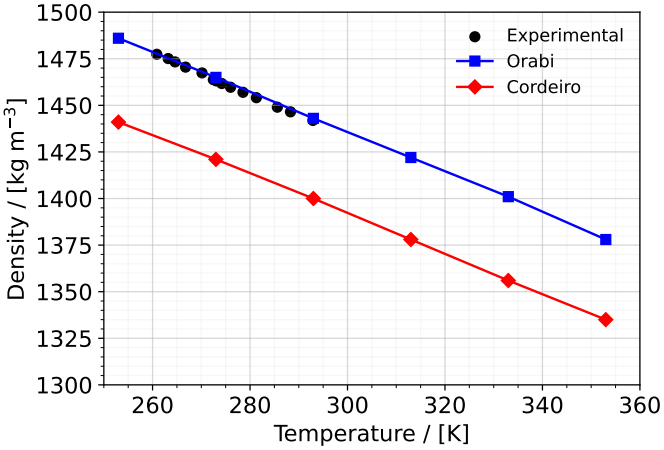

Figure 3.2: Densities of anhydrous H_2O_2 at various temperatures using the Cordeiro [73] and Orabi [74] force fields at 1 bar with the experimental values [149]. Error bars are estimated based on the standard deviation and are much smaller than the symbols used in the figure.

the whole range of mole fractions (0 - 1.0) in very good agreement with the experimental values.

3.3.2 Viscosities

The viscosities were calculated by a non-equilibrium molecular dynamics (NEMD) method, available within GROMACS. For a Newtonian liquid, an applied external force induces a velocity gradient in the system, according to the Navier-Stokes equation. From the constitutive relation between the response strain rate and applied shear stress, we can determine the viscosity of the liquid [196]. We used an amplitude of 0.02 nm/ps^2 for the acceleration profile. The viscosities of H_2O_2 aqueous solutions for various H_2O_2 mole fractions (0 to 1.0) at $T = 293$ K were computed. Figure 3.4 shows the values of viscosity using the Orabi (a) and Cordeiro (b) force fields in combination with the TIP3P, mTIP3P and TIP4P/2005 force fields. The results including the TIP5P-E water force field are shown in Figure A.1 of Appendix A. The standard deviation is used to estimate error bars. The experimental values at 293 K are included for comparison [150]. The viscosities of pure water (i.e., mole fraction = 0) are in good agreement with the computed values using the TIP3P, mTIP3P, TIP4P/2005, and TIP5P-E force fields [197]. The experimental value of the viscosity of pure H_2O_2 at 293 K is 1.25 mPa s [150]. The computed value is 1.36 mPa s by using the Orabi force field, and it is 1.34 mPa s by

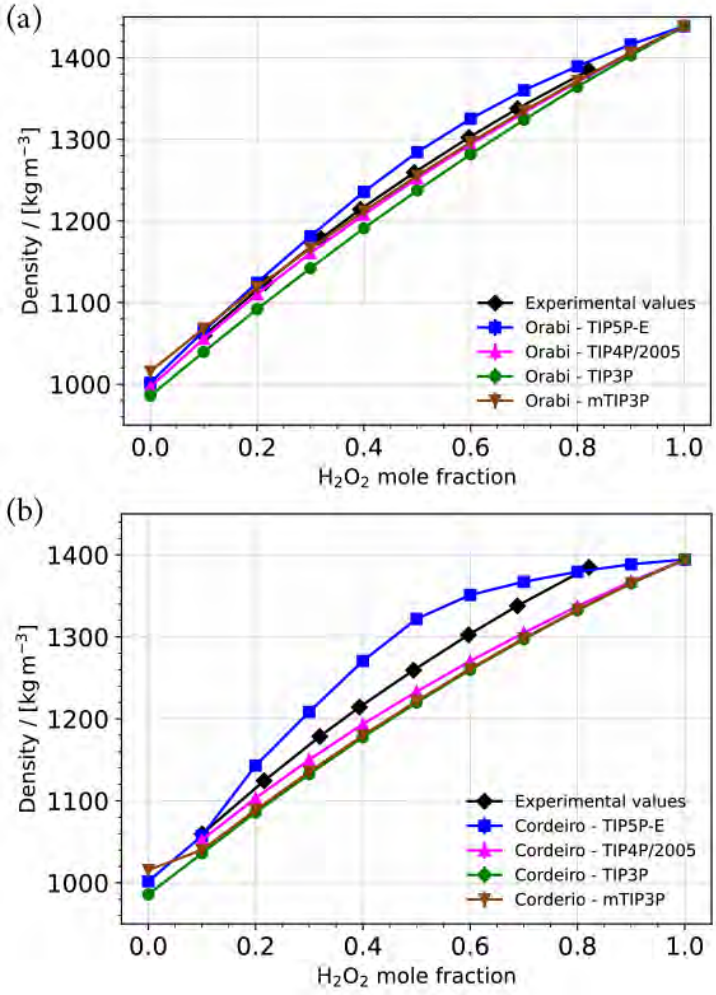

Figure 3.3: Densities of H_2O_2 aqueous solution for various mole fractions of H_2O_2 at $T = 298$ K and 1 bar using the (a) Orabi [74] and (b) Cordeiro [73] force fields in combination with the TIP3P [60], mTIP3P [75], TIP4P/2005 [61] and TIP5P-E [62, 63] water force fields. Experimental values [157] are added for comparison. Error bars are estimated based on the standard deviation and are much smaller than the symbols used in the figure.

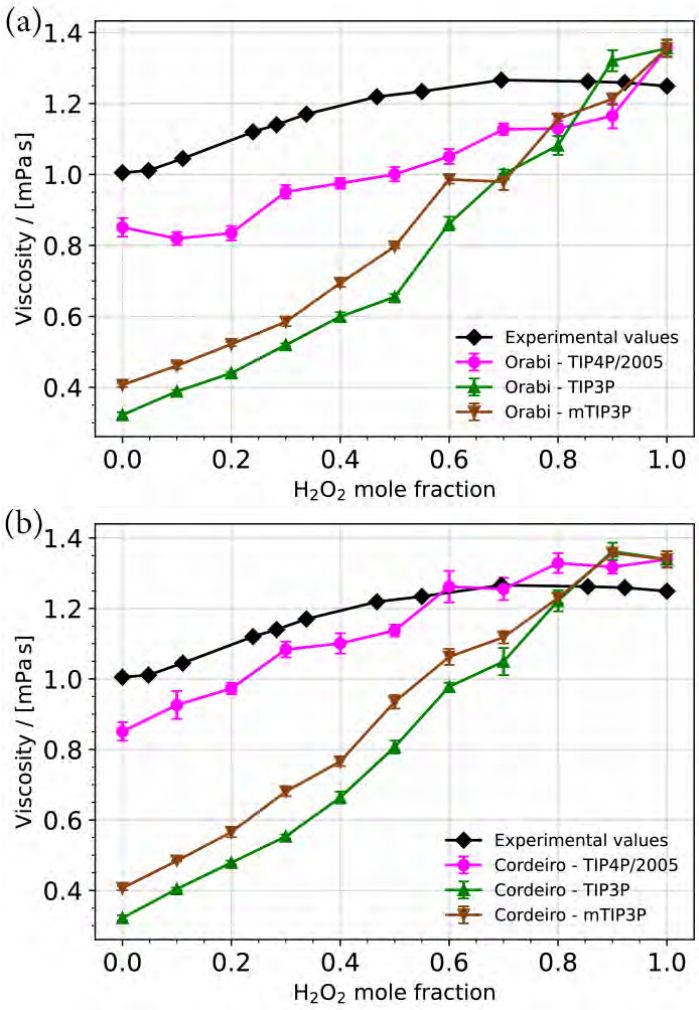

Figure 3.4: Viscosities of H_2O_2 aqueous solution for various mole fractions of H_2O_2 at 293 K for the (a) Orabi [74] and (b) Cordeiro [73] force fields in combination with the TIP3P [60], mTIP3P [75] and TIP4P/2005 [61]. The results including the TIP5P-E water force field are shown in Figure A.1 of Appendix A. Error bars are estimated based on the standard deviation. The experimental values [150] at 293 K are added for comparison.

using the Cordeiro force field. The combination of the Orabi force field with the mTIP3P or TIP4P/2005 underestimates the viscosities of H_2O_2 aqueous solutions for mole fractions up to 0.9. The Orabi-TIP3P model underestimates the values up to a mole fraction of 0.8, above which it slightly overestimates. The combination of the Cordeiro force field with the mTIP3P or TIP3P or TIP4P/2005 water force fields follows a similar trend. The Cordeiro-mTIP3P and Cordeiro-TIP3P models underestimate the viscosities up to a mole fraction of 0.8, above which it slightly overestimates. The Cordeiro-TIP4P/2005 model, however, underestimates the values of viscosities by 7% up to a mole fraction of 0.5 while it overestimates by ca. 5% for H_2O_2 mole fractions higher than 0.8. Contrary to the other water force fields, the TIP5P-E water force field in combination with either the Orabi or Cordeiro force fields predicts a relatively high peak in viscosity at the intermediate mole fractions (mole fraction of 0.5), see Figure A.1 of Appendix A. This may be due to structural changes which the TIP5P-E water force field induces in the system. This is addressed in Section 3.3.4 using radial distribution functions. We conclude that the TIP4P/2005 water force field in combination with the Orabi force field or the Cordeiro force field predicts the viscosities of H_2O_2 aqueous solutions in better agreement with the experimental values.

3.3.3 Self-diffusion coefficients

Self-diffusion coefficients were calculated from the mean-squared displacements (MSD) and were corrected for finite-size effects with the Yeh-Hummer equation [85, 108]

$$D = D_{\mathrm{MD}} + \frac{k_{\mathrm{B}} T \xi}{6\pi\eta L}, \tag{3.2}$$

where D and D_{MD} denote the diffusion coefficient calculated with and without the finite-size effects corrections, respectively. k_{B} is the Boltzmann constant, T is the absolute temperature (in K), ξ is a dimensionless number which for a cubic simulation box is equal to 2.837, L is the length of the cubic simulation box, and η is the computed viscosity of the system. We used the *gmx msd* tool to obtain the MSD as a function of time. D_{MD} is obtained by fitting the MSD to

$$\langle r^2 \rangle_{\mathrm{MSD}} = 2dD_{\mathrm{MD}}t, \tag{3.3}$$

where $d = 3$ is the dimension of the system. The self-diffusion coefficients were calculated from 1 ns to 20 ns NVT trajectories. Figure A.3 of Appendix A shows an example of MSD versus time on a logarithmic scale.

Figure 3.5 shows the self-diffusion coefficients of H_2O_2 and water in aqueous H_2O_2 solutions for the whole range of hydrogen peroxide mole fractions (0 to 1.0). The results, including the TIP5P-E water force field, are shown in Figure A.2 of Appendix A. The self-diffusion coefficients of pure water (i.e., mole fraction=0)

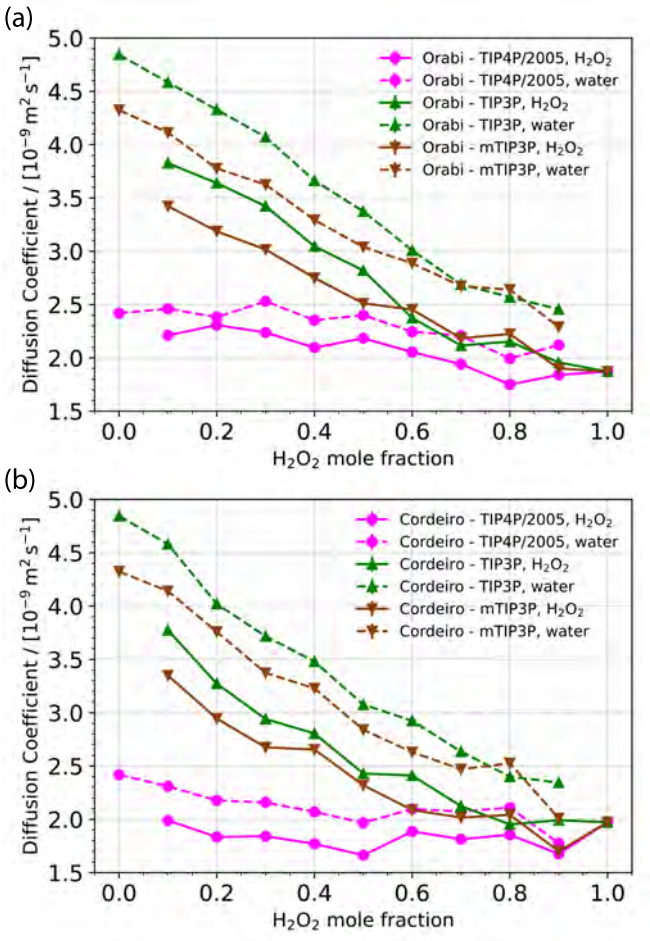

Figure 3.5: Self-diffusion coefficients of water molecules and H_2O_2 molecules in H_2O_2 aqueous solutions for different mole fractions of H_2O_2 at 298 K using the (a) Orabi [74] and (b) Cordeiro [73] force fields in combination with the TIP3P [60], mTIP3P [75], and TIP4P/2005 [61] water force fields. The results including the TIP5P-E water force field are shown in Figure A.2 of Appendix A. Error bars are estimated based on the standard deviation and are much smaller than the symbols used in the figure.

for the four water force fields are in good agreement with the values reported in Refs. [61, 62, 198]. The TIP5P-E and TIP4P/2005 water force fields predict the value of the self-diffusion coefficient in better agreement with the experimental value (2.3×10^{-9} m^2/s [199]).

The self-diffusion coefficients of both the water and the H_2O_2 molecules decrease monotonically by increasing the mole fraction of H_2O_2 using the Orabi-TIP3P or Orabi-mTIP3P models. There is a similar trend for the Cordeiro-TIP3P and Cordeiro-mTIP3P models. The TIP4P/2005 water force field in combination with either the Orabi force field or the Cordeiro force field predicts a relatively constant self-diffusion coefficient for both water and H_2O_2 for the whole range of mole fractions. This is in agreement with a recent experimental study [142] where it was concluded that the self-diffusion coefficients of H_2O_2 in solutions are insensitive to its concentration. The TIP5P-E water force field in combination with either the Orabi or Cordeiro force fields predicts a minimum at a mole fraction of 0.5 for the self-diffusion coefficients of both water and H_2O_2. This is correlated with its very high value of viscosities (see Figure A.1 of Appendix A).

3.3.4 Radial Distribution Functions

In Sections 3.3.2 and 3.3.3, we concluded that the TIP5P-E water force field in combination with either the Orabi force field or the Cordeiro force field for H_2O_2 does not predict viscosities of H_2O_2 aqueous solutions, and thereby self-diffusion coefficients of H_2O_2 in aqueous solution, well. To identify the reason behind, structural properties of H_2O_2 aqueous solution at various mole fractions were investigated using the radial distribution functions (RDF), and hydrogen bonding pattern were explored. Note that there are 4 atom types in each system: hydrogen of water (H_w), oxygen of water (O_w), hydrogen of H_2O_2 (H_p), and oxygen of H_2O_2 (O_p).

The RDFs for O_w and H_w in pure water using the mTIP3P, TIP5P-E and TIP4P/2005 water force fields are shown in Figure 3.6 (a). The results show a first peak at approximately 0.18 nm, and a second peak at approximately 0.32 nm. The peak heights slightly differ between the water force fields with the TIP4P/2005 predicting a higher value followed by the TIP5P-E, and then the mTIP3P predicting a smaller value.

The respective RDFs in H_2O_2 aqueous solutions using the Orabi force field in combination with the three water force fields for systems with mole fractions of 0.1, 0.5, and 0.9 are also shown in Figure 3.6 (b, c, d). The RDFs for O_w and H_w for systems using the Cordeiro force field in combination with the mTIP3P, TIP5P-E, and TIP4P/2005 are shown in Figure A.4 of Appendix A. In the system with a mole fraction of 0.1, the position of the peaks is independent of the water force fields. As the mole fraction of H_2O_2 is increased to 0.5 and 0.9, the position of the peaks does not change in systems where the mTIP3P or TIP4P/2005 force field is used. In the

systems where the TIP5P-E water force field is used, however, the RDF changes: the height of the peaks become smaller and an additional structural correlation appears in the system with a mole fraction of 0.5. This additional correlation between the water molecules persists till 0.8 nm, whereas for the systems in which the mTIP3P or TIP4P/2005 is used, the structural correlation persists only till 0.6 nm. In the Orabi-TIP5P-E system with a mole fraction 0.9, the first two peaks disappear. A similar trend can be observed for the combinations involving the Cordeiro force field with the mTIP3P, TIP5P-E, and TIP4P/2005 water force fields (see Figure A.4 of Appendix A). In the Cordeiro-TIP5P-E combination with a mole fraction of 0.5, however, the structural correlation between the water molecules is stronger than that of the corresponding Orabi-TIP5P-E combination. This can be seen from a more prominent peak after 0.4 nm compared to the other models.

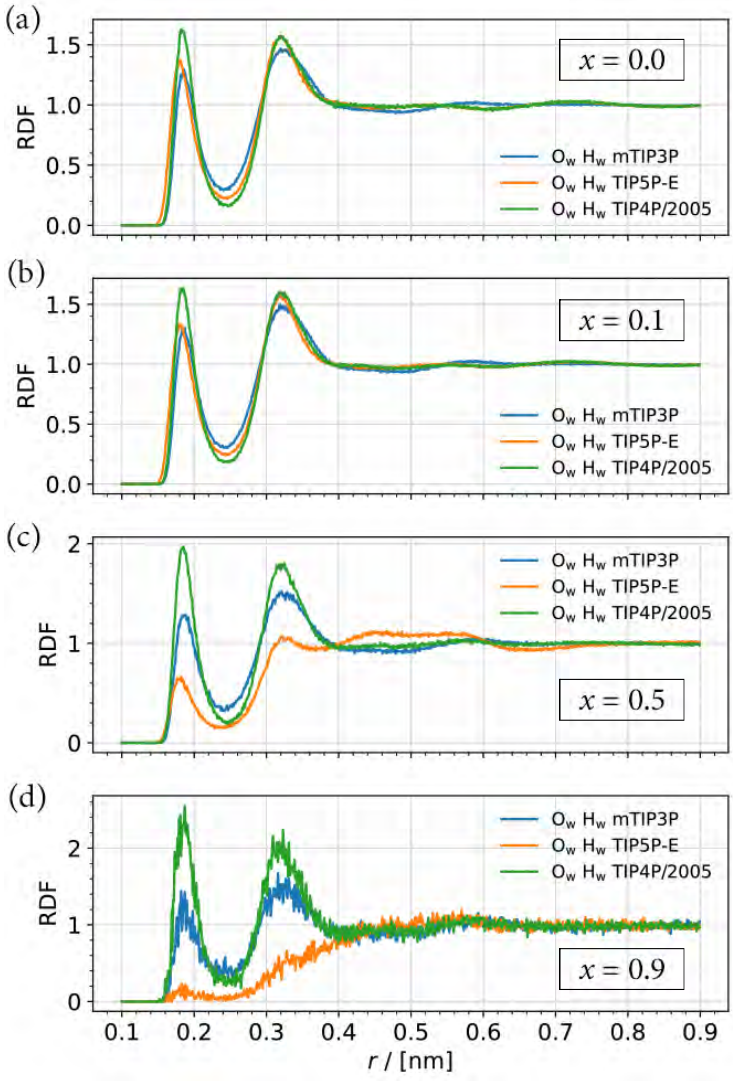

Figure 3.6: Radial distribution functions (RDFs) as a function of radial distance, r [nm], for O_w (O of water) - H_w (H of water) for H_2O_2 aqueous solutions with $x = 0.1$ (b), $x = 0.5$ (c), and $x = 0.9$ (d) at 298 K and 1 bar using the Orabi force field in combination with the mTIP3P [75], TIP5P-E [62, 63], and TIP4P/2005 [61] water force fields, where x is the mole fraction of H_2O_2. The RDF for pure water is plotted in (a).

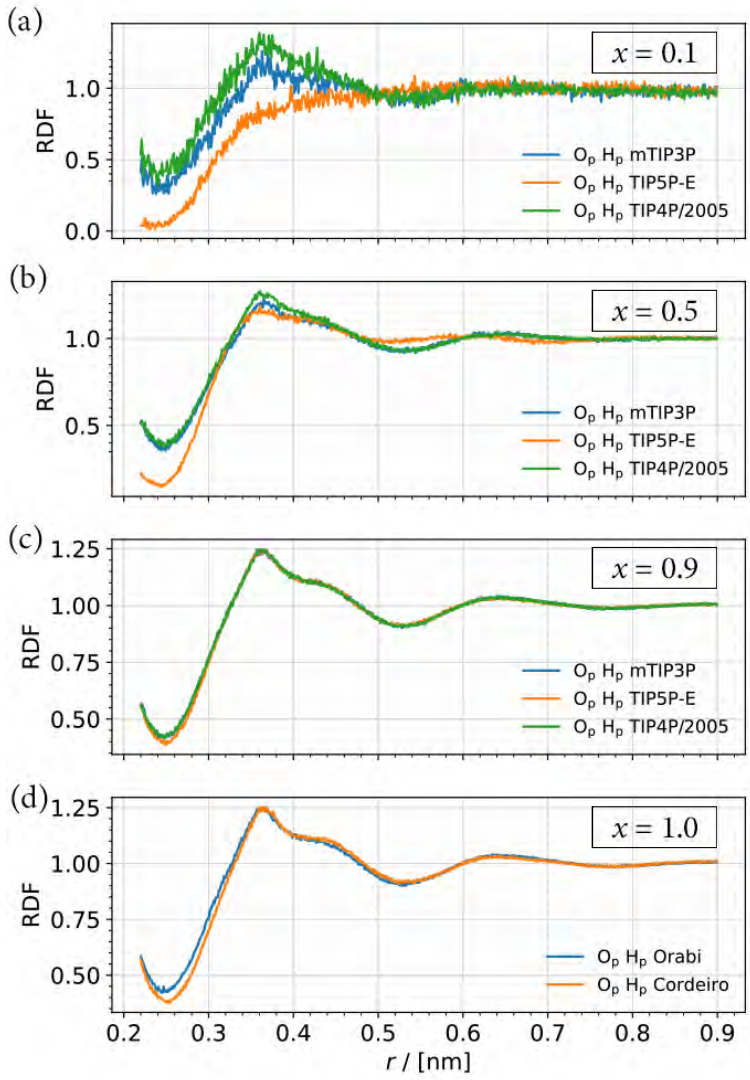

Figure 3.7: Radial distribution functions (RDFs) as a function of radial distance, r [nm], for O_p (O of H_2O_2) - H_p (H of H_2O_2) for H_2O_2 aqueous solutions with $x = 0.1$ (b), $x = 0.5$ (c), and $x = 0.9$ (d) at 298 K and 1 bar using the Orabi [74] force field in combination with the mTIP3P [75], TIP5P-E [62, 63], and TIP4P/2005 [61] water force fields, where x is the mole fraction of H_2O_2. The first peak (at ca. 0.19 nm) was removed to distinguish the differences between the combinations clearly. The RDF for pure H_2O_2 is plotted in (d) using the Orabi force field and the Cordeiro force field.

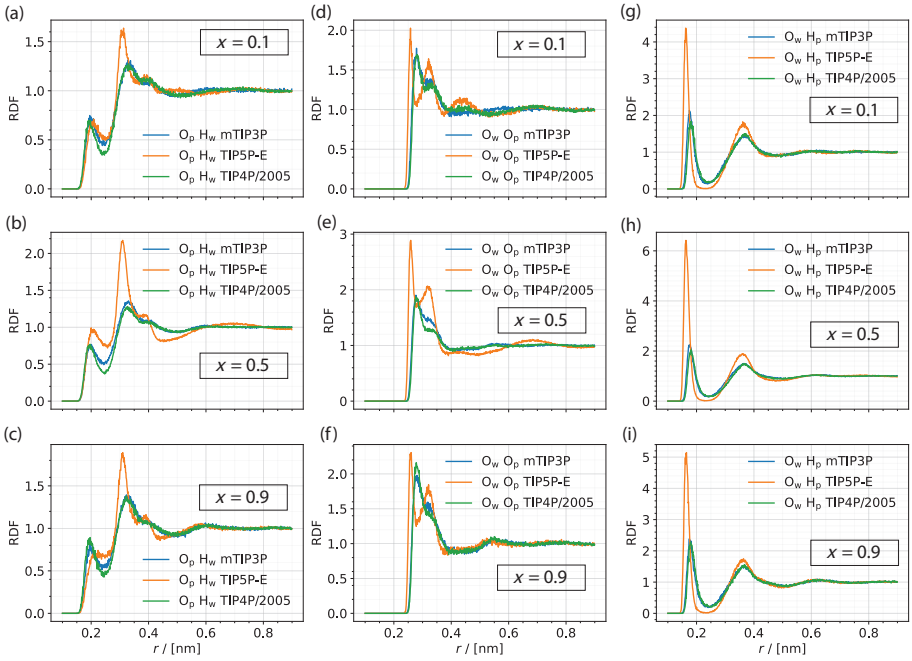

Figure 3.8: Radial distribution functions (RDFs) as a function of radial distance, r [nm], for O_p (O of H_2O_2) and H_w (H of water) (a - c), O_w (O of water) and O_p (O of H_2O_2) (d - f), and O_w (O of water) and H_p (H of H_2O_2) (g - i) for systems using the mTIP3P [75], TIP5P-E [62, 63], and TIP4P/2005 [61] water force fields in combination with the Orabi force field for $x = 0.1$, $x = 0.5$, and $x = 0.9$ at 298 K and 1 bar, where x is the mole fraction of H_2O_2.

The RDFs for O_p and H_p in H_2O_2 aqueous solution with mole fractions of 0.1, 0.5 and 0.9 using the Orabi force field in combination with the three water force fields are shown in Figure 3.7 (a, b, c). Similarly, the respective RDFs using the Cordeiro force field in combination with the three water force fields are shown in Figure A.5 of Appendix A. The RDF of O_p and H_p in pure H_2O_2 using the Orabi and the Cordeiro force fields are also shown in Figure 3.7 (d). The first peak in the RDF has a large amplitude, therefore we removed it to be able to distinguish the differences between the systems more clearly (see Figure A.6 of Appendix A). RDFs of the system at a mole fraction of 0.9 are almost identical using the three different water force fields with a second peak at 0.37 nm. By decreasing the mole fraction of H_2O_2 to 0.5, and 0.1, the RDFs remain the same for the systems in which the mTIP3P-E or the TIP4P/2005 is used. For the system in which the TIP5P-E water force field is used, however, the RDF changes drastically. This is also the case with the Cordeiro-TIP5P-E model. The RDF for pure H_2O_2 using the Orabi force field is almost identical as the system using the Cordeiro force field.

The RDFs for O_p and H_w, O_p and O_w, and O_w and H_p using the Orabi force field with the three water force fields (mTIP3P, TIP4P/2005, and TIP5P-E) for solutions with mole fractions of 0.1, 0.5 and 0.9, are shown in Figure 3.8. Likewise, RDFs with the Cordeiro force field and the water force fields are shown in Figure A.7 of Appendix A. In systems where the mTIP3P and TIP4P/2005 water force fields were used, RDFs have the same structure in which the position of the first peak is in good agreement with X-ray measurements on crystals of $H_2O_2{\cdot}2H_2O$ [200] and simulation results [74]. On the contrary, the structural properties in systems where the TIP5P-E force field was used, have changed. A comparable effect can be seen in Figure A.7 of Appendix A where the Cordeiro-TIP5P-E combination is used.

The number of water molecules in the micro and first solvation shells of H_2O_2 molecule were obtained by integrating up to the first and second minima of the RDF for O_p - O_w, respectively. The results are shown in Table A.3 and A.4 of Appendix A. Orabi & English [74] reported 3.0 and 9.4 water molecules in the micro and first solvation shells, respectively, for a single peroxide molecule in 500 water molecules using the mTIP3P water force field. Authors in Ref. [165] report 6.0 water molecules in the first solvation shell of H_2O_2 using a hybrid quantum-classical simulation. According to our results, the number of water molecules in the first solvation shell at mole fractions of 0.1 and 0.9 are lower for systems where the TIP5P-E water force field is used. At a mole fraction of 0.5, however, the number of water molecules in the first solvation shell slightly increases.

3.3.5 Hydrogen Bond Analysis

The number of hydrogen bonds (calculated as the summation of hydrogen bonds between H_2O_2 - H_2O_2, H_2O_2 - water and water - water) per H_2O_2 molecule for combinations of the Orabi and Cordeiro force fields with the water force fields is shown in Figure 3.9. We used the geometric criterion for hydrogen bonds proposed in Ref. [201]. Accordingly, a hydrogen bond is identified when the angle formed by the hydrogen, the acceptor, and donor atoms is below 30°, with the distance between the acceptor and donor atoms to be less than 0.36 nm. The geometric criterion is depicted in Figure A.8 of Appendix A. The number of hydrogen bonds for both the Orabi and Cordeiro force fields in combination with the TIP4P/2005, TIP3P and mTIP3P water force fields exhibit a steady increase until a mole fraction of 0.9. Existing literature indicates the existence of about 4 hydrogen bonds between hydrogen peroxide and water molecules [165, 167]. For pure H_2O_2 systems, the number of hydrogen bonds sharply decreases to about 5 for both the Orabi and Cordeiro systems. The Orabi-TIP5P-E and Cordeiro-TIP5P-E combinations are however different compared to the others. These combinations indicate a minimum in the number of hydrogen bonds at a mole fraction of 0.4 (around 3 hydrogen bonds for Orabi-TIP5P-E and 2 for Cordeiro-TIP5P-E). This minima for the number of hydrogen bonds at the intermediate concentrations for both these systems are concurrent with the high viscosities and low diffusion seen in Figures A.1 and A.2 of Appendix A.

Analysis of the RDFs, solvation shells, and the number of hydrogen bonds of the TIP5P-E systems indicate a variation in the arrangement of water molecules around a H_2O_2 molecule. We attribute this to the presence of the two dummy atoms representing the lone electron pairs of the oxygen atom of the water molecule in the TIP5P-E water force field. This is in agreement with the work by Nutt & Smith [202] who compared the performance of three water force fields, TIP5P, TIP4P, and mTIP3P in providing a reliable description for protein solvation in water. These authors concluded that TIP5P behaves differently from TIP4P and mTIP3P as the RDFs between the hydrogen of the protein and oxygen of water for their protein-TIP5P system exhibit a shift in the peak position and peak heights, similar to the RDFs in our systems (see Figure 3.8 (g-i)). This anomalous behavior of TIP5P was attributed to the presence of the two dummy atoms representing the lone electron pairs of the oxygen atom of the water molecule in TIP5P. As we observed the same trend in our aqueous systems of H_2O_2, we conclude that the combination of the TIP5P-E water force field and either of the H_2O_2 force fields induce stronger interactions between the water molecules and H_2O_2 due to the presence of the two dummy atoms representing the lone electron pairs of the oxygen atom of the water molecule using the TIP5P-E water force field. This leads to the incongruity of the viscosities and self-diffusion coefficients of the TIP5P-E systems compared to the other systems.

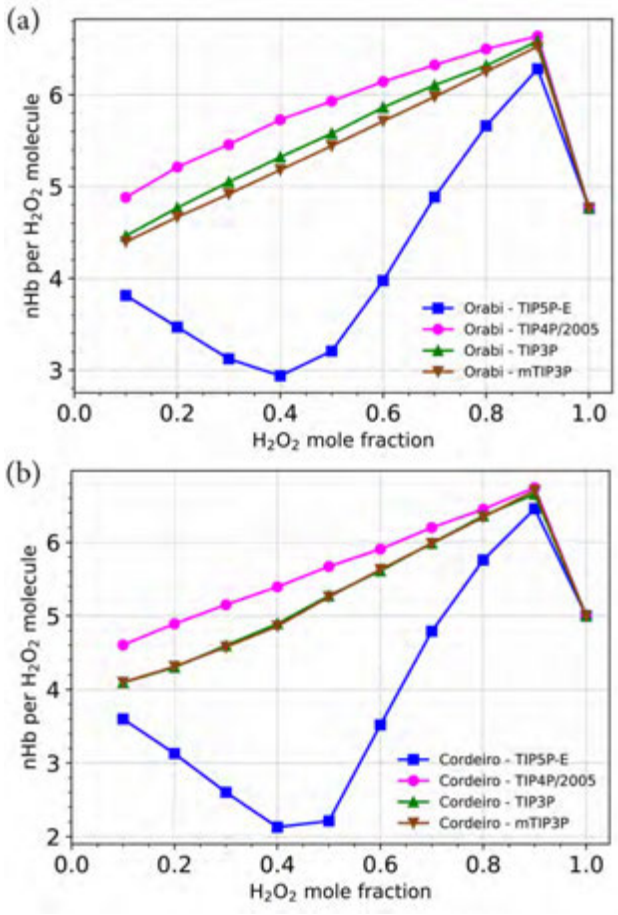

Figure 3.9: Number of hydrogen bonds per H_2O_2 molecule for systems with various mole fractions of H_2O_2 at $T = 298$ K and 1 bar using the (a) Orabi [74] and (b) Cordeiro [73] force fields in combination with the TIP3P [60], mTIP3P [75], TIP4P/2005 [61] and TIP5P-E [62, 63] water force fields.

Table 3.2: Excess chemical potentials (μ^{ex}), the Henry volatility coefficient (K_v^{px}), and the Henry coefficient (H_s^{cp}), using the Orabi and the Cordeiro force fields in combination with the TIP4P/2005, TIP3P, and mTIP3P water force fields. Errors are estimated using standard deviations of independent simulations.

Model	μ^{ex}/[K]	K_v^{px}/[Pa]	H_s^{cp}/[mol/m^3 Pa]
Orabi - TIP4P/2005	-3734 ± 30	512 ± 52	109 ± 11
Orabi - TIP3P	-3836 ± 27	365 ± 32	153 ± 14
Orabi - mTIP3P	-3963 ± 14	239 ± 11	232 ± 11
Cordeiro - TIP4P/2005	-4142 ± 32	132 ± 14	424 ± 46
Cordeiro - TIP3P	-4392 ± 58	58 ± 11	989 ± 190
Cordeiro - mTIP3P	-4487 ± 57	42 ± 7	1357 ± 275

3.3.6 Henry Coefficients

The Henry coefficients were computed for H_2O_2 in water using the Orabi and Cordeiro force fields in combination with the various water force fields. It should be noted that we have not further considered the TIP5P-E water force field for the solubility calculations as it has been ascertained from the earlier sections that neither the Cordeiro nor Orabi force fields in combination with the TIP5P-E water force field could accurately predict the densities, viscosities and self-diffusion coefficients of H_2O_2 aqueous systems. The results of the solubility calculations are provided in Table 3.2. The reported experimental values range from 670 to 1400 [mol/m^3 Pa] [203–206]. It is evident that the Cordeiro force field in combination with the TIP3P or mTIP3P water force fields predicts the Henry constants that are within the range of the reported experimental values.

3.4 Conclusions

We performed MD and CFCMC simulations to study thermodynamic properties of aqueous solutions of H_2O_2. The quality of the available force fields of H_2O_2, Cordeiro [73] and Orabi [74], was evaluated by comparing the results with experiments. The densities of pure H_2O_2 computed using the Orabi force field are in excellent agreement with the experimental values for the temperature range of 253 K to 353 K. The Cordeiro force field underestimates the densities of pure H_2O_2 by 3%. We computed densities, viscosities, and self-diffusion coefficients of H_2O_2 in aqueous solutions for the whole range of mole fractions of H_2O_2 (0 to 1.0) at ambient temperatures and pressures using four widely used water force fields: TIP3P, mTIP3P, TIP4P/2005, and TIP5P-E. The results show

that the TIP4P/2005 water force field in combination with the Orabi force field can predict the densities of H_2O_2 aqueous solution in excellent agreement with experimental values. Both the Orabi and Cordeiro force fields in combination with the TIP4P/2005 water force field predict the viscosities of H_2O_2 in reasonable agreement with experimental results. The TIP5P-E water force field leads to a very high value (maximum) for viscosity of H_2O_2 aqueous solutions at a mole fraction of 0.5, and thereby a very small value (minimum) for self-diffusion coefficient of H_2O_2 and water. The TIP4P/2005 force field in combination with either of the Orabi or Cordeiro force fields predicts a relatively constant diffusion coefficient for the whole range of H_2O_2 mole fractions that is in agreement with a recent experimental study [142]. Analysis of the RDFs, solvation shells, and the number of hydrogen bonds of the TIP5P-E systems indicate a variation in the arrangement of water molecules around a H_2O_2 molecule. We attribute this to the presence of the two dummy atoms representing the lone electron pairs of the oxygen atom of the water molecule in the TIP5P-E water force field, which leads to a stronger interaction between water molecules and H_2O_2 molecules and therefore a deviation in the dynamic properties (viscosities and self-diffusion coefficients) of these systems. Finally, we computed the Henry coefficients of H_2O_2 in water. The values using the Cordeiro force field in combination with either of the TIP3P or mTIP3P water force fields are within the range of experimental values. The quantitative data presented in this work can be used by macroscopic plasma fluid models to determine the uptake of H_2O_2 from the gas phase plasma by liquid [47] or to interpret and complement experimental findings [33].

Chapter 4

Predictive force field for Nitric Oxide and its dimer

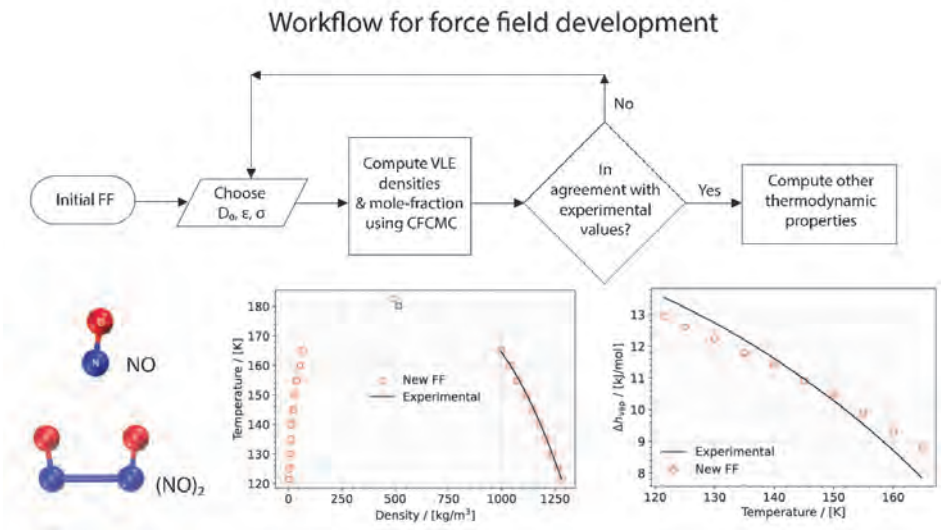

This chapter is based on the following publication: T. H. G. Saji, T. J. H. Vlugt, S. Calero and B. Bagheri, *Modeling nitric oxide and its dimer: force field development and thermodynamics of dimerization*, Physical Chemistry Chemical Physics, **27**, 13662 (2025).

Overview

Nitric Oxide, NO, is a free radical that forms dimers, $(NO)_2$, at its vapor-liquid coexisting temperatures. In this chapter, we developed an all-atom force field for NO and $(NO)_2$. To assess the performance of this force field, we computed the vapor-liquid equilibrium (VLE) properties of the reactive NO-$(NO)_2$ system, as well as those of pure NO and pure $(NO)_2$, using Continuous Fractional Component Monte Carlo (CFCMC) simulations. We then compared the results with the available experimental data and predictions from two previously developed force fields. For the reactive NO-$(NO)_2$ system, we performed CFCMC simulations in the reactive Gibbs ensemble in which the formation of NO dimers, $2\,NO \rightleftharpoons (NO)_2$, is considered. The predicted coexistence vapor-liquid densities, dimer mole fractions in the liquid phase, saturated vapor pressures, and heats of vaporization using our force field in the temperature range 120 K to 170 K are in excellent agreement with experimental values. In addition, we conducted a systematic parameter study to analyze the sensitivity of the new force field parameters and the isolated molecule partition functions of $(NO)_2$ on the VLE properties of the reactive NO-$(NO)_2$ system. The results indicate that the VLE properties of the reactive NO-$(NO)_2$ system are affected by both the force field parameters of the involved species as well as the isolated molecule partition functions of $(NO)_2$.

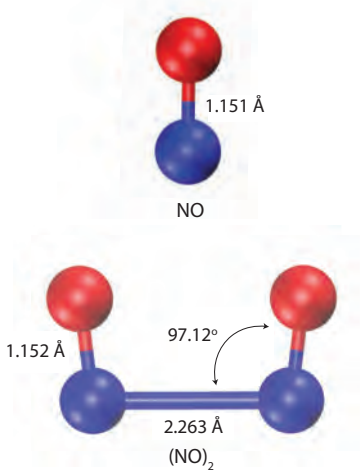

Figure 4.1: Experimental values for bond distances and angles of NO and its dimer, $(NO)_2$ [207, 208]. The blue and red spheres represent N and O atoms, respectively. The visualization is created using the Visual Molecular Dynamics (VMD) software [192].

4.1 Introduction

Electric gas discharge plasmas generated in O_2 and N_2 containing gases are sources of producing considerable amount of nitric oxide (NO) radicals [209, 210]. The molecule NO serves as a precursor for production of other reactive nitrogen species such as nitrogen dioxide (NO_2), dinitrogen trioxide (N_2O_3), dinitrogen tetraoxide (N_2O_4), nitrites (NO_2^-), nitrates (NO_3^-), peroxynitrite ($ONOO^-$), peroxynitrous acid (ONOOH), and others, either directly in the gas phase plasma or upon absorption in aqueous solutions [33, 211]. NO and its byproducts play a key role in plasma processing of liquids and biological materials for applications in biomedicine [34, 212, 213] and agriculture [214–216]. Biomedical applications of plasmas are based on the selective delivery of reactive oxygen and nitrogen species to living tissues for the treatment of chronic wounds and skin infections, and in oncology [217, 218]. In plasma-agriculture, a specific mixture of reactive oxygen and nitrogen species, directly or dissolved in water, is used as fertilizer and/or pesticide for the growth of plants [219–221]. For these applications, it is crucial to quantify the amount of plasma species that are absorbed by aqueous solutions from the gas phase plasmas. Macroscopic models of plasma-liquid systems

are commonly used to predict the densities of species in the gas phase plasma and in the aqueous phase [43, 44, 46, 47, 50]. In these models, the transfer of plasma species from the gas phase into aqueous solutions is incorporated using solubility coefficients of individual species. The solubility coefficients of individual plasma species are commonly used to interpret experimental findings [33, 211]. Experimental solubility coefficients, however, are only available for a few species and solutions, and with limited accuracy. This limits the predictive power of macroscopic models in determining the concentrations of plasma species in the aqueous phase [4]. Molecular simulations are a natural choice to compute the solubility coefficients of plasma species. We aim to use force field-based molecular simulations to compute the solubility coefficients of NO species. It is important to note that the accuracy of force field-based molecular simulations depends on the quality of the force fields used to describe the solute species in the gas phase, the properties of aqueous solutions, and their interactions (see Chapter 3). To the best of our knowledge, there are no all-atom force field parameters for NO that can predict its vapor-liquid-equilibrium (VLE) properties in agreement with available experimental results. This motivated us to first develop a predictive all-atom force field for NO. In a future study, we plan to focus on interaction mechanisms of NO species with aqueous solutions and computing its solubility coefficients.

NO has an unpaired electron in the molecular orbital π^* that is delocalized between the N and O atoms [222]. NO tends to make dimers, trimers, and higher order oligomers with itself; the extend of which depends on temperature and pressure [71, 72]. Kohler [223] reported that in the liquid phase, the existence of dimers is predominant, while the gas phase is mostly comprised of monomers. Marinakis *et al.* [72] also reported that the liquid phase consists predominantly of dimers, but the presence of higher oligomers may also be possible. The mole fraction of dimers in the liquid phase decreases with increasing temperature as studied by Walsh *et al.* [224], Kohler [223], and Marinakis *et al.* [72]. According to Smith & Johnston, [225] the mole fraction of dimers in the liquid phase in the temperature range of 110 - 120 K, is in the range of 0.95 - 0.91. High-level quantum mechanical calculations indicate that the planar cis-ONNO configuration is the most stable form of the NO dimer, with the non-planar trans-ONNO lying about 50 kJ/mol higher in energy [226, 227]. However, Marinakis *et al.,* [72] suggested that non-planar NO dimers may still be present in the liquid phase. Therefore, the development of force field parameters for NO should account for dimer formation in the liquid phase.

Several force fields are available for NO [72, 76, 77, 228–230]. The formation of NO dimers was considered in the force fields developed by Kohler [228], Hirschfelder [229], and Lachet *et al.* [76] using a single-site model for NO and a two-site model for $(NO)_2$. The force field developed by Lachet *et al.* [76] can predict the experimental thermodynamic and transport properties of the reactive NO-$(NO)_2$ system better than the force fields developed by Kohler [228]

and Hirschfelder [229], as shown in the original paper by Lachet *et al.* [76]. As atomistic information is lacking in the force field developed by Lachet *et al.*, [76] due to the treatment of NO as a single-site model, this force field is not suitable for applications where the atomistic information of the N and O atoms in NO molecules is needed. [72] The force fields for NO developed by Marinakis *et al.* [72], Yang *et al.* [230], and Zhou *et al.* [77] are of all-atom type. In the work by Marinakis *et al.*, [72] the formation of NO dimer was implemented using additional attractive and repulsive Gaussian potential terms on top of van der Waals interactions, making it less compatible with widely used molecular simulation packages. Moreover, the transferability of the Gaussian potential to other systems, such as mixtures with water, is not well understood. For example, it remains unclear which mixing rules should be applied in such cases. The force field developed by Yang *et al.* [230] for NO does not take dimer formation into account. Furthermore, this model consists of a 9-6 Lennard-Jones potential with a sixth-order combination law, which is not readily implemented in all popular simulation engines. The force field for NO developed by Zhou *et al.* [77] only takes into account the non-bonded (electrostatic and van der Waals) interactions of the molecule. This force field was optimized to reproduce the experimental density and enthalpy of vaporization of liquid NO at its boiling point. However, it does not take into account the tendency of NO monomers to dimerize (i.e., no dimers are formed in the model). Therefore, this force field is incapable of reproducing the experimental $(NO)_2$ mole fraction in the liquid phase.

In this chapter, we developed an all-atom force field for NO and its dimer, $(NO)_2$, which include 12-6 Lennard-Jones and Coulombic potential energy functions. We assumed that NO exists only as monomers and dimers, and dimers exist in a planar *cis*-ONNO configuration [226]. We computed the VLE properties of the reactive NO-$(NO)_2$ system (e.g., coexistence densities, dimer mole fractions in liquid phase, saturated vapor pressures, and heats of vaporization) using Continuous Fractional Component Monte Carlo (CFCMC) simulations in the reactive Gibbs ensemble [65–67, 231–233]. The VLE properties of the reactive NO-$(NO)_2$ system computed using our force field parameters are in excellent agreement with the experimental values. The performance of our newly optimized force field is also compared with two existing force fields, Lachet *et al.* [76] and Zhou *et al.*, [77] that have been used extensively [234–237].

The rest of the chapter is organized as follows. The CFCMC simulations are described in Section 4.2. In Section 4.3, the details of the new force field parameters are provided. The isolated molecule partition functions for NO and $(NO)_2$ are discussed in Section 4.4. The validation of the new force field with the experimental VLE properties and the comparison of the force field with existing NO force fields is investigated in Section 4.5. In Section 4.5 the sensitivity of the VLE properties on the isolated molecule partition functions of the dimer and the Lennard-Jones potential parameters is discussed. Finally, concluding remarks are

provided in Section 5.4.

4.2 Methodology

CFCMC simulations [95–97] using the open-source Brick-CFCMC software [97–99] were used to assess the validity of our force field parameters for NO and $(NO)_2$ compared to experimental findings. We performed a series of systematic CFCMC simulations in the reactive Gibbs ensemble (RGE) [65–67, 231–233] at constant temperature, number of atoms, and volume, to reproduce the experimental vapor-liquid coexistence densities, coexistence pressures, dimer mole fractions, and heats of vaporization of the reactive NO-$(NO)_2$ system for the temperature range of 121.5 K to 165 K. From these, the critical temperature, density, and pressure of the system were calculated. RGE is a combination of the Gibbs ensemble (GE), [100, 238] which consists of two simulation boxes, one for each of the vapor and liquid phases to model the VLE, and the reaction ensemble, [66, 231, 233] which in our case models the following equilibrium reaction

$$2\ \mathrm{NO} \rightleftharpoons (\mathrm{NO})_2\,. \tag{4.1}$$

We also performed CFCMC simulations in the single-component Gibbs ensemble (GE) [87, 239] at constant temperature, number of molecules, and volume to compare the performance of our force field with the force fields developed by Lachet *et al.* [76] and Zhou *et al.* [77] To do this, we computed the coexistence densities and pressures of pure NO for the temperature range 120 K to 170 K and pure $(NO)_2$ for the temperature range 120 K to 300 K.

For the RGE, there are two sets of fractional groups; [100] (1) fractional group for individual components/molecules involved in the system for molecule transfers and (2) fractional group for reactions. The contributions of fractional components are not taken into account when computing the ensemble averages [100].

The fractional group for molecule transfers facilitates molecule transfers between the vapor and liquid simulation boxes. The reactive NO-$(NO)_2$ system contains two such fractional groups, one each for NO and $(NO)_2$. As mentioned earlier, the strength of the interactions of the molecules in these group are modulated by their corresponding λ values ($\lambda_{\mathrm{Gibbs,NO}}$ and $\lambda_{\mathrm{Gibbs,(NO)_2}}$). There are three trial moves associated with the fractional molecules for molecule transfers [100, 240]: (1) attempts to change the value of λ_{Gibbs}; (2) attempts to transfer a fractional molecule from one simulation box to another; (3) attempts to convert a fractional molecule in a box to a "whole" molecule, and simultaneously, transform a "whole" molecule in the other box into a fractional molecule.

For the NO-$(NO)_2$ system, the fractional group for reactions contains fractional molecules of either the reactants (2 NO) or the reaction products $(NO)_2$. The interactions of these molecules with the other molecules in the simulation is

modulated by the parameter, $\lambda_{\text{reaction}}$. One fractional group for reactions was added each to the liquid and vapor simulation boxes. The trial moves associated with the fractional molecules in this group are [241]: (1) attempts to change the value of $\lambda_{\text{reaction}}$; (2) attempts to convert the fractional molecules of reactant to fractional molecules of reaction product, or vice-versa; (3) attempts to convert the fractional molecules of the reactant (or the reaction product) in a box to "whole" molecules of the reaction product (or the reactant), and simultaneously, transform "whole" molecules of the reaction product (or the reactant) to fractional molecules of reactant (or the reaction product).

The GE simulation of unreactive NO and $(NO)_2$ systems contains the fractional group for molecule transfers and not the fractional group for reactions. In addition to the trial moves associated with the fractional molecules present in the RGE and the GE simulations, both the simulation setups have thermalization trial moves (molecule translations, rotations and volume changes). Since the molecules in the simulation are rigid, the sampling of the intramolecular degrees of freedom are not considered.

The simulation in the RGE is considered equilibrated when a combined phase equilibrium and chemical equilibrium is achieved. The two simulation boxes in this ensemble can exchange molecules and volume until the two phases reach phase equilibrium. Phase equilibrium is achieved when the liquid and vapor chemical potentials, μ, of individual species are equal ($\mu_{\text{NO, liquid}} = \mu_{\text{NO, vapor}}$ and $\mu_{(\text{NO})_2\text{, liquid}} = \mu_{(\text{NO})_2\text{, vapor}}$). The chemical potential in the phase x (liquid or vapor) for the component i (NO or $(NO)_2$) is given by [100]

$$\begin{aligned}\mu_{x,i} = &-k_{\text{B}}T \ln\left[\frac{V_x}{\Lambda_i^3(N_{x,i}+1)}\right] \\ &- k_{\text{B}}T \ln\left[\frac{p_{x,i}(\lambda_{\text{Gibbs},i}=1)}{p_{x,i}(\lambda_{\text{Gibbs},i}=0)}\right],\end{aligned} \tag{4.2}$$

where k_{B} is the Boltzmann constant, T is the temperature, V_x is the volume of the simulation box that represents phase x, Λ_i is the thermal de Broglie wavelength of component i, $N_{x,i}$ is the number of molecules of component i in phase x. $p_{x,i}(\lambda_{\text{Gibbs, }i} = 1)$ and $p_{x,i}(\lambda_{\text{Gibbs, }i} = 0)$ are the probabilities that $\lambda_{\text{Gibbs, }i}$ (coupling parameter of fractional molecule for molecule transfers for component i) are 1 and 0, respectively, in phase x. Chemical equilibrium is attained when $2\,\mu_{\text{NO, liquid}} = \mu_{(\text{NO})_2\text{, liquid}}$ and $2\,\mu_{\text{NO, vapor}} = \mu_{(\text{NO})_2\text{, vapor}}$ [242, 243]. For a system containing S components in phase x, where components 1 to R are reactants and R+1 to S are reaction products, the chemical potentials of the components follow

the relations [99, 233]

$$\sum_{i=1}^{R} \nu_i \mu_{i,x} = -k_{\mathrm{B}}T \ln \left\langle \prod_{i=1}^{R} \left(\frac{q_i}{\Lambda_i^3 \rho_{i,x}}\right)^{\nu_i} \right\rangle - k_{\mathrm{B}}T \ln \left[\frac{p_{i,x}(\lambda_{\mathrm{reaction},x} = 1)}{p_{i,x}(\lambda_{\mathrm{reaction},x} = 0)}\right], \tag{4.3}$$

$$\sum_{i=R+1}^{S} \nu_i \mu_{i,x} = -k_{\mathrm{B}}T \ln \left\langle \prod_{i=R+1}^{S} \left(\frac{q_i}{\Lambda_i^3 \rho_{i,x}}\right)^{\nu_i} \right\rangle - k_{\mathrm{B}}T \ln \left[\frac{p_{i,x}(\lambda_{\mathrm{reaction},x} = 1)}{p_{i,x}(\lambda_{\mathrm{reaction},x} = 0)}\right], \tag{4.4}$$

where, q_i is the isolated molecular partition function (excluding the translational part) of component i, ν_i is the stoichiometric coefficient of component i in the reaction, $\rho_{i,x}$ is the number density of the species i in phase x. $p_i(\lambda_{\mathrm{reaction},\ x} = 1)$ and $p_i(\lambda_{\mathrm{reaction},\ x} = 0)$ are the probabilities that $\lambda_{\mathrm{reaction},\ x}$ (coupling parameter of fractional group for reactions for phase x) approaches 1 and 0, respectively, for component i.

For a two-component system such as NO-$(NO)_2$, which follows the reaction in Equation 4.1, Equations 4.3 and 4.4 simplify to

$$\nu_i \mu_{i,x} = -k_{\mathrm{B}}T \ln \left[\frac{q_i}{\Lambda_i^3 \rho_{i,x}}\right]^{\nu_i} - k_{\mathrm{B}}T \ln \left[\frac{p_{i,x}(\lambda_{\mathrm{reaction},\ x} = 1)}{p_{i,x}(\lambda_{\mathrm{reaction},\ x} = 0)}\right], \tag{4.5}$$

where i are the components NO and $(NO)_2$. From Equations 4.3 - 4.5 it is clear that to perform CFCMC simulations in the RGE, partition functions of the isolated molecules involved in the reaction are required. More discussion about the partition functions of NO and $(NO)_2$ are given in Section 4.4. The simulation in the GE is equilibrated when there is equilibrium between the vapor and liquid phases (phase equilibrium).

The critical temperatures and densities were obtained by fitting the liquid and vapor phase densities to the law of rectilinear diameters [244]

$$\frac{\rho_{\mathrm{l}} + \rho_{\mathrm{g}}}{2} = \rho_{\mathrm{c}} + A(T - T_{\mathrm{c}}), \tag{4.6}$$

$$\rho_{\mathrm{l}} - \rho_{\mathrm{g}} = B(T - T_{\mathrm{c}})^{\beta}, \tag{4.7}$$

where ρ_{l} and ρ_{g} correspond to the density of liquid and vapor phases, respectively, along the VLE curve, ρ_{c} is the critical density, and T_{c} is the critical temperature.

A and B are system dependent fitting parameters. For the RGE, β is selected as the value that corresponds to the maximum of the coefficient of determination (R^2) for the linear regression fit of $(\frac{\rho_l - \rho_g}{\rho_0})^{\frac{1}{\beta}}$ versus temperature [242], where ρ_0 is an arbitrary number density which is set to $1\,\text{Å}^{-3}$. In the single-component GE, β is taken as 0.32 [54].

To compute the coexistence pressures of the RGE and the GE systems, a series of NPT simulations for vapor phase were performed to match the vapor phase densities of the RGE and the GE. The P-T saturation points were fitted to a correlation of the form [241]

$$P_{\text{sat}}(T) = A \exp\left[\frac{-B}{T}\right], \tag{4.8}$$

where A and B are system-dependent fitting parameters. The critical saturated vapor pressure, P_c, was obtained by extrapolating the above correlation to T_c.

The molar heat of vaporization was calculated as the difference between the average molar enthalpy of the vapor and liquid simulation boxes of the RGE [76]

$$\Delta h_{\text{vap}} = h_{\text{vapor}} - h_{\text{liquid}}, \tag{4.9}$$

where Δh_{vap} is the molar heat of vaporization and h_{liquid}, h_{vapor} are the true molar enthalpies of the liquid and vapor simulation boxes, respectively. True molar enthalpy (h_x) is defined as [245]

$$h_x = \frac{H_x}{\sum_i n_{i,x}} \tag{4.10}$$

where H_x is the total enthalpy in phase x (liquid or vapor) and $n_{i,x}$ is the number of moles of component i (NO or $(NO)_2$) in phase x. For the calculation of the molar heat of vaporization, the internal energies and volumes were obtained from RGE calculations and the saturated pressures were obtained from a series of NPT simulations. The total true molar enthalpy is taken as the sum of h_{liquid} and h_{gas}.

For all simulations in the RGE, 10^3 initialization cycles were performed followed by an equilibration of 8×10^6 cycles. This was followed by 5 independent production runs of 3×10^6 cycles, each. Note that one cycle refers to N number of trial moves, where N is the total number of molecules present in the system. The error bars are computed from the standard deviation of 5 independent production runs. The initial system size for the simulations in the RGE was a total of 400 molecules for temperatures below 140 K and 500 molecules for temperatures above 140 K. The trial moves were selected with the following probabilities: thermalization trial moves (which includes both translations and rotations) (69 %), particle exchanges (15 %), volume trial moves (1 %) and reaction trial moves (15 %). For the GE simulations, 10^3 initialization cycles were performed followed by an

equilibration of 8×10^6 cycles and a production run of 8×10^6 cycles. The error bars for the GE simulations are computed from the standard deviation of 5 blocks into which the production run was divided. The trial moves were selected with the following probabilities: thermalization trial moves (84 %), particle exchanges (15 %) and volume trial moves (1 %). Periodic boundary conditions were considered in all directions for both the RGE and the GE.

4.3 Force Fields

The structures of NO and $(NO)_2$ were considered rigid according to the corresponding experimental geometries [207, 208] (see Figure 4.1). We considered two terms in the total potential energy function (E_{total}), electrostatic interactions ($E_{\text{electrostatic}}$) and van der Waals interactions (E_{vdW}),

$$E_{\text{total}} = E_{\text{electrostatic}} + E_{\text{vdW}}. \tag{4.11}$$

For the electrostatic interactions, the Coulombic potential energy function is considered

$$E_{\text{electrostatic}} = \frac{1}{4\pi\epsilon_o}\frac{q_i q_j}{r_{ij}}, \tag{4.12}$$

where q represents the atomic partial charges, r_{ij} is the distance separating the charges, and ϵ_o is the permittivity of vacuum. The atomic partial charges of NO were obtained from the ratio between the experimental dipole moment [246] and the experimental bond length of NO [207]. The partial charges on the atoms of $(NO)_2$ were taken to be the same as that of NO. For the van der Waals interactions, the 12-6 Lennard-Jones (L-J) potential energy function is considered

$$E_{\text{vdW}} = 4\epsilon_{ij}\left[\left(\frac{\sigma_{ij}}{r_{ij}}\right)^{12} - \left(\frac{\sigma_{ij}}{r_{ij}}\right)^{6}\right], \tag{4.13}$$

where σ represents the distance at which the particle-particle interaction energy is zero, and ϵ represents the depth of the potential well. The Lorentz-Berthelot [81] mixing rules were used for the L-J parameters of two dissimilar non-bonded atoms, $\sigma_{ij} = \frac{\sigma_i+\sigma_j}{2}$, $\epsilon_{ij} = \sqrt{\epsilon_i\epsilon_j}$. A cutoff radius of 10 Å was used for both the Lennard-Jones and Coulombic interactions. The Ewald summation method [181, 182] was used to treat long-range Coulombic interactions. The energies and pressures of the simulations were corrected with long-range tail corrections for the L-J interactions [54]. After numerous trials of varying the σ and ϵ parameters (110 combinations were tested in total), we arrived at the values provided in Table 4.1. These parameters are referred to as the New FF in the rest of this chapter. A detailed discussion on the sensitivity analysis of the New FF parameters is provided in Section 4.5.3.

Table 4.1: Our new force field parameters for NO and $(NO)_2$ molecules which are referred to as New FF in the text.

Atoms	ϵ/k_B/[K]	σ/[Å]	q/[e]
		NO	
N	48.50	3.09	0.0288
O	56.29	2.94	−0.0288
		$(NO)_2$	
N	47.00	3.02	0.0288
O	54.52	2.87	−0.0288

Lachet *et al.* [76] treat NO as a single L-J sphere with the 12-6 potential function. To model $(NO)_2$, two NO L-J sites separated by a distance of 2.237 Å were used. The individual L-J parameters for each NO site in the dimer are considered to be the same as those for the monomer. The L-J parameters of the force field developed by Lachet *et al.* [76] are listed in Table B.9 of Appendix B. Lachet *et al.* [76] neglect electrostatic interactions in their models of NO and $(NO)_2$. The cutoff for the L-J potential was taken as half the length of the simulation box, and interactions beyond the cutoff distance were considered using the long-range tail correction. [54] The force fields for NO and $(NO)_2$ developed by Lachet *et al.* [76] are referred to as Lachet FF in the rest of the chapter.

In the work by Zhou *et al.* [77], NO is modeled as a two-site rigid body with partial charges and 12-6 L-J potential on both sites. In their model, the N and O atoms of NO are separated by a distance of 1.15 Å. The Lorentz-Berthelot mixing rules [81] were used for the L-J parameters of two dissimilar nonbonded atoms. The L-J parameters and partial charges taken from the work by Zhou *et al.* [77] are listed in Table B.9 of Appendix B and are referred to as Zhou FF in the rest of this chapter. Zhou *et al.* [77] did not parameterize a force field for $(NO)_2$.

4.4 Isolated Molecular Partition Functions

As explained in Section 4.2, to calculate the chemical potential of a component in a reaction, the isolated molecular partition function, $q_{\text{total}}(V,T)$, of that component is needed (see Equation 4.5). We calculated the isolated molecular partition functions of NO and $(NO)_2$ according to [99] (see Section 2.4)

$$q_{\text{total}}(V,T) = q_{\text{trans}}(V,T)q_{\text{vib}}(T)q_{\text{rot}}(T)q_{\text{elec}}(T). \tag{4.14}$$

The values of the vibrational frequencies and rotational constants required to calculate the isolated molecular partition functions of NO and $(NO)_2$ are given in

Tables B.2 and B.3 of Appendix B. The rotational symmetry number (σ_{rot}) for both NO and $(NO)_2$ is equal to 1. The degeneracies of the electronic ground state (g_{el}) for NO and $(NO)_2$ are 2 and 1, respectively. The value of D_0 for NO was calculated from the enthalpies of formation of NO, N and O, which were obtained from the JANAF tables [247]; $D_{0,\text{NO}} = 629.82\,\text{kJ/mol}$. The atomization energy of $(NO)_2$, $D_{0,(NO)_2}$, was not readily available in the JANAF tables, [247] but can be calculated by

$$D_{0,(NO)_2} = 2D_{0,\text{NO}} + \text{BDE}_{(NO)_2}, \tag{4.15}$$

where $\text{BDE}_{(NO)_2}$ is the bond dissociation energy of $(NO)_2$, which is the energy required to break the N-N bond of $(NO)_2$.

The values of $\text{BDE}_{(NO)_2}$ reported in literature, depending on the accuracy of the theoretical method or experimental technique used, are in the range of 7.64 to 13.8 kJ/mol [208, 227, 231, 248–252]. Due to the large variations in the values of $\text{BDE}_{(NO)_2}$ reported in literature, an approach used by Turner *et al.* [252] and Johnson *et al.* [231] was to adjust the value of $\text{BDE}_{(NO)_2}$ to reproduce the experimental dimer mole fraction in the liquid phase. With this approach, Turner *et al.* [252] obtained a value of $\text{BDE}_{(NO)_2}$= 10.9 kJ/mol and Johnson *et al.* [231] achieved a value of $\text{BDE}_{(NO)_2}$= 13.6 kJ/mol. In our work, we also varied the value of $\text{BDE}_{(NO)_2}$ between 7.64 and 13.8 kJ/mol to predict the mole fractions of dimer in the liquid phase as well as the VLE properties of the reactive NO-$(NO)_2$ system in agreement the available data. After numerous iterations, we obtained a value of $\text{BDE}_{(NO)_2}$= 13.06 kJ/mol which corresponds to a value of $D_{0,(NO)_2}$= 1269 kJ/mol.

The isolated molecular partition functions of NO and $(NO)_2$ were calculated according to Equation 4.14 for temperatures ranging from 121.5 K to 165 K. A correlation was fitted to the respective isolated molecular partition functions, which is given by

$$\ln\left[\frac{qV_0}{\Lambda^3}\right]_{\text{NO}} = \frac{75396.84}{T} + 11.26, \tag{4.16}$$

$$\ln\left[\frac{qV_0}{\Lambda^3}\right]_{(NO)_2} = \frac{152020.74}{T} + 19.42, \tag{4.17}$$

where q is the isolated molecule partition function excluding the translational contribution.

4.5 Results and Discussion

The validation of the New FF with the experimental VLE properties of the reactive NO-$(NO)_2$ system is discussed in Section 4.5.1. The performance of the New FF compared to the Lachet FF and Zhou FF in predicting the VLE properties of pure NO and pure $(NO)_2$ are discussed in Section 4.5.2. Finally, the dependence of the

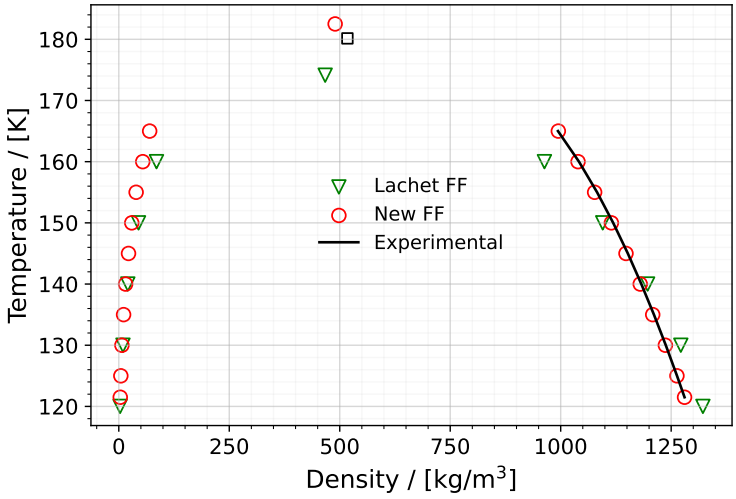

Figure 4.2: Vapor-liquid coexistence densities of the NO-$(NO)_2$ system predicted using the New FF as a function of temperature (red circles). Error bars for the New FF are estimated based on the standard deviation of 5 independent simulations and are much smaller than the symbols used in the figure. The orthobaric densities obtained using the Lachet FF [76] (green triangles) along with the experimental liquid densities [253] (black line) are added for comparison. The experimental critical point (black square) is also shown in the figure.

VLE of the reactive NO-$(NO)_2$ system on the $D_{0,(NO)_2}$ and L-J parameters (σ and ϵ) is investigated in Section 4.5.3.

4.5.1 Reactive NO-$(NO)_2$ systems

Coexistence Densities

The coexistence densities of the liquid and vapor phases were computed at ten different temperatures ranging from 121.5 K to 165 K using the New FF and the Lachet FF. The results are presented in Figure 4.2 along with the available experimental data [253]. The raw data are available in Table B.5 of Appendix B. The average absolute deviation between the liquid densities calculated using the New FF and the experimental liquid densities is 2.32 kg/m^3 (0.2 %). Our results using the Lachet FF are also in agreement with those presented in the original paper by Lachet *et al.* [76]. The Lachet FF overestimates the liquid densities at lower temperatures (120 K to 140 K) and underestimates the liquid densities at

Table 4.2: Critical temperatures (T_c), densities (ρ_c), and pressures (P_c) calculated using the New FF and the Lachet FF [76]. Errors (written as subscripts) are estimated using standard deviations of 5 independent simulations. Experimental values [253] are added for comparison.

	T_c/[K]	ρ_c/[kg/m^3]	P_c/[MPa]
New FF	$182.51_{0.54}$	$489.59_{1.52}$	$6.24_{0.15}$
Lachet FF [76]	174.03	466.60	6.37
Experimental [253]	180.15	517.35	6.48

higher temperatures (>140 K). The average absolute deviation between the liquid densities calculated using the Lachet FF and the experimental liquid densities is 36.89 kg/m^3 (3.3 %) which is much larger than that calculated using the New FF.

The predicted critical temperature (T_c), density (ρ_c), and pressure (P_c) using the New FF and Lachet FF are presented in Table 4.2 along with experimental data [253]. The predicted critical density using the New FF is 489.59 kg/m^3 which is within 27.76 kg/m^3 (5.4 %) of the experimental value. The critical temperature predicted using the New FF is 182.51 K which has a deviation of 1.3 % from the experimental critical temperature. The critical density and temperature predicted by the Lachet FF deviate from the experimental values by 9.8 % and 3.4 %, respectively.

4

Dimer mole fractions

The mole fraction of $(NO)_2$ in the liquid phase of the NO-$(NO)_2$ system obtained using the New FF and the Lachet FF is presented in Figure 4.3. The raw data are presented in Table B.6. The experimental values, in the temperature range from 110 K to 120 K, are taken from the work of Smith & Johnston [225]. Walsh *et al.* [224] used a modified Wertheim's association theory and Kohler [223] used the theory of corresponding states of mixture to theoretically estimate the dimer mole fractions in the liquid phase. The data from both works are presented in Figure 4.3 for comparison.

At 110 K, the predicted $(NO)_2$ mole fraction using the New FF is 0.92, while the corresponding experimental value is 0.95. The mole fraction of dimers predicted using the New FF monotonically decreases with increasing temperature. $(NO)_2$ mole fraction obtained using the New FF is in better agreement with the estimate values of Walsh *et al.* [224] for the temperature range (121.5 K to 165 K). The dimer mole fractions predicted using the Lachet FF is in better agreement with the estimates by Kohler [223]. We note that our calculations using the Lachet FF are in agreement with those presented in the original work by Lachet *et al.* [76]. In the vapor phase, monomers have a more dominant presence for the temperature

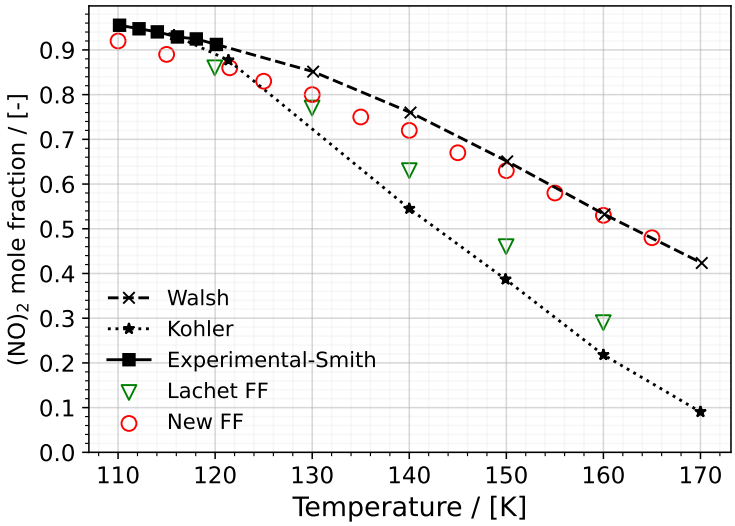

Figure 4.3: Dimer mole fractions in the NO-$(NO)_2$ liquid phase, which is at coexistence with the vapor phase, predicted using the New FF (red circles) as well as the Lachet FF [76] (green triangles) as a function of temperature. Error bars for the New FF are estimated based on the standard deviation of 5 independent simulations and are much smaller than the symbols used in the figure. The experimental mole fractions (black squares) from 110 K to 120 K [225] and extrapolated estimates of Walsh *et al.* [224] and Kohler [223] from 120 K to 170 K are added for comparison.

range 121.5 K to 165 K. The presence of dimers increases as the temperature increases, although slightly (see Table B.6 of Appendix B). At 121.5 K, the New FF predicts a dimer mole fraction of 6 %, whereas the Lachet FF predicts a dimer mole fraction of 0.4 %. One reason for the lower mole fraction of $(NO)_2$ predicted in the work of Lachet *et al.* [76] compared to our work using the New FF could be attributed to the differences between the standard chemical potential, μ^0 (defined as $\mu^0 = -k_B T \ln\left[\frac{qV_0}{\Lambda^3}\right]$ [233, 242]) of $(NO)_2$ and 2 NO. The differences between the standard chemical potential of $(NO)_2$ and 2 NO used in the work of Lachet *et al.* favor more NO molecules in the system [76, 254].

Coexistence Pressures

In Figure 4.4, the inverse temperature dependence of the coexistence pressures of the NO-$(NO)_2$ system predicted using the New FF and the Lachet FF are presented

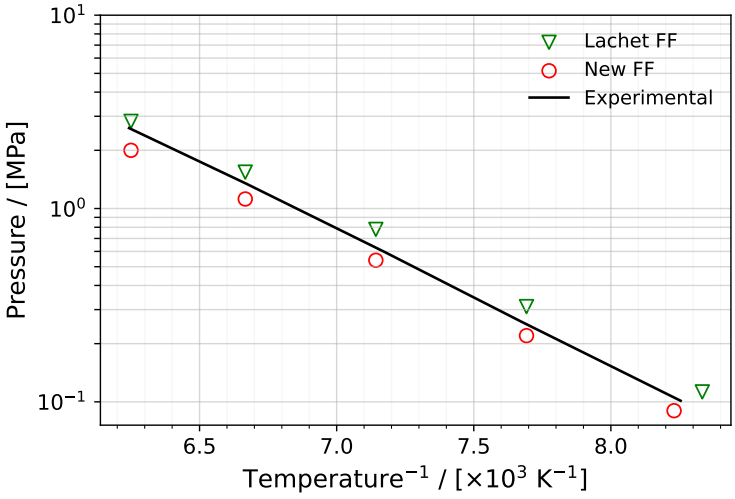

Figure 4.4: Inverse temperature dependence of the coexistence pressures of the NO-$(NO)_2$ system predicted using the New FF (red circles) and the Lachet FF [76] (green triangles), in logarithmic scale. Error bars for the New FF are computed based on the standard deviation and are smaller than the symbols used in the figure. Experimental data [253] for the coexistence pressures is represented by the black line.

on a logarithmic scale. The experimental values are also added for comparison. The average absolute deviations between the computed vapor pressures using the New FF and the experimental vapor pressures is 15 %. The corresponding value for Lachet FF is 17 %. Higher values of vapor pressures predicted using the Lachet FF compared to the New FF could be traced back to the different isolated molecular partition functions used in Lachet *et al.* [76] compared to our work; or alternatively the differences between the standard chemical potential ($\mu^0 = -k_B T \ln\left[\frac{qV_0}{\Lambda^3}\right]$) of $(NO)_2$ and 2 NO used in Lachet *et al.* [76] compared to our work, which leads to differences in compositions. The isolated molecular partition functions in the work of Lachet *et al.* [76] favor more NO molecules in both the vapor and liquid simulation boxes compared to our systems. This leads to higher vapor pressures for Lachet *et al.* [76]. The critical pressure is obtained by extrapolating the vapor pressure curve to the critical temperature using Equation 4.8. The critical pressure using the New FF is 6.24 MPa (3.9 % deviation from the experimental critical pressure) and that predicted using the Lachet FF is 6.37 MPa (1.7 % deviation from the experimental value). See Table 4.2.

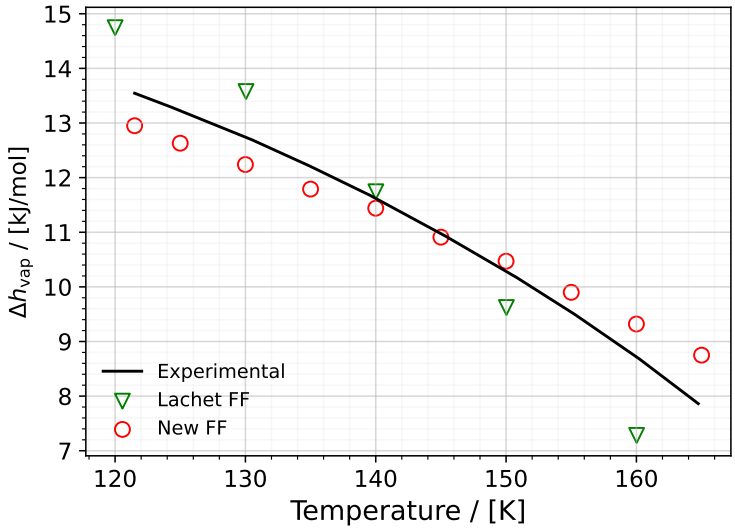

Figure 4.5: Heat of vaporization versus temperature for the reactive NO-$(NO)_2$ system obtained using the New FF (red circles) and the Lachet FF [76] (green triangles). Error bars for the New FF are computed based on the standard deviation of 5 independent simulations and are much smaller than the symbols used in the figure. Experimental values [253] (black line) are added for comparison.

Heats of Vaporization

The temperature dependence of the heats of vaporization for the system containing NO and its dimer predicted using the New FF and the Lachet FF is shown in Figure 4.5 (see Equation 4.9). The experimental values are also shown for comparison. The results using the New FF are in good agreement with the experimental vaporization enthalpies. The average absolute deviation between the experimental enthalpies of vaporization and those predicted by the New FF is 0.46 kJ/mol (4.4 %). This value for the Lachet FF is 0.82 kJ/mol (8 %). The Lachet force field overestimates the heats of vaporization at lower temperatures (120 K and 130 K) and underestimates at higher temperatures (150 K and 160 K). At 140 K the Lachet FF is in good agreement with the experimental value.

4.5.2 Non-reactive pure NO and pure $(NO)_2$ systems

Properties of pure NO

The coexistence densities of pure (unreactive) NO computed using the New FF, the Lachet FF, and the force field developed by Zhou *et al.* [77] (Zhou FF), as a function of temperature, are shown in Figure 4.6. The saturated vapor pressures of pure NO for temperatures between 120 K and 160 K computed using these three force fields are shown in Figure 4.7. The predicted critical densities, temperatures and pressures of pure NO are shown in Table B.10 of Appendix B. The vapor phase densities of pure NO using the Lachet FF are in excellent agreement with the vapor phase densities computed using the New FF. The liquid densities of NO using the New FF are higher than those computed using the Lachet FF for the entire temperature range of 120 K to 160 K. The differences between the liquid densities of NO calculated using the Lachet FF and the New FF are reduced as the temperature reaches the critical temperature (168.20 K for Lachet FF and 167.34 K for the New FF). The vapor densities computed using the Zhou FF are much lower (on average 99 %) than those calculated using the Lachet FF and the New FF, while the liquid densities predicted using the Zhou FF are much higher (on average 48 %) than the densities of the other two force fields. This is because the Zhou FF was optimized to reproduce the experimental density of liquid NO-$(NO)_2$ without taking the presence of dimer $(NO)_2$ into account. The values of the L-J energy parameter ϵ of N and O in the Zhou FF are also higher (by 68 %) than the New FF (see Table B.9 of Appendix B) which leads to lower vapor phase densities, as higher ϵ contributes to higher intermolecular interactions in the liquid, making it difficult for molecules to move to the vapor phase. This is evident in Figure 4.7, where the saturated vapor pressures (P_{sat}) of the Zhou FF are lower, showing a difference of ca. 4 MPa at 160 K, compared to the New FF and the Lachet FF. The critical saturated vapor pressure (P_{c}) of the Zhou FF is larger than that of the New FF and Lachet FF as the critical temperature (T_{c}) of the Zhou FF is higher compared to the other two force fields. The New FF and the Lachet FF have comparable values of P_{sat} as their vapor phase densities have similar values (see Figure 4.6). The values of P_{c} of the New FF and the Lachet FF differ only by 0.18 MPa.

Properties of pure $(NO)_2$

Figure 4.8 shows the vapor and liquid densities of pure (unreactive) $(NO)_2$ as a function of temperature computed using the Lachet FF and the New FF. The saturated vapor pressures of pure $(NO)_2$ as a function of the temperature computed using the New FF and Lachet FF are shown in Figure 4.9. Note that the results for the Zhou FF is not included as there are no force field parameters for $(NO)_2$ in the original work of Zhou *et al.* [77].

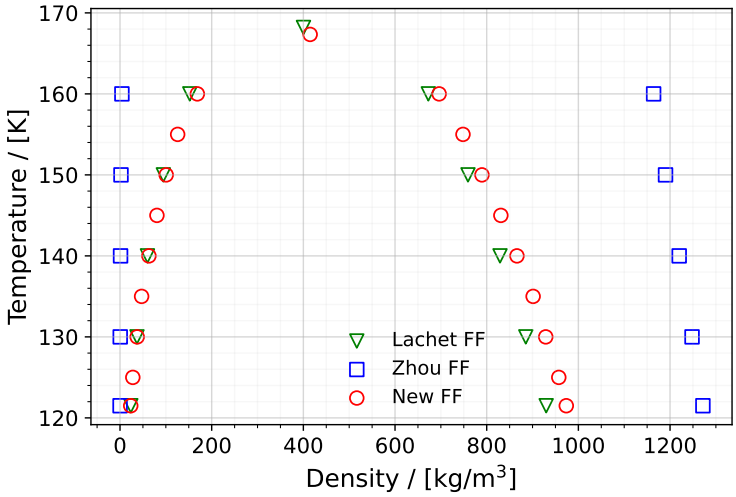

Figure 4.6: Coexisting vapor and liquid densities of pure (unreactive) NO using the New FF (red circles), the Zhou FF [77] (blue squares) and the Lachet FF [76] (green triangles). Error bars are estimated based on the standard deviation of 5 blocks into which the production run was divided and are much smaller than the symbols used in the figure. The critical points of both the New FF and Lachet FF are indicated in the figure. The critical points of the Zhou FF are not shown in the figure, but they are listed in Table B.10 of Appendix B.

The predicted critical temperatures, densities, and pressures are listed in Table B.10 of Appendix B. The predicted critical temperature, T_c, using the New FF is 243.78 K which is smaller than the predicted critical temperature using the Lachet FF (298.37 K). The critical densities (ρ_c) predicted by the two force fields are in agreement (454.28 kg/m^3 for the New FF and 449.95 kg/m^3 for the Lachet FF).

The saturated vapor pressures calculated using the Lachet FF and the New FF are shown in Figure 4.9. P_{sat} values computed using the Lachet FF are smaller (on average by 77.2 %) than the P_{sat} values computed using the New FF in the temperature range of 125 K to 225 K. However, the P_c computed using the Lachet FF is larger than the P_c calculated using the New FF by 0.8 MPa. This is attributed to the larger T_c predicted by the Lachet FF compared to the T_c predicted by the New FF (see Table B.10 of Appendix B).

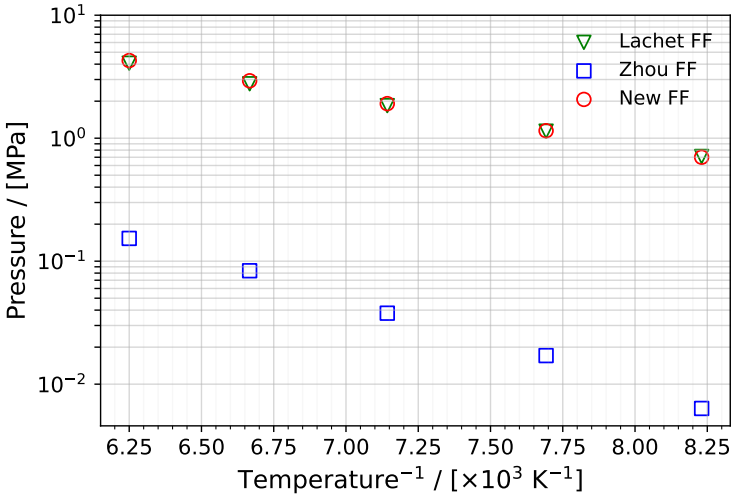

Figure 4.7: Inverse temperature dependence of the saturated vapor pressures of pure NO using the New FF (red circles), the Zhou FF [77] (blue squares) and the Lachet FF [76] (green triangles), on logarithmic scale. Error bars for the New FF are computed based on the standard deviation and are smaller than the symbols used in the figure.

4.5.3 Sensitivity Analysis

The VLE properties of the reactive NO-$(NO)_2$ system are sensitive to the atomization energy of $(NO)_2$ ($D_{0,(NO)_2}$) and the L-J parameters, σ and ϵ of NO and $(NO)_2$. We performed a series of simulations to systematically analyze the dependence of the VLE properties of the reactive NO-$(NO)_2$ system on $D_{0,(NO)_2}$ and L-J parameters, and hence reflect upon the uniqueness of our new force field parameters. These simulations and their main results are discussed below.

Effect of $D_{0,(NO)_2}$ on VLE properties of reactive NO-$(NO)_2$ system

In the first series of simulations, we considered three values for $D_{0,(NO)_2}$ which correspond to three values of $BDE_{(NO)_2}$ that are within the range of the reported experimental and theoretical values for $BDE_{(NO)_2}$ in the literature (7.64 - 13.8 kJ/mol) [208, 226, 248–251, 255, 256]. These values are listed in Table B.11 of Appendix B. $D_{0,(NO)_2}$=1269 kJ/mol is the value with which the VLE properties could be computed in agreement with experiments (see Section 4.5.1). In these simulations, the L-J parameters and the partial charges are fixed as in Table 4.1. These simulations are performed in the reactive Gibbs ensemble.

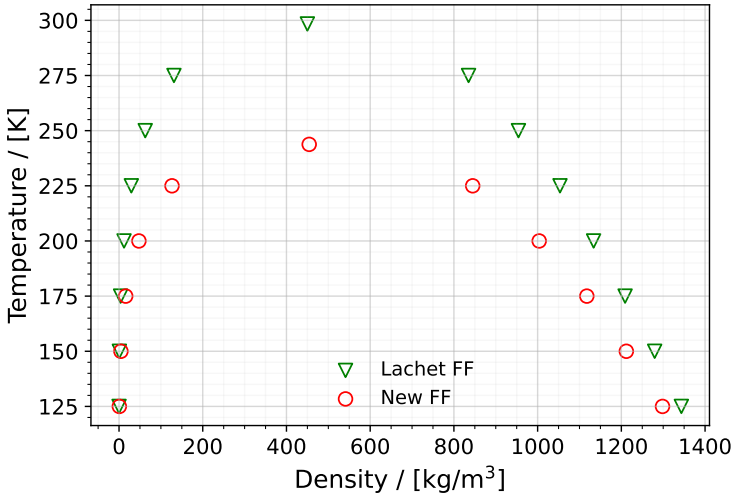

Figure 4.8: Coexisting vapor and liquid densities of pure $(NO)_2$ using the New FF (red circles) and the Lachet FF [76] (green triangles). Error bars are estimated based on the standard deviation of 5 blocks into which the production run was divided and are much smaller than the symbols used in the figure. The critical points are also shown in the figure.

The vapor-liquid coexistence densities and $(NO)_2$ mole fractions in the liquid phase of the reactive NO-$(NO)_2$ system for these four values of $D_{0,(NO)_2}$ are shown in Figures B.2 and B.3 of Appendix B, respectively. Even though the values of $D_{0,(NO)_2}$ are only different by 4 kJ/mol (difference between the highest and lowest value in the set), the differences in the corresponding dimer mole fractions in the liquid phase is significant (56 % difference in the mole fractions at 160 K between the systems with the highest and lowest value of $D_{0,(NO)_2}$). Moreover, higher values of $D_{0,(NO)_2}$ tend to have more negative slopes for the liquid densities (see Figure B.2 of Appendix B). This could be attributed to the presence of more dimer species in the liquid phase. This results in a higher critical temperature compared to the systems with lower values of $D_{0,(NO)_2}$ (see Table B.11 of Appendix B).

Effect of L-J parameters on VLE properties of reactive NO-$(NO)_2$ system

In a second series of simulations, the values of $D_{0,(NO)_2}$=1269 kJ/mol and partial charges (see Table 4.1) are fixed, while twelve different combinations of L-J parameters are considered. In each combination, the L-J parameters (σ or ϵ) of NO and/or $(NO)_2$ are varied by $\pm$ 10% compared to the respective parameters of the New FF. These parameters are labeled FF-a to FF-l: $\sigma_{(NO)_2}$ in FF-a (b),

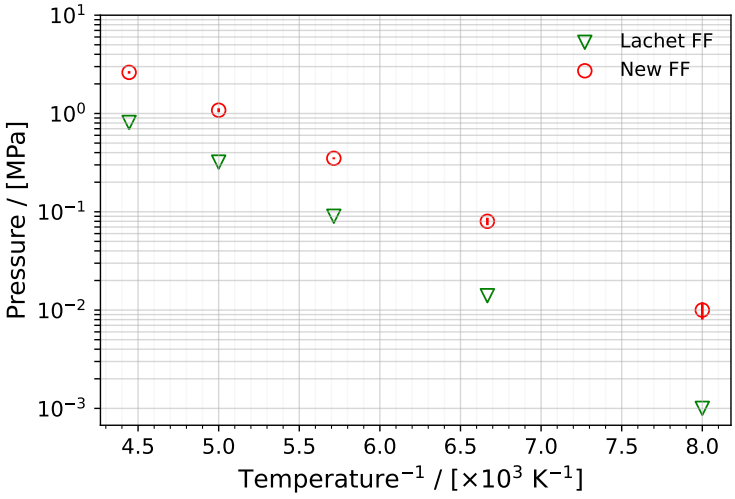

Figure 4.9: Inverse temperature dependence of the saturated vapor pressures of pure $(NO)_2$ using the New FF (red circles) and the Lachet FF [76] (green triangles), on logarithmic scale. Error bars for the New FF are computed based on the standard deviation.

$\epsilon_{(NO)_2}$ in FF-c (d), σ_{NO} in FF-e (f), ϵ_{NO} in FF-g (h), σ_{NO} and $\sigma_{(NO)_2}$ in FF-i (j), and ϵ_{NO} and $\epsilon_{(NO)_2}$ in FF-k (l), are varied by -10% (10%). These parameters are shown in Table B.12 of Appendix B. These simulations are also performed in the reactive Gibbs ensemble.

The coexistence densities, dimer mole fractions in the liquid phase, coexistence pressures, heats of vaporization, and total enthalpies of the reactive NO-$(NO)_2$ system were computed using FF-a to FF-l and are shown in Figures B.4 - B.9 of Appendix B.

An increase in the L-J parameters of $(NO)_2$, $\sigma_{(NO)_2}$ (FF-b) or $\epsilon_{(NO)_2}$ (FF-d), or NO, σ_{NO} (FF-f) or ϵ_{NO} (FF-h), results in an increase in the mole fraction of that species, $(NO)_2$ (see Figures B.4 and B.5 of Appendix B) or NO (see Figures B.6 and B.7 of Appendix B), in the liquid phase of the system. Increasing the values of the L-J parameters of a species makes it energetically favorable to increase the concentration of that species in the system. This can be seen by comparing two simple L-J systems that differ in the values of the L-J parameters, as shown in Figure B.10 of Appendix B (two systems with the same value of σ but different values of ϵ) and Figure B.11 of Appendix B (two systems with the same value of ϵ but different values of σ). With an increase in σ or ϵ, the area of the attractive potential L-J increases. Therefore, with the increase in the values of the L-J

parameters (σ or ϵ) of NO or $(NO)_2$, it becomes energetically favorable to increase the concentration of NO or $(NO)_2$ in the NO-$(NO)_2$ system.

The increase in the mole fraction of $(NO)_2$ or NO affects the VLE properties of the reactive system, including the total enthalpies of the system. An increase in the dimer mole fraction lowers the total enthalpy of the system; see Figures B.4, B.5, B.6 and B.7 of Appendix B. This is supported by the exothermic nature of dimer formation, which causes heat dissipation, and thereby, reduction of the total enthalpy of the system. However, an increase in monomer concentrations increases the total enthalpy of the system. This scenario may be supported by the endothermic nature of N-N bond dissociation between two NO entities in $(NO)_2$), which leads to an increase in the total enthalpy of the system. The dimer mole fractions in the liquid phase when the L-J parameters of NO and $(NO)_2$ (σ in FF-i (j) and ϵ in FF-k (l) are simultaneously varied by $\pm 10\%$ compared to the New FF, follow a similar trend as when only the L-J parameters of $(NO)_2$ is varied ($\sigma_{(NO)_2}$ in FF-a (b) and $\epsilon_{(NO)_2}$ in FF-c (d)); see Figures B.8 and B.9 of Appendix B. This could be because the liquid phase is predominantly composed of dimers.

Although we demonstrated that the VLE properties of the reactive NO-$(NO)_2$ system depends on both $D_{0,(NO)_2}$ (or subsequently $BDE_{(NO)_2}$) and the L-J parameters of NO and $(NO)_2$ species, this may not be the case for all the reactive systems. An example is a reactive NO_2-N_2O_4 system. The VLE properties of reactive NO_2-N_2O_4 are almost exclusively affected by the values of $BDE_{N_2O_4}$ and not by the values of L-J parameter as can be inferred by the work of Polat *et al.* [242]. As explained by Johnson *et al.*, [231], the values of BDE determine the association strength of a fluid. A fluid is weakly (strongly) associating if the value of BDE is small (large) [231]. The concluded value of BDE for $(NO)_2$ in our study is 13.06 kJ/mol (i.e., $D_{0,(NO)_2}$=1269 kJ/mol), which is much smaller than value of BDE for N_2O_4 (∼50 kJ/mol) [241]. Accordingly, NO_2-N_2O_4 fluid is a more strongly associating fluid than NO-$(NO)_2$ fluid. Therefore, the dependence of the VLE properties of a reactive fluid on the values of L-J parameters may be determined by the association strength of that fluid.

4.6 Conclusions

Our force field is capable of predicting the VLE properties of the reactive NO-$(NO)_2$ system (i.e., coexistence vapor-liquid densities, dimer mole fractions in liquid phase, saturated vapor pressures, and heats of vaporization) in excellent agreement with experimental values for the temperature range 120 K to 170 K. For pure NO, the predicted VLE properties using our force field parameters agree well with those using the Lachet FF. However, there are large deviations between the predictions using the Zhou FF and predictions using our force field parameters or the Lachet FF. The Zhou FF was developed to reproduce the experimental density and heat

of vaporization of NO at its boiling point without considering the formation of a dimer at this temperature. This may be the reason for the large deviations of the VLE properties of pure NO predicted by the Zhou FF from those predicted by the New FF and Lachet FF. For pure $(NO)_2$, the liquid densities using the Lachet FF are larger (on average, by 11 %) than the predictions using our force field parameters. The Lachet FF predicts smaller saturated vapor pressures (on average ca. 80 %) compared to our force field. We also performed a systematic parameter study to analyze the impact of individual L-J parameters (σ and ϵ of NO and $(NO)_2$) as well as the atomization energy of $(NO)_2$, $D_{0,(NO)_2}$, or alternatively the bond dissociation energy of $(NO)_2$, $BDE_{(NO)_2}$, on the VLE properties of the reactive NO-$(NO)_2$ system. Our results show that the VLE properties of the reactive NO-$(NO)_2$ system are affected by both the L-J parameters and the atomization energy of the NO dimer. This is in contrast to a previously studied reactive NO_2-N_2O_4 system where the VLE properties are mainly affected by the atomization energy of NO_2 dimer. This can be attributed to the association strength of reactive fluids. A fluid is weakly (strongly) associating if the value of BDE is small (large). The concluded value of the BDE for $(NO)_2$ in our study is 13.06 kJ/mol, which is much smaller than the BDE of N_2O_4 (∼50 kJ/mol). Accordingly, the NO_2-N_2O_4 fluid is a more strongly associating fluid than the NO-$(NO)_2$ fluid. Therefore, the VLE properties of reactive NO-$(NO)_2$ system are affected by both L-J parameters and the atomization energy of the dimer, while the VLE properties of reactive NO_2-N_2O_4 are only affected by the atomization energy of the dimer.

Chapter 5

Coupling Solvation Thermodynamics and Chemical Speciation: A Simulation-Based Approach to NO_x Uptake in Aqueous Environments

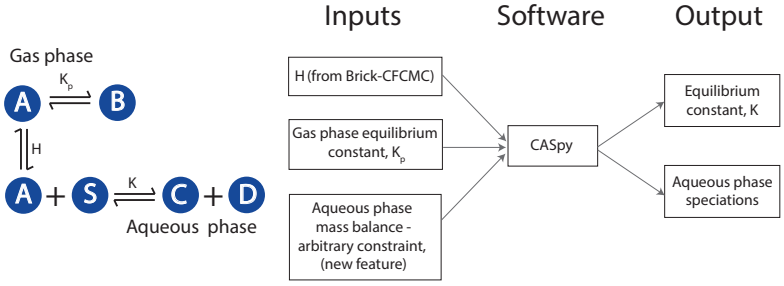

This chapter is based on the following publication: T. H. G. Saji, T. J. H. Vlugt, S. Calero and B. Bagheri, *Coupling Solvation Thermodynamics and Chemical Speciation: A Simulation-Based Approach to NO_x Uptake in Aqueous Environments*, Journal of Chemical Theory and Computation, **22**, 528 (2026).

Overview

We present a simulation-based framework to characterize the solvation and aqueous-phase reactivity of nitric oxide (NO) and nitrogen dioxide (NO_2) in water. Using Continuous Fractional Component Monte Carlo (CFCMC) simulations, we compute Henry coefficients and chemical potentials of NO and NO_2, while Molecular Dynamics (MD) simulations provide diffusion coefficients for NO. The results for NO are quantitatively in agreement with the experimental data when using the Saji force field. For NO_2, we model the chemical equilibrium involving hydrolysis and acid-base reactions that generate HNO_2, HNO_3, NO_2^-, NO_3^-, and H_3O^+. By combining the chemical potentials obtained via CFCMC with a thermodynamic equilibrium model, we resolve the temperature- and pressure-dependent speciation and pH of the system. The model captures a transition from nitrous to nitric species with increasing temperature and predicts ionic distributions and pH shifts under varying NO_x gas fluxes. This work provides a transferable methodology to connect molecular simulations with chemical speciation in reactive aqueous systems.

5.1 Introduction

Investigating plasma-water systems presents significant challenges due to their highly dynamic and coupled nature. Even for a fixed feed gas, power source, system geometry, and initial liquid properties, the plasma and liquid continuously evolve over time, influencing each other. This interplay makes experimental diagnostics of plasma-water systems extremely challenging [4]. Computational studies of plasma-water systems can provide valuable information by predicting and analyzing the formation of reactive species in the gas-phase plasma and its transport to the liquid phase [43–47, 50, 257]. Ideally, one would aim for a comprehensive, time- and space-resolved model that couples gas-phase plasma dynamics with liquid-phase chemistry. Such a model could predict the formation of species in both phases and their dependence on system parameters such as voltage, frequency, and waveform of the applied electrical power [4]. Achieving this requires a multiscale computational platform, as contrasting regimes of physics and chemistry hold on each side of the plasma-water interface. The classical behavior of electrons dominates in the gas-phase plasma, whereas quantum effects govern the interactions in the liquid phase. These two phases also have dramatically different electron densities as well as characteristic length and time scales [258]. Common computational approaches to plasma-water systems focus on a specific aspect of the system under certain assumptions, often using continuum models [43–47, 50, 257].

In these models, liquid properties are treated implicitly, or phenomenological parameters such as Henry coefficients are used to model the transport of species into the aqueous phase. As such parameters are known only for a limited set of species and conditions, the predictive power of continuum models of plasma-water systems remains limited. Molecular simulations are a natural choice for computing quantities such as solubility coefficients for plasma species.

In this work, we focus on modelling the absorption of nitric oxide (NO) and nitrogen dioxide (NO_2) into water using force field-based molecular simulations. NO and NO_2 are key species as part of the reactive nitrogen species (RNS) produced in the gas phase plasma [259–263], which have biological significance [217, 218].

NO is a hydrophobic species with low solubility in water and is absorbed by water without undergoing reactions. We therefore consider system (a) in Figure 5.1 where NO in the gas phase is in physical equilibrium with NO in the liquid phase. We use Continuous Fractional Component Monte Carlo (CFCMC) simulations [94, 96, 97] to compute excess chemical potentials and consequently Henry coefficients of NO at temperatures ranging from 273 K to 333 K. Furthermore, we use Molecular Dynamics (MD) simulations to calculate the self-diffusion coefficients of NO in water containing mole fractions of 0.005, 0.015, 0.025 NO at temperatures ranging from 273 K to 333 K. We use our previously developed force field for NO (see Chapter 4) in combination with the TIP3P force field [60] to compute Henry coefficients and with the TIP4P/2005 [61] to calculate self-diffusion coefficients.

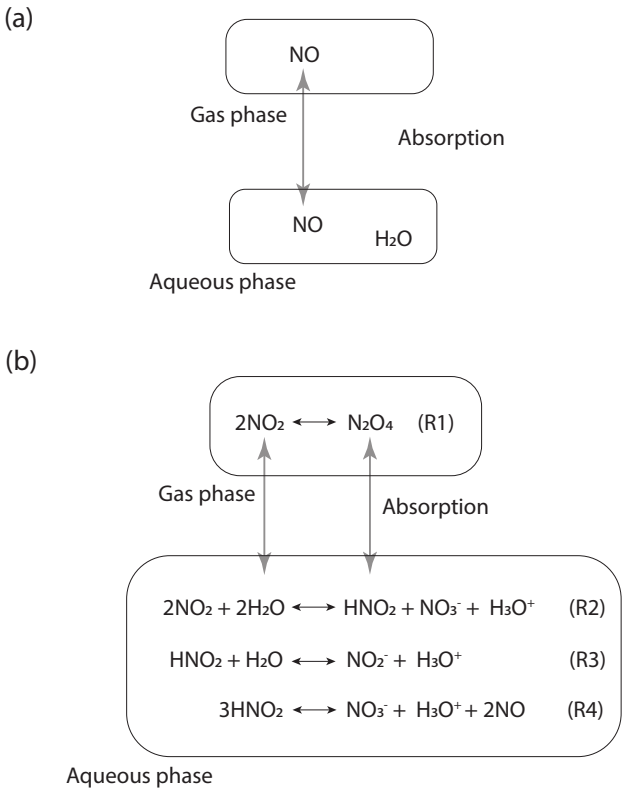

Figure 5.1: Schematic representation of (a) absorption of NO in water and (b) absorption of NO_2 and N_2O_4 in water with the subsequent equilibrium reactions involved.

By comparing the results with the experimental values [264–268] we reflect on the verification and validity of our force field for NO in combination with the TIP3P [60] and the TIP4P/2005 [61] force fields for water.

NO_2 undergoes a dimerization reaction at ambient conditions and forms N_2O_4 in the gas phase. Furthermore, NO_2 undergoes chemical reactions with water. We consider system (b) in Figure 5.1 in which the dimerization reaction occurs in the gas phase (i.e., reaction R1). NO_2 and N_2O_4 are in physical equilibrium with their counterparts in the aqueous phase. Upon absorption of NO_2 in water, a hydrolysis reaction occurs to form nitrous acid (HNO_2) and nitric acid (HNO_3) [269–273] through reaction R2. Since HNO_3 is a strong acid [274], we assume the complete dissociation of HNO_3 in water to give nitrate (NO_3^-) and hydronium (H_3O^+) ions. We incorporate the partial dissociation of HNO_2 to form nitrite ions (NO_2^-) and H_3O^+ through reaction R3 because HNO_2 is a relatively weak acid compared to HNO_3. HNO_2 can also dissociate to form HNO_3, H_2O, and NO through reaction R4.

Note that we do not include the evaporation of water into the gas phase, as we study the system at temperatures in the range of 273 K to 333 K, which is well below the boiling point of water. In addition, we do not include the dissociation of NO_2 to form NO and O_2 in the gas phase, as this reaction is not favorable at the temperatures and pressures we consider in this work [271, 275]. Since our study focuses on the thermodynamic equilibrium of the system, transient species such as N_2O_3 or its isomer ONONO [271] are not considered, as these species are thermodynamically unstable.

We use CFCMC simulations [95–97] to compute the excess chemical potentials and, consequently, the Henry coefficients of the species involved. We calculate the isolated molecule partition functions of these species and therefore the standard-state ideal gas chemical potential. Finally, using these data, we determine the chemical composition (i.e., speciations) at a given gas-phase composition at total gas pressures ranging from 10^{-7} kPa to 10^2 kPa and at temperatures ranging from 273 K to 333 K using the CASpy chemical reaction equilibrium solver [68]. We provide information on how the properties of water are altered when a specific flux of NO_2 and N_2O_4 species reaches the interface.

The data generated in this chapter have potential applications in continuum simulations of plasma-water systems, where data on plasma species is currently limited. The impact of this chapter extends beyond plasma technology, as NO_x species play key roles in numerous chemical processes in both nature and industry. Examples include atmospheric chemistry, where NO_x species are produced by lightning in air [276, 277], aerosol chemistry [278], gas separation and purification processes in industrial applications [279].

The rest of the chapter is organized as follows. The methods are described in Section 5.2. We discuss the results of the NO-water system (system (a) in Figure 5.1) in Section 5.3.1 and those of the NO_2-water system (system (b) in

Figure 5.1) in Section 5.3.2. We compare our results with the available data in the literature where possible. Finally, concluding remarks are presented in Section 5.4.

5.2 Methodology

5.2.1 Force Fields

In this work, all the species studied were modelled using all-atom classical non-polarizable force fields. The Coulombic potential energy function is considered for the electrostatic interactions, and the 12-6 Lennard-Jones (LJ) potential energy function is considered for the van der Waals interactions. The Lorentz-Berthelot [81] mixing rules were used for the vdW interactions of unlike atoms. A cutoff radius of 12.5 Å was used for both the Lennard-Jones and Coulombic interactions. The Ewald summation method [181, 182] was used to treat long-range Coulombic interactions. The energies and pressures were corrected with long-range tail corrections for the LJ interactions [54].

For NO, we used our previously developed force field (Saji FF) (see Chapter 4), where NO is considered as a rigid molecule. The partial charges and the LJ parameters are presented in Table C.8 of Appendix C. The force fields for NO_2 and its dimer N_2O_4 were taken from the work of Bourasseau *et al.* [280]. NO_2 is treated as a rigid molecule. N_2O_4 is also treated as a rigid molecule except for the torsion about the N−N bond [241]. The torsion potential coefficients, partial charges, and the LJ parameters are provided in Tables C.1 and C.2 of Appendix C, respectively. For H_3O^+ ions, the force field developed by Noroozi *et al.* [281] was used where the H_3O^+ is considered to be a rigid ion.

The parameters of the potential energy functions of H_3O^+ are provided in Table C.3 of Appendix C. For HNO_2, NO_2^-, and NO_3^-, the force fields developed by Cordeiro *et al.* [282] are used. In the original work by Cordeiro *et al.* [282], the bending potential energy functions of HNO_2, NO_2^-, and NO_3^- are described using the cosine-based angle potential function, which is of the form

$$E_{\text{bend}}(\theta) = \frac{1}{2} k^{\theta} \left(\cos(\theta) - \cos(\theta_0)\right)^2 , \tag{5.1}$$

where θ is the bond angle and k^{θ} is the force constant. Since the software that is used to perform the CFCMC simulations in this work (Brick-CFCMC [97–99]) does not support the above bending potential, the cosine-based angle potential was fitted to the harmonic angle potential, which is of the form

$$E_{\text{bend}}(\theta) = \frac{1}{2} k \left(\theta - \theta_0\right)^2 , \tag{5.2}$$

where θ is the bond angle and k is the force constant of the harmonic angle potential. The force constant in the harmonic potential (k) is related to the force

constant in the cosine-based potential (k^θ)

$$k = k^\theta \sin^2(\theta_0). \tag{5.3}$$

The parameters and coefficients of the potential energy functions of NO_2^-, NO_3^- and HNO_2 are provided in Tables C.4 - C.7 of Appendix C. Figure C.10 of Appendix C shows a comparison of the harmonic and cosine-based angle potential functions for HNO_2 molecule. At room temperature (300 K), the thermal energy (k_BT) is approximately 2.5 kJ/mol. The deviation between the cosine-based potential and its harmonic approximation becomes significant only at energies above 200 kJ/mol, which corresponds to angular changes far larger than those sampled under thermal fluctuations in our simulations. Therefore, within the energy range relevant to our study, the harmonic approximation accurately reproduces the cosine-based potential. We note that in the original force field for NO_3^- developed by Cordeiro *et al.* [282], an improper dihedral term is defined with an equilibrium angle of 0°, restricting the molecule to the planar geometry. In our simulations, the NO_3^- molecule is treated as a rigid body, which inherently fixes its internal geometry including planarity. As a result, the explicit inclusion of an improper dihedral term becomes redundant and is therefore neglected in our simulations.

The two water models used in this chapter are the TIP3P [60] and TIP4P/2005 [61] models. In Chapter 3, we showed that the TIP3P could predict the solubility of H_2O_2 molecule, which is also a plasma species, and the TIP4P/2005 could predict the self-diffusion coefficients of H_2O_2 molecule in good agreement with the experimental values. We therefore used the TIP3P water model to calculate the Henry coefficients and the TIP4P/2005 to study the diffusion of NO in water. The interaction of all solutes with water in the NO_2-water system is modelled using the TIP3P water model.

5.2.2 MD Simulations

Molecular Dynamics (MD) simulations were performed using the open-source Large-scale Atomic/Molecular Massively Parallel Simulator (LAMMPS) [283]. The equations of motion are integrated with the Velocity-Verlet [54] algorithm, with a time step of 2 fs. Each system contained 1000 molecules in a simulation box of length 31 Å. The system is energy minimized using the conjugate gradient algorithm [284], which is then followed by equilibration in the NPT ensemble for 10 ns. This is followed by an equilibration in the constant number of atoms/molecules, volume and temperature (NVT) ensemble for 5 ns. The production runs of 20 ns in the NVT ensemble were used to calculate thermodynamic properties such as viscosities and self-diffusivities using the OCTP [109] plugin in LAMMPS. The Nosé-Hoover thermostat [54, 188, 285] (with a coupling constant of 0.1 ps) and barostat (coupling constant of 1 ps) are used to keep the temperatures and pressure constant. Periodic boundary conditions

were applied in all directions. The SHAKE algorithm is used to constrain the NO bond.

The self-diffusion coefficient (D_{MD}) is calculated from the mean-squared displacement of all molecules of species of interest [109]

$$D_{\mathrm{MD}} = \lim_{t\to\infty} \frac{1}{2t} \frac{1}{3N_i} \left\langle \sum_{j=1}^{N_i} (\mathbf{r}_{j,i}(t) - \mathbf{r}_{j,i}(0))^2 \right\rangle \tag{5.4}$$

where t is the correlation time, N_i is the number of molecules of species i, and $\mathbf{r}_{j,i}$ is the position vector of j^{th} molecule of species i. The viscosities are calculated from the auto-correlation function of all the components of the traceless stress tensor (see Equation 2.67) [109]. The self-diffusion coefficients were corrected for finite-size effects with the Yeh-Hummer equation (see Equation 2.66) [85, 108]

$$D = D_{\mathrm{MD}} + \frac{k_{\mathrm{B}} T \xi}{6\pi\eta L}. \tag{5.5}$$

Three independent simulation runs were performed to obtain statistics, where each production run is divided into 2 blocks, giving 6 independent production blocks in total. The error bars are computed from the standard deviation of the 6 independent production blocks.

5

5.2.3 MC Simulations

Continuous Fractional Component Monte Carlo (CFCMC) simulations [95–97] using the open-source Brick-CFCMC software [97–99] were performed in the constant number of atoms/molecules, pressure and temperature (NPT) ensemble. In CFCMC simulations, fractional molecules (compared to the "whole" molecules) are introduced within the simulation system. The interactions of these fractional molecules are scaled using a continuous coupling parameter λ, the value of which ranges from 0 to 1. $\lambda = 0$ corresponds to the fractional molecule that acts as an ideal gas molecule and has no interactions with the other molecules of the system. $\lambda = 1$ means the fractional molecule is a whole molecule and has full interactions with the other molecules in the system. To ensure a flat observed probability distribution of λ, a bias is introduced using the Wang-Landau algorithm [101]. This biases the coupling parameter λ with a weight function $W(\lambda)$, thus ensuring the sampling issues due to energy barriers in λ space are not encountered. We used 100 bins to obtain a histogram for λ values and their probability of occurrence $p(\lambda)$. The Boltzmann average of an observable (A) is calculated using [100]

$$\langle A \rangle = \frac{\langle A \exp[-W(\lambda)] \rangle_{\mathrm{biased}}}{\langle \exp[-W(\lambda)] \rangle_{\mathrm{biased}}}. \tag{5.6}$$

The excess chemical potential (μ^{ex}) is the difference between the total chemical potential and the ideal gas chemical potential of a molecule (see Chapter 3). For small and/or weakly polar molecules, such as NO, NO_2, N_2O_4 and H_2O, μ^{ex} can be calculated from the ratio of the Boltzmann sampled probability distribution, $p(\lambda)$ at $\lambda = 0$ and $\lambda = 1$.

$$\mu_i^{\text{ex}} = -k_{\text{B}}T \ln \left[\frac{p(\lambda = 1)}{p(\lambda = 0)} \right]. \tag{5.7}$$

Here, k_{B} is the Boltzmann constant and T is the absolute temperature. For large and/or strongly polar molecules, such as NO_2^-, NO_3^- and H_3O^+, $W(\lambda)$ can be large ($> 100\, k_{\text{B}}T$), making it difficult to obtain a flat observed probability distribution of λ, resulting in large uncertainties while computing μ_i^{ex} using Equation 5.7. Thermodynamic integration is a viable alternative to compute μ^{ex} of large and/or strongly polar molecules as it does not require sampling of the full λ space with equal probability [98]. Instead, values of $\left\langle \frac{\partial U}{\partial \lambda} \right\rangle$ are computed from a series of independent simulations at different fixed values of λ for $\lambda \in [0, 1]$. Here, U is the total potential energy of the system. μ^{ex} is then computed by integrating $\left\langle \frac{\partial U}{\partial \lambda} \right\rangle$

$$\mu_i^{\text{ex}} = \int_0^1 \left\langle \frac{\partial U}{\partial \lambda} \right\rangle \mathrm{d}\lambda. \tag{5.8}$$

We note that thermodynamic integration is computationally more expensive than CFCMC simulations to compute μ^{ex}. Therefore, we only use the thermodynamic integration method to compute μ^{ex} of large and/or strongly polar species. As shown by Polat *et al.* [98], both methods produce statistically equivalent results for small and neutral species. Consequently, for such systems we use CFCMC to calculate μ^{ex} with accuracy comparable to thermodynamic integration but at a significantly reduced computational cost. To maintain charge neutrality of the system, ionic species (an anion and a cation) are combined to form a fractional group [68, 99] such that the total charge within the fractional group is zero.

The Henry volatility coefficient (K_v^{px}) in units of [Pa] is obtained from the excess chemical potential using [107]

$$K_v^{\text{px}} = \rho\, k_{\text{B}}T \exp \left[\frac{\mu^{\text{ex},\infty}}{k_{\text{B}}T} \right], \tag{5.9}$$

where ρ is the number density of the solvent. The Henry coefficient (H_s^{cp}) in units of [mol/m^3 Pa] is obtained using the following conversion: $H_s^{\text{cp}} \approx \frac{\rho_{H_2O}}{M_{H_2O} K_v^{\text{px}}}$ in which ρ_{H_2O} is the density of water, and M_{H_2O} is the molar mass of water [52]. The Henry coefficient (H_s^{cp}) will have SI units only if ρ, k_{B}, T, and M are in SI units.

For Henry coefficient calculations, 5×10^6 equilibration cycles were performed. 5 independent production runs of 3×10^6 cycles were performed to obtain statistics.

Note that one cycle refers to N number of trial moves, where N is the total number of molecules. The error bars were calculated from the standard deviation of the 5 independent production runs.

5.2.4 Calculating Speciations

In this section, we describe the procedure by which we calculate the mole fraction of H_2O, NO_2, NO_2^-, N_2O_4, HNO_2, NO_3^-, H_3O^+, and NO in the aqueous phase for the NO_2-water system.

The equilibrium constant of the dimerization reaction R1 in the gas phase is defined as $K_p = \left[\frac{P_{N_2O_4} P_0}{P_{NO_2}^2}\right]$, wherein P_{NO_2} and $P_{N_2O_4}$ are the partial pressures of NO_2 and N_2O_4, respectively. $P_0 = \rho_0 \, k_B \, T$, where ρ_0 is the reference number density taken as 1 molecule $Å^{-3}$. In Appendix C, we show that K_p can be written as follows

$$K_p = \exp\left[\frac{\mu^0_{N_2O_4} - 2\mu^0_{NO_2}}{-RT}\right], \tag{5.10}$$

where $\mu^0_{N_2O_4}$ and $\mu^0_{NO_2}$ are standard state ideal gas chemical potential of N_2O_4 and NO_2 molecules. R is the ideal gas constant. The composition of the gas phase for a particular total gas pressure (P_{total}) and temperature (T) can be calculated using the following relation

$$N^2_{N_2O_4} + N_{N_2O_4} N_{NO_2} - \frac{N^2_{NO_2} V_0 P_{total} K_p}{k_B T} = 0, \tag{5.11}$$

where $N_{N_2O_4}$ and N_{NO_2} are the number of molecules of N_2O_4 and NO_2, in the gas phase, respectively. V_0 equals 1 $Å^3$. The derivation of Equation 5.11 is presented in Appendix C. The composition of the gas phase at total gas pressures ranging from 10^{-7} kPa to 10^2 kPa and different temperatures (273, 298, 313, and 333 K) is listed in Table C.10 of Appendix C. These values are in good agreement with reported values in the literature [241, 286].

We calculate the mole fraction of the six species in the aqueous phase such that the conservation of total charge and mass is satisfied via the following relations, whose derivations are provided in Appendix C,

$$\begin{aligned} N_{H_2O} + 2N_{NO_3^-} - N_{NO} + N_{NO_2^-} &= 0, \\ N_{NO_3^-} - 2N_{NO} - N_{HNO_2} - N_{NO_2^-} &= 0, \\ N_{NO_3^-} + N_{NO_2^-} - N_{H_3O^+} &= 0, \end{aligned} \tag{5.12}$$

and the equilibrium of the reactions R2 - R4 (see Figure 5.1) is attained via the

following relation

$$\sum_{i=1}^{N_{\text{species}}} \nu_{i,j}\mu_i = 0, \tag{5.13}$$

where N_i indicates the number of a particular species i, N_{species} is the total number of species involved (solutes and solvent) involved in the chemical reaction j, $\nu_{i,j}$ is the stoichiometric coefficient of the species i in the reaction j, and μ_i is the chemical potential of the species i. Note that the stoichiometric coefficients of the reaction products are considered positive, whereas those of the reactants are considered negative. We added a new functionality to the CASpy solver that allows users to define an arbitrary constraint for mass balances.

The chemical potential of a solute i, μ_i, using the ideal gas reference state, as used in Brick-CFCMC [68, 99], is

$$\mu_i = \mu_i^0 + RT \ln\left[\frac{\rho_i}{\rho_0}\right] + \mu_i^{\text{ex}}, \tag{5.14}$$

where μ_i^0 is the standard state ideal gas chemical potential of solute i, as defined in the Brick-CFCMC software [68, 99], R is the ideal gas constant, T is the absolute temperature, ρ_i is the number density of solute i, ρ_0 is the reference number density, taken as 1 molecule Å^{-3}. μ_i^{ex} is the excess chemical potential of the solute i in the solvent, which is computed using Equations 5.7 or 5.8.

The chemical potential of the solvent (μ_{s}), as used in Brick-CFCMC [68, 99], is calculated using the ideal gas reference state

$$\mu_{\text{s}} = \mu_{\text{s}}^0 + RT \ln\left[\frac{\rho_{\text{pure}}}{\rho_0}\right] + \mu_{\text{s}}^{\text{ex}} - RT\left[\frac{1 - X_{\text{s}}}{X_{\text{s}}}\right], \tag{5.15}$$

where μ_{s}^0 is the standard state ideal gas chemical potential of the solvent, ρ_{pure} is the number density of the pure solvent, X_{s} is the mole fraction of the solvent in the solution, and $\mu_{\text{s}}^{\text{ex}}$ is the excess chemical potential of the solvent, which is computed using Equation 5.7. The fourth term, $RT\left[\frac{1-X_{\text{s}}}{X_{\text{s}}}\right]$, originates from the Gibbs-Duhem equation [287]. The value of this term is small as the mole fraction of the solvent (X_{s}) is close to unity.

By substituting Equations 5.14 and 5.15 in Equation 5.13, and with some rearrangement, the following relation is obtained for each reaction j [68]

$$\begin{aligned}\prod_{i=1}^{N_{\text{species}}} X_i^{\nu_{i,j}} = \exp\left[-\sum_{i=1}^{N_{\text{species}}} \frac{\nu_{i,j}(\mu_i^0 + \mu_i^{\text{ex}})}{RT}\right] \times \\ \exp\left[-\nu_{s,j} \ln\left(\frac{\rho_{\text{pure}}}{\rho_0}\right)\right] \times \\ \exp\left[\nu_{s,j}\left(\frac{1 - X_{\text{s}}}{X_{\text{s}}}\right)\right] \left[\frac{V\rho_0}{\sum_{i=1}^{N_{\text{species}}} N_i}\right]^{\nu_{\text{tot-s},\,j}} X_{\text{s}}^{\nu_{s,j}},\end{aligned} \tag{5.16}$$

where $\nu_{s,j}$ is the stoichiometric coefficient of the solvent in reaction j, N_i is the number of molecules of species i, and $\nu_{\text{tot-s},j}$ is the sum of stoichiometric coefficients of the solutes (all species except solvent) involved in reaction j. The left-hand side of Equation 5.16 is the equilibrium constant of reaction j, K_j. The value of K_j can be exponentially large or exponentially small, therefore its natural logarithm $\ln[K]$ is often reported in the literature.

Equations 5.12 and 5.16 are solved using an iterative procedure which is implemented in the open-source Python solver, CASpy [68]. To estimate the uncertainties of the $\ln[K]$ and mole fractions of species, we performed an error-propagation analysis based on Monte Carlo sampling. For each of the eight species, values of μ^{ex} were selected from Gaussian distributions whose means and standard deviations were taken from the computed values of μ^{ex} (see Table 5.3). These sampled values of μ^{ex} were used as input to CASpy, which then computed the corresponding $\ln[K]$ and mole fraction of species. A total of 20,000 Monte Carlo samples were generated. The resulting probability distribution of $\ln[K]$ and mole fractions of species were binned into histograms, to which Gaussian functions were fitted. The means and standard deviations obtained from these fitted Gaussian distributions were taken as the final uncertainties in $\ln[K]$ and mole fractions of species. This procedure was repeated for all four temperatures (273, 298, 313, and 333 K) in this chapter. The probability distributions as a function of $\ln[K]$ and mole fraction of species at 273 K at a total gas pressure of 10^1 kPa are shown as histograms in Figures C.14 and C.15 of Appendix C, respectively. The corresponding fits to a Gaussian distribution are also shown. The means and standard deviations of the mole fractions of species obtained using error propagation analysis at 273 K and at a total gas pressure of 10^1 kPa are listed in Table C.17 of Appendix C.

The standard state ideal gas chemical potential, μ_i^0, is calculated using the isolated molecule partition function (q_{total}) of the species i using the relation

$$\mu_i^0 = -k_{\text{B}}T \ln\left[\frac{qV_0}{\Lambda^3}\right], \tag{5.17}$$

where q is the isolated molecule partition function of the system excluding the translation partition function, $q_{\text{total}} = \frac{qV_0}{\Lambda^3}$ where Λ is the thermal de Broglie wavelength of the species and $V_0 = 1$ Å^3 is a reference state for the translational part of the isolated molecule partition function in Brick-CFCMC software. The isolated molecule partition function is described extensively in Chapter 2 and in Refs. [68, 99]. The required inputs to calculate the isolated molecule partition function of H_2O, NO_2^-, NO_3^-, HNO_2, and H_3O^+ are obtained from the JANAF tables [247] and the NIST database [288], and are presented in Table C.9 of Appendix C. To calculate the electronic contribution to the isolated molecule partition function of each species, atomization energy of that species is required. The atomization energy of the nitrate ions (D_{0,NO_3^-}) is not readily available and

Table 5.1: Correlation function for the isolated molecule partition function $\ln\left[\frac{qV_0}{\Lambda^3}\right]$ in the form of $\frac{A}{T} + B$ for H_2O, NO_2^-, NO_3^-, HNO_2, and H_3O^+. Here T is the temperature, and A and B are constants. The input data for calculating the isolated molecule partition function are obtained from the JANAF tables [247] and the NIST database [288], and are listed in Table C.9 of Appendix C.

	H_2O	NO_2^-	NO_3^-	HNO_2	H_3O^+
A	109485.30	157645.91	171511.92	149658.54	36727.67
B	11.11	15.35	17.66	18.36	11.57

is calculated using the following equation

$$D_{0,NO_3^-} = D_{0,NO_3} + \text{E.A}(NO_3), \tag{5.18}$$

where D_{0,NO_3} and E.A(NO_3) are the atomization energy and electron affinity of NO_3 molecules, respectively. E.A(NO_3) is taken as 3.09 eV [289]. We calculated the value of $\ln\left[\frac{qV_0}{\Lambda^3}\right]$ as a function of temperature by writing it in the form of $\frac{A}{T} + B$. The values of parameters A and B for H_2O, NO_2^-, NO_3^-, HNO_2, and H_3O^+ are listed in Table 5.1. For NO species, the isolated molecule partition function is calculated using the parameters A and B provided in Chapter 4. For NO_2 and N_2O_4 the parameters A and B provided by Lasala *et al.* [241] are used. The values of the standard-state ideal gas chemical potential, μ^0, for H_2O, NO_2, N_2O_4, HNO_2, NO_2^-, NO_3^-, H_3O^+, and NO at 273 K, 298 K, 313 K, and 333 K are listed in Table 5.2.

5.3 Results and Discussion

5.3.1 NO - water

Self-diffusion coefficients

The self-diffusion coefficients of NO for three different mole fractions of NO in water (0.005, 0.015, 0.025) at temperatures ranging from $273-333$ K, were computed and are shown in Figure 5.2. D_{NO} increases with temperature for all the concentrations of NO. At a given temperature, values of D_{NO} for different concentrations of NO are close to each other (average difference of 4%). The computed values of D_{NO}

Table 5.2: Values of the standard state ideal gas chemical potential, μ^0(as defined in the Brick-CFCMC software [68, 99]), in units of [kJ/mol] for the species studied in this work for different temperatures. The calculated values of μ^0 are in agreement with available literature data ($\mu^0_{H_3O^+,\ 313\ K}$ = -338.21 kJ/mol [68]) within the chemical accuracy. These values are obtained using the input data presented in Table C.9 of Appendix C.

T/[K]	H_2O	NO_2	N_2O_4	HNO_2	NO_2^-	NO_3^-	H_3O^+	NO
273	-935.51	-959.95	-1953.21	-1286.02	-1345.23	-1465.89	-331.63	-652.41
298	-937.79	-963.36	-1958.03	-1289.79	-1348.72	-1469.72	-334.02	-654.75
313	-939.18	-965.40	-1960.93	-1292.09	-1350.84	-1472.05	-335.47	-656.15
333	-941.06	-968.13	-1964.79	-1295.20	-1353.70	-1475.21	-337.44	-658.02

are in excellent agreement with experimental values (Malinski *et al.* [266] at 298 K and Zacharia & Deen [265] at 310 K). The self-diffusion coefficients of water for these systems for the temperature range of 273 K - 333 K are shown in Figure C.8 of Appendix C, and are in good agreement with the self-diffusion coefficients of TIP4P/2005 water model. The viscosities of NO-water systems at different temperatures are given in Figure C.9 of Appendix C. The systems with different mole fractions of NO have comparable viscosities as TIP4P/2005 water model for the temperature range of 273 K - 333 K.

5

Henry coefficients

The computed values of μ^{ex} of NO for the temperature range 273 K - 333 K are listed in Table 5.3. Henry coefficients for NO (calculated from μ^{ex}) for the temperature range 273 K to 333 K are shown in Figure 5.3. The Henry coefficients for NO (H_{NO}) decreases from 1.7 $\times 10^{-5}$ mol/m^3 Pa at 273 K to 1.45 $\times 10^{-5}$ mol/m^3 Pa at 298 K and remains approximately constant from 298 K to 333 K. The experimental values of H_{NO} at 298 K from the work of Zacharia and William [265], Zafiriou and McFarland [267], and Komiyama and Inoue [268], are also shown in the figure. The computed H_{NO} at 298 K is within the range of the reported experimental values.

From the above results, we conclude that the force field which we developed for NO in Chapter 4, combined with the TIP4P/2005 [61] and TIP3P water models [60] predicts the thermodynamic properties of NO in water in excellent agreement with experimental values. The computed values of μ^{ex} of NO are used

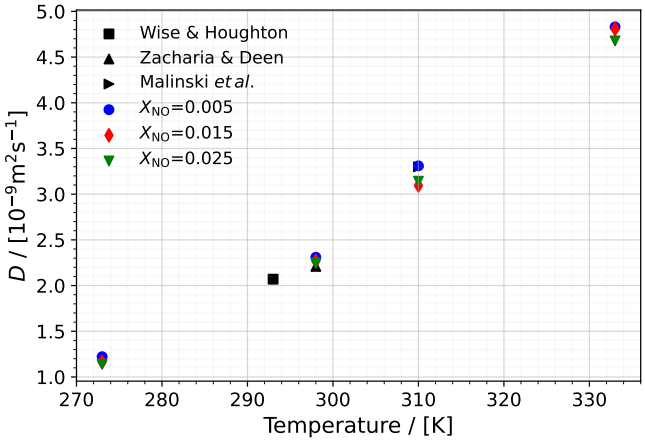

Figure 5.2: Self-diffusion coefficients of NO in NO-water systems for different mole fractions of NO (X_{NO}) in water (X_{NO} = 0.005, 0.015, 0.025) at different temperatures using the Saji *et al.* force field model (see Chapter 4) and the TIP4P/2005 [61] water model. Error bars are estimated based on the standard deviation of 6 production blocks, and are much smaller than the symbols used in the figure. The experimental self-diffusion coefficients obtained from the work of Wise & Houghton [264], Zacharia & Deen [265], and Malinski *et al.* [266] are shown in black symbols.

in the next section for calculating the solubility of NO_2 in water and its speciation.

5.3.2 NO_2 - water

The values of μ^{ex} for H_2O, NO_2, N_2O_4, HNO_2, $NO_3^- + H_3O^+$, and NO at 273 K, 298 K, 313 K, and 333 K are presented in Table 5.3. Note that μ^{ex} of $NO_3^- + H_3O^+$ is calculated in a single simulation taking NO_3^- and H_3O^+ as a single fractional group to maintain charge neutrality. The μ^{ex} of $NO_2^- + H_3O^+$ is not calculated because the equilibrium constant required for the reaction R3 was taken from [290]. μ^{ex} of all species increases with increasing temperature. NO and NO_2 have positive values of μ^{ex} while all other species have negative values of μ^{ex}. This indicates that NO and NO_2 are less hydrophilic compared to other species present in the system. The values of the Henry coefficients, H_s^{cp}, for H_2O, NO_2, N_2O_4, HNO_2, and NO at different temperatures are presented in Table 5.4. A higher value of H_s^{cp} indicates a higher solubility in water and therefore a higher hydrophilicity of the species. Species that are more hydrophilic (more negative values of μ^{ex}) have a higher value of H_s^{cp}. The computed value of H_s^{cp} for NO_2 differs by a factor of 2 to 3

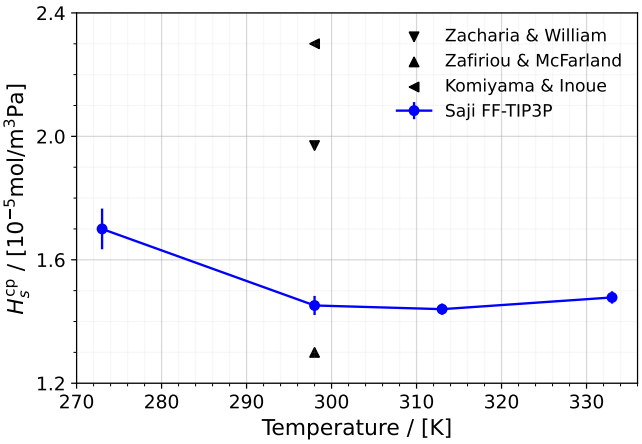

Figure 5.3: Henry coefficients for NO in water for temperatures ranging from 273 K to 333 K using the Saji *et al.* force field (see Chapter 4) and TIP3P water model [60]. Error bars are estimated based on the standard deviation of 5 independent production runs. Experimental Henry coefficient of NO in water at 298 K is added for comparison [265, 267, 268].

5

Table 5.3: Computed values of μ^{ex} for the species studied in this work using the TIP3P water model [60] for different temperatures in units of kJ/mol. The standard deviations are given in subscripts. The computed values of μ^{ex} are in agreement with available literature data ($\mu^{ex}_{H_2O,298\ K}$ = -26.11 kJ/mol [281]). Note that the μ^{ex} of NO_3^- + H_3O^+ is computed from 3 independent simulations taking NO_3^- and H_3O^+ as a single fractional group to maintain charge neutrality. μ^{ex} of NO_2^- + H_3O^+ is not computed as the equilibrium constant required for the reaction $HNO_{2(aq)}$+$H_2O_{(l)}$ ⇌ $NO_{2\ (aq)}^-$+ $H_3O^+_{(aq)}$ were taken from Ref [290].

T/[K]	H_2O	NO_2	N_2O_4	HNO_2	NO_3^- + H_3O^+	NO
273	$-26.97_{0.07}$	$4.98_{0.06}$	$-6.2_{0.1}$	$-16.0_{0.2}$	$-751.2_{0.1}$	$7.43_{0.09}$
298	$-25.66_{0.09}$	$6.17_{0.08}$	$-5.3_{0.1}$	$-14.9_{0.3}$	$-745.0_{0.2}$	$8.29_{0.05}$
313	$-24.91_{0.05}$	$6.68_{0.04}$	$-4.5_{0.1}$	$-14.2_{0.2}$	$-740.7_{0.2}$	$8.66_{0.03}$
333	$-23.99_{0.04}$	$7.30_{0.06}$	$-3.2_{0.1}$	$-13.6_{0.1}$	$-735.9_{0.2}$	$9.03_{0.04}$

Table 5.4: Computed values of Henry coefficients (H_s^{cp}) in units of mol/(m^3 Pa) for the species studied in this work using the TIP3P water model [60] for different temperatures. The standard deviations are given in subscripts.

T/[K]	H_2O / [10^1]	NO_2 / [10^{-5}]	N_2O_4 / [10^{-3}]	HNO_2 / [10^{-1}]	NO/ [10^{-5}]
273	$6.2_{0.2}$	$4.9_{0.1}$	8.7_{1}	$5.1_{0.4}$	$1.70_{0.07}$
298	$1.26_{0.04}$	$3.43_{0.07}$	$3.2_{0.3}$	$1.7_{0.2}$	$1.45_{0.03}$
313	$0.56_{0.02}$	$3.05_{0.06}$	$2.2_{0.3}$	$0.93_{0.07}$	$1.44_{0.02}$
333	$0.22_{0.003}$	$2.75_{0.06}$	$1.26_{0.06}$	$0.51_{0.02}$	$1.48_{0.02}$

Table 5.5: Values of ln[K] for reactions R2, R3, and R4 at different temperatures. Note that ln[K] for reactions R2 and R4 were computed using CASpy while for reaction R3, the values of ln[K] were taken from [290]. The evaluation of the uncertainties in ln[K] for reactions R2 and R4 is discussed in Section 5.2.4.

ln[K]	273 K	298 K	313 K	333 K
R2	$3.7_{0.1}$	$1.4_{0.2}$	$0.0_{0.1}$	$-1.38_{0.08}$
R3	-11.986	-11.599	-11.396	-11.154
R4	$-26.3_{0.3}$	$-25.9_{0.4}$	$-25.7_{0.2}$	$-25.4_{0.1}$

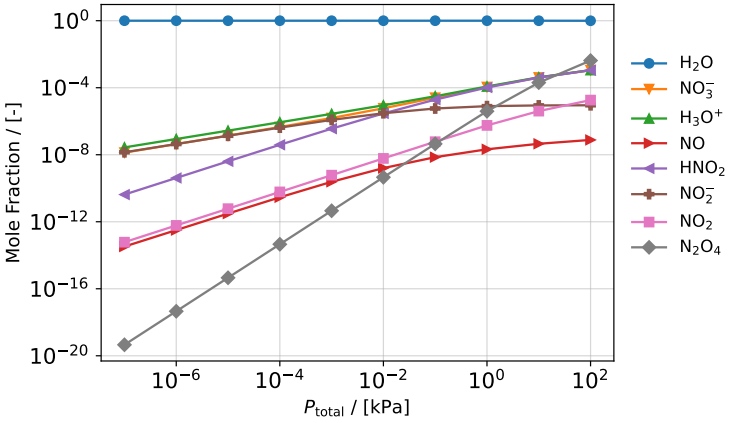

Figure 5.4: The mole fractions of species in the aqueous phase as a function of total gas pressure (P_{total}) at 298 K.

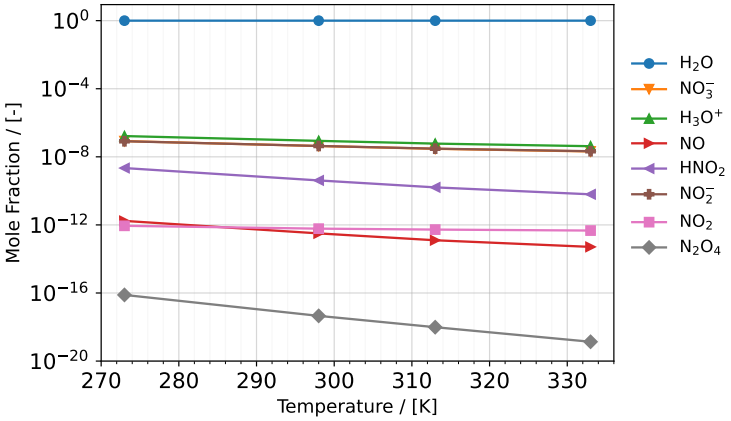

Figure 5.5: The mole fractions of species in the aqueous phase as a function of temperature at total gas pressure (P_{total}) of 10^{-6} kPa.

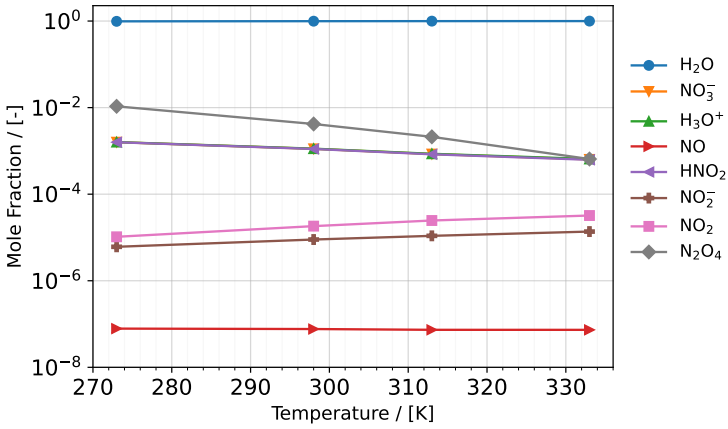

Figure 5.6: The mole fractions of species in the aqueous phase as a function of temperature at total gas pressure (P_{total}) of 10^2 kPa.

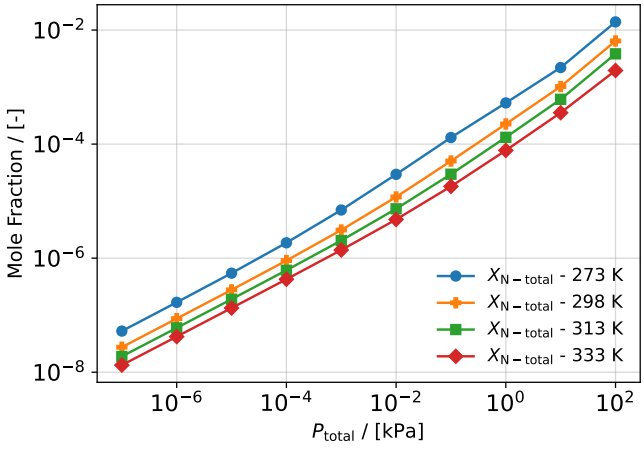

Figure 5.7: The sum of the mole fractions of nitrogen-containing species in the aqueous phase ($X_{\text{N-total}}$) as a function of total gas pressure (P_{total}) at 273 K, 298 K, 313 K and 333 K.

compared to the existing experimental values (6.9×10^{-5} - 1.2×10^{-4} mol/m^3 Pa at 298 K) [268, 291, 292], while that of HNO_2 also differs by a factor of $2-3$ with experimental values (3.7×10^{-1} - 4.8×10^{-1} mol/m^3 Pa at 298 K) [293–295]. The value of H_s^{cp} of N_2O_4 is lower than the experimental values [268, 296] by an order of magnitude (1.4×10^{-3} - 3.1×10^{-3} mol/m^3 Pa at 298 K). It should be noted that experimental measurement of H_s^{cp} for species that react with water is inherently difficult, as gas-liquid systems may not be maintained at equilibrium during measurement [294].

The values of $\ln[K]$ of the reactions R2 and R4 at 273, 298, 313, and 333 K are calculated using the procedure described in Section 5.2.4 and are presented in Table 5.5. Since the HNO_2 dissociation to form nitrite and hydronium ions is well studied and documented, we calculated the value of $\ln[K]$ for reaction R3 using the reported value of pK_a in literature, where pK_a is the negative logarithm to the base ten of the acid dissociation constant (K_a). We used a value of 3.29 [269] for the pK_a of HNO_2. The relation between $\ln[K]$ and pK_a is

$$\ln[K] = -\ln[10]\ \mathrm{p}K_a - \ln[55.55]. \tag{5.19}$$

The derivation of Equation 5.19 is presented in Appendix C. The values of $\ln[K]$ of reactions R3 and R4 increase with increasing temperature, indicating more formation of reaction products with increasing temperature. The value of $\ln[K]$ of reaction R2 decreases with increasing temperature, leading to lower formation of reaction products with increasing temperature. This shows that reaction R2 is an exothermic reaction, which is in agreement with existing experimental and computational works [271, 273].

The gas phase equilibrium constant (K_p) determines the gas phase composition of the system. The number of NO_2 and N_2O_4 molecules in the gas phase as a function of total gas pressure (P_{total}) and temperature (T) are calculated using Equation 5.11, and are presented in Table C.10 of Appendix C. Note that the total gas pressure (P_{total}) in our system is the sum of the partial pressures of NO_2 (P_{NO_2}) and N_2O_4 ($P_{N_2O_4}$). For a given P_{total}, the concentration of NO_2 in the gas phase increases and the dimer concentration decreases with increasing temperature. In contrast, increasing P_{total} at a given temperature leads to a higher dimer concentration and a lower concentration of NO_2.

The speciations in the aqueous phase of the system are determined by the composition of the gas phase and the values of $\ln[K]$ of the reactions in the aqueous phase. The speciations in the aqueous phase of the system at different pressures and temperatures are presented in Figures 5.4, 5.5, and 5.6.

The mole fractions of the species as a function of P_{total} at 298 K are shown in Figure 5.4. The mole fractions of the species as a function of P_{total} at 273 K, 313 K and 333 K are presented in Figures C.11, C.11 and C.11 of Appendix C, respectively. The mole fractions of the species are also listed in Tables C.11 - C.14 of Appendix C. The aqueous concentrations of all species, except water, increase

by increasing P_{total} from 10^{-7} to 10^{2} kPa. The concentration of water decreases with increasing P_{total} as the increase of the concentration of NO_2 in the system leads to the equilibrium of reaction R2 being shifted further towards the reaction products, and therefore a lower concentration of water. Nitrate (NO_3^-) and nitrite (NO_2^-) ions have similar concentrations until 10^{-3} kPa, after which the difference in concentrations increases with increasing pressure. The concentration of hydronium ions (H_3O^+) is equal to the sum of the concentrations of NO_3^- and NO_2^- to satisfy the charge neutrality of the system. The concentration of nitrous acid (HNO_2) has a steady increase with P_{total}. The concentration of nitric oxide (NO) also has a steady increase with P_{total} until 10^{-2} kPa, after which the increase in the concentration tapers off.

The equilibrium of reaction R4 is shifted to the reactant side as the value of $\ln[K]$ for reaction R4 is much negative (values of $\ln[K]$ range from -26.26 at 273 K to -25.41 at 333 K). This is in agreement with the work of Menezes & Popowicz [271] who reported that the dissociation reaction of HNO_2 to form NO_3^-, H_3O^+ and NO, is not thermodynamically favorable below 400 K.

The pH of the system decreases with increasing pressure as a result of the increase in the presence of nitric and nitrous acids. Figures 5.5 and 5.6 show the mole fractions of species in the aqueous phase as a function of temperature at a total gas pressure (P_{total}) of 10^{-6} kPa and 10^{2} kPa, respectively. The data is listed in Tables C.15 and C.16 of Appendix C. The concentrations of the species in the aqueous phase decrease with increasing temperature, except for water. The concentration of water increases because with increasing temperature, the $\ln[K]$ of reaction R2 decreases, indicating a shift in the reaction equilibrium to the reactant side.

A shift of the equilibrium reaction of R2 towards the reactant side should translate to more NO_2 concentration in the aqueous phase. The decreasing solubility of nitrogen dioxide with increasing temperature leads to an overall decrease in the aqueous concentration of the species with temperature, especially at lower values of P_{total} (< 10 kPa). At higher P_{total} (≥ 10 kPa), there is an increased presence of NO_2 dimers (N_2O_4) in the solution (as also reported in experimental works [291]), which tend to dissociate with increasing temperature, therefore increasing the NO_2 aqueous concentration with increasing temperature (see Table C.16 of Appendix C). The concentration of nitrite ions increases with temperature at P_{total} greater than 0.1 kPa.

The ratio between the mole fractions of NO_2^- and HNO_2 in the aqueous phase, $\frac{X_{NO_2^-}}{X_{HNO_2}}$, depends on the values of $\ln[K]$ of reaction R3. $\ln[K]$ of reaction R3 becomes more positive with increasing temperature. Therefore, it is expected to have an increase in $\frac{X_{NO_2^-}}{X_{HNO_2}}$ with increasing temperature. $\frac{X_{NO_2^-}}{X_{HNO_2}}$ increases from 3.75×10^{1} at 273 K to 1.06×10^{2} at 298 K for P_{total} of 10^{-6} kPa. However, by

increasing pressure to 10^2 kPa, $\frac{X_{NO_2^-}}{X_{HNO_2}}$ only increases from 3.83×10^{-3} at 273 K to 8.07×10^{-3} at 298 K. This is because the equilibrium of reaction R2 shifts towards the reaction products with an increase in the pressure (more NO_2 concentration), leading to a higher mole fraction of HNO_2. Figure 5.7 shows the total nitrogen content ($X_{\text{N-total}}$) present in the system as a function of the total pressure for four different temperatures. $X_{\text{N-total}}$ increases with increasing pressure and decreases with increasing temperature.

We would like to emphasize the importance of accurate data for parameters such as the atomization energy (D_0) of the species. The atomization energy of a species contributes considerably to the determination of the chemical equilibrium of the reaction. The chemical accuracy of *ab initio* calculations, which are used to determine the value of D_0 of species, is 4.184 kJ/mol [297]. This variance in the atomization energy contributes to differences in the reaction equilibrium constant. For example, we varied the atomization energy of NO within the chemical precision, and we found that $\ln[K]$ is different by 3.2 $\ln[K]$ points for reaction R4. The different values of atomization energies that are used in different studies ultimately lead to different results. Another important parameter is the value of the electron affinity of NO_3, which is used to calculate the atomization energy of NO_3^-. Although we have used a value of 3.09 eV, the reported values in the literature vary from 2.48 eV [289] to 3.94 eV [298]. Therefore, depending on the values of the atomization energies and electron affinities of the species, the reaction equilibrium could shift towards reactants or the reaction products.

5

5.4 Conclusions

We studied the interaction of NO and NO_2 with water. NO was modelled using the Saji FF, and the thermodynamic properties were computed using MD and CFCMC simulations. The self-diffusion coefficients of NO in water were calculated in water containing mole fractions of 0.005, 0.015, and 0.025 NO at temperatures ranging from 273 K - 333 K. The values of self-diffusion coefficients are in good agreement with the experimental values. The Henry coefficient of NO was computed for temperatures ranging from 273 K - 333 K. Experimental values are only available at 298 K, and the computed Henry coefficient at 298 K is in agreement with the experimental ones. The interaction of NO_2 in water is characterized by the initial hydrolysis of NO_2 to form nitrous and nitric acids, the subsequent ionization reaction of nitrous acid to form nitrate and hydronium ions and the disproportionation reaction of nitrous acid to form nitric acid, nitric oxide and water. We modified the CASpy solver, a chemical reaction equilibrium solver, to handle arbitrary constraints in chemical reaction equilibria, to study this interaction. The values of μ^{ex} of the species involved in the reactions are required as input in CASpy, and were computed using CFCMC simulations. Since NO_2

dimerizes to form N_2O_4, the gas phase composition at different pressures and temperatures must be calculated using the gas phase equilibrium constant. The calculation shows that the concentration of N_2O_4 in the gas phase increases with increasing pressure and decreases with increasing temperature. The equilibrium of reaction for the hydrolysis of NO_2 in water shifts to the reactant side with an increase in temperature, indicating that this reaction is an exothermic reaction. The composition in the aqueous phase as a function of pressure is computed. All species except water have an increase in their aqueous concentrations with increasing pressure, while that of water decreases. The pH of the system decreases with increasing pressure as the amount of nitrous and nitric acids increases. The speciations as a function of temperature are also computed. The aqueous concentrations of all species other than water decrease with increasing temperature. At higher pressures, the concentrations of NO_2 and NO_2^- also increases with increasing temperature. The ratio between the aqueous mole fractions of NO_2^- and HNO_2 increases with increasing temperature as the equilibrium of reaction R3 shifts towards the reaction products with an increase in temperature. We also discussed the importance of accurate data for parameters such as the atomization energy for calculating the reaction equilibrium.

Chapter 6

Predicting Absorption and Diffusion of Plasma-Generated $O(^3P)$, $O(^1D)$, and Other RONS in Aqueous Environments Using Molecular Simulations

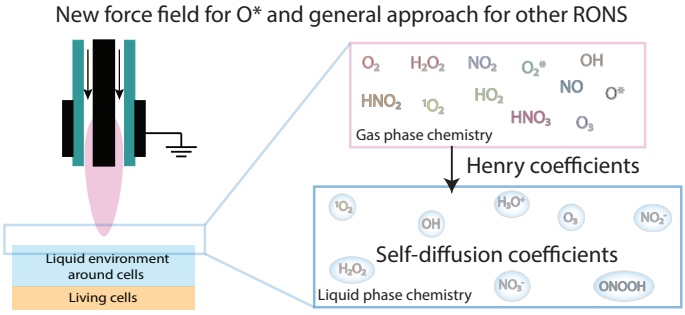

This chapter is based on the following publication: T. H. G. Saji, T. J. H. Vlugt, S. Calero and B. Bagheri, *Predicting Absorption and Diffusion of Plasma-Generated $O(^3P)$, $O(^1D)$, and Other RONS in Aqueous Environments Using Molecular Simulations, Journal of Physical Chemistry B,* ***130****, 4792 (2026).*

Overview

We study the interactions of plasma-generated Reactive Oxygen and Nitrogen Species (RONS) with water due to their importance for applications in health and agriculture. Atomic oxygen, a key RONS, is produced by plasma in both its triplet ground state, O(^{3}P) and its singlet excited state, O(^{1}D). Experimental studies indicate that when plasma interacts with water, atomic oxygen can remain sufficiently stable to enter the aqueous phase. Recent measurements show that ground-state oxygen atoms can persist for tens of microseconds and penetrate hundreds of micrometres into the aqueous phase. However, quantitative data on the solubility and diffusion of atomic oxygen remain scarce. This is likely due to limitations in experimental diagnostics and the challenges that the complex electronic structure of atomic oxygen presents to modelling approaches. To overcome these challenges, we developed state-specific force fields to model the interactions of O(^{3}P) and O(^{1}D) with water to account for quantum-state-dependent interactions. Using these force fields, we provide the first estimates of temperature- and quantum-state-dependent self-diffusion and Henry coefficients of atomic oxygen in aqueous environments. Building upon these results, we propose a general framework to estimate the solubility and diffusion of other plasma-generated charge-neutral RONS in water by representing each species as a charge-neutral Lennard-Jones particle. The influence of particle size, solute-solvent interaction strength, and temperature on the transport and thermodynamic properties of RONS was systematically investigated. This approach enables the estimation of the Henry coefficients and the diffusion coefficients of RONS in water based on particle size, solute-solvent interactions, and temperature. These estimates provide key parameters for device-level plasma-liquid simulations and offer molecular-scale insight for interpreting experimental findings.

6.1 Introduction

Plasma-liquid interactions have become an active research area due to their central role in applications spanning health care, agriculture, and environmental remediation [4, 299]. Electric gas discharge plasmas generated in N_2- or O_2-containing gas mixtures produce a rich cocktail of reactive oxygen and nitrogen species (RONS), including hydrogen peroxide (H_2O_2), hydroxyl radical ($OH^\bullet$), hydroperoxyl radical ($HO_2^\bullet$), atomic oxygen ($O^\bullet$), molecular oxygen in the singlet delta state $O_2(^1\Delta_g)$, nitrous acid (HNO_2), nitric acid (HNO_3), nitric oxide ($NO^\bullet$), nitrogen dioxide ($NO_2^\bullet$), dinitrogen tetroxide (N_2O_4), and many others [33]. Many of these species possess disinfective or nutritive properties [33, 300, 301]. Upon contact with a liquid, the reactivity carried by the gas-phase plasma is transferred into the liquid phase, leading to a wide range of chemical pathways [302]. Experiments have shown that plasma-generated RONS exist in the aqueous phase over a wide range of timescales. Short-lived radicals and excited species persist for sub-microseconds, while more stable species survive for milliseconds or longer [303, 304]. This makes plasma technology a promising tool for sustainable agriculture and biomedical applications. In biomedicine, RONS can be selectively delivered to tissues to treat chronic wounds, skin infections, and certain cancers [34, 212, 305–307]. In agriculture, specific mixtures of RONS, applied directly or dissolved in water, can act as fertilizers or pesticides to enhance plant growth [219–221]. For these applications, controlling and quantifying the composition of RONS in the aqueous phase is crucial.

The aqueous phase chemistry depends on multiple factors, including the properties of the plasma device (e.g., feed gas composition and power characteristics), the properties of the liquid phase, and environmental conditions such as pressure and temperature [4]. Computational simulations at the device-level [43–47, 50, 257] provide a complementary approach to predict the composition of the aqueous phase, but the accuracy is limited by the scarcity of essential data, such as reaction rates and solubility coefficients. Molecular simulations offer a natural way to calculate these parameters for plasma-generated species.

We have previously investigated the interactions of H_2O_2, $NO^\bullet$, $NO_2^\bullet$, N_2O_4, HNO_2, HNO_3, NO_2^-, and NO_3^- with water and predicted their solubility coefficients using molecular simulations [308–310]. In this work, we first focus on calculating the solubility and diffusion of atomic oxygen ($O^\bullet$) in water. We then propose a general approach to predict these properties for other plasma-generated charge-neutral species. For convenience, the bullet used to indicate radicals is omitted in the remainder of the chapter.

Plasma sources generate atomic oxygen in the ground triplet state, $O(^3P)$, or the excited singlet state, $O(^1D)$ [311, 312]. Atomic oxygen has increasingly been identified as a key player in plasma chemistry and in a range of biomedical

applications [313–317]. Experiments have shown that atomic oxygen can persist during transfer from the gas-phase plasma into the aqueous phase [306, 318, 319, 319]. Recently, Myers *et al.* [304] reported experimental measurements of the Henry coefficient of ground-state oxygen atoms in water, concluding that oxygen atoms persist for tens of microseconds in water and can penetrate hundreds of micrometers into the aqueous phase [304]. The authors also estimated the diffusion of ground-state oxygen atoms in water at 328 K using DFT-based molecular dynamics simulations and indicated the presence of uncertainties in DFT-based estimates [304]. The latter has motivated us to conduct a comprehensive and systematic study of the transport and thermodynamic properties of atomic oxygen in aqueous environments.

Accurate modeling of atomic oxygen in aqueous environments is a challenge because of its complex electronic structure and open shell character. Atomic oxygen has an electronic configuration of $1s_2\,2s_2\,2p_4$. It has fifteen microstates associated with the quantum states ^{3}P, ^{1}D and ^{1}S. Nine microstates correspond to $^3P_{2,1,0}$, five correspond to $^1D_2$, and one corresponds to $^1S_0$. According to Hund's rules, the ground state is $^3P_2$. Spin–orbit coupling lifts the degeneracy of the triplet state, with the $^3P_1$ and $^3P_0$ levels lying approximately 1.89 kJ/mol, and 2.71 kJ/mol higher above the ground level, respectively. The $^1D_2$ and $^1S_0$ states lie significantly higher, at about 189.82 kJ/mol and 404.25 kJ/mol above the ground state [320–323].

Earlier theoretical and experimental research on atomic oxygen-water interactions focused mainly on the possible formation of oxywater species as structural isomers of hydrogen peroxide, H_2O_2 [160, 324–336]. Recent studies have investigated the interaction between atomic oxygen and water in the context of plasma-liquid systems. Yusupov *et al.* [337] used ReaxFF molecular dynamics simulations and predicted the formation of two OH radicals by hydrogen abstraction from water. Verlackt *et al.* [338] applied DFTB-based molecular dynamics to singlet oxygen interacting with water and reported the formation of oxywater, which remained stable for approximately 10 ps. Xu *et al.* [339] used DFT-based molecular dynamics and identified oxywater as an intermediate in the reaction between singlet oxygen and water, ultimately leading to the formation of H_2O_2. Suijker & Bagheri [323] examined the interactions between atomic oxygen and a single water molecule using high-level quantum mechanical calculations (at the level of CASSCF and CCSD(T)) without spin-orbit corrections. The results show that the $^3P_2$, $^3P_1$, and $^3P_0$ triplet states split upon interaction with a water molecule. The highest excited energy surface exhibits a fully repulsive character, while the first and lowest-energy surfaces display shallow potential wells of about 1.37 kJ/mol and 2.41 kJ/mol below the total energy of a triplet oxygen atom and a water molecule, which could be a numerical artifact. The five microstates of the $^1D_2$ energy surface also split: four are repulsive (two of which remain degenerate), while one exhibits an attractive potential well with a depth of approximately

114-149 kJ/mol below the total energy of a singlet oxygen atom and a water molecule. It was concluded that atomic oxygen and a single water molecule do not form a stable complex on any of the triplet energy surfaces. Only on one of the singlet energy surfaces does the interaction lead to the formation of an oxywater species. The authors also investigated the transition of singlet oxywater to hydrogen peroxide via a (1,2)-hydrogen shift and predicted the corresponding reaction rates. Furthermore, the study showed that the singlet oxywater species become more stable when an implicit solvent model of water was included in their calculations [323].

Due to the high computational cost of *ab initio* quantum mechanical calculations, we use force field-based molecular simulations to estimate the solubility and diffusion of atomic oxygen in water. Several interaction pathways exist for atomic oxygen and water. In this work, we focus on pathways that do not involve chemical reactions, for which a force field description is appropriate. The force field parameters that describe the interaction between atomic oxygen and water molecules are extracted from the energy surfaces of Suijker & Bagheri [323] by representing each energy surface with a 12-6 Lennard-Jones (L-J) potential. Using these state-specific force fields, we are able to capture the dependence of the oxygen-water interaction on the quantum state of atomic oxygen. To identify each state and the corresponding force field parameter set, we adopt the C_{2v} naming convention used by Suijker & Bagheri [323] for convenience. In this scheme, the ground triplet energy surface is labeled $3\,B_1(1)$, the first excited triplet state is $3\,B_2(1)$, and the second excited triplet state is $3\,A_2(1)$. For the singlet energy surfaces, $1\,A_1(1)$ is excluded, as it involves a reactive interaction that leads to oxywater formation. The other four excited singlet states are $1\,B_1(1)$, $1\,B_2(1)$, $1\,A_1(2)$, and $1\,A_2(1)$ with $1\,A_1(2)$ and $1\,A_2(1)$ being degenerate. A similar approach was used by Du *et al.* [340], who developed state-specific force field parameters for the OH radical interacting with water based on energy surfaces calculated for different quantum states of the OH radical.

As discussed above for atomic oxygen, its interaction with water depends on its quantum state and involves multiple energy surfaces. Similar considerations may apply to other plasma-produced species that interact with water, as different quantum states can give rise to distinct energy surfaces. The shape and depth of these energy surfaces depend on the accuracy of the quantum mechanical methods used. To obtain an overall understanding of the solubility and diffusion of plasma-generated species, we model each species, whether a radical or a molecule, as a charge-neutral particle. The interaction of this particle with water is represented using a 12-6 L-J potential, in the same manner as applied to atomic oxygen. We systematically vary the size of the particle and the strength of its interaction with water and calculate the corresponding solubility and diffusion coefficients at three different temperatures (300, 325 and 350 K). This approach allows us to estimate how the solubility and diffusion of plasma species depend on the strength of the

particle-water interaction, the particle size, and temperature.

The data generated in this work provide essential input for continuum-scale simulations of plasma-liquid systems and aid the interpretation of experimental results, where reliable transport and thermodynamic parameters for plasma-generated RONS are scarce. The impact of this study extends beyond plasma science and technology. This is due to the central role of RONS in numerous natural and industrial chemical and physical processes, including atmospheric and aerosol chemistry [341].

6.2 Methodology

6.2.1 Force Fields

Atomic Oxygen in water

In this work, we represent the interaction of O(^{3}P) and O(^{1}D) with H_2O using a 12-6 L-J potential, $4\epsilon_{ij}\left[\left(\frac{\sigma_{ij}}{r_{ij}}\right)^{12}-\left(\frac{\sigma_{ij}}{r_{ij}}\right)^{6}\right]$, where σ represents the distance at which the particle-particle interaction energy is zero, and ϵ represents the depth of the potential well. The L-J parameters are determined by fitting this functional form to the energy surfaces computed by Suijker & Bagheri, [323] who calculated the potential energy curves for an oxygen atom approaching the oxygen of a water molecule, starting at a distance of 10.0 Å. The calculations were performed using the Complete Active Space Self-Consistent Field method with 10 active electrons in 8 orbitals, (10,8)CASSCF, followed by the strongly contracted N-Electron Valence State Perturbation Theory (SC-NEVPT2) [342–344]. The inclusion of SC-NEVPT2 introduces dynamical correlations to the energies via perturbations. The correlation-consistent polarized valence triple-zeta, cc-pVTZ, basis set of Dunning and coworkers [345, 346] was used. The molecular complex has C_{2v} symmetry at all positions of the potential energy curve. At each position, the geometry of H_2O was kept fixed, with all atoms constrained to lie in one plane. All calculations were performed using the software ORCA [347] version 5.0.4. The potential energy curves were compared to available results in the literature. A detailed discussion of this comparison is provided in the work by Suijker & Bagheri [323]. A discussion on advantages and limitations of CASSCF, SC-NEVPT2, and other methods are well described in quantum chemistry textbooks [348] and ORCA [347] manual. We note that, in this work, the 12-6 L-J functional form is used to represent the interaction of O(^{3}P) or O(^{1}D) with H_2O on the potential energy surfaces that exhibit a purely repulsive character. These potential energy curves include the three triplet surfaces of $3\,A_2(1)$, $3\,B_2(1)$, and $3\,B_1(1)$ for the interaction of O(^{3}P) with H_2O and the four (out of 5) singlet surfaces of $1\,A_1(2)$, $1\,A_2(1)$, $1\,B_1(1)$, and $1\,B_2(1)$ for the interaction of O(^{1}D) with

H_2O. The singlet $1\,A_1(1)$ energy surface was deliberately omitted as it exhibits an attractive potential well with a depth of approximately 114-149 kJ/mol below the total energy of a singlet oxygen atom and a water molecule, indicating the formation of a chemically bonded complex. On the triplet energy surfaces, the first excited state, $3\,B_2(1)$, and the lowest-energy state, $3\,B_1(1)$, exhibit shallow potential wells of approximately 1.37 kJ/mol and 2.41 kJ/mol, below the total energy of a triplet oxygen atom and a water molecule, respectively. As discussed in the work by Suijker & Bagheri [323], these shallow minima may arise from basis set superposition error (BSSE) and could therefore be numerical artifacts. Even if the shallow wells on the $3\,B_2(1)$ and $3\,B_1(1)$ surfaces are not purely numerical artifacts, their depths (1-2.5 kJ/mol) remain far below the strength of a typical chemical bond, as these are of the order of the chemical accuracy. Therefore, fitting each of these triplet energy curves with a L-J functional form is a reasonable and physically justified approximation. The choice of L-J potential to represent the various energy surfaces is to maintain a simple consistent functional form for all the different energy surfaces. The L-J potentials describing the interaction of $O(^3P)$ with H_2O on the energy surfaces $3\,A_2(1)$, $3\,B_1(1)$, and $3\,B_2(1)$ are shown in Figures D.1, D.2 and D.3 of Appendix D. For each potential energy surface, the total energy of the system at an oxygen-oxygen distance of 10.0 Å was taken as the reference energy. The fit was performed for the range 1.1 Å to 10 Å, however, only a part of the curve is shown to clearly illustrate the differences between the fitted function and the quantum chemistry data. The corresponding L-J parameters for the interaction between O (from $O(^3P)$) and O_w (the oxygen atom of H_2O) are provided in Table D.1 of Appendix D. Similarly, the energy surfaces for $O(^1D)$ interacting with H_2O on the energy surfaces $1\,A_1(2)$, $1\,A_2(1)$, $1\,B_1(1)$, and $1\,B_2(1)$, along with their fitted L-J potentials, are shown in Figures D.4, D.5, D.6 and D.7 of Appendix D, and the associated L-J parameters are listed in Table D.1 of Appendix D. Note that the $1\,A_1(2)$ and $1\,A_2(1)$ energy surfaces are degenerate and yield identical L-J parameters. Therefore, $1\,A_2(1)$ energy surface is excluded from the analysis of the following sections. The TIP3P [60] force field for water is used to compute the excess chemical potential, μ^{ex}, and the Henry solubility coefficients, H_s^{cp}. The TIP4P/2005 [61] water model is used to calculate the self-diffusion coefficients of $O(^3P)$ and $O(^1D)$.

L-J particle in water

To obtain a comprehensive understanding of the solubility and diffusion of plasma-generated species in water, we modeled each species, a radical or a molecule, as a charge-neutral particle. The interaction between this particle and water molecules was described using a standard 12-6 L-J potential. To systematically explore how particle size, particle interaction strength, and temperature influence self-diffusion coefficients (D), excess chemical potentials

(μ^{ex}), and Henry coefficients (H_s^{cp}), we performed a parameter study. We used five different values of ϵ/k_{B} (21.59 K - 167.22 K) and five different values of σ (2.83 Å - 3.83 Å) to represent the interaction of the particle with water at three different temperatures (300, 325, and 350 K). The TIP4P/2005 [61] force field for water is used to compute all thermodynamic properties of the L-J particle in water.

For all simulations, a cutoff radius of 12 Å was used for both L-J and Coulombic interactions. The Ewald summation method [181, 182] was used to treat long-range Coulombic interactions. The energies and pressures were corrected with long-range tail corrections for the L-J interactions [54].

6.2.2 Monte Carlo Simulations

Continuous Fractional Component Monte Carlo (CFCMC) simulations [95–97] using the open-source Brick-CFCMC software [97–99] were performed in the NPT ensemble to compute the excess chemical potentials (μ^{ex}) and subsequently the Henry coefficients (H_s^{cp}). In CFCMC simulations, fractional molecules are incorporated whose interactions are scaled using a continuous coupling parameter λ. The value of λ ranges from 0 to 1, where $\lambda = 0$ corresponds to the fractional molecules behaving as ideal gas molecules with no interactions with the rest of the system, and $\lambda = 1$ represents "whole" molecules that have full interaction with the other molecules in the system. The excess chemical potential is computed as:

$$\mu_i^{\text{ex}} = -k_{\text{B}}T \ln \frac{p(\lambda = 1)}{p(\lambda = 0)}, \tag{6.1}$$

where $p(\lambda{=}1)$ and $p(\lambda{=}0)$ are the Boltzmann sampled probability distributions of λ at 1 and 0, respectively, k_{B} is the Boltzmann constant and T is the absolute temperature [99]. The Henry volatility coefficient K_v^{px} in units of [Pa] is obtained by using

$$K_v^{\text{px}} = \rho\, k_{\text{B}}T \exp\left[\frac{\mu^{\text{ex},\infty}}{k_{\text{B}}T}\right], \tag{6.2}$$

where ρ is the number density of the solvent. The Henry coefficient (H_s^{cp}) in units of [mol/m^3 Pa] can be obtained from K_v^{px} using $H_s^{\text{cp}} \approx \frac{\rho_{\text{H}_2\text{O}}}{M_{\text{H}_2\text{O}} K_v^{\text{px}}}$ in which $\rho_{\text{H}_2\text{O}}$ is the density of water and $M_{\text{H}_2\text{O}}$ is the molar mass of water [52]. The Henry coefficient (H_s^{cp}) will have SI units only if ρ, k_{B}, T, and M are in SI units. For more methodological details, the reader is referred to our previous works [308–310].

For computing μ^{ex} and H_s^{cp} of atomic oxygen, O, a fractional atom of O was placed in a cubic box with 500 water molecules. The values of μ^{ex} and H_s^{cp} of the L-J particle were also computed by placing a fractional particle in a cubic box containing 500 water molecules. For all CFCMC simulations 5×10^6 equilibration cycles were carried out, followed by 5×10^6 production cycles. Here, one cycle

refers to N number of trial moves, where N is the total number of molecules. Error bars were calculated from the standard deviations obtained from five independent production runs.

6.2.3 Molecular Dynamics Simulations

Molecular Dynamics (MD) simulations were performed using the open-source Large-scale Atomic/Molecular Massively Parallel Simulator (LAMMPS) [283] in the NPT ensemble. The Velocity-Verlet algorithm was used to integrate the equations of motion [54]. A time step of 2 fs was used. To compute the self-diffusion coefficient (D) of O, systems containing 995 water molecules and 5 O atoms were simulated. To determine D for the plasma particle in water, systems containing 999 water molecules and 1 plasma particle were used. In both cases, the workflow described in Ref [349] was followed. The Nosé-Hoover thermostat [54, 188, 285] (with a coupling constant of 0.1 ps) and barostat (coupling constant of 1 ps) were used to keep the temperatures and pressure constant. The self-diffusion coefficients were corrected for finite-size effects with the Yeh-Hummer equation [85, 108]. For more details on the computation of self-diffusion coefficients, the reader is referred to our previous works [308, 310]. Periodic boundary conditions were applied in all directions. To obtain statistics, three independent simulations were performed. Each production run of the simulation was further divided into two blocks, giving six independent production blocks in total. The reported error bars correspond to the standard deviations of the values obtained from the six production blocks.

6.3 Results and Discussion

6.3.1 Atomic Oxygen in water

The self-diffusion coefficients of O(^{3}P) in water using force fields fitted to the $3\,B_1(1)$, $3\,B_2(1)$, and $3\,A_2(1)$ energy surfaces computed by Suijker & Bagheri [323] at temperatures in the range of 273 - 333 K are shown in Figure 6.1. Similarly, the self-diffusion coefficients of O(^{1}D) in water at 273 - 333 K using force fields fitted to the $1\,B_1(1)$, $1\,B_2(1)$, and $1\,A_1(2)$ energy surfaces computed by Suijker & Bagheri [323] are shown in Figure 6.2. The corresponding numerical values are listed in Table D.2 of Appendix D. For both O(^{3}P) and O(^{1}D), the self-diffusion coefficients increase with increasing temperature.

For O(^{3}P), D associated with the $3\,B_1(1)$ energy surface has the highest values, while that associated with the $3\,A_2(1)$ energy surface has the lowest values. A similar trend is observed for the singlet states, where D associated with the $1\,B_1(1)$ energy surface has the highest values, while that associated with the $1\,A_1(2)$ energy surface has the lowest values. In both cases, the force fields for the energy

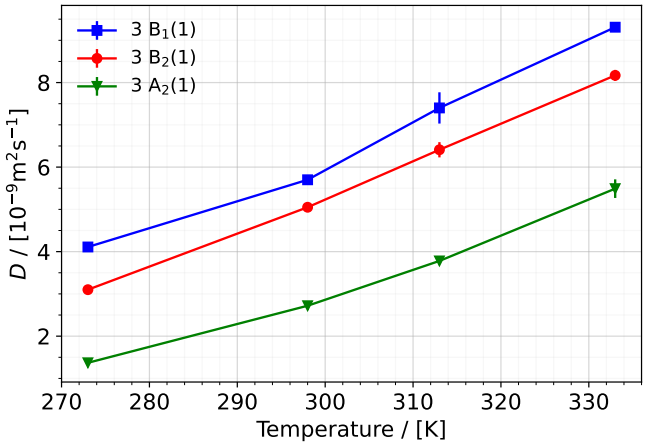

Figure 6.1: Self-diffusion coefficients of O(^{3}P) in water at 273 - 333 K using force fields fitted to the $3\,B_1(1)$, $3\,B_2(1)$, and $3\,A_2(1)$ energy surfaces computed by Suijker & Bagheri [323]. The water model used is the TIP4P/2005 model [61]. Error bars are estimated based on the standard deviation of 6 production blocks.

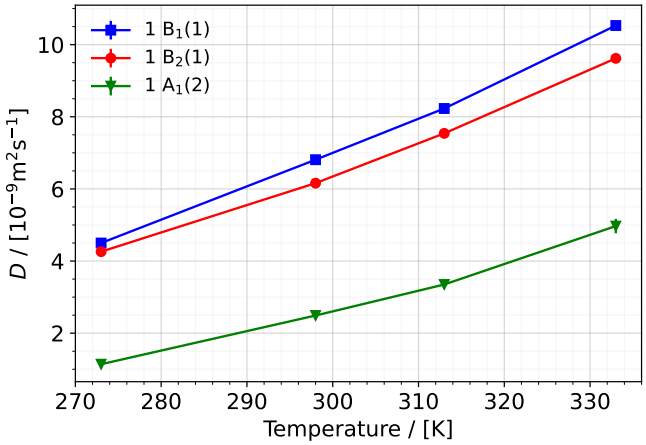

Figure 6.2: Self-diffusion coefficients of O(^{1}D) in water at 273 - 333 K using force fields fitted to the $1\,B_1(1)$, $1\,B_2(1)$, and $1\,A_1(2)$ energy surfaces computed by Suijker & Bagheri [323]. The water model used is the TIP4P/2005 model [61]. Error bars are estimated based on the standard deviation of 6 production blocks, and are much smaller than the symbols used in the figure.

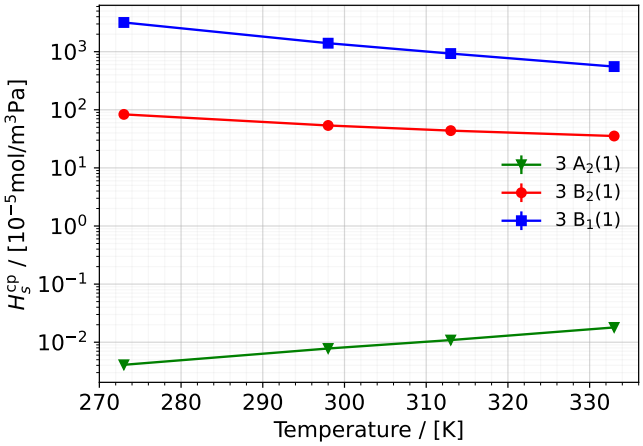

Figure 6.3: Henry coefficients of O(^{3}P) in water at 273 - 333 K in logarithmic scale using force fields fitted to the 3 $B_1(1)$, 3 $B_2(1)$, and 3 $A_2(1)$ energy surfaces computed by Suijker & Bagheri [323]. The water model used is the TIP3P model [60]. Error bars are estimated based on the standard deviation of 5 production blocks, and are much smaller than the symbols used in the figure.

surfaces characterized by a higher value of ϵ/k_B and a lower value of σ yield higher self-diffusion coefficients.

The Henry coefficients (H_s^{cp}) of O(^{3}P) at 273 - 333 K in logarithmic scale using force fields fitted to the 3 $B_1(1)$, 3 $B_2(1)$, and 3 $A_2(1)$ energy surfaces computed by Suijker & Bagheri [323] are shown in Figure 6.3. The corresponding results for O(^{1}D) obtained from force fields fitted to the 1 $B_1(1)$, 1 $B_2(1)$, and 1 $A_1(2)$ energy surfaces computed by Suijker & Bagheri [323] are shown in Figure 6.4. In Figure 6.3, H_s^{cp} associated with the 3 $B_1(1)$ and 3 $B_2(1)$ energy surfaces decrease with temperature, while that derived from the 3 $A_2(1)$ energy surface increases with temperature. A similar trend is observed in Figure 6.4, where the values of H_s^{cp} associated with the 1 $B_1(1)$ and 1 $B_2(1)$ energy surfaces decrease with temperature, while H_s^{cp} corresponding to the 1 $A_1(2)$ energy surface increase with temperature. This behaviour can be explained by the van 't Hoff equation for the temperature dependence of the Henry coefficients [52]

$$(\ln[H_s^{cp}])(1/T) = \frac{-\Delta_{sol}H}{R}, \tag{6.3}$$

where $\Delta_{sol}H$ is the enthalpy of dissolution of the species and R is the gas constant [52]. If $-\Delta_{sol}H$ is negative, the dissolution is endothermic, and the dissolution process is exothermic if $\Delta_{sol}H > 0$.

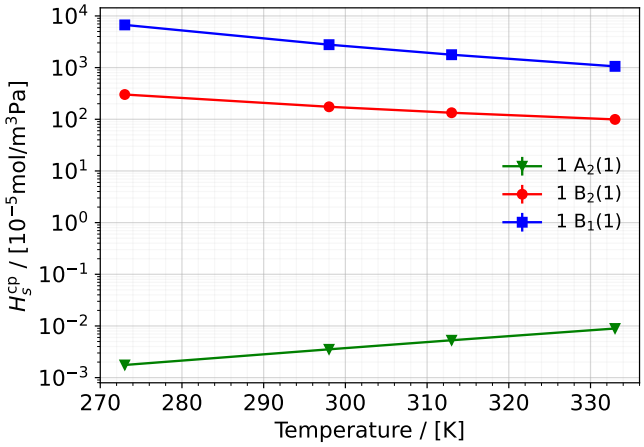

Figure 6.4: Henry coefficients for O(^{1}D) in water at 273 - 333 K in logarithmic scale using force fields fitted to 1 B_1(1), 1 B_2(1), and 1 A_1(2) energy surfaces computed by Suijker & Bagheri [323]. The water model used is the TIP3P model [60]. Error bars are estimated based on the standard deviation of 5 production blocks, and are much smaller than the symbols used in the figure.

Figures D.8 and D.9 of Appendix D show the Henry coefficients of O(^{3}P) and O(^{1}D) as a function of the inverse temperature. The H_s^{cp} associated with the 3 A_2(1) and 1 A_1(2) energy surfaces exhibit a negative slope compared to the other energy surfaces. This indicates a positive $\Delta_{sol}H$ and consequently, an endothermic dissolution. These results indicate that the interaction of O(^{3}P) on the 3 A_2(1) energy surface and O(^{1}D) on the 1 A_1(2) energy surface with water are comparatively weaker. This interpretation is consistent with the lower depths of the L-J wells (ϵ/k_B) of the force fields associated with the 3 A_2(1) and 1 A_1(2) (4.2 K and 6 K, respectively), which reflect a weaker interaction between the atomic oxygen in these energy surfaces and water relative to the other energy surfaces. H_s^{cp} associated with 3 B_1(1) energy surface exceeds that of 3 B_2(1), a trend attributable to the higher ϵ/k_B and a lower σ of the force field of 3 B_1(1) compared to that of 3 B_2(1). Similarly, force field corresponding to 1 B_1(1) energy surface has a higher ϵ/k_B and a lower σ than that of 1 B_2(1), and therefore, yields a higher value of H_s^{cp}. However, the specific roles of the individual L-J parameters (ϵ/k_B and σ) in determining the thermodynamic properties of these systems are yet to be elucidated.

In a recent study, Myers *et al.* [304] demonstrated that solvated O(^{3}P) atoms can be imaged in liquid water using a femtosecond laser for two-photon absorption laser-induced fluorescence (fs-TALIF). The authors reported that O(^{3}P) atoms

exhibit chemical lifetimes of at least tens of microseconds in water and, aided by plasma-induced flow, can penetrate several hundred micrometres into the liquid. The authors used DFT-based MD simulations and predicted a value of 1.5×10^{-9} m^2/s for the diffusion coefficient of $O(^3P)$ in water at 328 K. This diffusion coefficient was then used to estimate the collisional quenching rate and the corresponding effective branching ratio, which enabled an estimation of the density of $O(^3P)$ in water. Using the latter with the measurements of the density of $O(^3P)$ in the gas phase, a dimensionless Henry coefficient of approximately 10 was inferred for $O(^3P)$ at a plasma-effluent temperature of 350 K [304]. In our work, we obtain a dimensionless Henry coefficient of approximately 13.8 for the ground $3\,B_1(1)$ state of $O(^3P)$ at 333 K, which is in good agreement with the estimated value of Myers *et al.* [304]. We also predict a self-diffusion coefficient of $9.3 \times 10^{-9}\,m^2/s$ for the ground $3\,B_1(1)$ state of $O(^3P)$ at 333 K, which is slightly higher than the value predicted by Myers *et al.* [304].

6.3.2 L-J particle in water

As shown in the previous section, the interactions between different quantum states of atomic oxygen and water lead to distinct L-J parameters (ϵ/k_B and σ), which in turn affect the Henry coefficients (H_s^{cp}) and self-diffusion coefficients (D). Motivated by these findings, and considering that other plasma species may also exist in different quantum states with varying interaction energies, we systematically investigated how these differences influence Henry coefficients and self-diffusion coefficients. This provides the community with estimated values for other species. In Figure 6.5, the self-diffusion coefficients of L-J particle in water are plotted as a function of ϵ/k_B for different σ at 300 K. The numerical data are given in Tables D.5 - D.9 of Appendix D. In general, D decreases as ϵ/k_B increases. This could be ascribed to the increased interaction between the L-J particle and the water molecules, which decreases the mobility, and hence the self-diffusion coefficients. However, the slope of D as a function of ϵ/k_B becomes less negative with increasing ϵ/k_B, indicating a decreasing sensitivity of D to the interaction strength at higher values of ϵ/k_B. D also decreases with increasing σ, which is shown in Figure 6.6, where D as a function of σ is plotted for different values of ϵ/k_B. This could be ascribed to the decrease in mobility as a result of the increasing size of the L-J particle. This leads to a decrease in D. The self-diffusion coefficients as a function of σ^{-1} are plotted in Figure D.10 of Appendix D, which also highlights the above trend. A comparison of Figures 6.5 and 6.6 shows that changes in σ have a more profound effect on D than changes in ϵ/k_B. Consequently, the higher values of D of $3\,B_1(1)$ and $1\,B_1(1)$, compared to the other energy surfaces, could be primarily attributed to their lower values of σ than to their lower values of ϵ/k_B. The temperature dependence of the self-diffusion coefficients on temperature is presented in Figures D.11 and D.12 of Appendix D,

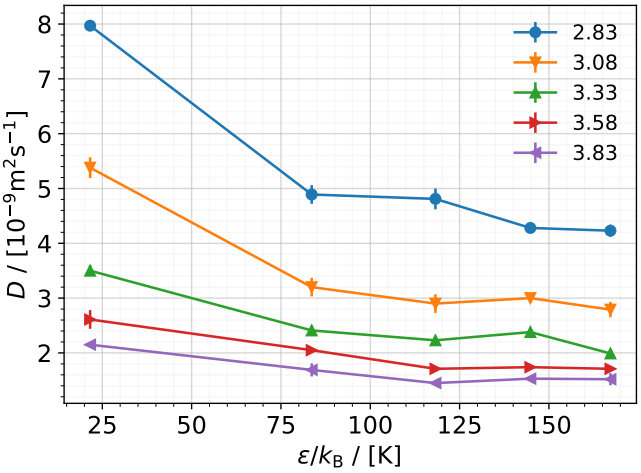

Figure 6.5: Self-diffusion coefficients of L-J particle in water as a function of ϵ/k_B for different values of σ at 300 K. The water model used is the TIP4P/2005 model [61]. Numbers in the legend represent values of σ. Error bars are estimated based on the standard deviation of 6 production blocks.

where D as a function of ϵ/k_B and σ, are plotted, respectively, for three different temperatures (300-350 K). As expected, D increases with temperature. Consistent with previous observations, the values of D become largely independent with higher values of ϵ/k_B. This is evident at all three temperatures investigated. In contrast, D decreases steadily with increasing σ for all temperatures.

The excess chemical potentials (μ^{ex}) as a function of ϵ/k_B for L-J particle of different σ at 300 K are presented in Figure 6.7. The data is presented in Tables D.10 - D.14 of Appendix D. A positive value of μ^{ex} indicates that repulsive interactions dominate, whereas a negative value of μ^{ex} signifies that attractive interactions are dominant. μ^{ex} decreases with increasing ϵ/k_B, indicating that the L-J particle becomes more hydrophilic as the interaction strength of the L-J particle with water molecules increases (increase in ϵ/k_B). Figure D.13 of Appendix D shows that μ^{ex} increases with increasing σ, reflecting a reduced affinity of the L-J particle for the water molecules as the size of the particle increases. This behaviour could be attributed to the steric effects caused by the increase in the excluded volume associated with larger σ values. The effect of temperature on μ^{ex} is shown in Figures D.14 and D.15 of Appendix D, where μ^{ex} as a function of ϵ/k_B and σ, are plotted respectively, for three temperatures between 300 and 350 K. In both cases, μ^{ex} shifts to higher values with increasing temperature.

As discussed in Section 6.2.2, H_s^{cp} varies inversely with the exponential of μ^{ex}.

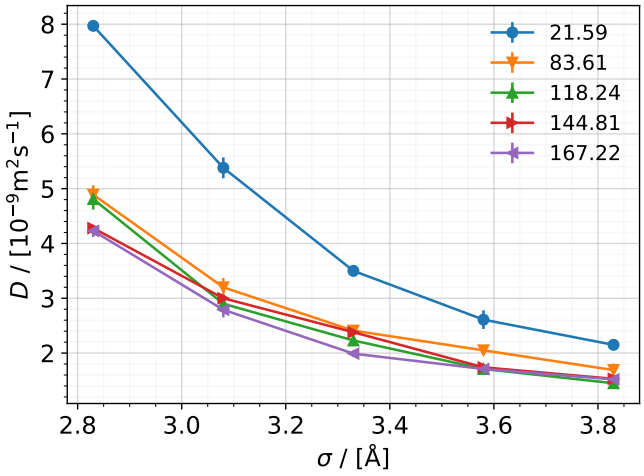

Figure 6.6: Self-diffusion coefficients of L-J particle in water as a function of σ for different values of ϵ/k_B at 300 K. The water model used is the TIP4P/2005 model [61]. Numbers in the legend represent values of ϵ/k_B. Error bars are estimated based on the standard deviation of 6 production blocks.

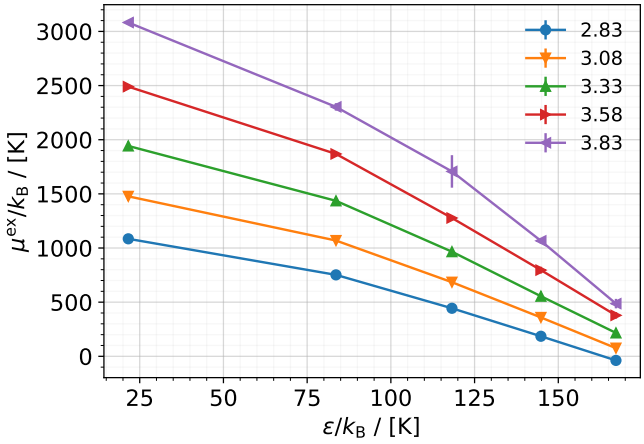

Figure 6.7: Excess chemical potentials of L-J particle as a function of ϵ/k_B for different values of σ at 300 K. The water model used is the TIP4P/2005 model [61]. Numbers in the legend represent values of σ. Error bars are estimated based on the standard deviation of 5 production blocks.

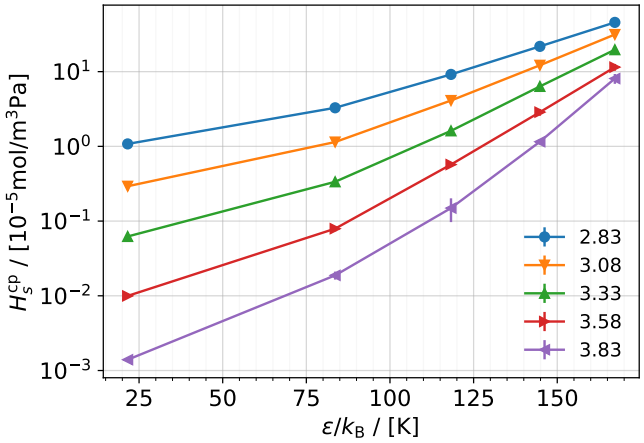

Figure 6.8: Henry coefficients of L-J particle in water as a function of ϵ/k_B for different values of σ at 300 K in logarithmic scale. The water model used is the TIP4P/2005 model [61]. Numbers in the legend represent values of σ. Error bars are estimated based on the standard deviation of 5 production blocks.

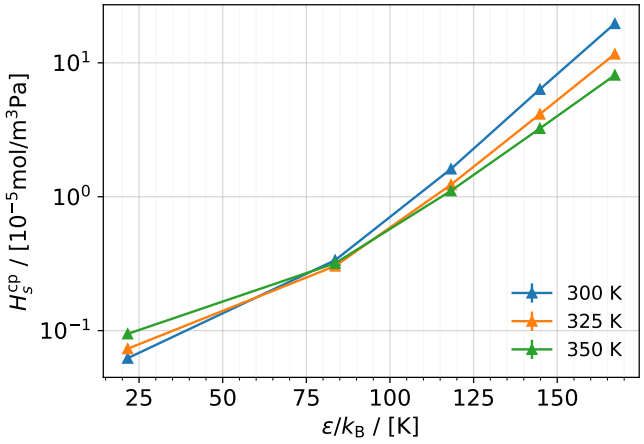

Figure 6.9: Henry coefficients of L-J particle in water as a function of ϵ/k_B in logarithmic scale for the value of $\sigma = 3.33$ Å at different temperatures (300-350 K). The water model used is the TIP4P/2005 model [61]. Error bars are estimated based on the standard deviation of 5 production blocks.

Therefore, H_s^{cp} is expected to increase with increasing ϵ/k_B and decreasing σ. This trend is evident in Figure 6.8 (and Figure D.16 of Appendix D), where the Henry coefficients (H_s^{cp}) are shown as a function of ϵ/k_B (σ) for L-J particle of different σ (ϵ/k_B) at 300 K. A comparison of Figures 6.8, D.16 and Tables D.15 - D.19 indicates that ϵ/k_B has a more profound effect on H_s^{cp} compared to σ. Therefore, the higher values of H_s^{cp} of $^3B_1(1)$ and $^1B_1(1)$, compared to the other energy surfaces, arise primarily due to their higher values of ϵ/k_B than their lower values of σ. From the work of Lachet *et al.*[76], the following L-J parameters for nitric oxide (NO), modeled as a single interaction site, can be obtained: $\epsilon_{NO}/k_B = 130$ K, $\sigma_{NO} = 3.40$ Å. Combining these values with the corresponding parameters for water (ϵ_{H_2O}/k_B and σ_{H_2O} for the TIP4P/2005 water model) using the Lorentz-Berthelot [81] mixing rules, the following values can be obtained for the interaction strength of NO particle with water: $\epsilon/k_B = 110.08$ K and $\sigma = 3.28$ Å. From Figure 6.8, these parameters correspond to a Henry coefficient for NO, $H_{NO}^{cp} \approx 1.3 \times 10^{-5}$ mol/m^3 Pa. This value is in good agreement with experimental data (1.3 - 2.3 $\times 10^{-5}$ mol/m^3 Pa) reported in the literature [265, 267, 268]. It is also consistent with our previous computational results for the Henry coefficient of NO reported in Ref. [308]. Performing such an analysis for other species would be possible, provided that suitable single-site force fields are available.

Figure 6.9 presents H_s^{cp} as a function of ϵ/k_B for three different temperatures. For L-J particles in TIP4P/2005 water, the solute-solvent interactions become stronger than the solvent-solvent interactions at $\epsilon/k_B > 93.20$ K. Up to this value, H_s^{cp} increases with temperature, indicating that the dissolution of the sphere in water is an endothermic process and that the L-J sphere is hydrophobic in nature. However, when ϵ/k_B is greater than 93.20 K, H_s^{cp} decreases with temperature, signifying a transition to exothermic dissolution and the correspondingly hydrophilic nature of the L-J sphere.

6.4 Conclusions

We parameterized state-specific force fields to describe the interaction between atomic oxygen and water on the triplet and singlet energy surfaces and computed the self-diffusion and Henry coefficients over the temperature range of 273 - 333 K. On the triplet energy surfaces, the ground state $^3B_1(1)$ yielded the highest values of D and H_s^{cp}. On the singlet energy surfaces, the first excited state, $^1B_1(1)$, exhibited the highest values. The lowest-lying singlet energy surface for atomic oxygen interacting with water was excluded, as it involves in a chemical reaction leading to the formation of a singlet oxywater species. Force field users are advised to identify the relevant quantum state of the atomic oxygen for their specific application and to use the corresponding parameter values listed in Table D.1 of Appendix D. To identify the influence of individual L-J parameters (σ and

ϵ/k_B) on D and H_s^cp, we systematically varied the values of σ and ϵ/k_B for a charge-neutral particle in water at temperatures between 300 and 350 K. Our analysis shows that the self-diffusion coefficients are governed by the particle size (σ), while the Henry coefficients are more sensitive to the strength of the interaction with water (ϵ/k_B). Finally, we find that the dissolution process changes from endothermic to exothermic once the solute-solvent interactions become stronger than the solvent-solvent interactions. These findings provide key parameters essential for macroscopic simulations of plasma-liquid systems and for interpreting experimental observations.

Chapter 7

Predicting Absorption and Diffusion of Plasma-Generated RONS in Electrolytic Solutions

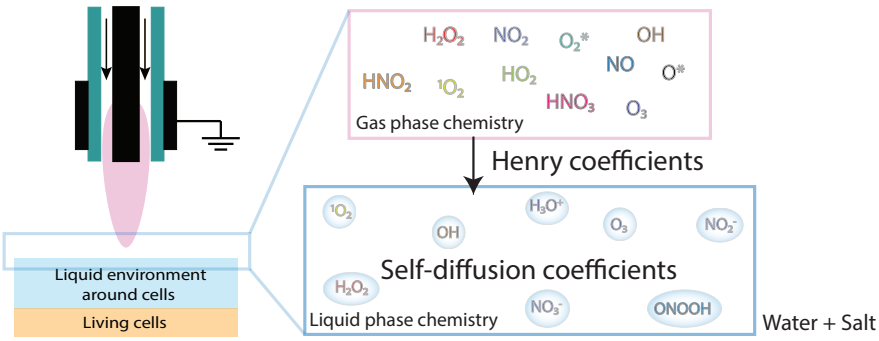

This chapter is based on the following publication: T. H. G. Saji, T. J. H. Vlugt, S. Calero and B. Bagheri, *Predicting Absorption and Diffusion of Plasma-Generated RONS in Electrolytic Solutions, manuscript in preparation.*

Overview

Reactive oxygen and nitrogen species (RONS) generated by electric gas discharge plasmas in O_2 or N_2 containing gas mixtures have disinfectant and nutritive properties that have life science applications. In these applications, the RONS come in contact with a liquid environment. In this chapter, we consider an electrolytic solution, composed of water and NaCl, to mimic the liquid environment. Each RONS is modelled as a charge-neutral L-J particle. We used the TIP4P/2005 water models. The Madrid-2019 force fields were used to model the the aqueous NaCl solution. We investigate the effects of solute particle size and interaction strength on the self-diffusion coefficients (D) and Henry coefficients (H_s^{cp}) of the solute for varying NaCl concentrations. Our results indicate that for a 1.00 m increase in salt molality, D decreases by ca. 12% on average. The corresponding changes in the excess chemical potential (which is needed to compute H_s^{cp}) and H_s^{cp} are ca. 19% increase and ca. 22% decrease, respectively. The decrease in the Henry coefficient as salt concentration increases suggests a salting-out effect for the charge-neutral L-J particles.

7.1 Introduction

Electric gas discharge plasmas generated in O_2- or N_2-containing gas mixtures produce reactive oxygen and nitrogen species (RONS) [4, 138]. These species exhibit disinfectant and nutritive properties [33, 300, 301] that have various applications in life sciences, including biomedicine and agriculture [34, 212, 219–221, 305–307]. In these applications, the RONS generated in the gas phase come in contact with a liquid medium [302]. In the previous chapters of this thesis, the coefficients governing mass transport, namely the diffusion coefficient (D) and Henry coefficient (H_s^{cp}), were described considering pure water as the liquid medium. However, in life science applications, the aqueous phase is rarely composed of pure water and often contains dissolved salts [350–353]. Therefore, in this chapter, we extend our investigations to understand the impact of salt with various concentrations on D and H_s^{cp}.

Sakti *et al.* [354] observed that D of water molecules and ions decrease with increasing salt (sodium trifluoromethanesulfonate) concentration. Peng & Wan [355] investigated the effect of salt concentrations on the H_s^{cp} of volatile organic compounds such as benzene and toluene. These authors found that H_s^{cp} decreases with increasing NaCl concentration, indicating a salting-out effect. Görgényi *et al.* [356] analyzed the salting-out effect of different Li^+, Na^+, K^+, NH_4^+ and Mg^{2+} salts on chloroform, benzene, chlorobenzene and anisole in water. These authors observed a decrease in the values of H_s^{cp} for the organic probes in salt water compared to in pure water. However, to the best of our knowledge, a systematic study of how solute particle size and interaction strength influence both the diffusion coefficients and Henry coefficients for varying salt concentrations has not yet been performed.

In this chapter, we investigated the effects of salt concentrations on D and H_s^{cp} of RONS with different sizes and interaction strength (attractive potential energy between solute and water molecules). We used NaCl as the salt in our study because NaCl is the dominant salt in extracellular fluid [357]. The extracellular fluid roughly contains 0.9 wt% NaCl [358]. This corresponds to a molality of 0.15 m. In this chapter, molality of salt is defined as $\left[\frac{\mathrm{mol}_{\mathrm{salt}}}{\mathrm{kg}_{\mathrm{solvent}}}\right]$ We considered four different salt concentrations (0.00 m, 0.33 m, 0.67 m, and 1.00 m). As in Chapter 6, RONS are represented as charge-neutral particles with varying L-J parameters (σ and ϵ/k_{B}).

7.2 Methodology

7.2.1 Force Fields

To obtain an understanding of the effects of salt concentrations on the solubility and diffusion of plasma-generated species in water, we modelled each species, a radical or a molecule, as a charge-neutral particle. The particle size, particle interaction strength, and salt concentrations (molalities) were systematically varied to study their influence on self-diffusion coefficients (D), excess chemical potentials (μ^{ex}), and Henry coefficients (H_s^{cp}). As in Chapter 6, for studying the self-diffusion coefficients, we used five different values of ϵ/k_{B} (21.59 K - 167.22 K) and five different values of σ (2.83 Å - 3.83 Å) to represent the interaction of the particle with water for four different molalities (0.00 m, 0.33 m, 0.67 m, and 1.00 m). For the analysis of excess chemical potentials (μ^{ex}) and Henry coefficients (H_s^{cp}), five different values of ϵ/k_{B} (21.59 K - 167.22 K), four different values of σ (2.83 Å - 3.58 Å) and four different molalities (0.00 m, 0.33 m, 0.67 m, and 1.00 m) were used. The water is modelled using the TIP4P/2005 model [61]. The Na^+ and Cl^- Madrid-2019 force fields were used to model the aqueous NaCl solution [359]. This force field uses scaled charges for ions, with monovalent ions using a charge of 0.85 e for accurate description of thermodynamic and transport properties of aqueous solution [360]. The force field parameters used in this work are given in Table E.1 of Appendix E. A cut-off radius of 12 Å was used for both L-J and Coulombic interactions. The Ewald summation method [181, 182] was used to treat long-range Coulombic interactions. The energies and pressures were corrected with long-range tail corrections for the L-J interactions [54].

7.2.2 Molecular Dynamics Simulation

Molecular Dynamics (MD) simulations were performed using the open-source Large-scale Atomic/Molecular Massively Parallel Simulator (LAMMPS) [283]. The MD simulations were used to compute D and were performed in the NPT ensemble. The equations of motion were integrated using the Velocity-Verlet algorithm [54]. A time step of 2 fs was used. The MD simulations contained 500 water molecules and 1 L-J particle. The varying salt concentrations were modelled using a varying number of Na^+ and Cl^- ions, which are given in Table E.2 of Appendix E. The Nosé-Hoover thermostat [54, 188, 285] (with a coupling constant of 0.1 ps) and barostat (coupling constant of 1 ps) were used. D was corrected for finite-size effects using computed viscosities according to Equation 2.66. Periodic boundary conditions were applied in all directions. To obtain statistics, two independent simulations were performed. Each simulation production run (20 ns) was further divided into two blocks, yielding a total of four independent production blocks. The reported error bars correspond to the standard deviations of the values

obtained from the four production blocks. All MD simulations were performed at 300 K and 1 bar.

7.2.3 CFCMC Simulations

Continuous Fractional Component Monte Carlo (CFCMC) simulations [95–97] using the open-source Brick-CFCMC software [97–99] in the NPT ensemble were performed to compute the excess chemical potentials (μ^{ex}) and the Henry coefficients (H_s^{cp}). More details regarding the CFCMC simulations can be found in Section 2.3.1 of this thesis. The excess chemical potential and Henry coefficients are computed using Equations 2.61 and 2.64. The simulation was performed with the same number of molecules for each species as in the corresponding MD simulation system. Trial moves included translation, rotation, volume change trial moves, along with λ change, and hybrid trial moves that combined swap and identity change trial moves [99]. 5×10^6 equilibration cycles were carried out, followed by 5×10^6 production cycles. Error bars were calculated from the standard deviations obtained from four independent production runs. All CFCMC simulations were performed at 300 K and 1 bar.

7.3 Results and Discussion

7.3.1 Self-Diffusion Coefficients

In Figure 7.1, the self-diffusion coefficients of L-J particles in water are plotted as a function of particle size, σ, for different salt concentrations at a ϵ/k_{B} value of 118.24 K. The corresponding numerical data are provided in Tables E.8 - E.12 of Appendix E. D as a function of ϵ/k_{B} for different salt concentrations at a σ value of 3.08 Å is shown in Figure 7.2, and the corresponding numerical data is given in Tables E.8 - E.12 of Appendix E.

The viscosities required for the finite size effect correction of D are given in Tables E.3 - E.7 of Appendix E. The viscosity increases with increasing salt concentration, as seen in Ref. [361]. On average (where the average is computed from systems represented by varying values of σ (2.83 Å - 3.83 Å) and ϵ/k_{B} (21.59 K - 167.22 K)), the viscosity increases by 16.96% for an increase in molality of 1.00 m.

Consistent with the observations reported in the previous chapter, D decreases as σ and ϵ/k_{B} increase. An increase in salt concentrations leads to a decrease in the values of D. On average, considering systems represented by varying values of σ (2.83 Å - 3.83 Å) and ϵ/k_{B} (21.59 K - 167.22 K)), D decreases by ca. 12% for an increase in molality of 1.00 m. This is a result of the decreased mobility of the L-J particle resulting from the increasing salt concentration in the simulation system.

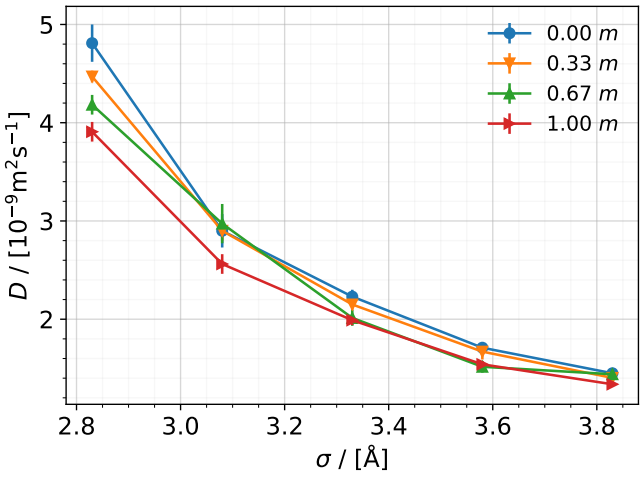

Figure 7.1: Self-diffusion coefficients of L-J particle in water as a function of particle size, σ for different salt concentrations at a ϵ/k_B value of 118.24 K. The water model used is the TIP4P/2005 model [61]. Numbers in the legend represent values of salt molalities (m). Error bars are estimated based on the standard deviation of 4 production blocks.

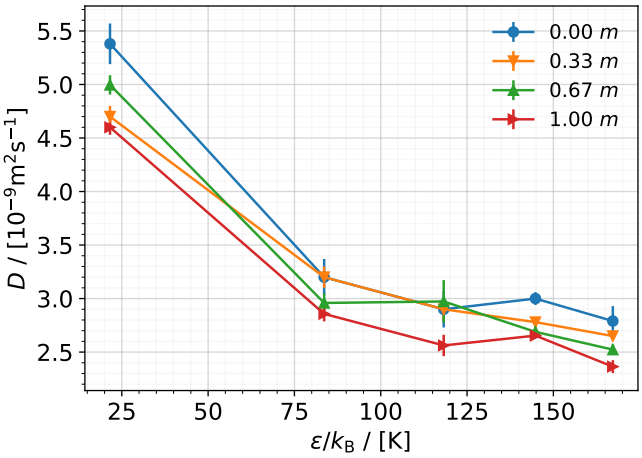

Figure 7.2: Self-diffusion coefficients of L-J particle in water as a function of ϵ/k_B for different salt concentrations at a σ value of 3.08 Å. The water model used is the TIP4P/2005 model [61]. Numbers in the legend represent values of salt molalities (m). Error bars are estimated based on the standard deviation of 4 production blocks.

7.3.2 Excess Chemical Potentials

The excess chemical potentials (μ^{ex}) as a function of function of particle size, σ, for different salt concentrations at a ϵ/k_B value of 118.24 K is shown in Figure 7.3. The corresponding numerical data is given in Tables E.13 - E.16 of Appendix E. μ^{ex} as a function of for different salt concentrations at a σ value of 3.08 Å is shown in Figure 7.4, the numerical data for which is given Tables E.13 - E.16 of Appendix E. In line with the observations from the previous chapter, μ^{ex} becomes increasingly positive with increasing values of σ, whereas it becomes less positive with increasing values of ϵ/k_B. In general, an increase in salt concentrations leads to an increase in the values of μ^{ex}. On average, across systems characterized by values of σ (2.83 Å - 3.58 Å) and ϵ/k_B (21.59 K - 167.22 K)), μ^{ex} increases by ca. 19% for an increase in molality of 1.00 m.

7.3.3 Henry coefficients

The Henry coefficients (H_s^{cp}) as a function of particle size, σ, for different salt concentrations at a ϵ/k_B value of 118.24 K are shown in Figure 7.5. The corresponding numerical data are listed in Tables E.17 - E.20 of Appendix E. H_s^{cp} as a function of ϵ/k_B for different salt concentrations at a σ value of 3.08 Å is

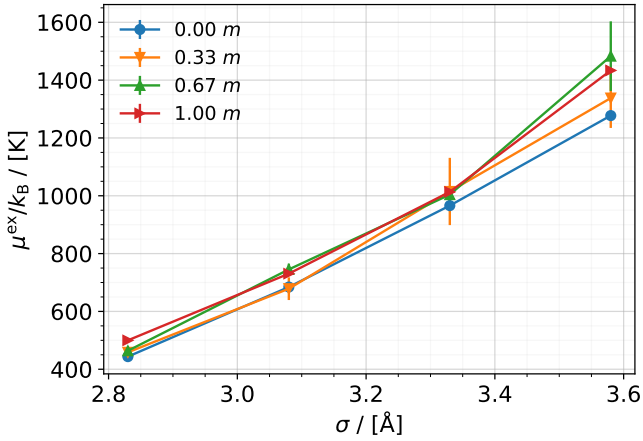

Figure 7.3: Excess chemical potentials of L-J particle as a function of σ for different salt concentrations at a ϵ/k_B value of 118.24 K. The water model used is the TIP4P/2005 model [61]. Numbers in the legend represent values of salt molalities (m). Error bars are estimated based on the standard deviation of 4 production blocks.

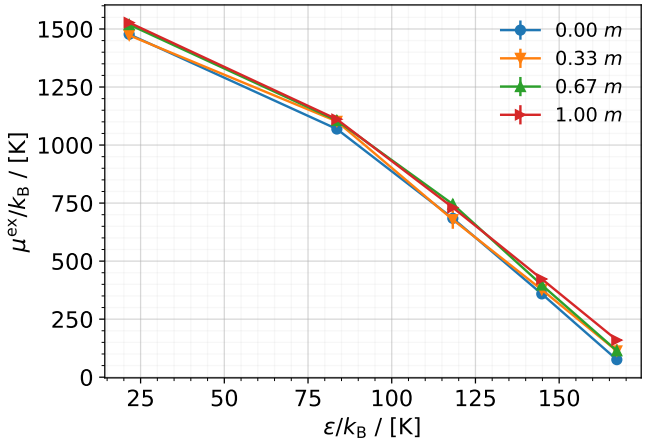

Figure 7.4: Excess chemical potentials of L-J particle as a function of ϵ/k_B for different salt concentrations at a σ value of 3.08 Å. The water model used is the TIP4P/2005 model [61]. Numbers in the legend represent values of salt molalities (m). Error bars are estimated based on the standard deviation of 4 production blocks.

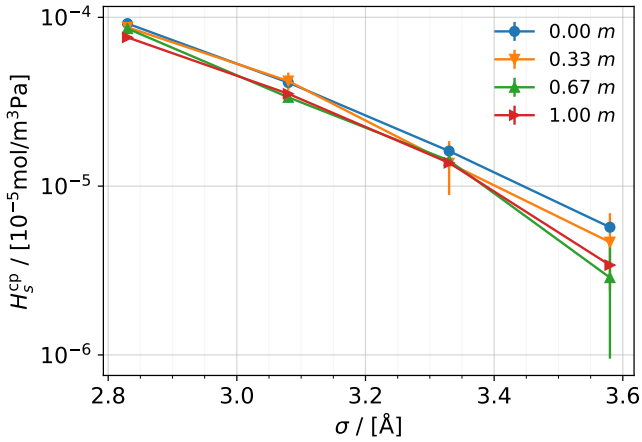

Figure 7.5: Henry coefficients of L-J particle in water as a function of σ for different salt concentrations at a ϵ/k_B value of 118.24 K in logarithmic scale. The water model used is the TIP4P/2005 model [61]. Numbers in the legend represent values of salt molalities (m). Error bars are estimated based on the standard deviation of 4 production blocks.

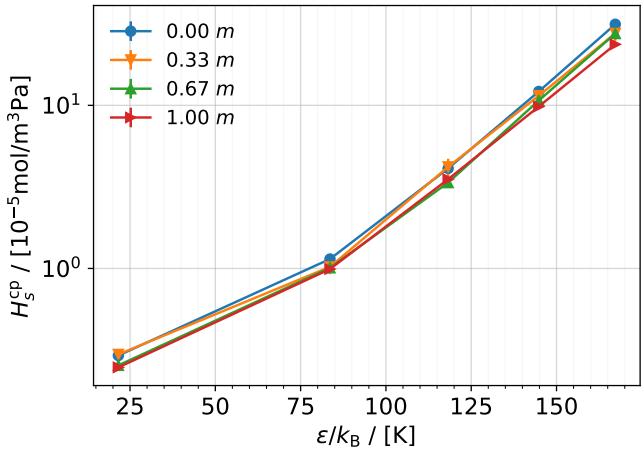

Figure 7.6: Henry coefficients of L-J particle in water as a function of ϵ/k_B for different salt concentrations at a σ value of 3.08 Å in logarithmic scale. The water model used is the TIP4P/2005 model [61]. Numbers in the legend represent values of salt molalities (m). Error bars are estimated based on the standard deviation of 4 production blocks.

shown in Figure 7.6, the numerical data for which is provided in Tables E.17 - E.20 of Appendix E. Consistent with the results in Chapter 6, H_s^{cp} decreases with increasing values of σ and increases with increasing values of ϵ/k_{B}. In general, an increase in salt concentrations leads to a decrease in the values of H_s^{cp}. On average, for systems characterized by varying values of σ (2.83 Å - 3.58 Å) and ϵ/k_{B} (21.59 K - 167.22 K)), H_s^{cp} decreases by ca. 22% for an increase in molality of 1.00 m. This is an indication of the salting-out effect, wherein the solubility of a solute decreases with increasing salt concentration in the aqueous phase [362].

7.4 Conclusions

We performed a systematic analysis to identify the influence of salt concentrations on D and H_s^{cp}. The values of D and H_s^{cp} were computed for a charge-neutral particle in water characterized by varying values of σ and ϵ/k_{B} at a temperature of 300 K and a pressure of 1 bar. We identified that D decreases with increasing salt concentrations (a ca. 12% decrease on average was observed for an increase in molality of 1.00 m). In contrast, μ^{ex} (which is required to compute H_s^{cp}), becomes increasingly positive with increase in salt concentration. On average, a ca. 19% increase in the values of μ^{ex} was observed for an increase in molality by 1.00 m. Consequently, an increase in salt concentrations leads to a decrease in the values of H_s^{cp} (ca. 22% decrease for a 1.00 m increase in salt concentration). This indicates a salting-out effect for the charge-neutral particles. These findings are key to understanding the effects of salt concentrations on the mass transport of reactive species from gas phase to liquid phase.

Conclusions and Outlook

In this thesis, the Henry coefficients and self-diffusion coefficients of reactive oxygen and nitrogen species were computed using the Continuous Fractional Component Monte Carlo and Molecular Dynamics techniques, respectively, in order to study the aqueous phase composition during plasma application. Additionally, the aqueous phase reactions were investigated using the CASpy solver, which is a chemical reaction equilibrium solver. We established a transferable methodology to characterize solvation and aqueous phase reactivity of the reactive oxygen and nitrogen species (RONS). The RONS were broadly classified based on their reactivity with water and the availability of an accurate force field to represent the species. In Chapter 3, the H_2O_2 molecule, which does not react with water to form new species and has accurate force fields available, is investigated. Nitric oxide, which does not react with water, but does not have an accurate all-atom force field, is analyzed in Chapter 4. In Chapter 5, the NO_2 radical is investigated, which reacts with water and has an accurate force field representing the species. Chapter 6 presents newly parameterized state-specific force fields for the interaction of atomic oxygen with water. In Chapter 7, the effect of solute particle size and interaction strength on the diffusion and Henry coefficients of the solute for varying salt concentrations is investigated.

We identified that TIP4P/2005 water force fields could predict the transport properties of water [363] and aqueous solutions of H_2O_2 in better agreement with experiments than the TIP3P water model. TIP3P, however, could predict the excess chemical potentials of water in better agreement with experimental values [68], compared to the TIP4P/2005 water model. The TIP5P-E water model was found to have anomalous interactions with the solute, increasing the viscosity of the aqueous H_2O_2 solutions and thereby decreasing the self-diffusion coefficients

of H_2O_2 and water in the aqueous H_2O_2 solutions.

During the development of a new force field for the reactive NO-$(NO)_2$ system, we found that the atomization energies play a crucial role in determining the dimer mole fractions and therefore the VLE properties of the system. However, there are large variations ($\sim$ 6 kJ/mol) in the values of bond (N-N) dissociation energies of $(NO)_2$ reported in the literature. This translates to a variation in the atomization energy of $(NO)_2$, which in turn significantly affect the VLE properties of the NO-$(NO)_2$ system. This highlights the need for an accurate computation of the quantum mechanical data of molecules to obtain an accurate description of the VLE properties. We also observed that the mole fraction of the dimer depended on the L-J parameters (σ and ϵ/k_B) of the species involved in the reactive system (in this case NO and $(NO)_2$). Increasing the values of the L-J parameters of a species was found to be energetically favorable for increasing the concentration of the species in the system. This could be attributed to an increase in intermolecular attraction, as indicated by the increase in the area of the L-J attractive potential with increasing values of L-J parameters.

The equilibrium of chemical reactions is strongly influenced by the atomization energies of the species involved. Varying the atomization energy of, for example, NO in reaction R4 of Chapter 5 led to a difference of 3.2 $\ln[K]$ points. This underscores the importance of accurately computing the quantum-chemical properties of the species to accurately predict chemical reaction equilibria. Another important quantum-chemical property is the electron affinity of the species. The electron affinity of NO_3 is used to calculate the atomization energy of NO_3^- (see Equation 5.18). Consequently, accurate computation of the electron affinities is essential for reliable prediction of chemical reaction equilibria.

With the newly determined values of the input parameters obtained in this work, it is essential to systematically evaluate their influence on the predictions of plasma–fluid models. The incorporation of updated Henry coefficients and transport coefficients may alter predicted species fluxes and interfacial mass-transfer, thereby affecting the aqueous-phase composition. For example, in Chapter 7 we identified a ca. 22 % decrease in the Henry coefficients with a 1.00 m increase in the salt concentration. However, such variations in Henry coefficients arising from changes in salt concentration are not accounted for in all plasma–liquid models. Therefore, a rigorous sensitivity analysis is required to quantify how variations in these parameters propagate through the coupled plasma–liquid modeling framework and influence key observables. More broadly, plasma–water interactions are governed by numerous interdependent operating and material parameters, including applied voltage, excitation frequency, gas identity and composition, pressure, temperature, and interfacial properties. Each of these factors will influence plasma chemistry, species generation, transport across the gas–liquid interface, solvation dynamics, and subsequent aqueous-phase reactions. A key question is whether it is possible to identify the dominant

parameters or combinations of parameters that have the largest influence on the resulting aqueous-phase composition. Addressing this challenge requires systematic sensitivity analysis and an uncertainty quantification framework. By incorporating sensitivity analysis and uncertainty quantification within the plasma–fluid modelling workflow, one can prioritize important parameters and enhance the robustness and reliability of predictions for application-specific plasma–liquid systems.

Summary

Non-thermal plasma (NTP) generated in air or O_2-N_2 mixtures with inert gases produces a cocktail of reactive oxygen and nitrogen species (RONS) that have applications in environmental remediation, biomedical engineering, and agriculture. For these diverse applications, the overarching objective is to enable end users to design plasma systems that deliver a targeted aqueous-phase chemical composition tailored to specific application requirements. Achieving this objective requires a comprehensive understanding of plasma–water interactions.

In this thesis, we focussed on establishing a simulation-based framework to characterize the solvation and aqueous-phase reactivity of plasma-generated RONS. In addition, we determined key input parameters, such as Henry coefficients (for solubility and mass transfer) and self-diffusion coefficients (for mass transport by diffusion), for RONS. These coefficients are essential for the accurate implementation of plasma–fluid models of plasma-water reactors. For RONS that undergo hydrolysis, the equilibrium of the chemical reactions was computed. We started with examining the predictive capability of the force fields available for H_2O_2, which is a RONS. Two force fields for H_2O_2 were available in the literature, those developed by Cordeiro (Biochimica et Biophysica Acta (BBA) - Biomembranes, 2014, 1838, 438-444) (Cordeiro FF) and Orabi & English (Journal of Chemical Theory and Computation, 2018, 14, 2808-2821) (Orabi FF). The predicted densities of anhydrous H_2O_2 using Orabi FF showed excellent agreement with the experimental values over the temperature range of 253 K to 353 K. The thermodynamic and transport properties of aqueous H_2O_2 solutions were computed. Four water force fields, namely, TIP3P, mTIP3P, TIP4P/2005, and TIP5P-E, were used to model water. The TIP4P/2005 water force field in combination with the Orabi FF provided the most accurate predictions of the properties of aqueous H_2O_2

solutions relative to the experimental values. The Cordeiro FF in combination with either the TIP3P or mTIP3P water force fields predicted the Henry coefficients of H_2O_2 within the range of experimental values. Another important RONS is nitric oxide (NO). However, there are no accurate all-atom force fields for NO. To develop a new force field for NO, we used the vapor-liquid-equilibrium (VLE) properties of this species. Since NO dimerizes at the VLE temperatures, we considered the reactive NO-$(NO)_2$ system. The new force field developed accurately reproduces the VLE properties of the reactive NO-$(NO)_2$ system (i.e., coexistence vapor-liquid densities, dimer mole fractions in liquid phase, saturated vapor pressures, and heats of vaporization) in excellent agreement with experimental values for the temperature range 120 K to 170 K. It was also observed that the VLE properties of the reactive NO-$(NO)_2$ system are affected by both the Lennard-Jones parameters (σ and ϵ/k_B) of NO and $(NO)_2$ and the atomization energy ($D_{0,(NO)_2}$) of the NO dimer. This behaviour is in sharp contrast to the NO_2-N_2O_4 system, where the bond dissociation energy of the dimer is much higher than that of $(NO)_2$ and therefore the VLE of NO_2-N_2O_4 is dominated by the isolated molecule partition function. We investigated the interaction of NO with water using the newly developed force field for NO, the Saji FF. The values of self-diffusion coefficients (D) and Henry coefficients (H_s^{cp}) were in agreement with experimental values. We also examined the interaction of NO_2 with water. From literature, it was observed that NO_2 upon hydrolysis forms nitrous and nitric acids. Subsequently, nitrous acid undergoes ionization and disproportionation reactions. To study the different reactions, we modified the CASpy solver (Journal of Chemical Theory and Computation, 2023, 19, 2616–2629), a chemical reaction equilibrium solver, to handle arbitrary constraints in chemical reaction equilibria. We calculated the gas phase composition of NO_2 and its dimer, N_2O_4, as a function of pressure and temperature and found that the concentration of N_2O_4 in the gas phase increases with increasing pressure and decreases with increasing temperature. The hydrolysis of NO_2 was found to be an exothermic reaction, and the pH of the system decreases with increasing pressure and increases with increasing temperature. We parameterized state-specific force fields for the interaction of atomic oxygen with water on the triplet and singlet energy surfaces. Using these new force fields, we computed the self-diffusion and Henry coefficients for the temperature range of 273 - 333 K. It was observed that on the triplet energy surfaces, the ground state yielded the highest values of D and H_s^{cp}, while on the singlet energy surfaces, the first excited state exhibited the highest values. From a systematic study on the influence of individual L-J parameters (σ and ϵ/k_B) on D and H_s^{cp}, we found that the self-diffusion coefficients are governed by the particle size (σ), while the Henry coefficients are influenced more by the strength of the interaction with water (ϵ/k_B). The results presented here represent a significant step toward understanding the aqueous-phase chemistry occurring during plasma application, achieved by computing the mass-transfer and transport coefficients,

as well as the equilibrium constants of the chemical reactions involving RONS in the liquid phase.

Samenvatting

Niet-thermisch plasma (NTP) dat wordt gegenereerd in lucht of in mengsels van O_2 en N_2 met inerte gassen, produceert een mix van reactieve zuurstof- en stikstofverbindingen (RONS) die toepassingen vinden in milieusanering, biomedische techniek en landbouw. Voor deze uiteenlopende toepassingen is het overkoepelende doel om eindgebruikers in staat te stellen plasmasystemen te ontwerpen die een gerichte chemische samenstelling in de waterfase opleveren, afgestemd op de specifieke eisen van de toepassing. Om deze doelstelling te bereiken is een grondig begrip van de interacties tussen plasma en water vereist.

In dit proefschrift hebben we ons gericht op het opzetten van een op simulatie gebaseerd raamwerk om de solvatatie en de reactiviteit in de waterfase van door plasma gegenereerde RONS te karakteriseren. Daarnaast hebben we belangrijke invoerparameters voor RONS bepaald, zoals Henry-coëfficiënten (voor oplosbaarheid en massaoverdracht) en zelfdiffusiecoëfficiënten (voor massatransport door diffusie). Deze coëfficiënten zijn essentieel voor de nauwkeurige implementatie van plasma-vloeistofmodellen van plasma-waterreactoren. Voor RONS die hydrolyse ondergaan, werd het evenwicht van de chemische reacties berekend. We zijn begonnen met het onderzoeken van het voorspellend vermogen van de krachtvelden die beschikbaar zijn voor H_2O_2, een RONS. In de literatuur waren twee krachtvelden voor H_2O_2 beschikbaar, namelijk die ontwikkeld door Cordeiro (Biochimica et Biophysica Acta (BBA) - Biomembranes, 2014, 1838, 438-444) (Cordeiro FF) en Orabi English (Journal of Chemical Theory and Computation, 2018, 14, 2808-2821) (Orabi FF). De voorspelde dichtheden van watervrij H_2O_2 met behulp van Orabi FF kwamen uitstekend overeen met de experimentele waarden over het temperatuurbereik van 253 K tot 353 K. De thermodynamische en

transporteigenschappen van waterige H_2O_2-oplossingen werden berekend. Voor het modelleren van water werden vier waterkrachtvelden gebruikt, namelijk TIP3P, mTIP3P, TIP4P/2005 en TIP5P-E. Het TIP4P/2005-waterkrachtveld leverde in combinatie met de Orabi FF de meest nauwkeurige voorspellingen op van de eigenschappen van waterige H_2O_2-oplossingen ten opzichte van de experimentele waarden. De Cordeiro FF voorspelde in combinatie met het TIP3P- of het mTIP3P-waterkrachtveld de Henry-coëfficiënten van H_2O_2 binnen het bereik van de experimentele waarden. Een andere belangrijke RONS is stikstofmonoxide (NO). Er bestaan echter geen nauwkeurige all-atom-krachtvelden voor NO. Om een nieuw krachtveld voor NO te ontwikkelen, hebben we gebruikgemaakt van de damp-vloeistof-evenwichtseigenschappen (VLE) van deze stof. Aangezien NO bij de VLE-temperaturen dimeriseert, hebben we het reactieve NO-$(NO)_2$-systeem in aanmerking genomen. Het nieuw ontwikkelde krachtveld geeft de VLE-eigenschappen van het reactieve NO-$(NO)_2$-systeem (d.w.z. coëxistentiedichtheden van damp en vloeistof, molfracties van dimeren in de vloeibare fase, verzadigde dampdrukken en verdampingswarmten) nauwkeurig weer, in uitstekende overeenstemming met experimentele waarden voor het temperatuurbereik van 120 K tot 170 K. Er werd ook waargenomen dat de VLE-eigenschappen van het reactieve NO-$(NO)_2$-systeem worden beïnvloed door zowel de Lennard-Jones-parameters (σ en ϵ/k_B) van NO als van $(NO)_2$ en de atomisatie-energie ($D_{0,(NO)_2}$) van het NO-dimeer. Dit gedrag staat in schril contrast met het NO_2-N_2O_4-systeem, waar de bindingsdissociatie-energie van het dimeer veel hoger is dan die van $(NO)_2$ en de VLE van NO_2-N_2O_4 daarom wordt gedomineerd door de partitie-functie van het geïsoleerde molecuul. We hebben de interactie van NO met water onderzocht met behulp van het nieuw ontwikkelde krachtveld voor NO, het Saji FF. De waarden van de zelfdiffusiecoëfficiënten (D) en Henry-coëfficiënten (H_s^{cp}) kwamen overeen met de experimentele waarden. We hebben ook de interactie van NO_2 met water onderzocht. Uit de literatuur bleek dat NO_2 bij hydrolyse salpeterigzuur en salpeterzuur vormt. Vervolgens ondergaat salpeterigzuur ionisatie- en disproportioneringsreacties. Om de verschillende reacties te bestuderen, hebben we de CASpy-solver (Journal of Chemical Theory and Computation, 2023, 19, 2616–2629), een solver voor chemische reactie-evenwichten, aangepast om willekeurige beperkingen in chemische reactie-evenwichten te kunnen verwerken. We hebben de samenstelling in de gasfase van NO_2 en zijn dimeer, N_2O_4, berekend als functie van druk en temperatuur en vastgesteld dat de concentratie van N_2O_4 in de gasfase toeneemt bij stijgende druk en afneemt bij stijgende temperatuur. De hydrolyse van NO_2 bleek een exotherme reactie te zijn, en de pH van het systeem daalt bij toenemende druk en stijgt bij toenemende temperatuur. We hebben toestandsspecifieke krachtvelden geparametriseerd voor de interactie tussen atomair zuurstof en water op de triplet- en singlet-energieoppervlakken. Met behulp van deze nieuwe krachtvelden hebben we de zelfdiffusie- en Henry-coëfficiënten berekend voor

het temperatuurbereik van 273 - 333 K. Er werd waargenomen dat op de triplet-energieoppervlakken de grondtoestand de hoogste waarden van D en H_s^{cp} opleverde, terwijl op de singlet-energieoppervlakken de eerste aangeslagen toestand de hoogste waarden vertoonde. Uit een systematische studie naar de invloed van afzonderlijke L-J-parameters (σ en ϵ/k_{B}) op D en H_s^{cp}, hebben we vastgesteld dat de zelfdiffusiecoëfficiënten worden bepaald door de deeltjesgrootte (σ), terwijl de Henry-coëfficiënten meer worden beïnvloed door de sterkte van de interactie met water (ϵ/k_{B}). De hier gepresenteerde resultaten vormen een belangrijke stap in de richting van een beter begrip van de chemie in de waterfase die plaatsvindt tijdens plasmatoepassing, verkregen door de berekening van de massaoverdrachts- en transportcoëfficiënten, evenals de evenwichtsconstanten van de chemische reacties waarbij RONS in de vloeibare fase betrokken zijn.

Appendix A- Supporting data for Chapter 3

A

Table A.1: Parameters of potential energy functions corresponding to bond-stretching, bond-bending, torsional, van der Waals and electrostatic energies developed by Cordeiro [73] for H_2O_2.

Parameter	Functional form	Units	Value
b_{OH}	$\frac{1}{4}k_b(b^2 - {b_0}^2)^2$	[nm]	0.0981
$k_{\mathrm{b(OH)}}$	$\frac{1}{4}k_b(b^2 - {b_0}^2)^2$	[kJ/mol/nm^4]	2.306×10^7
b_{OO}	$\frac{1}{4}k_b(b^2 - {b_0}^2)^2$	[nm]	0.1443
$k_{\mathrm{b(OO)}}$	$\frac{1}{4}k_b(b^2 - {b_0}^2)^2$	[kJ/mol/nm^4]	6.47×10^6
θ_{HOO}	$\frac{1}{2}k_\theta(\cos\theta - \cos\theta_0)^2$	[deg]	100.36
$k_{\theta\mathrm{(HOO)}}$	$\frac{1}{2}k_\theta(\cos\theta - \cos\theta_0)^2$	[kJ/mol/deg^2]	524.48
C_0	$\sum_{n=0}^{5} C_n(\cos\psi)^n$	–	1.995
C_1	$\sum_{n=0}^{5} C_n(\cos\psi)^n$	–	-10.727
C_2	$\sum_{n=0}^{5} C_n(\cos\psi)^n$	–	15.226
C_3	$\sum_{n=0}^{5} C_n(\cos\psi)^n$	–	-2.244
C_4	$\sum_{n=0}^{5} C_n(\cos\psi)^n$	–	0.258
C_5	$\sum_{n=0}^{5} C_n(\cos\psi)^n$	–	0.000
ϵ_{O}	$4\epsilon_{ij}[(\frac{\sigma_{ij}}{r_{ij}})^{12} - (\frac{\sigma_{ij}}{r_{ij}})^6]$	[kJ/mol]	0.743
σ_{O}	$4\epsilon_{ij}[(\frac{\sigma_{ij}}{r_{ij}})^{12} - (\frac{\sigma_{ij}}{r_{ij}})^6]$	[nm]	0.303
ϵ_{H}	$4\epsilon_{ij}[(\frac{\sigma_{ij}}{r_{ij}})^{12} - (\frac{\sigma_{ij}}{r_{ij}})^6]$	[kJ/mol]	0.000
σ_{H}	$4\epsilon_{ij}[(\frac{\sigma_{ij}}{r_{ij}})^{12} - (\frac{\sigma_{ij}}{r_{ij}})^6]$	[nm]	0.000
q_{O}	$\frac{1}{4\pi\epsilon_o}\frac{q_iq_j}{r_{ij}}$	[e]	-0.42
q_{H}	$\frac{1}{4\pi\epsilon_o}\frac{q_iq_j}{r_{ij}}$	[e]	0.42

Table A.2: Parameters of potential energy functions corresponding to the bond-stretching, bond-bending, torsional, van der Waals, and electrostatic energies developed by Orabi & English [74] for H_2O_2.

Parameter	Functional form	Units	Value
b_{OH}	$\frac{1}{2}k_b(b-b_0)^2$	[nm]	0.0963
$k_{\mathrm{b(OH)}}$	$\frac{1}{2}k_b(b-b_0)^2$	[kJ/mol/nm^2]	435973
b_{OO}	$\frac{1}{2}k_b(b-b_0)^2$	[nm]	0.1442
$k_{\mathrm{b(OO)}}$	$\frac{1}{2}k_b(b-b_0)^2$	[kJ/mol/nm^2]	238906
θ_{HOO}	$\frac{1}{2}k_\theta(\theta-\theta_0)^2$	[deg]	99.92
$k_{\theta\mathrm{(HOO)}}$	$\frac{1}{2}k_\theta(\theta-\theta_0)^2$	[kJ/mol/rad^2]	505.426
δ	$k_\phi(1+\cos 2\phi-\delta)$	[deg]	0.0
$k_{\phi\mathrm{(HOOH)}}$	$k_\phi(1+\cos 2\phi-\delta)$	[kJ/mol]	8.452
ϵ_{O}	$4\epsilon_{ij}[(\frac{\sigma_{ij}}{r_{ij}})^{12}-(\frac{\sigma_{ij}}{r_{ij}})^{6}]$	[kJ/mol]	0.853
σ_{O}	$4\epsilon_{ij}[(\frac{\sigma_{ij}}{r_{ij}})^{12}-(\frac{\sigma_{ij}}{r_{ij}})^{6}]$	[nm]	0.298
ϵ_{H}	$4\epsilon_{ij}[(\frac{\sigma_{ij}}{r_{ij}})^{12}-(\frac{\sigma_{ij}}{r_{ij}})^{6}]$	[kJ/mol]	0.192
σ_{H}	$4\epsilon_{ij}[(\frac{\sigma_{ij}}{r_{ij}})^{12}-(\frac{\sigma_{ij}}{r_{ij}})^{6}]$	[nm]	0.039
q_{O}	$\frac{1}{4\pi\epsilon_o}\frac{q_iq_j}{r_{ij}}$	[e]	-0.41
q_{H}	$\frac{1}{4\pi\epsilon_o}\frac{q_iq_j}{r_{ij}}$	[e]	0.41

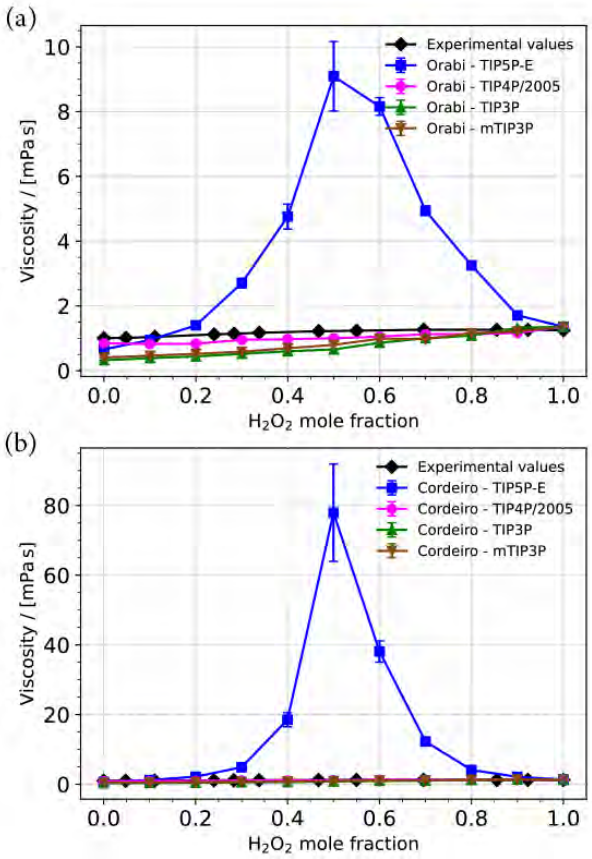

Figure A.1: Viscosities of aqueous H_2O_2 solutions for various mole fractions of H_2O_2 at 293 K and 1 bar for the (a) Orabi [74] and (b) Cordeiro [73] force fields in combination with the TIP3P [60], mTIP3P [75], TIP4P/2005 [61] and TIP5P-E [62, 63] force fields for water. Error bars are estimated based on the standard deviation. The experimental values [150] at 293 K and 1 bar are added for comparison.

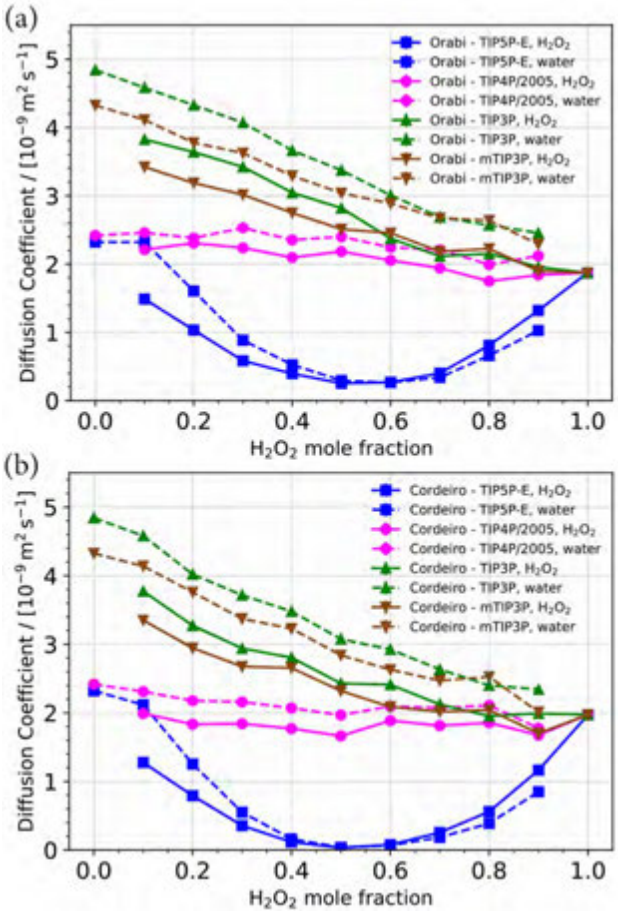

Figure A.2: Self-diffusion coefficients of water molecules and H_2O_2 molecules in aqueous solutions of H_2O_2 for different mole fractions of H_2O_2 at 298 K using the (a) Orabi [74] and (b) Cordeiro [73] force fields in combination with the TIP3P [60], mTIP3P [75], TIP4P/2005 [61] and TIP5P-E [62, 63] water force fields. Error bars are estimated based on the standard deviation and are much smaller than the symbols used in the figure.

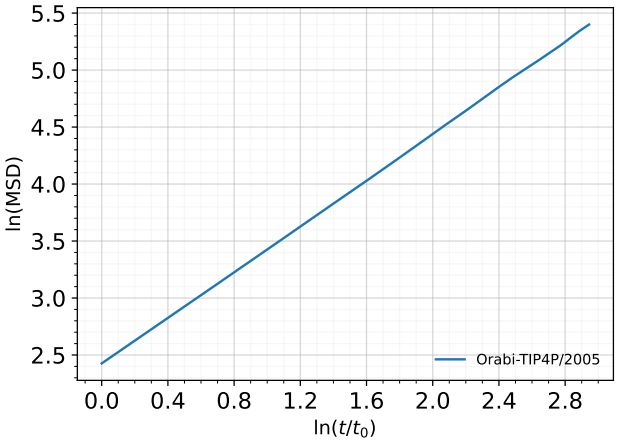

Figure A.3: Natural logarithm of the dimensionless mean square displacement (ln(MSD)) versus $\ln(t/t_0)$ (t stands for time and $t_0 = 1$ ns) for H_2O_2 in H_2O_2 aqueous solution for a H_2O_2 mole fraction of 0.5 using the Orabi - TIP4P/2005 force field combination. The simulation was run for 20 ns in the NVT ensemble from which 1 ns to 20 ns trajectory was used for calculating the self-diffusion coefficients.

Table A.3: The number of water molecules in the micro solvation shells of H_2O_2 in aqueous solutions for H_2O_2 mole fractions of 0.1, 0.5 and 0.9 for the Orabi and Cordeiro force fields in combination with the TIP4P/2005 [61], TIP5P-E [62, 63], TIP3P [60, 75] and mTIP3P [75] water force fields. The results are calculated by integrating the RDF for O_p - O_w up to the first minimum ($r_{\min,x}$), where x is the mole fraction of H_2O_2 in the system.

Model	0.1	$r_{\min,0.1}$/[nm]	0.5	$r_{\min,0.5}$/[nm]	0.9	$r_{\min,0.9}$/[nm]
Orabi - TIP4P/2005	2	0.31	1.26	0.31	0.25	0.31
Orabi - TIP5P-E	1.04	0.28	0.88	0.28	0.12	0.28
Orabi - TIP3P	2.09	0.31	1.17	0.31	0.24	0.31
Orabi - mTIP3P	2.49	0.31	1.39	0.32	0.29	0.32
Cordeiro - TIP4P/2005	1.77	0.3	1.15	0.31	0.23	0.31
Cordeiro - TIP5P-E	1.05	0.27	0.86	0.27	0.12	0.27
Cordeiro - TIP3P	2.17	0.31	1.06	0.3	0.24	0.31
Cordeiro - mTIP3P	2.26	0.31	0.98	0.3	0.22	0.31

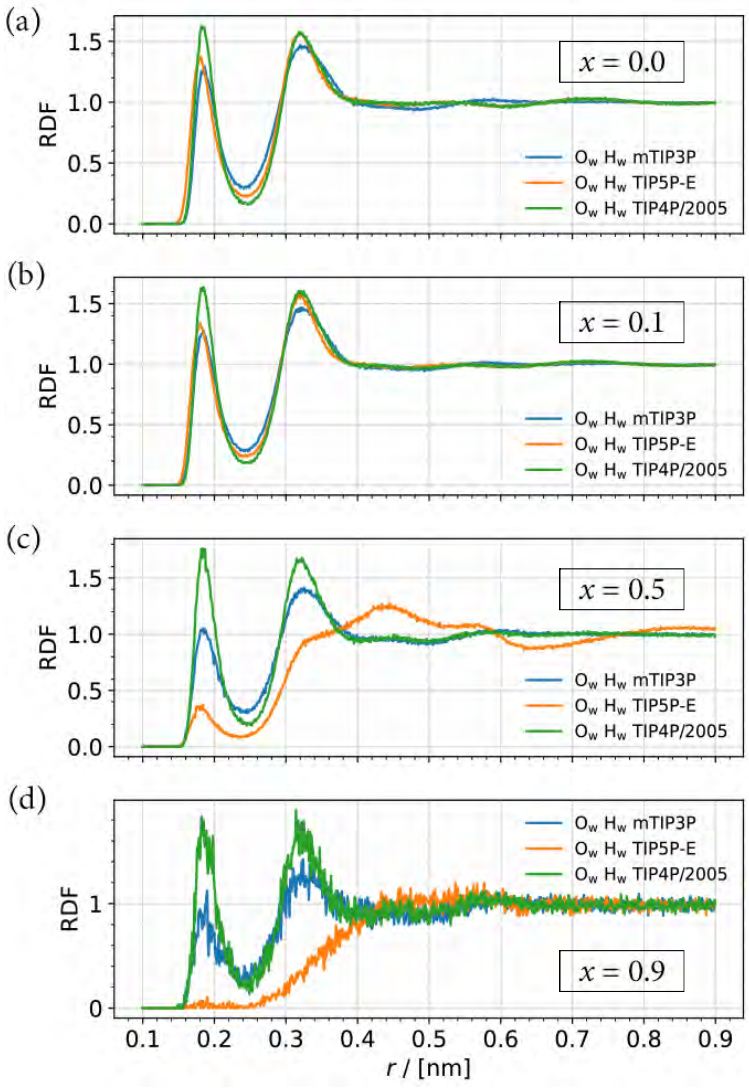

Figure A.4: Radial distribution functions (RDFs) as a function of radial distance, r [nm], for O_w (O of water) - H_w (H of water) for H_2O_2 aqueous solutions with $x = 0.1$ (b), $x = 0.5$ (c), and $x = 0.9$ (d), where x is the mole fraction of H_2O_2, at 298 K and 1 bar using the Cordeiro [73] force field in combination with the mTIP3P [75], TIP5P-E [62, 63], and TIP4P/2005 [61] water force fields. The RDF for pure water is plotted in (a).

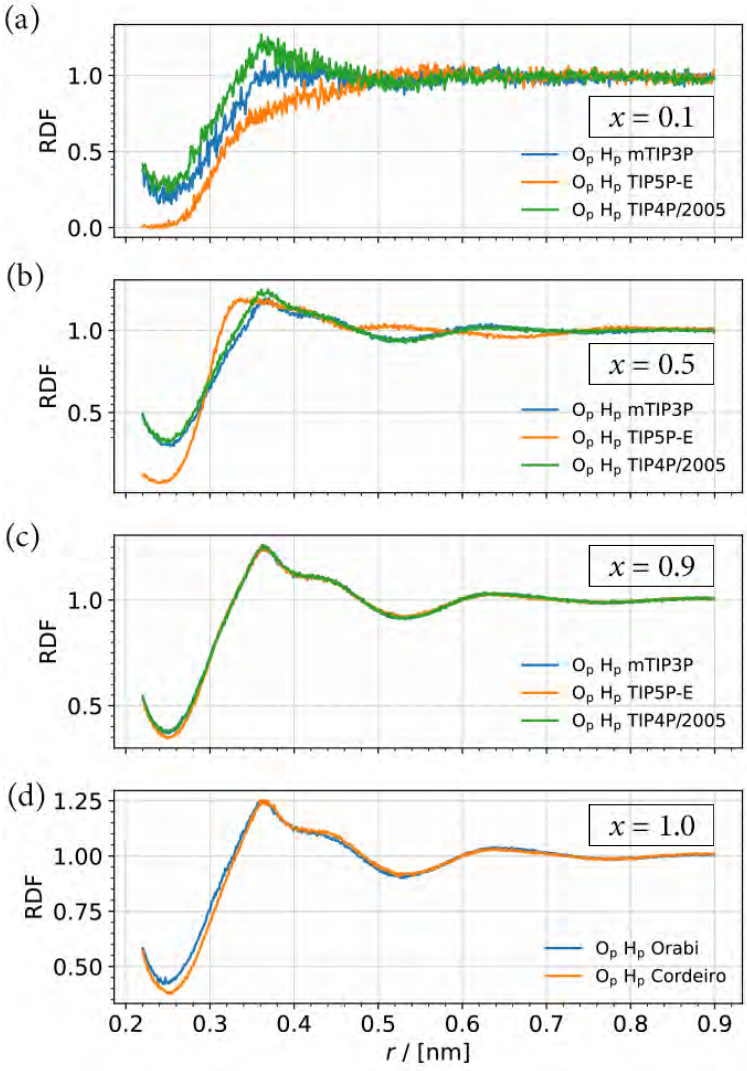

Figure A.5: Radial distribution functions (RDFs) as a function of radial distance, r [nm], for O_p (O of H_2O_2) - H_p (H of H_2O_2) for H_2O_2 aqueous solutions with $x = 0.1$ (b), $x = 0.5$ (c), and $x = 0.9$ (d), where x is the mole fraction of H_2O_2, at 298 K and 1 bar using the Cordeiro [73] force field in combination with the mTIP3P [75], TIP5P-E [62, 63], and TIP4P/2005 [61] water force fields. The first peak (at ca. 0.19 nm) was removed to distinguish the differences between the combinations clearly. The RDF for pure H_2O_2 is plotted in (d) using the Orabi force field and the Cordeiro force field.

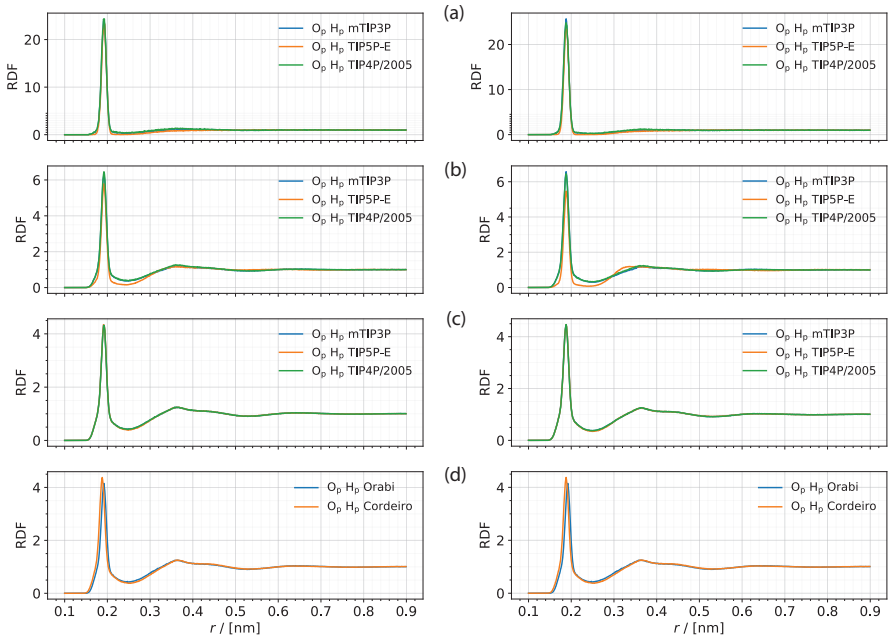

Figure A.6: Radial distribution functions (RDFs) as a function of radial distance, r [nm], for O_p (O of H_2O_2) - H_p (H of H_2O_2) for H_2O_2 aqueous solutions with $x = 0.1$ (a), $x = 0.5$ (b), and $x = 0.9$ (c), where x is the mole fraction of H_2O_2, at 298 K and 1 bar using the Orabi [74] (left) and Cordeiro [73] (right) force fields in combination with the mTIP3P [75], TIP5P-E [62, 63], and TIP4P/2005 [61] water force fields. The RDF for pure H_2O_2 is plotted in (d) using the Cordeiro force field and the Orabi force field.

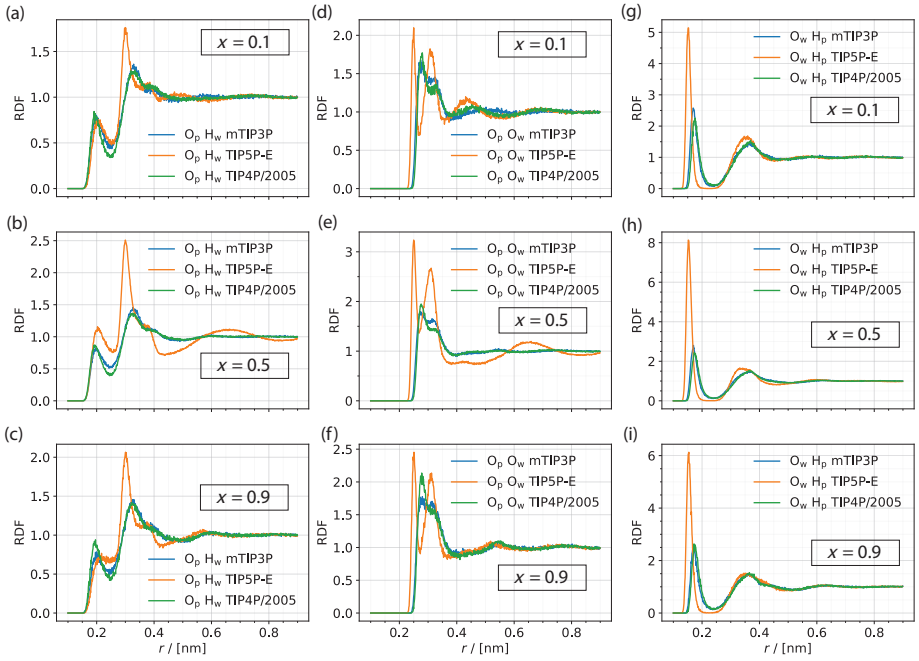

Figure A.7: Radial distribution functions (RDFs) as a function of radial distance, r [nm], for O_p (O of H_2O_2) and H_w (H of water) (a - c), O_w (O of water) and O_p (O of H_2O_2) (d - f), and O_w (O of water) and H_p (H of H_2O_2) (g - i) for systems using the mTIP3P [75], TIP5P-E [62, 63], and TIP4P/2005 [61] water force fields in combination with the Cordeiro [73] force field for $x = 0.1$, $x = 0.5$, and $x = 0.9$ at 298 K and 1 bar, where x is the mole fraction of H_2O_2.

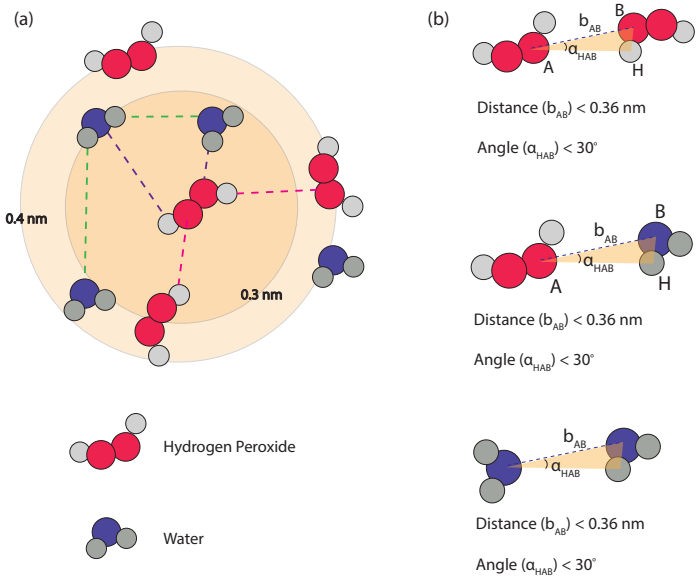

Figure A.8: (a) Schematic representation of the hydrogen bonding around a H_2O_2 molecule in a 0.5 mole fraction Orabi-TIP4P/2005 system. The micro solvation shell and the first solvation shell for a H_2O_2 are shown. See Table A.3 and Table A.4 for the radius where the micro solvation shell ($r_{\min,0.5} = 0.31\,\text{nm}$) and first solvation shell ($r_{\min,0.5} = 0.4\,\text{nm}$) are defined. Hydrogen bonding between two H_2O_2 molecules is represented with red dashed lines, while the hydrogen bonding between a H_2O_2 and a water molecule is shown with a blue dashed line. Green dashed lines represent hydrogen bonding between two water molecules. The number of hydrogen bonds per H_2O_2 molecule for a 0.5 mole fraction Orabi-TIP4P/2005 system is ca. 6, as seen in Figure 3.9. (b) The geometric criterion used for identifying hydrogen bonding between H_2O_2 - H_2O_2, H_2O_2 - water and water - water.

Table A.4: The number of water molecules in the first solvation shells of H_2O_2 in aqueous solutions for H_2O_2 mole fractions of 0.1, 0.5 and 0.9 for the Orabi and Cordeiro force fields in combination with the TIP4P/2005 [61], TIP5P-E [62, 63], TIP3P [60, 75] and mTIP3P [75] water force fields. The results are calculated by integrating the RDF for O_p - O_w up to the second minimum ($r_{\min,x}$), where x is the mole fraction of H_2O_2 in the system.

Model	0.1	$r_{\min,0.1}$/[nm]	0.5	$r_{\min,0.5}$/[nm]	0.9	$r_{\min,0.9}$/[nm]
Orabi - TIP4P/2005	6.9	0.4	3.28	0.4	0.62	0.39
Orabi - TIP5P-E	5.89	0.38	4.24	0.39	0.58	0.37
Orabi - TIP3P	6.37	0.39	3.67	0.4	0.66	0.4
Orabi - mTIP3P	6.82	0.39	3.53	0.39	0.72	0.41
Cordeiro - TIP4P/2005	5.6	0.38	3.21	0.39	0.71	0.41
Cordeiro - TIP5P-E	5.07	0.36	4.32	0.38	0.55	0.37
Cordeiro - TIP3P	5.56	0.38	3.55	0.4	0.73	0.42
Cordeiro - mTIP3P	5.55	0.38	3.59	0.4	0.68	0.4

Appendix B- Supporting data for Chapter 4

Table B.1: Experimental values for structural properties of NO and $(NO)_2$ [207, 208].

Structural properties	Experimental [207, 208]
NO	
r(NO)/Å	1.151
$(NO)_2$	
r(NN)/Å	2.263
r(NO)/Å	1.152
$\angle$ ONO/°	97.120

B

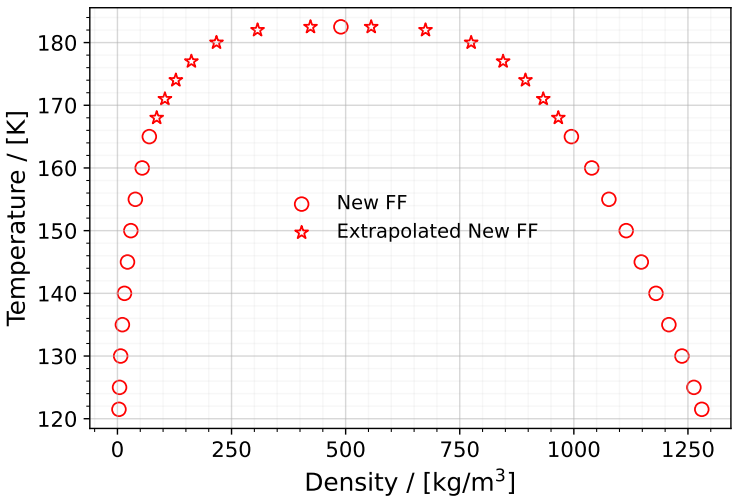

Figure B.1: Vapor-liquid coexistence densities (see Table 4.2) of the reactive NO-$(NO)_2$ system predicted using the New FF as a function of temperature (red circles). The extrapolated vapor-liquid coexistence densities obtained by fitting the liquid and vapor phase densities to the law of rectilinear diameters (Equations 4.6 and 4.7) are also shown (red stars). The coexistence temperature is also listed in Table 4.2.

Table B.2: Experimental vibrational frequencies of NO and $(NO)_2$ [208, 255, 364].

Vibrational frequencies/[cm^{-1}]	Experimental [208, 255, 364]
NO	
ν_1	1904.2
$(NO)_2$	
ν_1	1868
ν_2	239
ν_3	135
ν_4	117
ν_5	1789
ν_6	429

Table B.3: Experimental rotational constants of NO and $(NO)_2$ [365].

Rotational constants/[cm^{-1}]	Experimental [365]
NO	
B	1.67195
$(NO)_2$	
A	0.86159
B	0.18728
C	0.15363

Table B.4: $\ln(\frac{qV_0}{\Lambda^3})$ of NO and $(NO)_2$ as a function of temperature.

Temperature /[K]	$\ln(\frac{qV_0}{\Lambda^3})_{NO}$/[-]	$\ln(\frac{qV_0}{\Lambda^3})_{(NO)_2}$/[-]
121.5	631.82	1270.67
125	614.44	1235.59
130	591.23	1188.80
135	569.75	1145.50
140	549.79	1105.25
145	531.23	1067.84
150	513.89	1032.86
155	497.68	1000.20
160	482.49	969.55
165	468.19	940.76

Table B.5: Coexistence densities of the reactive NO-$(NO)_2$ system as a function of temperature, computed using the New FF (see Table 4.1). Experimental liquid densities [253] are listed for comparison. The subscripts show the standard deviations computed from the results of the 5 independent production runs.

Temperature /[K]	ρ_{gas} /[kg/m^3]	ρ_{liquid} /[kg/m^3]	$\rho_{liquid\text{-}Expt.}$ /[kg/m^3]
121.5	$3.31_{0.1}$	$1280.30_{1.0}$	1280.27
125	$4.61_{0.1}$	$1263.04_{0.8}$	1263.23
130	$7.04_{0.2}$	$1236.86_{0.6}$	1237.83
135	$10.84_{0.1}$	$1208.25_{0.9}$	1211.01
140	$15.40_{0.1}$	$1179.97_{1.0}$	1182.50
145	$22.01_{0.4}$	$1147.75_{0.7}$	1151.92
150	$29.36_{0.5}$	$1114.70_{1.4}$	1118.78
155	$39.22_{0.6}$	$1076.79_{0.7}$	1082.32
160	$54.20_{0.6}$	$1039.23_{1.5}$	1041.36
165	$69.85_{1.2}$	$994.66_{0.4}$	993.86

Table B.6: $(NO)_2$ mole fractions (χ) in gas and liquid of the reactive NO-$(NO)_2$ system as a function of temperature, computed using the New FF (see Table 4.1). The errors are within 1% of the reported values. Experimental $(NO)_2$ mole fractions [224, 225] are listed for comparison. Note that the experimental data for 110 K and 115 K are obtained from Smith & Johnston [225]. Data from 121.5 K to 165 K are extrapolated values obtained from Refs. [224, 252] using the WebPlotDigitizer tool [366].

Temperature /[K]	$\chi_{(NO)_2\,\text{gas}}$	$\chi_{(NO)_2\,\text{liquid}}$	$\chi_{(NO)_2\,\text{liquid-Expt.}}$
110	0.05	0.92	0.95
115	0.06	0.89	—
121.5	0.06	0.86	—
125	0.06	0.83	—
130	0.07	0.80	0.85
135	0.07	0.75	—
140	0.07	0.72	0.76
145	0.07	0.67	—
150	0.08	0.63	0.65
155	0.08	0.58	—
160	0.08	0.53	0.53
165	0.08	0.48	—

Table B.7: Saturated vapor pressures of the reactive NO-$(NO)_2$ system computed using the New FF (see Table 4.1). The standard deviations are given as subscripts. Experimental values [253] are listed for comparison.

Temperature /[K]	P_{sat} /[MPa]	$P_{\text{sat-Expt.}}$ /[MPa]
121.5	$0.09_{0.01}$	0.10
125	$0.13_{0.01}$	—
130	$0.22_{0.009}$	0.26
135	$0.35_{0.02}$	—
140	$0.54_{0.02}$	0.59
145	$0.79_{0.02}$	—
150	$1.12_{0.01}$	1.35
155	$1.51_{0.02}$	—
160	$2.00_{0.03}$	2.60
165	$2.65_{0.04}$	—

Table B.8: Average number of NO (N_{NO}) and $(NO)_2$ ($N_{(NO)_2}$) molecules and volumes (V) in the vapor and liquid simulation boxes of the reactive NO-$(NO)_2$ system computed at different temperatures using the New FF. The standard deviations are given in subscripts.

T/[K]	$N_{\mathrm{NO,\ liquid}}$	$N_{(NO)_2,\ \mathrm{liquid}}$	$N_{\mathrm{NO,\ vapor}}$	$N_{(NO)_2,\ \mathrm{vapor}}$	V_{liquid}/[Å^3]	V_{vapor}/[Å^3]
121.5	55_2	334_1	$3.6_{0.1}$	$0.23_{0.02}$	28264_{18}	63408_{18}
125	65_1	$328.4_{0.8}$	$5.1_{0.1}$	$0.34_{0.02}$	28590_{15}	63083_{15}
130	82_1	$318.7_{0.8}$	$7.7_{0.2}$	$0.54_{0.03}$	29084_{10}	62589_{10}
135	94_1	$288.4_{0.7}$	$3.93_{0.08}$	$0.30_{0.01}$	27755_{18}	21094_{18}
140	110_1	$279.5_{0.7}$	$5.36_{0.09}$	$0.41_{0.02}$	28349_{21}	20499_{21}
145	$131.4_{0.9}$	$267.5_{0.5}$	$7.4_{0.1}$	$0.59_{0.02}$	29043_{10}	19806_{10}
150	151_2	$254.8_{0.9}$	$12.8_{0.1}$	$1.03_{0.02}$	29629_{35}	25739_{35}
155	$168.9_{0.7}$	$230.9_{0.4}$	$20.8_{0.3}$	$1.73_{0.05}$	29297_{26}	31259_{26}
160	201_1	$227.7_{0.8}$	$15.6_{0.2}$	$1.39_{0.03}$	31615_{30}	17234_{30}
165	$241.5_{0.9}$	$223.3_{0.6}$	$27.0_{0.3}$	$2.46_{0.06}$	34580_{13}	23010_{13}

Table B.9: Force field parameters developed for the NO molecule by Zhou *et al.* [77] (Zhou FF) and Lachet *et al.* [76] (Lachet FF).

	Species	ϵ/[K]	σ/[Å]	q/[e]
Zhou FF	N	79.50	3.014	0.0288
	O	96.94	2.875	−0.0288
Lachet FF	NO	130.00	3.40	–

B

Table B.10: Critical temperatures (T_c), densities (ρ_c), and pressures (P_c) for pure NO and pure $(NO)_2$ computed using our newly developed force field (New FF) as well as the force fields developed by Zhou *et al.* [77] and Lachet *et al.* [76].

NO	T_c/[K]	ρ_c/[kg/m^3]	P_c/[MPa]
New FF	167.34	414.82	5.49
Zhou FF	277.15	427.23	8.66
Lachet FF	168.20	400.27	5.31

$(NO)_2$	T_c/[K]	ρ_c/[kg/m^3]	P_c/[MPa]
New FF	243.78	454.28	4.51
Lachet FF	298.37	449.95	5.31

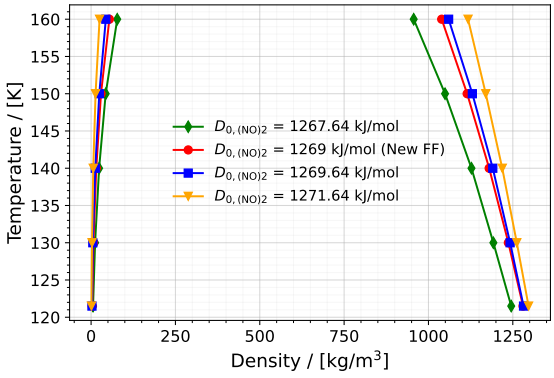

Figure B.2: Vapor-liquid coexistence densities of the reactive NO-$(NO)_2$ system for various values of $D_{0,(NO)_2}$ using the New FF.

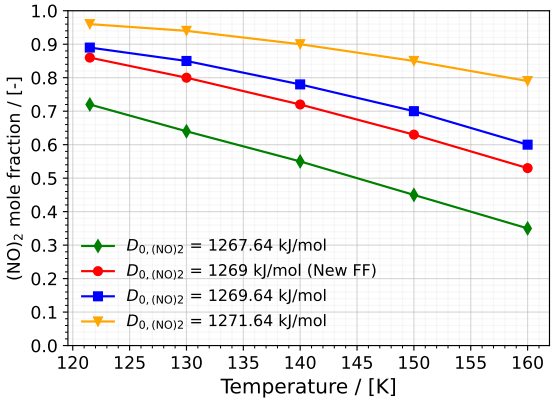

Figure B.3: Dimer mole fractions in the liquid phase of the reactive NO-$(NO)_2$ system for various values of $D_{0,(NO)_2}$ using the New FF.

Table B.11: Critical temperatures (T_c) and densities (ρ_c) for various values of $D_{0,(NO)_2}$ which were used to study the sensitivity of the VLE properties of the reactive NO-$(NO)_2$ system to the atomization energy of $(NO)_2$. L-J parameters and partial charges are taken from the New FF. $D_{0,(NO)_2} = 1269\,\mathrm{kJ/mol}$ (in bold) is the value with which the VLE properties can be obtained in excellent agreement with experiments.

$D_{0,(NO)_2}$/[kJ/mol]	T_c/[K]	ρ_c/[kg/m^3]
1267.64	175.94	472.85
1269	182.51	489.59
1269.64	182.26	500.81
1271.64	194.94	500.83

Table B.12: List of the force field parameters used to study the sensitivity of VLE properties to the L-J parameters, σ and ϵ, of NO and/or $(NO)_2$. The New FF is also included for comparison. In each combination, the L-J parameters of NO and/or $(NO)_2$ are varied by $\pm 10\%$ compared to the respective parameters of the New FF. The different combination compared to the New FF is shown in bold. ϵ/k_B is in units of Kelvin and σ is in units of Å.

	$\frac{\epsilon}{k_B}$ N-N_2O_2	$\sigma_{N\text{-}N_2O_2}$	$\frac{\epsilon}{k_B}$ O-N_2O_2	$\sigma_{O\text{-}N_2O_2}$	$\frac{\epsilon}{k_B}$ N-NO	$\sigma_{N\text{-}NO}$	$\frac{\epsilon}{k_B}$ O-NO	$\sigma_{O\text{-}NO}$
FF-a	47.00	**2.72**	54.52	**2.58**	48.50	3.09	56.29	2.94
FF-b	47.00	**3.32**	54.52	**3.16**	48.50	3.09	56.29	2.94
FF-c	**42.30**	3.02	**49.07**	2.87	48.50	3.09	56.29	2.94
FF-d	**51.70**	3.02	**59.97**	2.87	48.50	3.09	56.29	2.94
FF-e	47.00	3.02	54.52	2.87	48.50	**2.78**	56.29	**2.65**
FF-f	47.00	3.02	54.52	2.87	48.50	**3.40**	56.29	**3.23**
FF-g	47.00	3.02	54.52	2.87	**43.65**	3.09	**50.66**	2.94
FF-h	47.00	3.02	54.52	2.87	**53.35**	3.09	**61.92**	2.94
FF-i	47.00	**2.72**	54.52	**2.58**	48.50	**2.78**	56.29	**2.65**
FF-j	47.00	**3.32**	54.52	**3.16**	48.50	**3.40**	56.29	**3.23**
FF-k	**42.30**	3.02	**49.07**	2.87	**43.65**	3.09	**50.66**	2.94
FF-l	**51.70**	3.02	**59.97**	2.87	**53.35**	3.09	**61.92**	2.94
New FF	47.00	3.02	54.52	2.87	48.50	3.09	56.29	2.94

Table B.13: Critical temperatures (T_c) and densities (ρ_c) for the force field parameters listed in Table B.12, which were used to study the sensitivity of the VLE properties on σ and ϵ parameters.

	T_c/[K]	ρ_c/[kg/m^3]
FF-a	177.90	460.42
FF-b	189.86	463.39
FF-c	178.57	452.20
FF-d	190.54	523.43
FF-e	182.68	562.30
FF-f	184.56	368.04
FF-g	178.91	519.04
FF-h	190.60	447.92
FF-i	176.85	597.30
FF-j	188.48	406.17
FF-k	173.47	484.92
FF-l	189.97	495.64
New FF	182.51	489.59

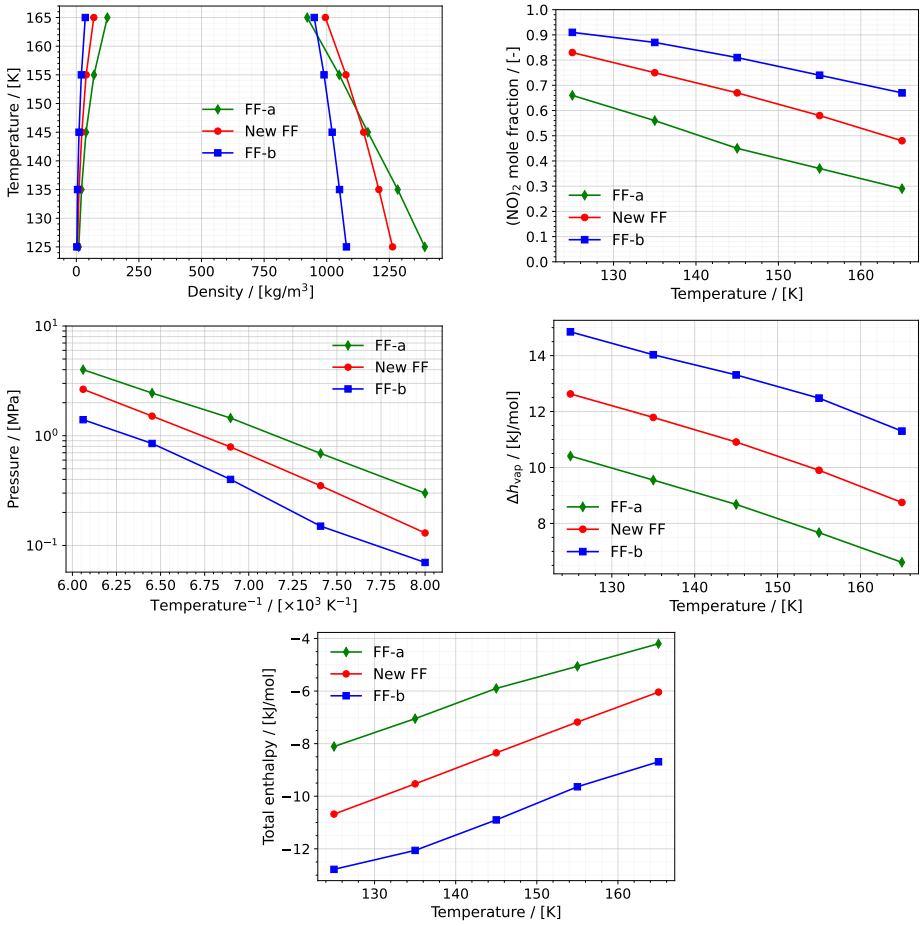

Figure B.4: Orthobaric coexistence densities (top left), $(NO)_2$ mole fractions in the liquid phase (top right), inverse temperature dependence of the saturated vapor pressures (centre left), heats of vaporization (centre right), and total true molar enthalpies (bottom centre) of the reactive NO-$(NO)_2$ system using FF-a (green diamonds), the New FF (blue squares), and FF-b (red circles). Refer to Table B.12 for the values of the parameters in FF-a and FF-b.

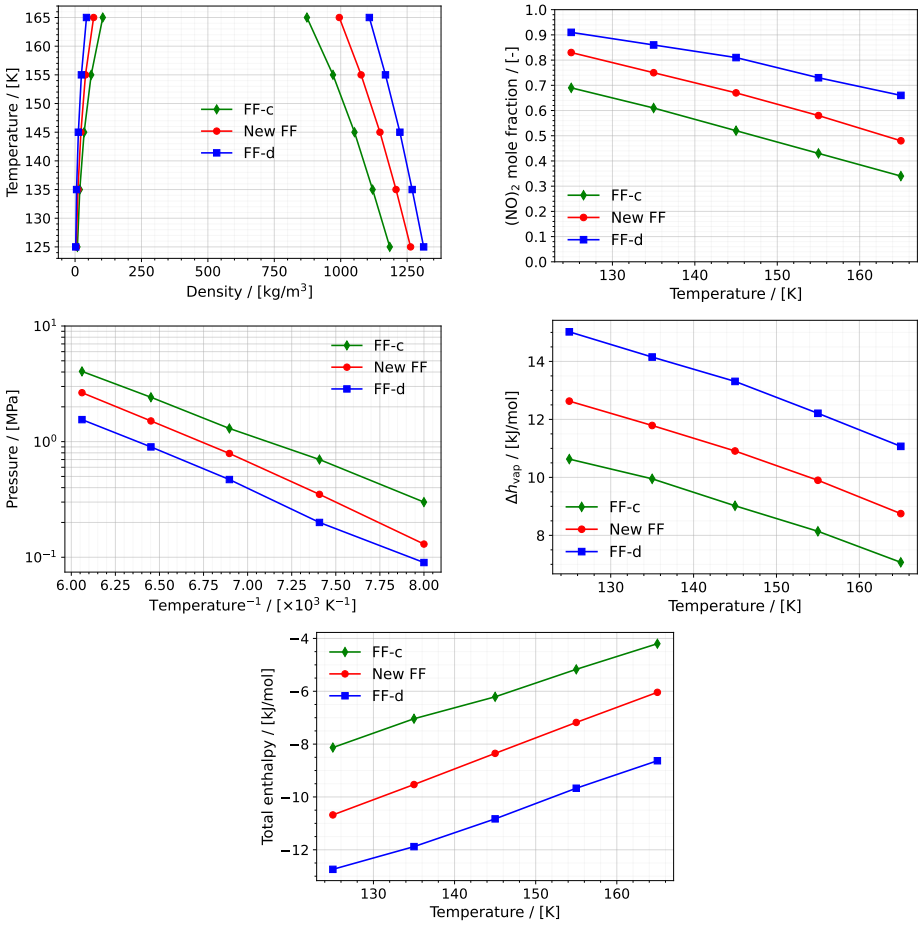

Figure B.5: Orthobaric coexistence densities (top left), $(NO)_2$ mole fractions in the liquid phase (top right), inverse temperature dependence of the saturated vapor pressures (centre left), heats of vaporization (centre right), and total true molar enthalpies (bottom centre) of the reactive NO-$(NO)_2$ system using FF-c (green diamonds), the New FF (blue squares), and FF-d (red circles). Refer to Table B.12 for the values of the parameters in FF-c and FF-d.

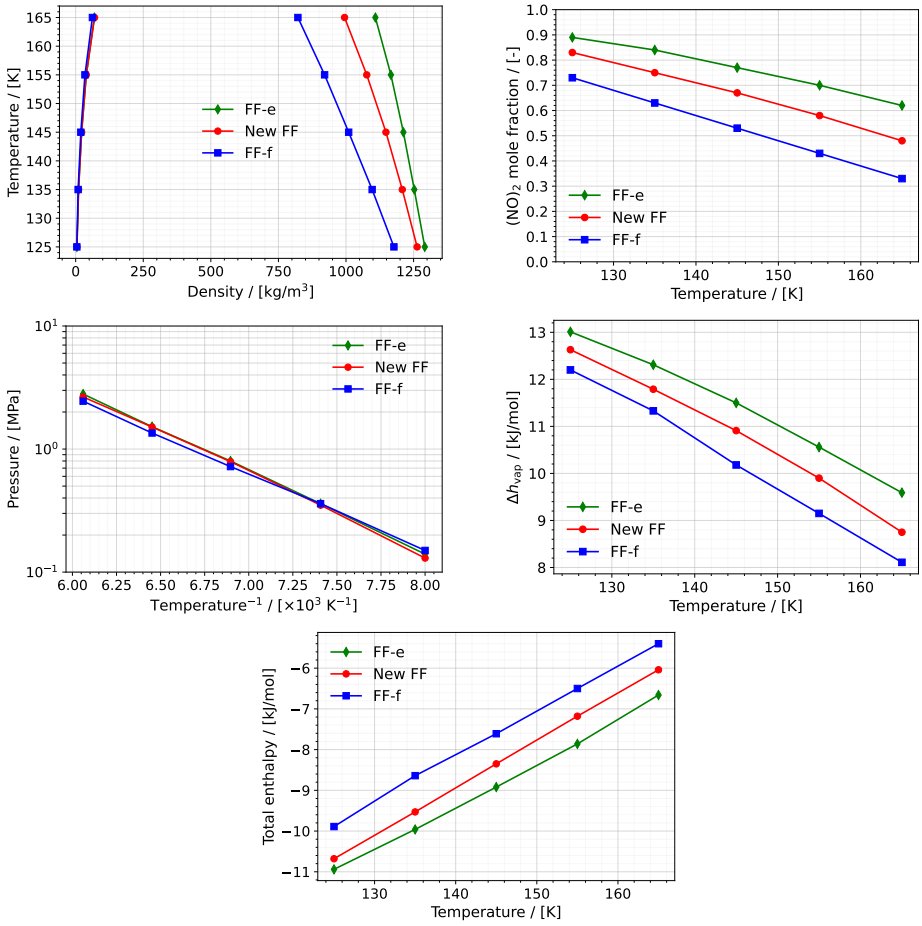

Figure B.6: Orthobaric coexistence densities (top left), $(NO)_2$ mole fractions in the liquid phase (top right), inverse temperature dependence of the saturated vapor pressures (centre left), heats of vaporization (centre right), and total true molar enthalpies (bottom centre) of the reactive NO-$(NO)_2$ system using FF-e (green diamonds), the New FF (blue squares), and FF-f (red circles). Refer to Table B.12 for the values of the parameters in FF-e and FF-f.

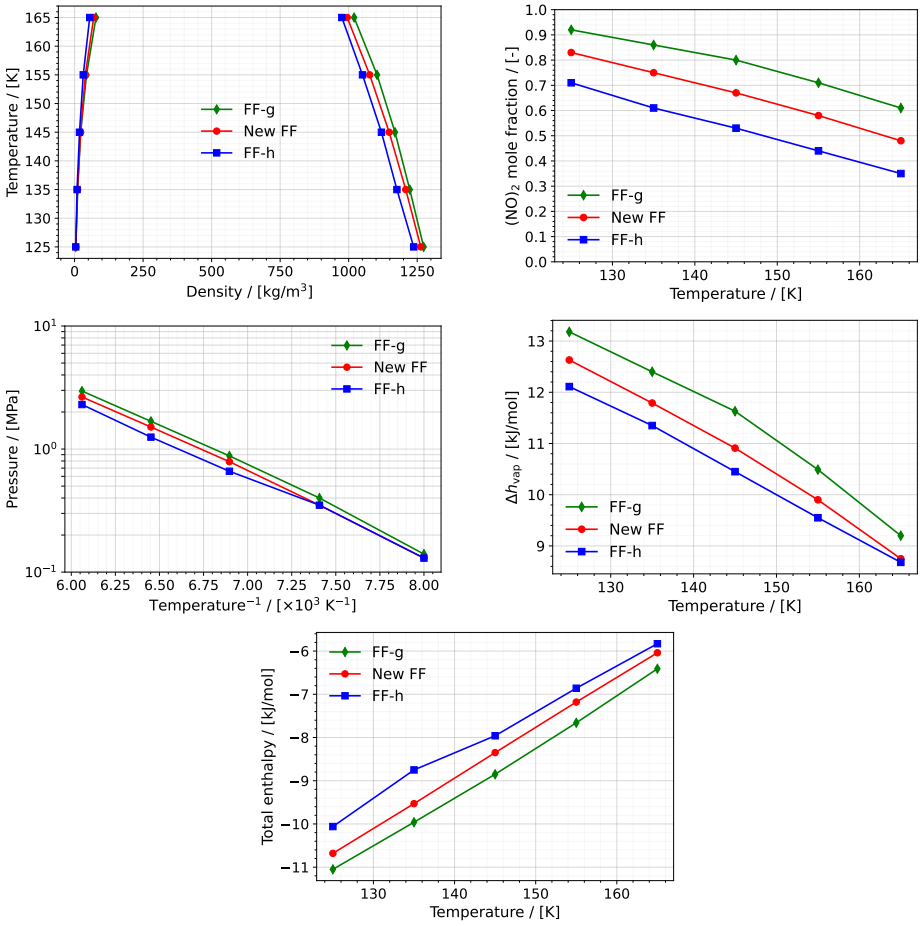

Figure B.7: Orthobaric coexistence densities (top left), $(NO)_2$ mole fractions in the liquid phase (top right), inverse temperature dependence of the saturated vapor pressures (centre left), heats of vaporization (centre right), and total true molar enthalpies (bottom centre) of the reactive NO-$(NO)_2$ system using FF-g (green diamonds), the New FF (blue squares), and FF-h (red circles). Refer to Table B.12 for the values of the parameters in FF-g and FF-h.

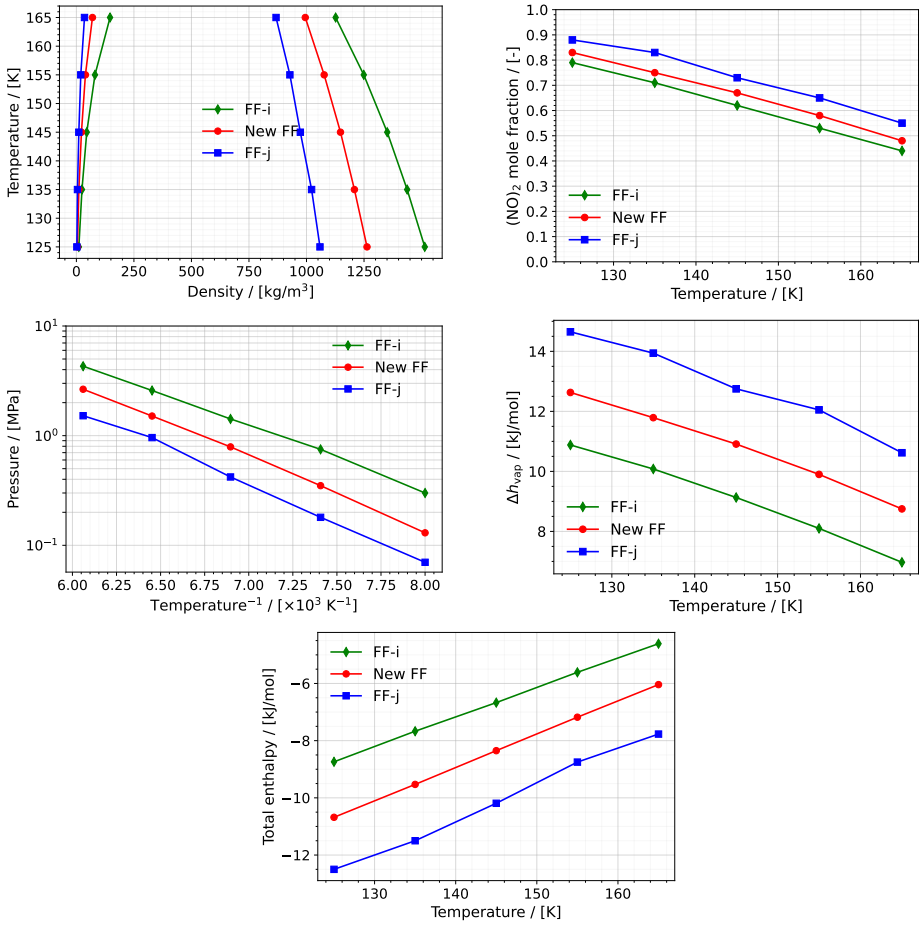

Figure B.8: Orthobaric coexistence densities (top left), $(NO)_2$ mole fractions in the liquid phase (top right), inverse temperature dependence of the saturated vapor pressures (centre left), heats of vaporization (centre right), and total true molar enthalpies (bottom centre) of the reactive NO-$(NO)_2$ system using FF-i (green diamonds), the New FF (blue squares), and FF-j (red circles). Refer to Table B.12 for the values of the parameters in FF-i and FF-j.

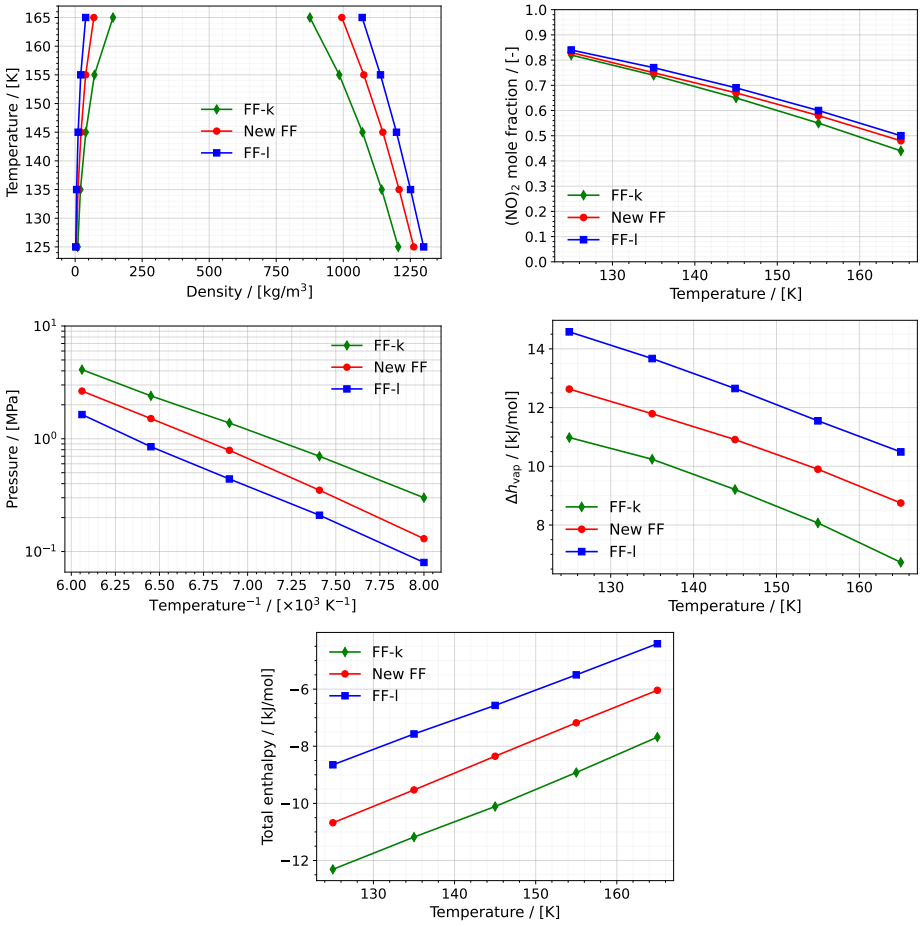

Figure B.9: Orthobaric coexistence densities (top left), $(NO)_2$ mole fractions in the liquid phase (top right), inverse temperature dependence of the saturated vapor pressures (centre left), heats of vaporization (centre right), and total true molar enthalpies (bottom centre) of the reactive NO-$(NO)_2$ system using FF-k (green diamonds), the New FF (blue squares), and FF-l (red circles). Refer to Table B.12 for the values of the parameters in FF-k and FF-l.

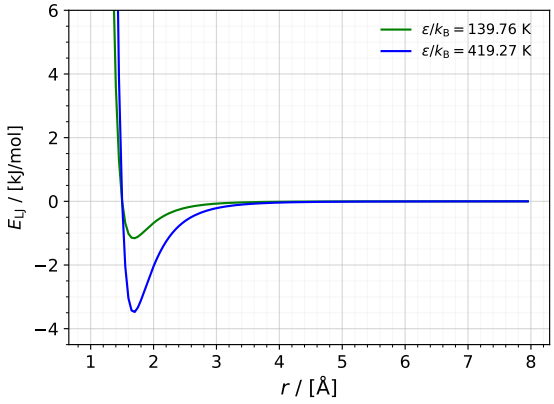

Figure B.10: Lennard-Jones potential energy for two single-bead particles with different values of ϵ/k_B (139.76 K and 419.27 K) and identical value of σ (1.5 Å).

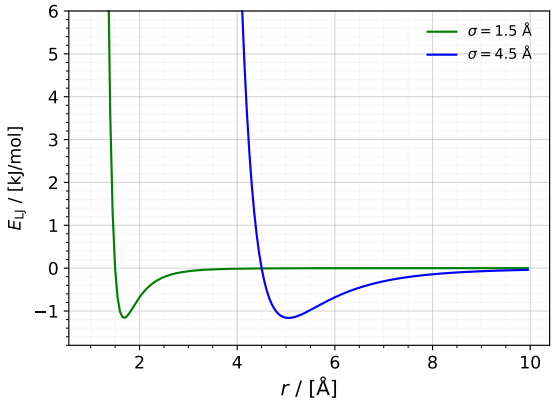

Figure B.11: Lennard-Jones potential energy for two single-bead particles with different values of σ (1.5 Å and 4.5 Å) and identical value of ϵ/k_B (139.76 K).

B

Appendix C- Supporting data for Chapter 5

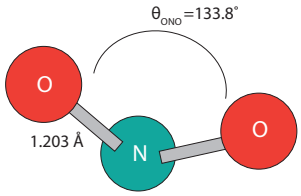

Figure C.1: Schematic representation of the NO_2 molecule, showing its bond lengths and angle. Note that the NO_2 molecule is considered rigid and therefore the bond lengths and angle are kept fixed at the equilibrium values.

C

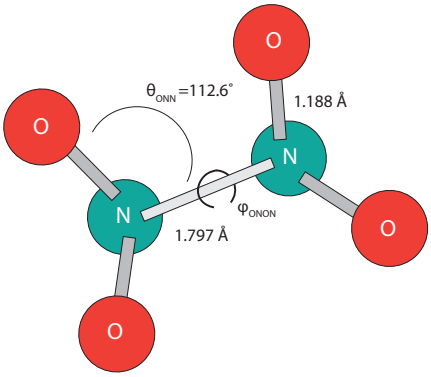

Figure C.2: Schematic representation of the N_2O_4 molecule, showing its bond lengths, angles, and dihedral. Note that the bond lengths and angles of N_2O_4 are kept fixed at the equilibrium values.

Table C.1: Parameters of potential energy functions corresponding to van der Waals and electrostatic energies developed by Bourasseau *et al.* [280] for NO_2.

Parameter	Functional form	Units	Value
ϵ_N/k_B	$4\epsilon_{ij}\left[\left(\frac{\sigma_{ij}}{r_{ij}}\right)^{12}-\left(\frac{\sigma_{ij}}{r_{ij}}\right)^{6}\right]$	[K]	50.36
σ_N	$4\epsilon_{ij}\left[\left(\frac{\sigma_{ij}}{r_{ij}}\right)^{12}-\left(\frac{\sigma_{ij}}{r_{ij}}\right)^{6}\right]$	[Å]	3.24
ϵ_O/k_B	$4\epsilon_{ij}\left[\left(\frac{\sigma_{ij}}{r_{ij}}\right)^{12}-\left(\frac{\sigma_{ij}}{r_{ij}}\right)^{6}\right]$	[K]	62.51
σ_O	$4\epsilon_{ij}\left[\left(\frac{\sigma_{ij}}{r_{ij}}\right)^{12}-\left(\frac{\sigma_{ij}}{r_{ij}}\right)^{6}\right]$	[Å]	2.93
q_N	$\frac{1}{4\pi\epsilon_o}\frac{q_i q_j}{r_{ij}}$	[e]	0.146
q_O	$\frac{1}{4\pi\epsilon_o}\frac{q_i q_j}{r_{ij}}$	[e]	-0.073

Table C.2: Parameters of potential energy functions corresponding to torsional, van der Waals and electrostatic energies developed by Bourasseau *et al.* [280] for N_2O_4.

Parameter	Functional form	Units	Value
c_0/k_B	$c_0 + c_1(1+\cos\phi) + c_2(1-\cos 2\phi) + c_3(1+\cos 3\phi)$	[K]	-40.046
c_1/k_B	$c_0 + c_1(1+\cos\phi) + c_2(1-\cos 2\phi) + c_3(1+\cos 3\phi)$	[K]	-9.196
c_2/k_B	$c_0 + c_1(1+\cos\phi) + c_2(1-\cos 2\phi) + c_3(1+\cos 3\phi)$	[K]	1826.432
c_3/k_B	$c_0 + c_1(1+\cos\phi) + c_2(1-\cos 2\phi) + c_3(1+\cos 3\phi)$	[K]	10.335
ϵ_N/k_B	$4\epsilon_{ij}\left[\left(\frac{\sigma_{ij}}{r_{ij}}\right)^{12} - \left(\frac{\sigma_{ij}}{r_{ij}}\right)^{6}\right]$	[K]	50.36
σ_N	$4\epsilon_{ij}\left[\left(\frac{\sigma_{ij}}{r_{ij}}\right)^{12} - \left(\frac{\sigma_{ij}}{r_{ij}}\right)^{6}\right]$	[Å]	3.24
ϵ_O/k_B	$4\epsilon_{ij}\left[\left(\frac{\sigma_{ij}}{r_{ij}}\right)^{12} - \left(\frac{\sigma_{ij}}{r_{ij}}\right)^{6}\right]$	[K]	62.51
σ_O	$4\epsilon_{ij}\left[\left(\frac{\sigma_{ij}}{r_{ij}}\right)^{12} - \left(\frac{\sigma_{ij}}{r_{ij}}\right)^{6}\right]$	[Å]	2.93
q_N	$\frac{1}{4\pi\epsilon_o}\frac{q_i q_j}{r_{ij}}$	[e]	0.588
q_O	$\frac{1}{4\pi\epsilon_o}\frac{q_i q_j}{r_{ij}}$	[e]	-0.294

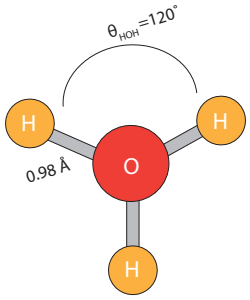

Figure C.3: Schematic representation of the H_3O^+ ion, showing its bond lengths and angles. Note that H_3O^+ is considered rigid, therefore the bond lengths and angles are kept fixed at the equilibrium values.

Table C.3: Parameters of potential energy functions corresponding to van der Waals and electrostatic energies developed by Noroozi *et al.* [281] for H_3O^+.

Parameter	Functional form	Units	Value
ϵ_H/k_B	$4\epsilon_{ij}\left[\left(\frac{\sigma_{ij}}{r_{ij}}\right)^{12}-\left(\frac{\sigma_{ij}}{r_{ij}}\right)^{6}\right]$	[K]	1.00
σ_H	$4\epsilon_{ij}\left[\left(\frac{\sigma_{ij}}{r_{ij}}\right)^{12}-\left(\frac{\sigma_{ij}}{r_{ij}}\right)^{6}\right]$	[Å]	1.00
ϵ_O/k_B	$4\epsilon_{ij}\left[\left(\frac{\sigma_{ij}}{r_{ij}}\right)^{12}-\left(\frac{\sigma_{ij}}{r_{ij}}\right)^{6}\right]$	[K]	76.54
σ_O	$4\epsilon_{ij}\left[\left(\frac{\sigma_{ij}}{r_{ij}}\right)^{12}-\left(\frac{\sigma_{ij}}{r_{ij}}\right)^{6}\right]$	[Å]	3.15
q_H	$\frac{1}{4\pi\epsilon_o}\frac{q_i q_j}{r_{ij}}$	[e]	0.7599
q_O	$\frac{1}{4\pi\epsilon_o}\frac{q_i q_j}{r_{ij}}$	[e]	-1.2797

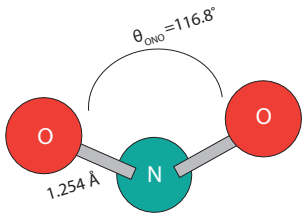

Figure C.4: Schematic representation of the NO_2^- ion, showing its bond lengths and angles. Note that the bond lengths of NO_2^- are kept fixed at their equilibrium values.

Table C.4: Parameters of potential energy functions corresponding to bending, van der Waals and electrostatic energies developed by Cordeiro *et al.* [282] for NO_2^-.

Parameter	Functional form	Units	Value
θ_{ONO}	$\frac{1}{2}k(\theta-\theta_0)^2$	[deg]	116.80
$k_{\theta(\mathrm{ONO})}/k_{\mathrm{B}}$	$\frac{1}{2}k(\theta-\theta_0)^2$	[K/deg^2]	119847.30
$\epsilon_{\mathrm{N}}/k_{\mathrm{B}}$	$4\epsilon_{ij}\left[\left(\frac{\sigma_{ij}}{r_{ij}}\right)^{12}-\left(\frac{\sigma_{ij}}{r_{ij}}\right)^{6}\right]$	[K]	76.78
σ_{N}	$4\epsilon_{ij}\left[\left(\frac{\sigma_{ij}}{r_{ij}}\right)^{12}-\left(\frac{\sigma_{ij}}{r_{ij}}\right)^{6}\right]$	[Å]	3.14
$\epsilon_{\mathrm{O}}/k_{\mathrm{B}}$	$4\epsilon_{ij}\left[\left(\frac{\sigma_{ij}}{r_{ij}}\right)^{12}-\left(\frac{\sigma_{ij}}{r_{ij}}\right)^{6}\right]$	[K]	207.01
σ_{O}	$4\epsilon_{ij}\left[\left(\frac{\sigma_{ij}}{r_{ij}}\right)^{12}-\left(\frac{\sigma_{ij}}{r_{ij}}\right)^{6}\right]$	[Å]	2.63
q_{N}	$\frac{1}{4\pi\epsilon_o}\frac{q_i q_j}{r_{ij}}$	[e]	0.40
q_{O}	$\frac{1}{4\pi\epsilon_o}\frac{q_i q_j}{r_{ij}}$	[e]	-0.70

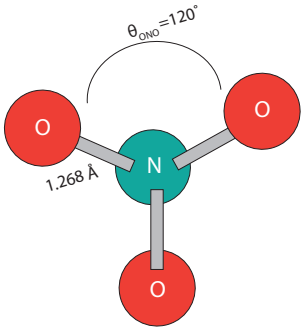

Figure C.5: Schematic representation of the NO_3^- ion, showing its bond lengths and angles (θ_{ONO}). Note that the bond lengths of NO_3^- are kept fixed at their equilibrium values.

Table C.5: Parameters of potential energy functions corresponding to bending, van der Waals and electrostatic energies developed by Cordeiro *et al.* [282] for NO_3^-. Note that the improper torsion for NO_3^- are neglected in this work as these potentials are not implemented in Brick-CFCMC.

Parameter	Functional form	Units	Value
θ_{ONO}	$\frac{1}{2}k(\theta-\theta_0)^2$	[deg]	120.00
$k_{\theta(ONO)}/k_B$	$\frac{1}{2}k(\theta-\theta_0)^2$	[K/deg^2]	105751.64
ϵ_N/k_B	$4\epsilon_{ij}\left[\left(\frac{\sigma_{ij}}{r_{ij}}\right)^{12}-\left(\frac{\sigma_{ij}}{r_{ij}}\right)^{6}\right]$	[K]	76.78
σ_N	$4\epsilon_{ij}\left[\left(\frac{\sigma_{ij}}{r_{ij}}\right)^{12}-\left(\frac{\sigma_{ij}}{r_{ij}}\right)^{6}\right]$	[Å]	3.14
ϵ_O/k_B	$4\epsilon_{ij}\left[\left(\frac{\sigma_{ij}}{r_{ij}}\right)^{12}-\left(\frac{\sigma_{ij}}{r_{ij}}\right)^{6}\right]$	[K]	207.01
σ_O	$4\epsilon_{ij}\left[\left(\frac{\sigma_{ij}}{r_{ij}}\right)^{12}-\left(\frac{\sigma_{ij}}{r_{ij}}\right)^{6}\right]$	[Å]	2.63
q_N	$\frac{1}{4\pi\epsilon_o}\frac{q_iq_j}{r_{ij}}$	[e]	0.65
q_O	$\frac{1}{4\pi\epsilon_o}\frac{q_iq_j}{r_{ij}}$	[e]	-0.55

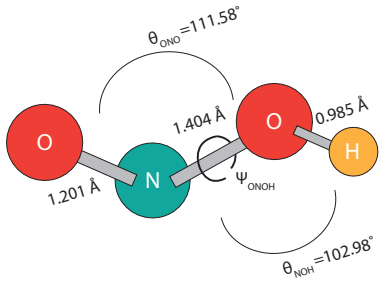

Figure C.6: Schematic representation of the HNO_2 molecule, showing its bond lengths, angles, and dihedrals (ψ_{ONOH}). Note that the bond lengths of HNO_2 molecule are kept fixed at their equilibrium values.

Table C.6: Parameters of potential energy functions corresponding to bending and torsional energies developed by Cordeiro *et al.* [282] for HNO_2.

Parameter	Functional form	Units	Value
θ_{ONO}	$\frac{1}{2}k(\theta-\theta_0)^2$	[deg]	111.58
$k_{\theta(\mathrm{ONO})}/k_{\mathrm{B}}$	$\frac{1}{2}k(\theta-\theta_0)^2$	[K/deg^2]	176678.39
θ_{NOH}	$\frac{1}{2}k(\theta-\theta_0)^2$	[deg]	102.98
$k_{\theta(\mathrm{NOH})}/k_{\mathrm{B}}$	$\frac{1}{2}k(\theta-\theta_0)^2$	[K/deg^2]	65147.46
p_0/k_{B}	$\sum_{i=0}^{5} p_i(\cos\psi)^i$	[K]	4638
p_1/k_{B}	$\sum_{i=0}^{5} p_i(\cos\psi)^i$	[K]	-706.8
p_2/k_{B}	$\sum_{i0=0}^{5} p_i(\cos\psi)^i$	[K]	-4544.4
p_3/k_{B}	$\sum_{i=0}^{5} p_i(\cos\psi)^i$	[K]	613.2
p_4/k_{B}	$\sum_{i=0}^{5} p_i(\cos\psi)^i$	[K]	0.00
p_5/k_{B}	$\sum_{i=0}^{5} p_i(\cos\psi)^i$	[K]	0.00

Table C.7: Parameters of potential energy functions corresponding to van der Waals and electrostatic energies developed by Cordeiro *et al.* [282] for HNO_2.

Parameter	Functional form	Units	Value
$\epsilon_{\mathrm{H}}/k_{\mathrm{B}}$	$4\epsilon_{ij}\left[\left(\frac{\sigma_{ij}}{r_{ij}}\right)^{12}-\left(\frac{\sigma_{ij}}{r_{ij}}\right)^{6}\right]$	[K]	0.00
σ_{H}	$4\epsilon_{ij}\left[\left(\frac{\sigma_{ij}}{r_{ij}}\right)^{12}-\left(\frac{\sigma_{ij}}{r_{ij}}\right)^{6}\right]$	[Å]	0.00
$\epsilon_{\mathrm{O(H)}}/k_{\mathrm{B}}$	$4\epsilon_{ij}\left[\left(\frac{\sigma_{ij}}{r_{ij}}\right)^{12}-\left(\frac{\sigma_{ij}}{r_{ij}}\right)^{6}\right]$	[K]	86.25
$\sigma_{\mathrm{O(H)}}$	$4\epsilon_{ij}\left[\left(\frac{\sigma_{ij}}{r_{ij}}\right)^{12}-\left(\frac{\sigma_{ij}}{r_{ij}}\right)^{6}\right]$	[Å]	3.04
$\epsilon_{\mathrm{N}}/k_{\mathrm{B}}$	$4\epsilon_{ij}\left[\left(\frac{\sigma_{ij}}{r_{ij}}\right)^{12}-\left(\frac{\sigma_{ij}}{r_{ij}}\right)^{6}\right]$	[K]	70.57
σ_{N}	$4\epsilon_{ij}\left[\left(\frac{\sigma_{ij}}{r_{ij}}\right)^{12}-\left(\frac{\sigma_{ij}}{r_{ij}}\right)^{6}\right]$	[Å]	2.86
$\epsilon_{\mathrm{O}}/k_{\mathrm{B}}$	$4\epsilon_{ij}\left[\left(\frac{\sigma_{ij}}{r_{ij}}\right)^{12}-\left(\frac{\sigma_{ij}}{r_{ij}}\right)^{6}\right]$	[K]	49.09
σ_{O}	$4\epsilon_{ij}\left[\left(\frac{\sigma_{ij}}{r_{ij}}\right)^{12}-\left(\frac{\sigma_{ij}}{r_{ij}}\right)^{6}\right]$	[Å]	3.04
q_{H}	$\frac{1}{4\pi\epsilon_o}\frac{q_i q_j}{r_{ij}}$	[e]	0.399
$q_{\mathrm{O(H)}}$	$\frac{1}{4\pi\epsilon_o}\frac{q_i q_j}{r_{ij}}$	[e]	-0.371
q_{N}	$\frac{1}{4\pi\epsilon_o}\frac{q_i q_j}{r_{ij}}$	[e]	0.093
q_{O}	$\frac{1}{4\pi\epsilon_o}\frac{q_i q_j}{r_{ij}}$	[e]	-0.121

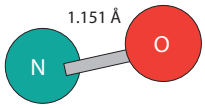

Figure C.7: Schematic representation of the NO molecule, showing its bond length. Note that the bond length of NO is kept fixed at its equilibrium value.

Table C.8: Parameters of potential energy functions corresponding to van der Waals and electrostatic energies developed by Saji *et al.* (see Chapter 4) for NO.

Parameter	Functional form	Units	Value
ϵ_N/k_B	$4\epsilon_{ij}\left[\left(\frac{\sigma_{ij}}{r_{ij}}\right)^{12}-\left(\frac{\sigma_{ij}}{r_{ij}}\right)^{6}\right]$	[K]	48.50
σ_N	$4\epsilon_{ij}\left[\left(\frac{\sigma_{ij}}{r_{ij}}\right)^{12}-\left(\frac{\sigma_{ij}}{r_{ij}}\right)^{6}\right]$	[Å]	3.09
ϵ_O/k_B	$4\epsilon_{ij}\left[\left(\frac{\sigma_{ij}}{r_{ij}}\right)^{12}-\left(\frac{\sigma_{ij}}{r_{ij}}\right)^{6}\right]$	[K]	56.29
σ_O	$4\epsilon_{ij}\left[\left(\frac{\sigma_{ij}}{r_{ij}}\right)^{12}-\left(\frac{\sigma_{ij}}{r_{ij}}\right)^{6}\right]$	[Å]	2.94
q_N	$\frac{1}{4\pi\epsilon_o}\frac{q_iq_j}{r_{ij}}$	[e]	0.0288
q_O	$\frac{1}{4\pi\epsilon_o}\frac{q_iq_j}{r_{ij}}$	[e]	-0.0288

Table C.9: Inputs required to calculate the isolated molecule partition function of involved species using the Brick-CFCMC software [68, 99]. The inputs are obtained from the JANAF tables [247] and the NIST database. For detailed expressions of the isolated molecule partition functions, refer to Chapter 2 and Polat *et al.* [68] Note that the isolated molecule partition functions for NO_2 and N_2O_4 were computed from the correlation functions provided by Lasala *et al.* [241], while the isolated molecule partition function of NO was computed from the correlation function provided in Chapter 4 (see Equation 4.16 and 4.17).

	H_2O	NO_2^-	NO_3^-	HNO_2	H_3O^+
Atomization energy/[kJ/mol]	917.80	1314.52	1431.87	1253.02	312.88
Electronic Degeneracy	1	1	1	1	1
Rotational Temperatures/[K]	40.11	5.50	0.64	4.46	15.96
	20.88	0.65	0.64	0.60	15.96
	13.36	0.58	0.32	0.53	9.23
Symmetry Number	2	2	3	1	3
Vibrational Temperatures/[K]	5261.62	1900.06	1509.97	5170.70	5412.29
	2294.85	1079.58	1194.73	2442.76	1511.41
	5404.06	1756.11	1972.03	1814.79	5570.62
			1034.96	1143.60	2231.13
			1972.03	861.30	5570.63
			1034.96	782.09	2231.13

Table C.10: Number of N_2O_4 molecules per NO_2 molecule in the ideal gas phase as a function of the total pressure in the gas phase (P_{total}) for different temperatures. These values are in excellent agreement with the computational values reported in the literature [241, 286].

P_{total} /[kPa]	273 K	298 K	313 K	333 K
1×10^{-7}	6.27×10^{-8}	7.49×10^{-9}	2.47×10^{-9}	6.50×10^{-10}
1×10^{-6}	6.27×10^{-7}	7.49×10^{-8}	2.47×10^{-8}	6.50×10^{-9}
1×10^{-5}	6.27×10^{-6}	7.49×10^{-7}	2.47×10^{-7}	6.50×10^{-8}
1×10^{-4}	6.27×10^{-5}	7.49×10^{-6}	2.47×10^{-6}	6.50×10^{-7}
1×10^{-3}	6.27×10^{-4}	7.49×10^{-5}	2.47×10^{-5}	6.50×10^{-6}
1×10^{-2}	6.24×10^{-3}	7.48×10^{-4}	2.47×10^{-4}	6.50×10^{-5}
1×10^{-1}	5.92×10^{-2}	7.43×10^{-3}	2.47×10^{-3}	6.50×10^{-4}
1×10^{0}	4.37×10^{-1}	7.00×10^{-2}	2.41×10^{-2}	6.46×10^{-3}
1×10^{1}	2.05×10^{0}	4.99×10^{-1}	2.05×10^{-1}	6.13×10^{-2}
1×10^{2}	7.44×10^{0}	2.28×10^{0}	1.15×10^{0}	4.49×10^{-1}

Table C.11: Mole fractions of the species studied in this work as a function of total gas pressure (P_{total}) at 273 K.

P_{total}/[kPa]	H_2O	NO_3^-	H_3O^+	NO	HNO_2	NO_2^-	NO_2	N_2O_4
1×10^{-7}	1.00×10^{0}	2.60×10^{-8}	5.24×10^{-8}	1.78×10^{-13}	2.23×10^{-10}	2.65×10^{-8}	8.85×10^{-14}	7.71×10^{-19}
1×10^{-6}	1.00×10^{0}	8.36×10^{-8}	1.66×10^{-7}	1.72×10^{-12}	2.19×10^{-9}	8.22×10^{-8}	8.85×10^{-13}	7.71×10^{-17}
1×10^{-5}	1.00×10^{0}	2.73×10^{-7}	5.25×10^{-7}	1.62×10^{-11}	2.12×10^{-8}	2.52×10^{-7}	8.85×10^{-12}	7.71×10^{-15}
1×10^{-4}	1.00×10^{0}	9.30×10^{-7}	1.66×10^{-6}	1.38×10^{-10}	1.96×10^{-7}	7.34×10^{-7}	8.85×10^{-11}	7.71×10^{-13}
1×10^{-3}	1.00×10^{0}	3.49×10^{-6}	5.37×10^{-6}	9.39×10^{-10}	1.62×10^{-6}	1.88×10^{-6}	8.84×10^{-10}	7.71×10^{-11}
1×10^{-2}	1.00×10^{0}	1.47×10^{-5}	1.85×10^{-5}	4.39×10^{-9}	1.10×10^{-5}	3.72×10^{-6}	8.79×10^{-9}	7.63×10^{-9}
1×10^{-1}	9.99×10^{-1}	6.48×10^{-5}	7.01×10^{-5}	1.35×10^{-8}	5.95×10^{-5}	5.29×10^{-6}	8.35×10^{-8}	6.87×10^{-7}
1×10^{0}	9.99×10^{-1}	2.45×10^{-4}	2.51×10^{-4}	2.95×10^{-8}	2.39×10^{-4}	5.93×10^{-6}	6.15×10^{-7}	3.74×10^{-5}
1×10^{1}	9.97×10^{-1}	6.86×10^{-4}	6.92×10^{-4}	5.10×10^{-8}	6.80×10^{-4}	6.10×10^{-6}	2.90×10^{-6}	8.25×10^{-4}
1×10^{2}	9.85×10^{-1}	1.59×10^{-3}	1.60×10^{-3}	7.84×10^{-8}	1.59×10^{-3}	6.09×10^{-6}	1.04×10^{-5}	1.07×10^{-2}

Table C.12: Mole fractions of the species studied in this work as a function of total gas pressure (P_{total}) at 298 K.

P_{total}/[kPa]	H_2O	NO_3^-	H_3O^+	NO	HNO_2	NO_2^-	NO_2	N_2O_4
1×10^{-7}	1.00×10^{0}	1.34×10^{-8}	2.74×10^{-8}	3.31×10^{-14}	4.20×10^{-11}	1.41×10^{-8}	6.03×10^{-14}	4.53×10^{-20}
1×10^{-6}	1.00×10^{0}	4.32×10^{-8}	8.67×10^{-8}	3.17×10^{-13}	4.11×10^{-10}	4.35×10^{-8}	6.03×10^{-13}	4.53×10^{-18}
1×10^{-5}	1.00×10^{0}	1.39×10^{-7}	2.74×10^{-7}	3.07×10^{-12}	4.04×10^{-9}	1.35×10^{-7}	6.03×10^{-12}	4.53×10^{-16}
1×10^{-4}	1.00×10^{0}	4.53×10^{-7}	8.67×10^{-7}	2.88×10^{-11}	3.92×10^{-8}	4.14×10^{-7}	6.03×10^{-11}	4.53×10^{-14}
1×10^{-3}	1.00×10^{0}	1.56×10^{-6}	2.75×10^{-6}	2.42×10^{-10}	3.59×10^{-7}	1.20×10^{-6}	6.03×10^{-10}	4.53×10^{-12}
1×10^{-2}	1.00×10^{0}	5.91×10^{-6}	8.91×10^{-6}	1.60×10^{-9}	2.91×10^{-6}	3.00×10^{-6}	6.02×10^{-9}	4.52×10^{-10}
1×10^{-1}	1.00×10^{0}	2.52×10^{-5}	3.10×10^{-5}	7.14×10^{-9}	1.94×10^{-5}	5.76×10^{-6}	5.98×10^{-8}	4.46×10^{-8}
1×10^{0}	1.00×10^{0}	1.11×10^{-4}	1.18×10^{-4}	2.11×10^{-8}	1.03×10^{-4}	7.94×10^{-6}	5.63×10^{-7}	3.96×10^{-6}
1×10^{1}	9.99×10^{-1}	4.09×10^{-4}	4.17×10^{-4}	4.51×10^{-8}	4.00×10^{-4}	8.78×10^{-6}	4.02×10^{-6}	2.01×10^{-4}
1×10^{2}	9.92×10^{-1}	1.12×10^{-3}	1.13×10^{-3}	7.66×10^{-8}	1.11×10^{-3}	8.96×10^{-6}	1.83×10^{-5}	4.18×10^{-3}

Table C.13: Mole fractions of the species studied in this work as a function of total gas pressure (P_{total}) at 313 K.

P_{total}/[kPa]	H_2O	NO_3^-	H_3O^+	NO	HNO_2	NO_2^-	NO_2	N_2O_4
1×10^{-7}	1.00×10^{0}	9.10×10^{-9}	1.89×10^{-8}	1.33×10^{-14}	1.65×10^{-11}	9.81×10^{-9}	5.32×10^{-14}	9.79×10^{-21}
1×10^{-6}	1.00×10^{0}	2.96×10^{-8}	5.98×10^{-8}	1.25×10^{-13}	1.60×10^{-10}	3.02×10^{-8}	5.32×10^{-13}	9.79×10^{-19}
1×10^{-5}	1.00×10^{0}	9.49×10^{-8}	1.89×10^{-7}	1.22×10^{-12}	1.58×10^{-9}	9.41×10^{-8}	5.32×10^{-12}	9.79×10^{-17}
1×10^{-4}	1.00×10^{0}	3.06×10^{-7}	5.98×10^{-7}	1.17×10^{-11}	1.55×10^{-8}	2.92×10^{-7}	5.32×10^{-11}	9.79×10^{-15}
1×10^{-3}	1.00×10^{0}	1.02×10^{-6}	1.89×10^{-6}	1.05×10^{-10}	1.47×10^{-7}	8.73×10^{-7}	5.32×10^{-10}	9.79×10^{-13}
1×10^{-2}	1.00×10^{0}	3.66×10^{-6}	6.05×10^{-6}	7.99×10^{-10}	1.28×10^{-6}	2.38×10^{-6}	5.31×10^{-9}	9.79×10^{-11}
1×10^{-1}	1.00×10^{0}	1.48×10^{-5}	2.01×10^{-5}	4.40×10^{-9}	9.49×10^{-6}	5.30×10^{-6}	5.30×10^{-8}	9.76×10^{-9}
1×10^{0}	1.00×10^{0}	6.51×10^{-5}	7.37×10^{-5}	1.59×10^{-8}	5.64×10^{-5}	8.61×10^{-6}	5.19×10^{-7}	9.32×10^{-7}
1×10^{1}	9.99×10^{-1}	2.69×10^{-4}	2.80×10^{-4}	3.94×10^{-8}	2.59×10^{-4}	1.04×10^{-5}	4.41×10^{-6}	6.74×10^{-5}
1×10^{2}	9.95×10^{-1}	8.46×10^{-4}	8.57×10^{-4}	7.35×10^{-8}	8.35×10^{-4}	1.09×10^{-5}	2.46×10^{-5}	2.11×10^{-3}

Table C.14: Mole fractions of the species studied in this work as a function of total gas pressure (P_{total}) at 333 K.

P_{total}/[kPa]	H_2O	NO_3^-	H_3O^+	NO	HNO_2	NO_2^-	NO_2	N_2O_4
1×10^{-7}	1.00×10^{0}	6.30×10^{-9}	1.33×10^{-8}	5.52×10^{-15}	6.51×10^{-12}	7.01×10^{-9}	4.66×10^{-14}	1.36×10^{-21}
1×10^{-6}	1.00×10^{0}	2.07×10^{-8}	4.21×10^{-8}	5.11×10^{-14}	6.27×10^{-11}	2.14×10^{-8}	4.66×10^{-13}	1.36×10^{-19}
1×10^{-5}	1.00×10^{0}	6.64×10^{-8}	1.33×10^{-7}	4.96×10^{-13}	6.18×10^{-10}	6.65×10^{-8}	4.66×10^{-12}	1.36×10^{-17}
1×10^{-4}	1.00×10^{0}	2.13×10^{-7}	4.20×10^{-7}	4.83×10^{-12}	6.09×10^{-9}	2.08×10^{-7}	4.66×10^{-11}	1.36×10^{-15}
1×10^{-3}	1.00×10^{0}	6.94×10^{-7}	1.33×10^{-6}	4.54×10^{-11}	5.91×10^{-8}	6.36×10^{-7}	4.66×10^{-10}	1.36×10^{-13}
1×10^{-2}	1.00×10^{0}	2.38×10^{-6}	4.22×10^{-6}	3.83×10^{-10}	5.42×10^{-7}	1.84×10^{-6}	4.66×10^{-9}	1.36×10^{-11}
1×10^{-1}	1.00×10^{0}	9.04×10^{-6}	1.37×10^{-5}	2.53×10^{-9}	4.41×10^{-6}	4.62×10^{-6}	4.66×10^{-8}	1.36×10^{-9}
1×10^{0}	1.00×10^{0}	3.85×10^{-5}	4.74×10^{-5}	1.14×10^{-8}	2.95×10^{-5}	8.92×10^{-6}	4.63×10^{-7}	1.35×10^{-7}
1×10^{1}	1.00×10^{0}	1.69×10^{-4}	1.82×10^{-4}	3.41×10^{-8}	1.57×10^{-4}	1.24×10^{-5}	4.39×10^{-6}	1.21×10^{-5}
1×10^{2}	9.97×10^{-1}	6.37×10^{-4}	6.50×10^{-4}	7.34×10^{-8}	6.23×10^{-4}	1.37×10^{-5}	3.21×10^{-5}	6.49×10^{-4}

Table C.15: Mole fractions of the species studied in this work as a function of temperature at total gas pressure (P_{total}) of 10^{-6} kPa.

T/[K]	H_2O	NO_3^-	H_3O^+	NO	HNO_2	NO_2^-	NO_2	N_2O_4
273	1.00×10^{0}	8.36×10^{-8}	1.66×10^{-7}	1.72×10^{-12}	2.19×10^{-9}	8.22×10^{-8}	8.85×10^{-13}	7.71×10^{-17}
298	1.00×10^{0}	4.32×10^{-8}	8.67×10^{-8}	3.17×10^{-13}	4.11×10^{-10}	4.35×10^{-8}	6.03×10^{-13}	4.53×10^{-18}
313	1.00×10^{0}	2.96×10^{-8}	5.98×10^{-8}	1.25×10^{-13}	1.60×10^{-10}	3.02×10^{-8}	5.32×10^{-13}	9.79×10^{-19}
333	1.00×10^{0}	2.07×10^{-8}	4.21×10^{-8}	5.11×10^{-14}	6.27×10^{-11}	2.14×10^{-8}	4.66×10^{-13}	1.36×10^{-19}

Table C.16: Mole fractions of the species studied in this work as a function of temperature at total gas pressure (P_{total}) of 10^2 kPa.

T/[K]	H_2O	NO_3^-	H_3O^+	NO	HNO_2	NO_2^-	NO_2	N_2O_4
273	9.85×10^{-1}	1.59×10^{-3}	1.60×10^{-3}	7.84×10^{-8}	1.59×10^{-3}	6.09×10^{-6}	1.04×10^{-5}	1.07×10^{-2}
298	9.92×10^{-1}	1.12×10^{-3}	1.13×10^{-3}	7.66×10^{-8}	1.11×10^{-3}	8.96×10^{-6}	1.83×10^{-5}	4.18×10^{-3}
313	9.95×10^{-1}	8.46×10^{-4}	8.57×10^{-4}	7.35×10^{-8}	8.35×10^{-4}	1.09×10^{-5}	2.46×10^{-5}	2.11×10^{-3}
333	9.97×10^{-1}	6.37×10^{-4}	6.50×10^{-4}	7.34×10^{-8}	6.23×10^{-4}	1.37×10^{-5}	3.21×10^{-5}	6.49×10^{-4}

Table C.17: Mole fractions of the species studied in this work as a function of temperature at a total gas pressure (P_{total}) of 10^1 kPa. The means and standard deviations are obtained from the error propagation analysis. Note that NO_2 and N_2O_4 are not included as the liquid phase mole fractions of the species that are present in the gas phase are fixed by the mass transfer from the infinite gas phase to the liquid phase via the corresponding Henry coefficients of the species.

T/[K]	H_2O	NO_3^-	H_3O^+	NO	HNO_2	NO_2^-
273	$9.97\times 10^{-1}{}_{10^{-5}}$	$6.9\times 10^{-4}{}_{3\times10^{-5}}$	$6.9\times 10^{-3}{}_{3\times10^{-5}}$	$5.1\times 10^{-8}{}_{7\times10^{-9}}$	$6.8\times 10^{-4}{}_{3\times10^{-5}}$	$6.10\times 10^{-6}{}_{4\times10^{-9}}$
298	$9.99\times 10^{-1}{}_{10^{-5}}$	$4.1\times 10^{-4}{}_{2\times10^{-5}}$	$4.2\times 10^{-4}{}_{2\times10^{-5}}$	$4.6\times 10^{-8}{}_{8\times10^{-9}}$	$4.0\times 10^{-4}{}_{2\times10^{-5}}$	$8.77\times 10^{-6}{}_{2\times10^{-9}}$
313	$9.99\times 10^{-1}{}_{10^{-5}}$	$2.69\times 10^{-4}{}_{10^{-6}}$	$2.80\times 10^{-4}{}_{10^{-6}}$	$3.9\times 10^{-8}{}_{10^{-9}}$	$2.59\times 10^{-4}{}_{10^{-6}}$	$1.04\times 10^{-5}{}_{10^{-7}}$
333	$9.99\times 10^{-1}{}_{10^{-5}}$	$1.69\times 10^{-4}{}_{5\times10^{-6}}$	$1.82\times 10^{-4}{}_{5\times10^{-6}}$	$3.4\times 10^{-8}{}_{2\times10^{-9}}$	$1.57\times 10^{-4}{}_{5\times10^{-6}}$	$1.23\times 10^{-5}{}_{4\times10^{-8}}$

Obtaining $\ln[K]$ from $\mathrm{p}K_\mathrm{a}$

The values of $\ln[K]$ reported in this work are within the CASpy software convention [68], $K = K_{\mathrm{CASpy}}$, and are calculated using

$$\ln[K] = \ln[K_{\mathrm{CASpy}}] = -\ln[10]\,\mathrm{p}K_\mathrm{a} - \ln[55.55], \tag{C.1}$$

where $\mathrm{p}K_\mathrm{a} = -\log_{10}[K_\mathrm{a}] = \frac{-\ln[K_\mathrm{a}]}{\ln[10]}$ in which K_a is the unitless acid dissociation constant [290], $K_\mathrm{a} = \frac{K'_\mathrm{a}}{C^0}$. K'_a is the acid dissociation constant in units of $[\frac{\mathrm{mol}}{\mathrm{L}}]$ and C^0 is a constant equal to 1 mol/L. We introduce these two definitions of the acid dissociation constant because, in the literature, values are reported either in units of $[\frac{\mathrm{mol}}{\mathrm{L}}]$ or as unitless quantities. Here, we present the derivation of Equation C.1 using reaction R3 as an example.

The acid dissociation constant, K_a, for reaction R3, $\mathrm{HNO_{2(aq)}}$+$\mathrm{H_2O_{(l)}} \rightleftharpoons$ $\mathrm{NO_2^-{}_{(aq)}}$+ $\mathrm{H_3O^+{}_{(aq)}}$ is given by

$$K_\mathrm{a} = \frac{a_{\mathrm{NO_2^-}}\, a_{\mathrm{H_3O^+}}}{a_{\mathrm{HNO_2}}\, a_{\mathrm{H_2O}}}, \tag{C.2}$$

where $a_Y = \frac{[Y]'}{C^0}$ is the activity of a particular species Y ($\mathrm{HNO_2}$, $\mathrm{H_2O}$, $\mathrm{NO_2^-}$, and $\mathrm{H_3O^+}$). $[Y]'$ is the concentration of Y in units of [mol/L]. The activity of water ($a_{\mathrm{H_2O}}$) is taken as one [367, 368] in dilute aqueous solutions ($a_{\mathrm{H_2O}} = 1$). By substituting a_Y into Equation C.2, K_a can be written in terms of a unitless concentration $[Y]$

$$K_\mathrm{a} = \frac{[\mathrm{NO_2^-}][\mathrm{H_3O^+}]}{[\mathrm{HNO_2}]}. \tag{C.3}$$

By defining c_{total} as the sum of the unitless concentration of all the species in the system, $c_{\mathrm{total}} = [\mathrm{NO_2^-}] + [\mathrm{H_3O^+}] + [\mathrm{HNO_2}] + [\mathrm{H_2O}]$, and by dividing the numerator and denominator of Equation C.3 by c_{total}, K_a can be written in terms of the mole fraction $X_Y = \frac{[Y]}{c_{\mathrm{total}}}$ as

$$K_\mathrm{a} = \frac{X_{\mathrm{NO_2^-}} X_{\mathrm{H_3O^+}}}{X_{\mathrm{HNO_2}}} c_{\mathrm{total}}. \tag{C.4}$$

The convention used in the CASpy software is that the equilibrium constant of reaction R3 is

$$K_{\mathrm{CASpy}} = \frac{X_{\mathrm{NO_2^-}} X_{\mathrm{H_3O^+}}}{X_{\mathrm{HNO_2}} X_{\mathrm{H_2O}}} \tag{C.5}$$

and therefore K_{CASpy} can be written in terms of K_a by the following equation

$$K_{\mathrm{CASpy}} = \frac{K_{\mathrm{a}}}{X_{\mathrm{H_2O}}\ c_{\mathrm{total}}}. \tag{C.6}$$

Taking the natural logarithm of Equation C.6 and substituting $X_{\mathrm{H_2O}} \approx 1$ and $c_{\mathrm{total}} \approx [\mathrm{H_2O}]$ (which are valid for weak acids such as $\mathrm{HNO_2}$), the following equation can be obtained

$$\ln[K_{\mathrm{CASpy}}] = \ln[K_{\mathrm{a}}] - \ln[\mathrm{H_2O}]. \tag{C.7}$$

Using the equation for the acid dissociation constant $\mathrm{p}K_{\mathrm{a}} = -\log_{10}[K_{\mathrm{a}}] = \frac{-\ln[K_{\mathrm{a}}]}{\ln[10]}$ and substituting it in Equation C.7, one obtains

$$\ln[K_{\mathrm{CASpy}}] = -\ln[10]\,\mathrm{p}K_{\mathrm{a}} - \ln[\mathrm{H_2O}]. \tag{C.8}$$

$[\mathrm{H_2O}]$ equals $\frac{[\mathrm{H_2O}]'}{C^0}$ in which $[\mathrm{H_2O}]'$ is approximately 55.55 mol/L. Therefore, the following equation can be obtained

$$\ln[K_{\mathrm{CASpy}}] = -\ln[10]\,\mathrm{p}K_{\mathrm{a}} - \ln[55.55]. \tag{C.9}$$

Calculating Mass Balances

In this section, we compute the mass balances for reactions R2, R3 and R4 in the main text. The mass balance for reaction R1 in the gas phase is not included, as there is a mass transfer from the infinite gas phase to the liquid phase when the total pressure and the composition of the gas phase are imposed. Let λ_2, λ_3 and λ_4 be the extent of reactions for reactions R2, R3 and R4 in the main text, respectively. It should be noted that λ_2, λ_3 and λ_4 are different from the coupling parameter (λ) from the CFCMC algorithm [95–97] introduced in Section 2.3.1. Considering the sources and sinks of each species, the net amount of each species can be written as

$$\mathrm{H_2O}^* = -2\lambda_2 - \lambda_3, \tag{C.10}$$

$$\mathrm{HNO_2^*} = \lambda_2 - \lambda_3 - 3\lambda_4, \tag{C.11}$$

$$\mathrm{NO_3^-}^* = \lambda_2 + \lambda_4, \tag{C.12}$$

$$\mathrm{NO_2^-}^* = \lambda_3, \tag{C.13}$$

$$\mathrm{H_3O^+}^* = \lambda_2 + \lambda_3 + \lambda_4, \tag{C.14}$$

$$\mathrm{NO}^* = 2\lambda_4, \tag{C.15}$$

where Y^* is the amount (in mole fraction) of species Y produced (for reaction products) or consumed (for reactants) in a reaction. By eliminating λ_3 and λ_4 using Equations C.13 and C.10 in the rest of the equation, the following equations are obtained

$$\mathrm{H_2O}^* = -2\lambda_2 - \mathrm{NO_2^-}^*, \tag{C.16}$$

$$\mathrm{NO_3^-}^* = \lambda_2 + \frac{\mathrm{NO}^*}{2}, \tag{C.17}$$

$$\mathrm{HNO_2^*} = \lambda_2 - \mathrm{NO_2^-}^* - \frac{3\mathrm{NO}^*}{2}. \tag{C.18}$$

Finally, eliminating λ_2 from Equations C.16, C.17, and C.18 leads to the following mass balances

$$2\mathrm{NO_3^-}^* - \mathrm{NO}^* + \mathrm{H_2O}^* + \mathrm{NO_2^-}^* = 0, \tag{C.19}$$

$$\mathrm{NO_3^-}^* - \mathrm{HNO_2^*} - 2\mathrm{NO}^* - \mathrm{NO_2^-}^* = 0. \tag{C.20}$$

These constraints are added to the CASpy software.

Dimerization constant in the gas phase

For the reaction $2\mathrm{NO_2(g)} \rightleftharpoons \mathrm{N_2O_4(g)}$ in the gas phase, the sum of the chemical potentials of the species (μ_i) weighted by their stoichiometric coefficients ($\nu_{i,j}$) is zero

$$\sum_{i=1}^{N_{\text{species}}} \nu_{i,j}\mu_i = 0. \tag{C.21}$$

The chemical potential of a species, as defined in Brick-CFCMC [68, 97–99], is given by

$$\mu_i = \mu_i^0 + RT \ln\left[\frac{\rho_i}{\rho_0}\right] + \mu_i^{\text{ex}}, \tag{C.22}$$

wherein μ_i^0 is the standard state ideal gas chemical potential of solute i, R is the ideal gas constant, T is the absolute temperature, ρ_i is the number density of solute i, ρ_0 is the reference number density, taken as 1 molecule Å^{-3}. μ_i^{ex} is the excess chemical potential of the solute i in the solvent. In the (ideal) gas phase, $\mu_i^{\text{ex}} = 0$ for all species. Combining the above equations, one arrives at

$$\mu^0_{\mathrm{N_2O_4}} + RT \ln\left[\frac{\rho_{\mathrm{N_2O_4}}}{\rho_0}\right] - 2\mu^0_{\mathrm{NO_2}} - 2RT \ln\left[\frac{\rho_{\mathrm{NO_2}}}{\rho_0}\right] = 0. \tag{C.23}$$

Upon rearrangement, Equation C.23 can be written as

$$\mu^0_{N_2O_4} - 2\mu^0_{NO_2} = RT \ln \left[\frac{\rho^2_{NO_2}}{\rho_{N_2O_4}\rho_0} \right]. \tag{C.24}$$

Using the ideal gas law, $\rho_i = \left[\frac{P_i}{k_B T}\right]$, for each species, the following equation is obtained

$$\mu^0_{N_2O_4} - 2\mu^0_{NO_2} = RT \ln \left[\frac{P^2_{NO_2}}{P_{N_2O_4}P_0} \right], \tag{C.25}$$

where $P_0 = \rho_0 \, k_B \, T$ and $\rho_0 = 1$ molecule Å^{-3}. By defining $K_p = \left[\frac{P_{N_2O_4}P_0}{P^2_{NO_2}}\right]$ the following equation is obtained

$$K_p = \exp \left[\frac{\mu^0_{N_2O_4} - 2\mu^0_{NO_2}}{-RT} \right]. \tag{C.26}$$

Gas phase composition

Using the definition for $K_p = \left[\frac{P_{N_2O_4}P_0}{P^2_{NO_2}}\right]$, where $P_0 = \rho_0 \, k_B \, T$ and $\rho_0 = 1$ molecule Å^{-3}, one obtains

$$P_{N_2O_4} = \frac{K_p P^2_{NO_2}}{P_0}. \tag{C.27}$$

From the ideal gas law, $P_i = \frac{N_i}{V} k_B T$. Using this result in Equation C.27, one arrives at the following equation:

$$N_{N_2O_4} = \frac{N^2_{NO_2} K_p}{V/V_0}, \tag{C.28}$$

where V is the total volume of the gas phase. From the ideal gas law, $V = \frac{N_{total} \, k_B T}{P_{total}}$, and substituting this equation in Equation C.28

$$N_{N_2O_4} = \frac{N^2_{NO_2} V_0 P_{total} K_p}{N_{total} \, k_B T}. \tag{C.29}$$

Since the gas phase is composed of both NO_2 and N_2O_4 molecules, the total number of molecules in the gas phase, N_{total}, is equal to the sum of molecules of NO_2 and N_2O_4. That is

$$N_{total} = N_{N_2O_4} + N_{NO_2}. \tag{C.30}$$

Using Equation C.30 in Equation C.29, $N_{\mathrm{N_2O_4}}$ can be equated to

$$N_{\mathrm{N_2O_4}} = \frac{N_{\mathrm{NO_2}}^2 V_0 P_{\mathrm{total}} K_{\mathrm{p}}}{\left(N_{\mathrm{N_2O_4}} + N_{\mathrm{NO_2}}\right) k_B T}, \tag{C.31}$$

which upon rearrangement, can be written as

$$N_{\mathrm{N_2O_4}}^2 + N_{\mathrm{N_2O_4}} N_{\mathrm{NO_2}} - \frac{N_{\mathrm{NO_2}}^2 V_0 P_{\mathrm{total}} K_{\mathrm{p}}}{k_B T} = 0. \tag{C.32}$$

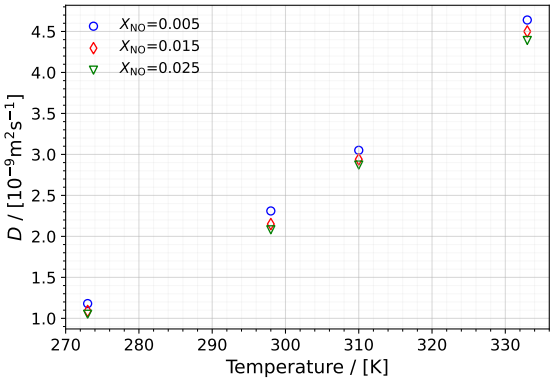

Figure C.8: Self-diffusion coefficients of water in NO aqueous solutions for different mole fractions of NO at different temperatures using the Saji *et al.* force field (see Equation 4.1) for NO and the TIP4P/2005 [61] water model. Error bars are estimated based on the standard deviation of 6 production blocks and are much smaller than the symbols.

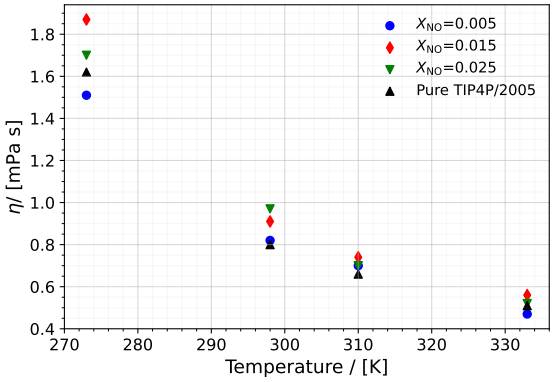

Figure C.9: Viscosities of NO aqueous solutions for different mole fractions of NO at different temperatures using the Saji *et al.* force field (see Equation 4.1) for NO and the TIP4P/2005 [61] water model. Error bars are estimated based on the standard deviation of 6 production blocks and are much smaller than the symbols.

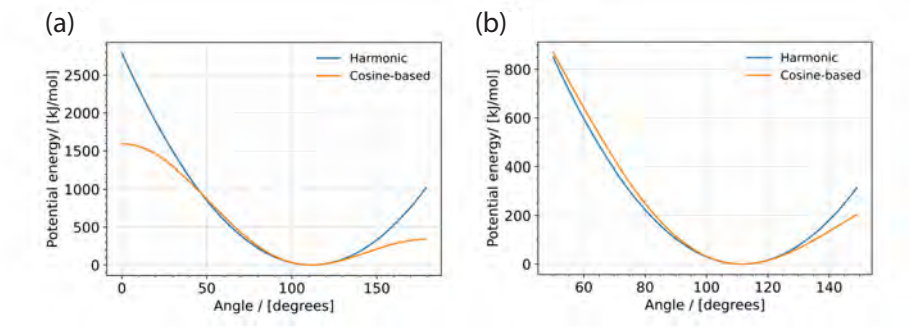

Figure C.10: Comparison of the harmonic and cosine-based angle potential functions for HNO_2 molecule in the range from 0° to 180° in (a) and a zoom in the range from 50° to 150° (b).

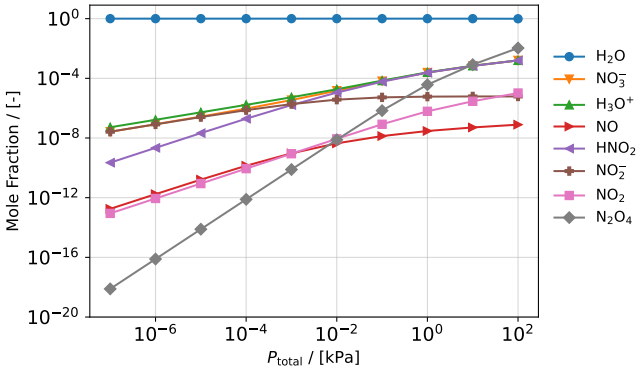

Figure C.11: The mole fractions of species in the aqueous phase as a function of the total gas pressure (P_{total}) at 273 K.

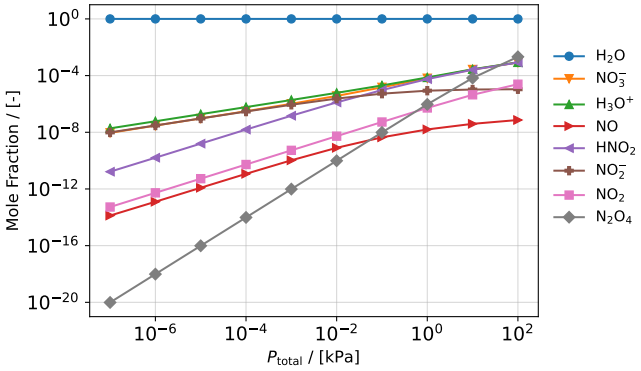

Figure C.12: The mole fractions of species in the aqueous phase as a function of the total gas pressure (P_{total}) at 313 K.

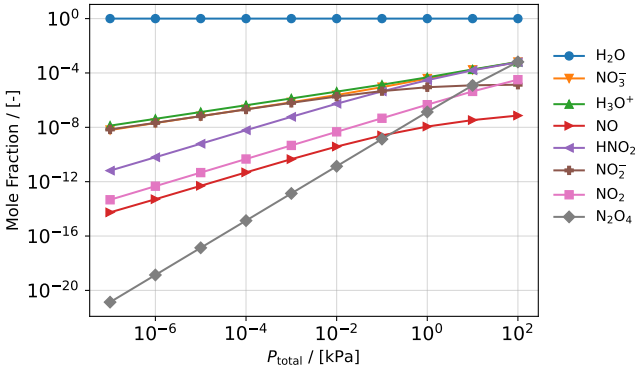

Figure C.13: The mole fractions of species in the aqueous phase as a function of the total gas pressure (P_{total}) at 333 K.

C

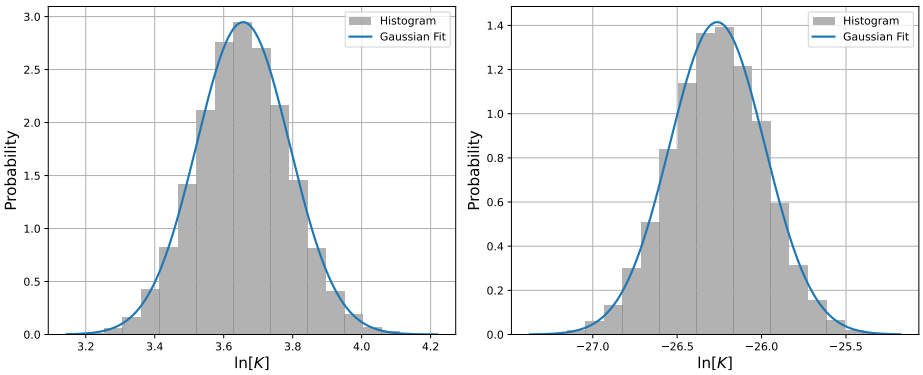

Figure C.14: The probability distributions as a function of $\ln[K]$ are shown as histograms. The left-hand side histogram is for reaction R2 ($2\,NO_2 + 2\,H_2O \rightleftharpoons HNO_2 + NO_3^- + H_3O^+$), and the right-hand side histogram is for reaction R4 ($3\,HNO_2 \rightleftharpoons NO_3^- + H_3O^+ + 2\,NO$). The corresponding fits to a Gaussian distribution function at 273 K are also shown.

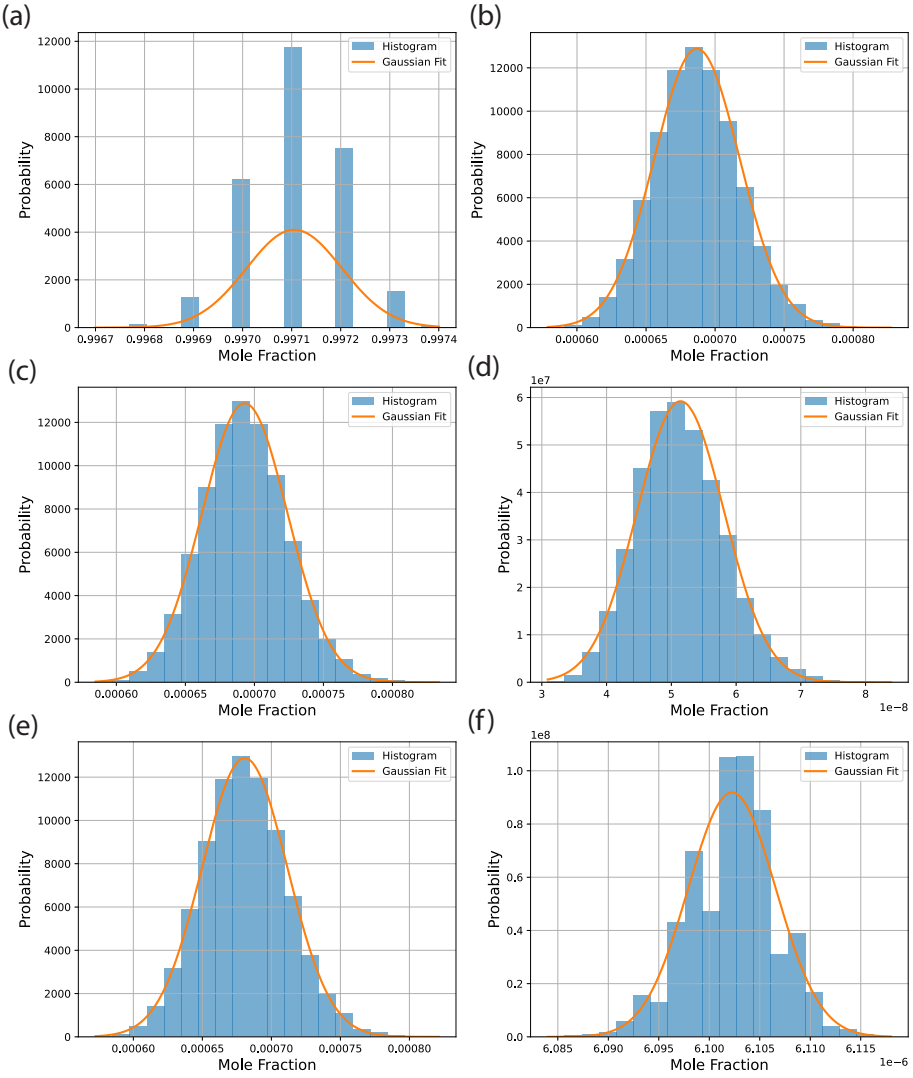

Figure C.15: The probability distributions as a function of the mole fraction for each species are shown as histograms. (a) corresponds to the histogram for H_2O, similarly (b) for NO_3^-, (c) for H_3O^+, (d) for NO, (e) for HNO_2, and (f) for NO_2^-. The corresponding fits to a Gaussian distribution function at 273 K are also shown.

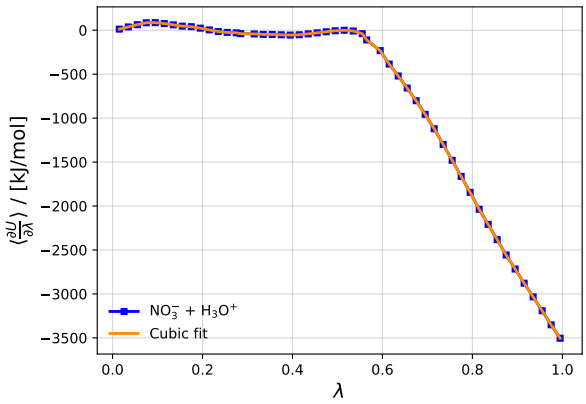

Figure C.16: $\left\langle \frac{\partial U}{\partial \lambda} \right\rangle$ as a function of λ and the corresponding cubic spline fit for the $NO_3^- + H_3O^+$ system in water at 298 K.

C

Appendix D- Supporting data for Chapter 6

D

Table D.1: L-J parameters for O-O_w (O_w being the oxygen atom of water molecule) obtained by fitting to the different energy surfaces from Suijker & Bagheri [323].

	ϵ/k_B / [K]	σ / [Å]
3 $A_2(1)$	4.2	3.965
3 $B_1(1)$	288.0	2.5
3 $B_2(1)$	163.2	2.7
1 $A_1(2)$	6.0	4.0
1 $A_2(1)$	6.0	4.0
1 $B_1(1)$	328.8	2.4
1 $B_2(1)$	205.2	2.56

Table D.2: Self-diffusion coefficients (in units of 10^{-9} m^2s^{-1}) of atomic oxygen at different temperatures (273 K - 333 K) using the force fields fitted to the different energy surfaces from Suijker & Bagheri [323]. The pressure is 1 bar. The self-diffusion coefficients are corrected for finite-size effects according to Equation 2.66. The water model used is the TIP4P/2005 water model [61]. The standard deviations are given in the subscripts.

	273 K	298 K	313 K	333 K
3 $A_2(1)$	$1.37_{0.05}$	$2.72_{0.06}$	$3.78_{0.06}$	$5.5_{0.2}$
3 $B_1(1)$	$4.11_{0.08}$	$5.7_{0.1}$	$7.4_{0.4}$	$9.3_{0.1}$
3 $B_2(1)$	$3.10_{0.05}$	$5.05_{0.07}$	$6.4_{0.2}$	$8.2_{0.1}$
1 $A_1(2)$	$1.14_{0.01}$	$2.49_{0.05}$	$3.35_{0.02}$	$5.0_{0.2}$
1 $B_1(1)$	$4.5_{0.1}$	$6.8_{0.1}$	$8.23_{0.06}$	$10.53_{0.09}$
1 $B_2(1)$	$4.260_{0.005}$	$6.16_{0.05}$	$7.54_{0.04}$	$9.62_{0.03}$

Table D.3: Excess chemical potentials (in units of K when divided by k_B) of atomic oxygen at different temperatures (273 K - 333 K) using the force fields fitted to the different energy surfaces from Suijker & Bagheri [323]. The pressure is 1 bar. The water model used is the TIP3P water model [60]. The standard deviations are given in the subscripts.

	273 K	298 K	313 K	333 K
3 $A_2(1)$	2536_4	2554_3	2558_6	2534_3
3 $B_1(1)$	-1168_4	-1051_4	-986_4	-908_7
3 $B_2(1)$	-173_4	-80_3	-30_2	-27_2
1 $A_1(2)$	2761_9	2786_4	2794_4	2782_2
1 $B_1(1)$	-1371_2	-1254_4	-1189_3	-1108_4
1 $B_2(1)$	-526_{10}	-431_9	-381_7	-316_9

Table D.4: Henry coefficients (in units of 10^{-5} mol/(m^3 Pa)) of atomic oxygen at different temperatures (273 K - 333 K) using the force fields fitted to the different energy surfaces from Suijker & Bagheri [323]. The pressure is 1 bar. The water model used is the TIP3P water model [60]. The standard deviations are given in the subscripts.

	273 K	298 K	313 K	333 K
3 $A_2(1)$	$0.00409_{0.00007}$	$0.00780_{0.00007}$	$0.0109_{0.0002}$	$0.0180_{0.0002}$
3 $B_1(1)$	3182_5	1399_2	928_1	554_1
3 $B_2(1)$	$83.3_{0.1}$	$53.7_{0.1}$	$43.8_{0.1}$	$35.4_{0.1}$
1 $A_1(2)$	$0.00176_{0.00006}$	$0.00353_{0.00007}$	$0.00529_{0.00007}$	$0.00893_{0.00006}$
1 $B_1(1)$	6705_6	2778_4	1776_2	1058_1
1 $B_2(1)$	301_1	$174.4_{0.5}$	$133.8_{0.3}$	$99.4_{0.3}$

Table D.5: Self-diffusion coefficients of the L-J particle (in units of 10^{-9} m^2s^{-1}) for different temperatures (300 K - 350 K) and for different values of ϵ/k_B (20 K - 170 K) for a value of $\sigma = 2.83$ Å. The pressure is 1 bar. The self-diffusion coefficients are corrected for finite-size effects according to Equation 2.66. The L-J parameters are the cross-interaction terms between the L-J particle and O of the water molecule. The standard deviations are given in the subscripts.

ϵ/k_B / [K]	300 K	325 K	350 K
21.59	$7.97_{0.04}$	$10.66_{0.07}$	$13.3_{0.4}$
83.61	$4.9_{0.2}$	$7.5_{0.2}$	$10.7_{0.1}$
118.24	$4.8_{0.2}$	$6.4_{0.1}$	$9.6_{0.2}$
144.81	$4.28_{0.05}$	$6.3_{0.1}$	$9.3_{0.1}$
167.22	$4.2_{0.1}$	$6.1_{0.1}$	$8.28_{0.01}$

Table D.6: Self-diffusion coefficients of the L-J particle (in units of 10^{-9} m^2s^{-1}) for different temperatures (300 K - 350 K) and for different values of ϵ/k_B (20 K - 170 K) for a value of $\sigma = 3.08$ Å. The pressure is 1 bar. The self-diffusion coefficients are corrected for finite-size effects according to Equation 2.66. The water model used is the TIP4P/2005 water model [61]. The standard deviations are given in the subscripts.

ϵ/k_B / [K]	300 K	325 K	350 K
21.59	$5.4_{0.2}$	$7.6_{0.2}$	$10.7_{0.1}$
83.61	$3.2_{0.2}$	$5.5_{0.1}$	$7.8_{0.1}$
118.24	$2.9_{0.2}$	$4.8_{0.1}$	$6.9_{0.3}$
144.81	$3.0_{0.1}$	$4.8_{0.1}$	$6.6_{0.1}$
167.22	$2.8_{0.1}$	$4.4_{0.1}$	$6.5_{0.2}$

Table D.7: Self-diffusion coefficients of the L-J particle (in units of 10^{-9} m^2s^{-1}) for different temperatures (300 K - 350 K) and for different values of ϵ/k_B (20 K - 170 K) for a value of $\sigma = 3.33$ Å. The pressure is 1 bar. The self-diffusion coefficients are corrected for finite-size effects according to Equation 2.66. The water model used is the TIP4P/2005 water model [61]. The standard deviations are given in the subscripts.

ϵ/k_B / [K]	300 K	325 K	350 K
21.59	$3.5_{0.1}$	$5.85_{0.02}$	$8.5_{0.2}$
83.61	$2.41_{0.03}$	$4.0_{0.1}$	$5.9_{0.2}$
118.24	$2.2_{0.1}$	$3.7_{0.2}$	$5.6_{0.1}$
144.81	$2.4_{0.1}$	$3.8_{0.1}$	$5.2_{0.2}$
167.22	$2.0_{0.1}$	$3.5_{0.1}$	$5.2_{0.1}$

Table D.8: Self-diffusion coefficients of the L-J particle (in units of 10^{-9} m^2s^{-1}) for different temperatures (300 K - 350 K) and for different values of ϵ/k_B (20 K - 170 K) for a value of $\sigma = 3.58$ Å. The pressure is 1 bar. The self-diffusion coefficients are corrected for finite-size effects according to Equation 2.66. The water model used is the TIP4P/2005 water model [61]. The standard deviations are given in the subscripts.

ϵ/k_B / [K]	300 K	325 K	350 K
21.59	$2.6_{0.2}$	$4.5_{0.1}$	$7.1_{0.3}$
83.61	$2.05_{0.03}$	$3.2_{0.1}$	$5.0_{0.1}$
118.24	$1.71_{0.02}$	$3.2_{0.1}$	$4.6_{0.1}$
144.81	$1.74_{0.03}$	$2.90_{0.03}$	$4.54_{0.02}$
167.22	$1.71_{0.01}$	$2.8_{0.1}$	$4.34_{0.04}$

Table D.9: Self-diffusion coefficients of the L-J particle (in units of 10^{-9} m^2s^{-1}) for different temperatures (300 K - 350 K) and for different values of ϵ/k_B (20 K - 170 K) for a value of $\sigma = 3.83$ Å. The pressure is 1 bar. The self-diffusion coefficients are corrected for finite-size effects according to Equation 2.66. The water model used is the TIP4P/2005 water model [61]. The standard deviations are given in the subscripts.

ϵ/k_B / [K]	300 K	325 K	350 K
21.59	$2.15_{0.02}$	$3.5_{0.1}$	$5.5_{0.1}$
83.61	$1.7_{0.1}$	$2.9_{0.1}$	$4.5_{0.3}$
118.24	$1.45_{0.02}$	$2.6_{0.1}$	$4.03_{0.02}$
144.81	$1.53_{0.01}$	$2.4_{0.1}$	$3.88_{0.04}$
167.22	$1.5_{0.1}$	$2.45_{0.04}$	$3.9_{0.1}$

Table D.10: Excess chemical potentials of the L-J particle (in units of K when divided by k_B) for different temperatures (300 K - 350 K) and for different values of ϵ/k_B (20 K - 170 K) for a value of $\sigma = 2.83$ Å. The pressure is 1 bar. The water model used is the TIP4P/2005 water model [61]. The standard deviations are given in the subscripts.

ϵ/k_B / [K]	300 K	325 K	350 K
21.59	1085_2	1143_2	1186_1
83.61	752_3	839_2	910_2
118.24	444_2	545_3	629_3
144.81	185_2	301_1	393_3
167.22	-37_2	82_2	184_3

Table D.11: Excess chemical potentials of the L-J particle (in units of K when divided by k_B) for different temperatures (300 K - 350 K) and for different values of ϵ/k_B (20 K - 170 K) for a value of $\sigma = 3.08$ Å. The pressure is 1 bar. The water model used is the TIP4P/2005 water model [61]. The standard deviations are given in the subscripts.

ϵ/k_B / [K]	300 K	325 K	350 K
21.59	1477_6	1551_2	1595_3
83.61	1069_6	1173_5	1252_4
118.24	684_6	805_6	895_2
144.81	359_6	498_2	601_4
167.22	76_5	222_3	341_7

Table D.12: Excess chemical potentials of the L-J particle (in units of K when divided by k_B) for different temperatures (300 K - 350 K) and for different values of ϵ/k_B (20 K - 170 K) for a value of $\sigma = 3.33$ Å. The pressure is 1 bar. The water model used is the TIP4P/2005 water model [61]. The standard deviations are given in the subscripts.

ϵ/k_B / [K]	300 K	325 K	350 K
21.59	1943_{10}	2027_2	2074_4
83.61	1436_{15}	1565_{13}	1651_{12}
118.24	966_{19}	1112_{10}	1215_6
144.81	555_{11}	717_9	839_8
167.22	216_{10}	382_8	518_2

Table D.13: Excess chemical potentials of the L-J particle (in units of K when divided by k_B) for different temperatures (300 K - 350 K) and for different values of ϵ/k_B (20 K - 170 K) for a value of $\sigma = 3.58$ Å. The pressure is 1 bar. The water model used is the TIP4P/2005 water model [61]. The standard deviations are given in the subscripts.

ϵ/k_B / [K]	300 K	325 K	350 K
21.59	2490_{11}	2570_{7}	2626_{8}
83.61	1869_{22}	2016_{10}	2088_{15}
118.24	1277_{10}	1436_{25}	1567_{22}
144.81	796_{31}	959_{21}	1113_{7}
167.22	378_{29}	572_{17}	721_{9}

Table D.14: Excess chemical potentials of the L-J particle (in units of K when divided by k_B) for different temperatures (300 K - 350 K) and for different values of ϵ/k_B (20 K - 170 K) for a value of $\sigma = 3.83$ Å. The pressure is 1 bar. The water model used is the TIP4P/2005 water model [61]. The standard deviations are given in the subscripts.

ϵ/k_B / [K]	300 K	325 K	350 K
21.59	3082_{8}	3190_{7}	3238_{11}
83.61	2303_{35}	2495_{21}	2576_{22}
118.24	1707_{15}	1858_{35}	1961_{29}
144.81	1066_{25}	1251_{48}	1435_{31}
167.22	487_{44}	737_{29}	947_{16}

Table D.15: Henry coefficients of the L-J particle (in units of 10^{-5} mol/(m^3 Pa)) for different temperatures (300 K - 350 K) and for different values of ϵ/k_B (20 K - 170 K) for a value of $\sigma = 2.83$ Å. The pressure is 1 bar. The water model used is the TIP4P/2005 water model [61]. The standard deviations are given in the subscripts.

ϵ/k_B / [K]	300 K	325 K	350 K
21.59	$1.078_{0.004}$	$1.119_{0.006}$	$1.19_{0.01}$
83.61	$3.28_{0.04}$	$2.83_{0.02}$	$2.64_{0.01}$
118.24	$9.18_{0.04}$	$7.04_{0.08}$	$5.88_{0.06}$
144.81	$21.8_{0.2}$	$14.89_{0.09}$	$11.54_{0.1}$
167.22	$45.6_{0.5}$	$29.2_{0.1}$	$21.01_{0.2}$

Table D.16: Henry coefficients of the L-J particle (in units of 10^{-5} mol/(m^3 Pa)) for different temperatures (300 K - 350 K) and for different values of ϵ/k_B (20 K - 170 K) for a value of $\sigma = 3.08$ Å. The pressure is 1 bar. The water model used is the TIP4P/2005 water model [61]. The standard deviations are given in the subscripts.

ϵ/k_B / [K]	300 K	325 K	350 K
21.59	$0.293_{0.006}$	$0.318_{0.002}$	$0.371_{0.004}$
83.61	$1.14_{0.03}$	$1.02_{0.02}$	$0.99_{0.01}$
118.24	$4.1_{0.1}$	$3.15_{0.05}$	$2.75_{0.02}$
144.81	$12.2_{0.3}$	$8.11_{0.08}$	$6.37_{0.09}$
167.22	$31.4_{0.7}$	$19.0_{0.1}$	$13.4_{0.3}$

Table D.17: Henry coefficients of the L-J particle (in units of 10^{-5} mol/(m^3 Pa)) for different temperatures (300 K - 350 K) and for different values of ϵ/k_B (20 K - 170 K) for a value of $\sigma = 3.33$ Å. The pressure is 1 bar. The water model used is the TIP4P/2005 water model [61]. The standard deviations are given in the subscripts.

ϵ/k_B / [K]	300 K	325 K	350 K
21.59	$0.062_{0.002}$	$0.0732_{0.0006}$	$0.095_{0.001}$
83.61	$0.34_{0.02}$	$0.30_{0.01}$	$0.32_{0.01}$
118.24	$1.6_{0.1}$	$1.23_{0.04}$	$1.11_{0.02}$
144.81	$6.3_{0.2}$	$4.1_{0.1}$	$3.24_{0.08}$
167.22	$19.7_{0.6}$	$11.6_{0.3}$	$8.1_{0.4}$

Table D.18: Henry coefficients of the L-J particle (in units of 10^{-5} mol/(m^3 Pa)) for different temperatures (300 K - 350 K) and for different values of ϵ/k_B (20 K - 170 K) for a value of $\sigma = 3.58$ Å. The pressure is 1 bar. The water model used is the TIP4P/2005 water model [61]. The standard deviations are given in the subscripts.

ϵ/k_B / [K]	300 K	325 K	350 K
21.59	$0.0100_{0.0004}$	$0.0138_{0.0003}$	$0.0196_{0.0004}$
83.61	$0.079_{0.006}$	$0.076_{0.002}$	$0.091_{0.004}$
118.24	$0.57_{0.02}$	$0.45_{0.03}$	$0.41_{0.03}$
144.81	$2.9_{0.3}$	$2.0_{0.1}$	$1.5_{0.2}$
167.22	12_{1}	$6.5_{0.3}$	$4.5_{0.1}$

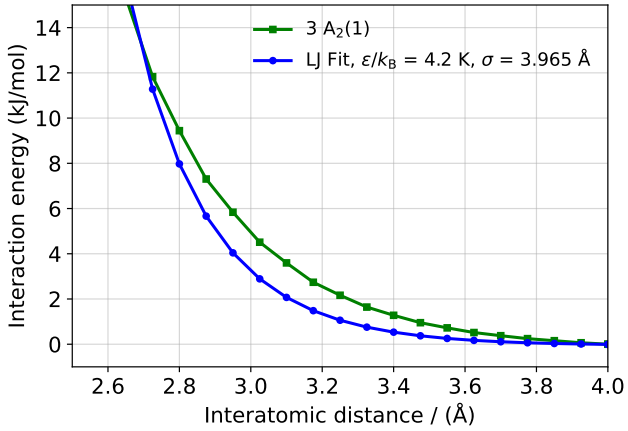

Figure D.1: Potential energy curve of the $3A_2(1)$ energy level obtained from *ab initio* quantum mechanical calculations retrieved from Suijker & Bagheri [323] (in green) and the corresponding L-J fit (in blue). The interatomic distance is between the atomic oxygen and the oxygen of the water molecule (O_w). Note that the L-J parameters (ϵ/k_B and σ) shown in the figure are the cross-interaction terms between O of the atomic oxygen and O of the water molecule. The fit was performed up to an interatomic distance of 10.0 Å, however, only a part of the curve is shown to clearly illustrate the differences between the fitted function and the *ab initio* data.

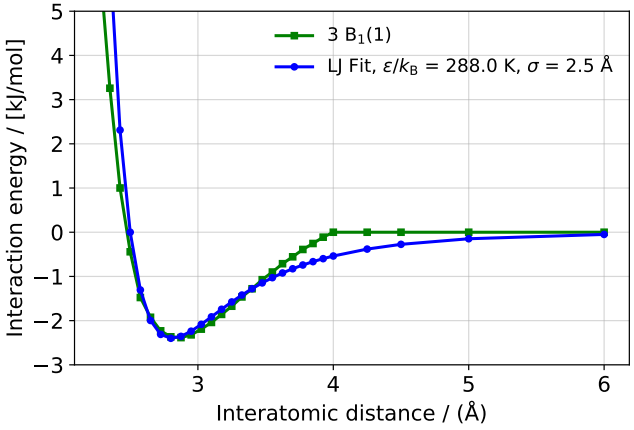

Figure D.2: Potential energy curve of the 3 $B_1(1)$ energy level obtained from *ab initio* quantum mechanical calculations retrieved from Suijker & Bagheri [323] (in green) and the corresponding L-J fit (in blue). The interatomic distance is between the atomic oxygen and the oxygen of the water molecule (O_w). Note that the L-J parameters (ϵ/k_B and σ) shown in the figure are the cross-interaction terms between O of the atomic oxygen and O of the water molecule. The fit was performed up to an interatomic distance of 10.0 Å, however, only a part of the curve is shown to clearly illustrate the differences between the fitted function and the *ab initio* data.

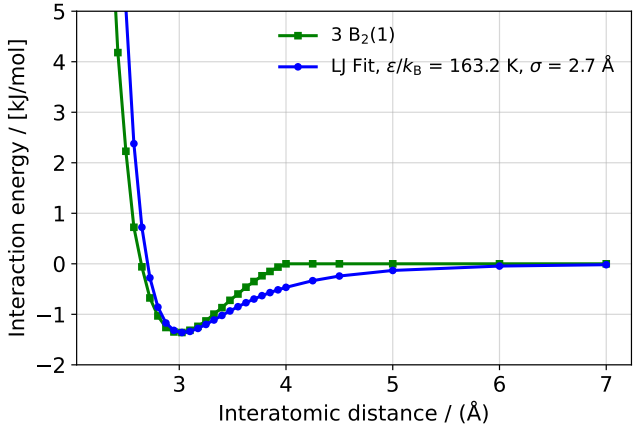

Figure D.3: Potential energy curve of the 3 $B_2(1)$ energy level obtained from *ab initio* quantum mechanical calculations retrieved from Suijker & Bagheri [323] (in green) and the corresponding L-J fit (in blue). The interatomic distance is between the atomic oxygen and the oxygen of the water molecule (O_w). Note that the L-J parameters (ϵ/k_B and σ) shown in the figure are the cross-interaction terms between O of the atomic oxygen and O of the water molecule. The fit was performed up to an interatomic distance of 10.0 Å, however, only a part of the curve is shown to clearly illustrate the differences between the fitted function and the *ab initio* data.

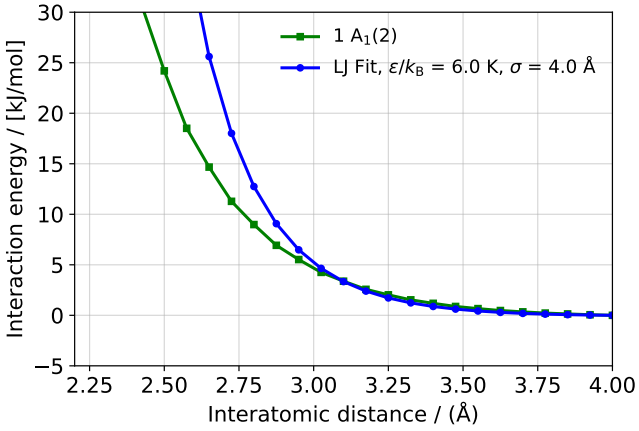

Figure D.4: Potential energy curve of the 1 $A_1(2)$ energy level obtained from *ab initio* quantum mechanical calculations retrieved from Suiker & Bagheri [323] (in green) and the corresponding L-J fit (in blue). The interatomic distance is between the atomic oxygen and the oxygen of the water molecule (O_w). Note that the L-J parameters (ϵ/k_B and σ) shown in the figure are the cross-interaction terms between O of the atomic oxygen and O of the water molecule. The fit was performed up to an interatomic distance of 10.0 Å, however, only a part of the curve is shown to clearly illustrate the differences between the fitted function and the *ab initio* data.

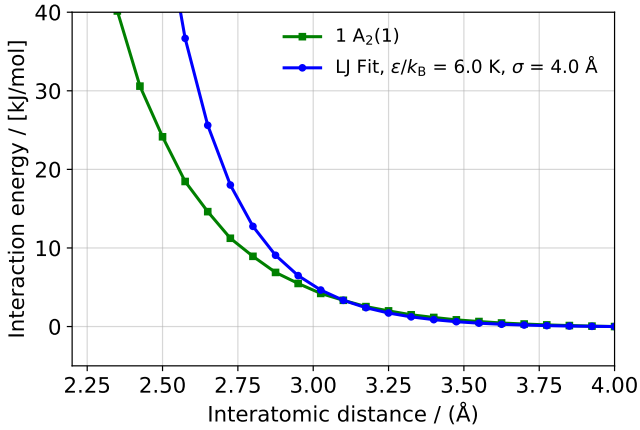

Figure D.5: Potential energy curve of the 1 $A_2(1)$ energy level obtained from *ab initio* quantum mechanical calculations retrieved from Suijker & Bagheri [323] (in green) and the corresponding L-J fit (in blue). The interatomic distance is between the atomic oxygen and the oxygen of the water molecule (O_w). Note that the L-J parameters (ϵ/k_B and σ) shown in the figure are the cross-interaction terms between O of the atomic oxygen and O of the water molecule. The fit was performed up to an interatomic distance of 10.0 Å, however, only a part of the curve is shown to clearly illustrate the differences between the fitted function and the *ab initio* data.

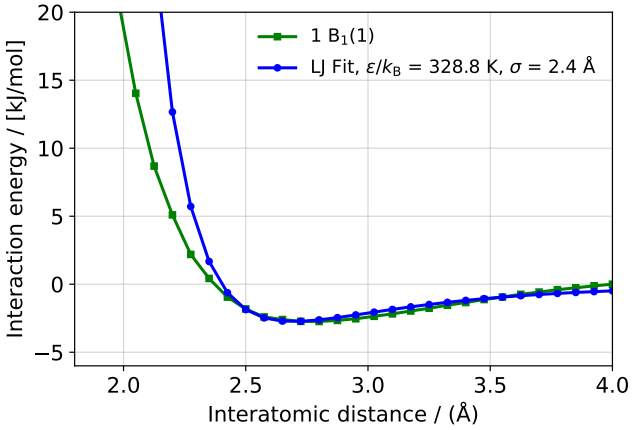

Figure D.6: Potential energy curve of the 1 $B_1(1)$ energy level obtained from *ab initio* quantum mechanical calculations retrieved from Suijker & Bagheri [323] (in green) and the corresponding L-J fit (in blue). The interatomic distance is between the atomic oxygen and the oxygen of the water molecule (O_w). Note that the L-J parameters (ϵ/k_B and σ) shown in the figure are the cross-interaction terms between O of the atomic oxygen and O of the water molecule. The fit was performed up to an interatomic distance of 10.0 Å, however, only a part of the curve is shown to clearly illustrate the differences between the fitted function and the *ab initio* data.

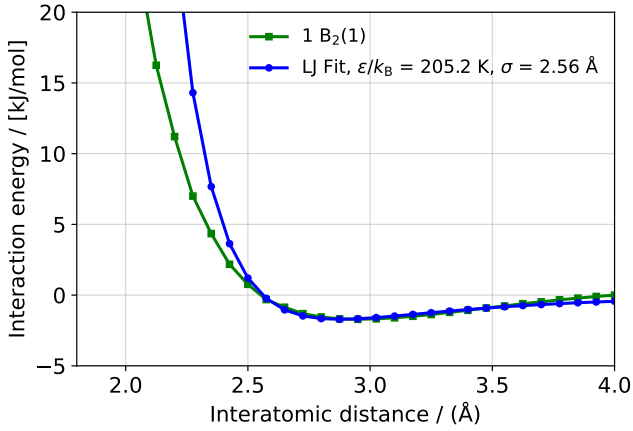

Figure D.7: Potential energy curve of the 1 $B_2(1)$ energy level obtained from *ab initio* quantum mechanical calculations retrieved from Suijker & Bagheri [323] (in green) and the corresponding L-J fit (in blue). The interatomic distance is between the atomic oxygen and the oxygen of the water molecule (O_w). Note that the L-J parameters (ϵ/k_B and σ) shown in the figure are the cross-interaction terms between O of the atomic oxygen and O of the water molecule. The fit was performed up to an interatomic distance of 10.0 Å, however, only a part of the curve is shown to clearly illustrate the differences between the fitted function and the *ab initio* data.

Table D.19: Henry coefficients of the L-J particle (in units of 10^{-5} mol/(m^3 Pa)) for different temperatures (300 K - 350 K) and for different values of ϵ/k_B (20 K - 170 K) for a value of $\sigma = 3.83$ Å. The pressure is 1 bar. The water model used is the TIP4P/2005 water model [61]. The standard deviations are given in the subscripts.

ϵ/k_B / [K]	300 K	325 K	350 K
21.59	$0.00140_{0.00005}$	$0.00205_{0.00006}$	$0.003_{0.0001}$
83.61	$0.019_{0.002}$	$0.017_{0.001}$	$0.023_{0.001}$
118.24	$0.15_{0.05}$	$0.12_{0.01}$	$0.13_{0.01}$
144.81	$1.2_{0.1}$	$0.8_{0.1}$	$0.59_{0.05}$
167.22	8_{1}	$3.9_{0.3}$	$2.4_{0.1}$

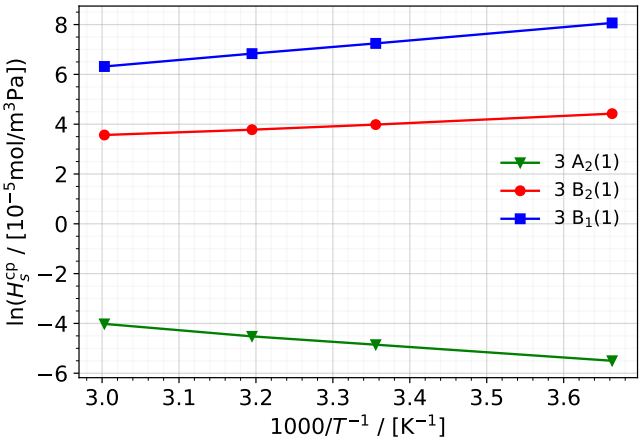

Figure D.8: Henry coefficients for O(^{3}P) in water as a function of inverse temperature in logarithmic scale using force fields fitted to 3 $B_1(1)$, 3 $B_2(1)$, and 3 $A_2(1)$ energy surfaces from Suijker & Bagheri [323]. The pressure is 1 bar.

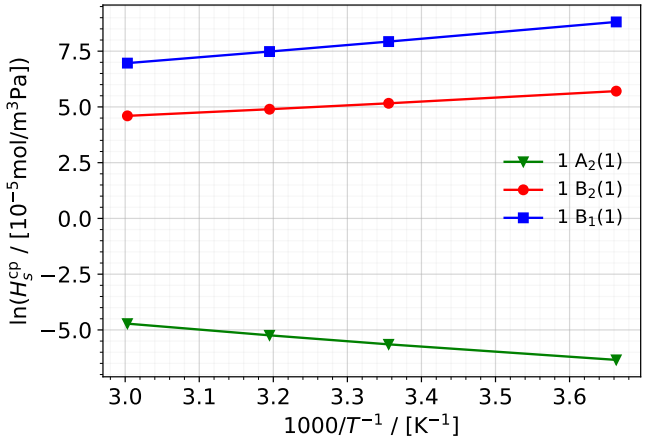

Figure D.9: Henry coefficients for O(^{1}D) in water as a function of inverse temperature in logarithmic scale using force fields fitted to 1 $B_1(1)$, 1 $B_2(1)$, and 1 $A_1(2)$ energy surfaces from Suijker & Bagheri [323]. The pressure is 1 bar.

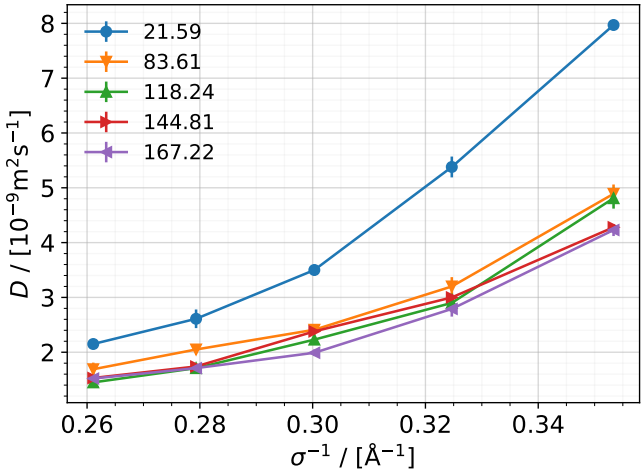

Figure D.10: Self-diffusion coefficients as a function of σ^{-1} for the L-J particle of different ϵ/k_B in water at 300 K. The pressure is 1 bar. The self-diffusion coefficients are corrected for finite-size effects according to Equation 2.66. The water model used is the TIP4P/2005 model [61]. Numbers in the legend represent values of ϵ/k_B. Error bars are estimated based on the standard deviation of 6 production blocks.

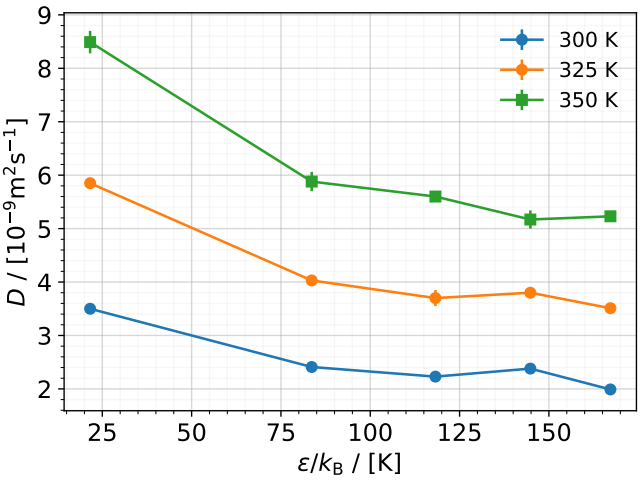

Figure D.11: Self-diffusion coefficients as a function of ϵ/k_B for the L-J particle of $\sigma = 3.33$ Å in water for different temperatures (300 K - 350 K). The pressure is 1 bar. The self-diffusion coefficients are corrected for finite-size effects according to Equation 2.66. The water model used is the TIP4P/2005 model [61]. Error bars are estimated based on the standard deviation of 6 production blocks.

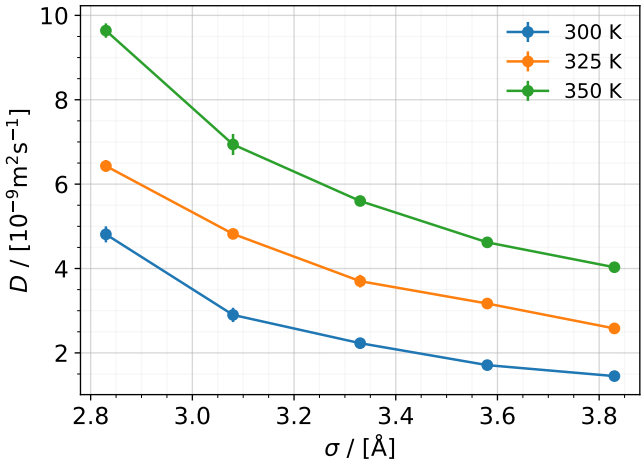

Figure D.12: Self-diffusion coefficients as a function of σ for the L-J particle of 118.24 K ϵ/k_B in water for different temperatures (300 K - 350 K). The pressure is 1 bar. The self-diffusion coefficients are corrected for finite-size effects according to Equation 2.66. The water model used is the TIP4P/2005 model [61]. Error bars are estimated based on the standard deviation of 6 production blocks.

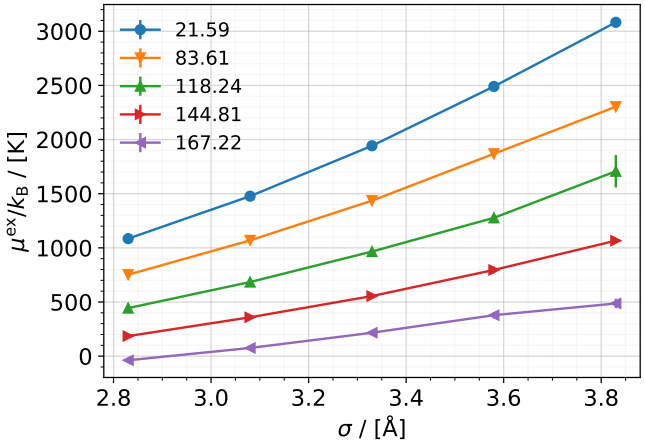

Figure D.13: Excess chemical potentials as a function of σ for the L-J particle of different ϵ/k_B in water at 300 K. The pressure is 1 bar. The water model used is the TIP4P/2005 model [61]. Numbers in the legend represent values of ϵ/k_B. Error bars are estimated based on the standard deviation of 5 production blocks.

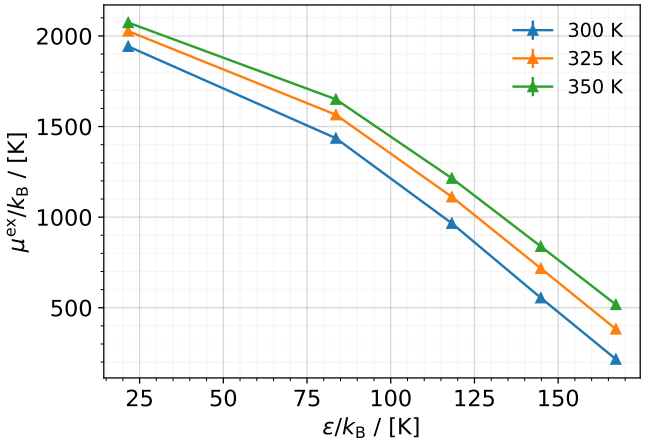

Figure D.14: Excess chemical potentials as a function of ϵ/k_B for the L-J particle of $\sigma = 3.33$ Å in water for different temperatures (300 K - 350 K). The pressure is 1 bar. The water model used is the TIP4P/2005 model [61]. Error bars are estimated based on the standard deviation of 5 production blocks.

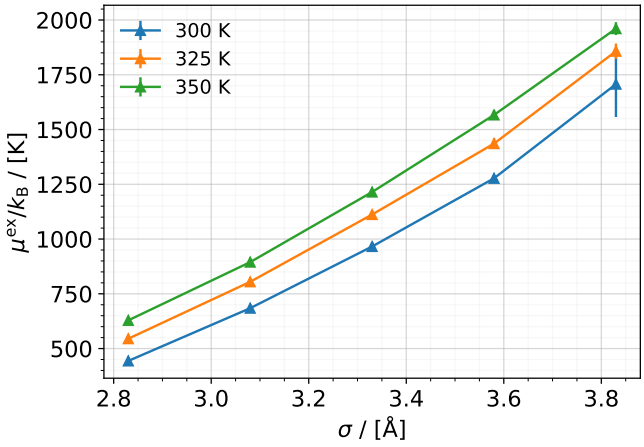

Figure D.15: Excess chemical potentials as a function of σ for the L-J particle of 118.24 K ϵ/k_B in water for different temperatures (300 K - 350 K). The pressure is 1 bar. The water model used is the TIP4P/2005 model [61]. Error bars are estimated based on the standard deviation of 5 production blocks.

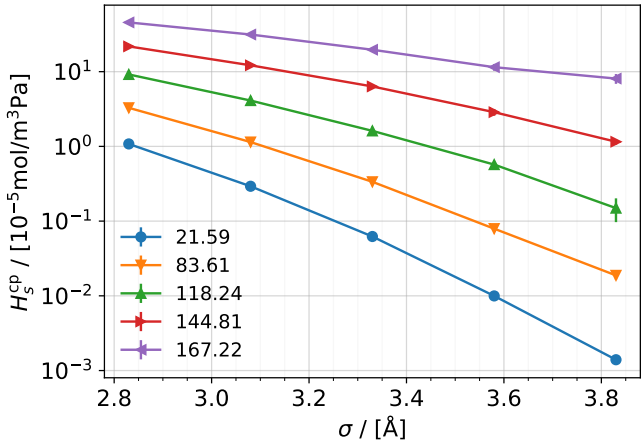

Figure D.16: Henry coefficients as a function of σ for the L-J particle of different ϵ/k_B in water at 300 K in logarithmic scale. The pressure is 1 bar. The water model used is the TIP4P/2005 model [61]. Numbers in the legend represent values of ϵ/k_B. Error bars are estimated based on the standard deviation of 5 production blocks.

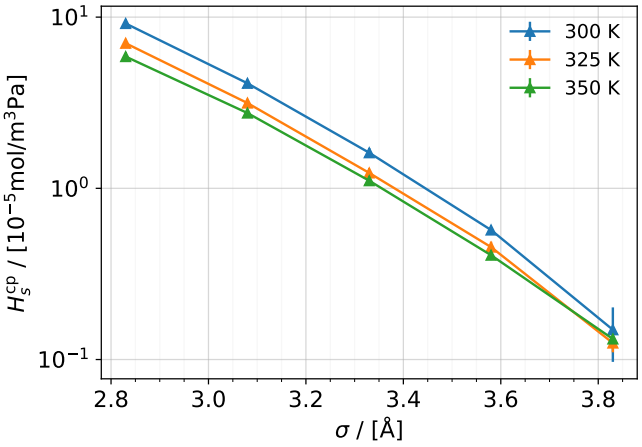

Figure D.17: Henry coefficients as a function of σ for the L-J particle of 118.24 K ϵ/k_B in water for different temperatures (300 K - 350 K) in logarithmic scale. The pressure is 1 bar. The water model used is the TIP4P/2005 model [61]. Error bars are estimated based on the standard deviation of 5 production blocks.

Appendix E- Supporting data for Chapter 7

Table E.1: L-J parameters of the different species used in this work. O_w is the oxygen atom of the TIP4P/2005 [61] water molecule. The partial charges of Na^+ and Cl^- are 0.85 e and -0.85 e, respectively.

	ϵ/k_B / [K]	σ / [Å]
Na^+ - Na^+	177.08484	2.21737
Na^+ - Cl^-	173.06027	3.00512
Cl^- - Cl^-	9.251769	4.69906
Na^+ - O_w	95.423247	2.60838
Cl^- - O_w	7.4548886	4.23867

Table E.2: The number of water molecules (N_{H_2O}), Na^+ (N_{Na^+}), and Cl^- (N_{Cl^-}) ions in the simulations. Molality, m, is in the units of $\left[\frac{\text{mol}_{\text{salt}}}{\text{kg}_{\text{ solvent}}}\right]$. The average box volume ($\langle V \rangle$) in units of Å^3 is reported for each molality.

m	N_{H_2O}	N_{Na^+}	N_{Cl^-}	$\langle V \rangle$
0	500	0	0	15058.5
0.33	500	3	3	15148.8
0.67	500	6	6	15238.6
1.00	500	9	9	15341.4

Table E.3: Viscosities of aqueous solution with the L-J particle (in units of mPa s) for different molalities (0.00 - 1.00 m) and for different values of ϵ/k_{B} (20 K - 170 K) for a value of $\sigma = 2.83\,\text{Å}$. The pressure is 1 bar. The L-J parameters are the cross interaction terms between the L-J particle and O of the water molecule. The standard deviations are given in the subscripts.

ϵ/k_{B} / [K]	0.00 m	0.33 m	0.67 m	1.00 m
21.59	$0.83_{0.02}$	$0.83_{0.02}$	$0.85_{0.02}$	$0.85_{0.02}$
83.61	$0.86_{0.01}$	$0.83_{0.01}$	$0.93_{0.02}$	$0.93_{0.02}$
118.24	$0.83_{0.01}$	$0.85_{0.02}$	$0.86_{0.01}$	$0.94_{0.01}$
144.81	$0.79_{0.02}$	$0.82_{0.02}$	$0.86_{0.01}$	$0.98_{0.04}$
167.22	$0.80_{0.01}$	$0.84_{0.01}$	$0.90_{0.02}$	$0.95_{0.01}$

Table E.4: Viscosities of aqueous solution with the L-J particle (in units of mPa s) for different molalities (0.00 - 1.00 m) and for different values of ϵ/k_{B} (20 K - 170 K) for a value of $\sigma = 3.08\,\text{Å}$. The pressure is 1 bar. The L-J parameters are the cross interaction terms between the L-J particle and O of the water molecule. The standard deviations are given in the subscripts.

ϵ/k_{B} / [K]	0.00 m	0.33 m	0.67 m	1.00 m
21.59	$0.82_{0.02}$	$0.84_{0.01}$	$0.88_{0.02}$	$0.93_{0.02}$
83.61	$0.82_{0.02}$	$0.85_{0.01}$	$0.90_{0.02}$	$0.94_{0.02}$
118.24	$0.83_{0.02}$	$0.82_{0.02}$	$0.89_{0.01}$	$0.96_{0.01}$
144.81	$0.82_{0.01}$	$0.85_{0.01}$	$0.90_{0.01}$	$0.99_{0.01}$
167.22	$0.81_{0.01}$	$0.86_{0.02}$	$0.92_{0.02}$	$0.95_{0.03}$

Table E.5: Viscosities of aqueous solution with the L-J particle (in units of mPa s) for different molalities (0.00 - 1.00 m) and for different values of ϵ/k_{B} (20 K - 170 K) for a value of $\sigma = 3.33\,\text{Å}$. The pressure is 1 bar. The L-J parameters are the cross interaction terms between the L-J particle and O of the water molecule. The standard deviations are given in the subscripts.

ϵ/k_{B} / [K]	0.00 m	0.33 m	0.67 m	1.00 m
21.59	$0.80_{0.01}$	$0.82_{0.03}$	$0.88_{0.01}$	$0.95_{0.01}$
83.61	$0.76_{0.03}$	$0.85_{0.02}$	$0.88_{0.01}$	$0.90_{0.03}$
118.24	$0.80_{0.01}$	$0.90_{0.03}$	$0.89_{0.01}$	$0.93_{0.01}$
144.81	$0.83_{0.05}$	$0.87_{0.02}$	$0.90_{0.01}$	$0.96_{0.02}$
167.22	$0.80_{0.01}$	$0.81_{0.03}$	$0.89_{0.01}$	$0.95_{0.01}$

Table E.6: Viscosities of aqueous solution with the L-J particle (in units of mPa s) for different molalities (0.00 - 1.00 m) and for different values of ϵ/k_{B} (20 K - 170 K) for a value of $\sigma = 3.58\,\text{Å}$. The pressure is 1 bar. The L-J parameters are the cross interaction terms between the L-J particle and O of the water molecule. The standard deviations are given in the subscripts.

ϵ/k_{B} / [K]	0.00 m	0.33 m	0.67 m	1.00 m
21.59	$0.81_{0.02}$	$0.81_{0.01}$	$0.87_{0.02}$	$0.91_{0.02}$
83.61	$0.78_{0.01}$	$0.86_{0.03}$	$0.87_{0.03}$	$0.96_{0.01}$
118.24	$0.83_{0.01}$	$0.86_{0.03}$	$0.91_{0.02}$	$0.96_{0.03}$
144.81	$0.78_{0.01}$	$0.81_{0.01}$	$0.90_{0.01}$	$0.99_{0.02}$
167.22	$0.81_{0.01}$	$0.87_{0.02}$	$0.94_{0.03}$	$0.98_{0.01}$

Table E.7: Viscosities of aqueous solution with the L-J particle (in units of mPa s) for different molalities (0.00 - 1.00 m) and for different values of ϵ/k_B (20 K - 170 K) for a value of $\sigma = 3.83\,\text{Å}$. The pressure is 1 bar. The L-J parameters are the cross interaction terms between the L-J particle and O of the water molecule. The standard deviations are given in the subscripts.

ϵ/k_B / [K]	0.00 m	0.33 m	0.67 m	1.00 m
21.59	$0.82_{0.02}$	$0.85_{0.01}$	$0.91_{0.04}$	$0.96_{0.01}$
83.61	$0.81_{0.01}$	$0.86_{0.02}$	$0.94_{0.04}$	$0.96_{0.02}$
118.24	$0.82_{0.01}$	$0.86_{0.03}$	$0.93_{0.02}$	$1.01_{0.05}$
144.81	$0.86_{0.02}$	$0.91_{0.01}$	$0.91_{0.01}$	$0.96_{0.01}$
167.22	$0.80_{0.02}$	$0.84_{0.02}$	$0.91_{0.01}$	$0.95_{0.01}$

Table E.8: Self-diffusion coefficients of the L-J particle (in units of 10^{-9} $\mathrm{m^2 s^{-1}}$) for different molalities (0.00 - 1.00 m) and for different values of ϵ/k_B (20 K - 170 K) for a value of $\sigma = 2.83\,\text{Å}$. The pressure is 1 bar. The self-diffusion coefficients are corrected for finite-size effects according to Equation 2.66. The L-J parameters are the cross interaction terms between the L-J particle and O of the water molecule. The standard deviations are given in the subscripts.

ϵ/k_B / [K]	0.00 m	0.33 m	0.67 m	1.00 m
21.59	$7.97_{0.04}$	$7.37_{0.04}$	$7.5_{0.2}$	$7.5_{0.2}$
83.61	$4.9_{0.2}$	$4.6_{0.1}$	$4.5_{0.1}$	$4.69_{0.05}$
118.24	$4.8_{0.2}$	$4.47_{0.06}$	$4.2_{0.1}$	$3.9_{0.1}$
144.81	$4.28_{0.05}$	$4.35_{0.06}$	$4.1_{0.1}$	$3.84_{0.08}$
167.22	$4.2_{0.1}$	$4.09_{0.07}$	$3.9_{0.1}$	$3.58_{0.04}$

Table E.9: Self-diffusion coefficients of the L-J particle (in units of 10^{-9} m^2s^{-1}) for different molalities (0.00 - 1.00 m) and for different values of ϵ/k_B (20 K - 170 K) for a value of σ = 3.08 Å. The pressure is 1 bar. The self-diffusion coefficients are corrected for finite-size effects according to Equation 2.66. The L-J parameters are the cross interaction terms between the L-J particle and O of the water molecule. The standard deviations are given in the subscripts.

ϵ/k_B / [K]	0.00 m	0.33 m	0.67 m	1.00 m
21.59	$5.4_{0.2}$	$4.7_{0.1}$	$5.0_{0.1}$	$4.60_{0.07}$
83.61	$3.2_{0.2}$	$3.2_{0.1}$	$2.96_{0.09}$	$2.86_{0.07}$
118.24	$2.9_{0.2}$	$2.9_{0.1}$	$3.0_{0.2}$	$2.6_{0.1}$
144.81	$3.00_{0.06}$	$2.78_{0.05}$	$2.69_{0.04}$	$2.65_{0.01}$
167.22	$2.8_{0.1}$	$2.65_{0.04}$	$2.52_{0.05}$	$2.36_{0.06}$

Table E.10: Self-diffusion coefficients of the L-J particle (in units of 10^{-9} m^2s^{-1}) for different molalities (0.00 - 1.00 m) and for different values of ϵ/k_B (20 K - 170 K) for a value of σ = 3.33 Å. The pressure is 1 bar. The self-diffusion coefficients are corrected for finite-size effects according to Equation 2.66. The L-J parameters are the cross interaction terms between the L-J particle and O of the water molecule. The standard deviations are given in the subscripts.

ϵ/k_B / [K]	0.00 m	0.33 m	0.67 m	1.00 m
21.59	$3.5_{0.1}$	$3.56_{0.03}$	$3.57_{0.05}$	$3.33_{0.04}$
83.61	$2.41_{0.03}$	$2.35_{0.02}$	$2.16_{0.08}$	$2.31_{0.03}$
118.24	$2.23_{0.07}$	$2.15_{0.06}$	$2.01_{0.08}$	$1.99_{0.05}$
144.81	$2.38_{0.05}$	$2.06_{0.03}$	$1.91_{0.07}$	$1.92_{0.02}$
167.22	$1.99_{0.06}$	$1.89_{0.09}$	$2.01_{0.03}$	$1.84_{0.02}$

Table E.11: Self-diffusion coefficients of the L-J particle (in units of 10^{-9} m^2s^{-1}) for different molalities (0.00 - 1.00 m) and for different values of ϵ/k_B (20 K - 170 K) for a value of $\sigma = 3.58$ Å. The pressure is 1 bar. The self-diffusion coefficients are corrected for finite-size effects according to Equation 2.66. The L-J parameters are the cross interaction terms between the L-J particle and O of the water molecule. The standard deviations are given in the subscripts.

ϵ/k_B / [K]	0.00 m	0.33 m	0.67 m	1.00 m
21.59	$2.6_{0.2}$	$2.4_{0.1}$	$2.41_{0.07}$	$2.36_{0.06}$
83.61	$2.05_{0.03}$	$1.8_{0.1}$	$1.93_{0.04}$	$1.74_{0.03}$
118.24	$1.71_{0.02}$	$1.67_{0.08}$	$1.52_{0.06}$	$1.54_{0.03}$
144.81	$1.74_{0.03}$	$1.63_{0.05}$	$1.61_{0.03}$	$1.50_{0.08}$
167.22	$1.71_{0.01}$	$1.67_{0.03}$	$1.52_{0.02}$	$1.45_{0.04}$

Table E.12: Self-diffusion coefficients of the L-J particle (in units of 10^{-9} m^2s^{-1}) for different molalities (0.00 - 1.00 m) and for different values of ϵ/k_B (20 K - 170 K) for a value of $\sigma = 3.83$ Å. The pressure is 1 bar. The self-diffusion coefficients are corrected for finite-size effects according to Equation 2.66. The L-J parameters are the cross interaction terms between the L-J particle and O of the water molecule. The standard deviations are given in the subscripts.

ϵ/k_B / [K]	0.00 m	0.33 m	0.67 m	1.00 m
21.59	$2.15_{0.02}$	$2.07_{0.04}$	$2.02_{0.03}$	$1.95_{0.07}$
83.61	$1.7_{0.1}$	$1.51_{0.02}$	$1.54_{0.04}$	$1.45_{0.03}$
118.24	$1.45_{0.02}$	$1.40_{0.04}$	$1.44_{0.03}$	$1.34_{0.02}$
144.81	$1.53_{0.01}$	$1.42_{0.02}$	$1.39_{0.03}$	$1.26_{0.04}$
167.22	$1.5_{0.1}$	$1.40_{0.04}$	$1.29_{0.02}$	$1.25_{0.02}$

Table E.13: Excess chemical potentials of the L-J particle (in units of K when divided by k_B) for different molalities (0.00 - 1.00 m) and for different values of ϵ/k_B (20 K - 170 K) for a value of $\sigma = 2.83$ Å. The pressure is 1 bar. The L-J parameters are the cross interaction terms between the L-J particle and O of the water molecule. The standard deviations are given in the subscripts.

ϵ/k_B / [K]	0.00 m	0.33 m	0.67 m	1.00 m
21.59	1085_2	1110_9	1113_{12}	1126_1
83.61	752_3	770_{12}	780_5	790_6
118.24	444_2	459_{10}	464_9	500_2
144.81	185_2	189_6	216_{26}	247_9
167.22	-38_2	-30_{11}	10_8	22_{12}

Table E.14: Excess chemical potentials of the L-J particle (in units of K when divided by k_B) for different molalities (0.00 - 1.00 m) and for different values of ϵ/k_B (20 K - 170 K) for a value of $\sigma = 3.08$ Å. The pressure is 1 bar. The L-J parameters are the cross interaction terms between the L-J particle and O of the water molecule. The standard deviations are given in the subscripts.

ϵ/k_B / [K]	0.00 m	0.33 m	0.67 m	1.00 m
21.59	1477_6	1473_9	1519_{12}	1528_1
83.61	1069_6	1102_{27}	1106_{18}	1111_4
118.24	684_6	679_{39}	745_{20}	731_3
144.81	359_6	377_{19}	397_{10}	423_9
167.22	76_5	113_{29}	114_1	160_6

Table E.15: Excess chemical potentials of the L-J particle (in units of K when divided by k_B) for different molalities (0.00 - 1.00 m) and for different values of ϵ/k_B (20 K - 170 K) for a value of $\sigma = 3.33$ Å. The pressure is 1 bar. The L-J parameters are the cross interaction terms between the L-J particle and O of the water molecule. The standard deviations are given in the subscripts.

ϵ/k_B / [K]	0.00 m	0.33 m	0.67 m	1.00 m
21.59	1943_{10}	1981_{15}	1965_{33}	1989_{1}
83.61	1436_{15}	1478_{34}	1490_{26}	$1530.0_{0.5}$
118.24	966_{19}	1015_{116}	1004_{22}	1013_{4}
144.81	555_{11}	579_{83}	650_{70}	710_{33}
167.22	216_{10}	234_{28}	254_{47}	270_{9}

Table E.16: Excess chemical potentials of the L-J particle (in units of K when divided by k_B) for different molalities (0.00 - 1.00 m) and for different values of ϵ/k_B (20 K - 170 K) for a value of $\sigma = 3.58$ Å. The pressure is 1 bar. The L-J parameters are the cross interaction terms between the L-J particle and O of the water molecule. The standard deviations are given in the subscripts.

ϵ/k_B / [K]	0.00 m	0.33 m	0.67 m	1.00 m
21.59	2490_{11}	2505_{44}	2512_{41}	2539_{1}
83.61	1869_{22}	1925_{63}	2032_{74}	2102_{2}
118.24	1277_{10}	1338_{103}	1483_{120}	1434_{6}
144.81	796_{31}	865_{109}	910_{205}	953_{88}
167.22	378_{29}	463_{199}	517_{125}	497_{100}

Table E.17: Henry coefficients of the L-J particle (in units of 10^{-5} mol/(m^3 Pa)) for different molalities (0.00 - 1.00 m) and for different values of ϵ/k_B (20 K - 170 K) for a value of $\sigma = 2.83\,\text{Å}$. The pressure is 1 bar. The L-J parameters are the cross interaction terms between the L-J particle and O of the water molecule. The standard deviations are given in the subscripts.

ϵ/k_B / [K]	0.00 m	0.33 m	0.67 m	1.00 m
21.59	$1.078_{0.004}$	$0.99_{0.03}$	$0.99_{0.4}$	$0.944_{0.002}$
83.61	$3.28_{0.04}$	$3.1_{0.1}$	$2.99_{0.05}$	$2.89_{0.06}$
118.24	$9.18_{0.04}$	$8.7_{0.3}$	$8.6_{0.3}$	$7.61_{0.59}$
144.81	$21.8_{0.2}$	$21.4_{0.4}$	20_2	$17.6_{\ 0.6}$
167.22	$45.6_{0.5}$	44_2	39_1	37_2

Table E.18: Henry coefficients of the L-J particle (in units of 10^{-5} mol/(m^3 Pa)) for different molalities (0.00 - 1.00 m) and for different values of ϵ/k_B (20 K - 170 K) for a value of $\sigma = 3.08\,\text{Å}$. The pressure is 1 bar. The L-J parameters are the cross interaction terms between the L-J particle and O of the water molecule. The standard deviations are given in the subscripts.

ϵ/k_B / [K]	0.00 m	0.33 m	0.67 m	1.00 m
21.59	$0.293_{0.006}$	$0.297_{0.09}$	$0.25_{0.01}$	$0.248_{0.001}$
83.61	$1.14_{0.03}$	$1.0_{0.1}$	$1.00_{0.06}$	$0.99_{0.01}$
118.24	$4.1_{0.1}$	$4.2_{0.5}$	$3.4_{0.2}$	$3.52_{0.31}$
144.81	$12.2_{0.3}$	$11.5_{0.7}$	$10.7_{0.4}$	$9.8_{0.3}$
167.22	$31.4_{0.7}$	27_3	$27.5_{0.2}$	$23.6_{0.4}$

Table E.19: Henry coefficients of the L-J particle (in units of 10^{-5} mol/(m^3 Pa)) for different molalities (0.00 - 1.00 m) and for different values of ϵ/k_B (20 K - 170 K) for a value of $\sigma = 3.33\,\text{Å}$. The pressure is 1 bar. The L-J parameters are the cross interaction terms between the L-J particle and O of the water molecule. The standard deviations are given in the subscripts.

ϵ/k_B / [K]	0.00 m	0.33 m	0.67 m	1.00 m
21.59	$0.062_{0.002}$	$0.546_{0.003}$	$0.058_{0.006}$	$0.0531_{0.0003}$
83.61	$0.34_{0.02}$	$0.29_{0.03}$	$0.28_{0.03}$	$0.2457_{0.0007}$
118.24	$1.6_{0.1}$	$1.4_{0.5}$	$1.4_{0.1}$	$1.37_{0.02}$
144.81	$6.3_{0.2}$	5_2	5_1	$3.8_{0.5}$
167.22	$19.7_{0.6}$	18_2	17_2	$16.4_{0.6}$

Table E.20: Henry coefficients of the L-J particle (in units of 10^{-5} mol/(m^3 Pa)) for different molalities (0.00 - 1.00 m) and for different values of ϵ/k_B (20 K - 170 K) for a value of $\sigma = 3.58\,\text{Å}$. The pressure is 1 bar. The L-J parameters are the cross interaction terms between the L-J particle and O of the water molecule. The standard deviations are given in the subscripts.

ϵ/k_B / [K]	0.00 m	0.33 m	0.67 m	1.00 m
21.59	$0.0100_{0.0004}$	$0.010_{0.001}$	$0.009_{0.001}$	$0.00851_{0.00004}$
83.61	$0.079_{0.006}$	$0.07_{0.02}$	$0.05_{0.01}$	$0.0492_{0.0005}$
118.24	$0.57_{0.02}$	$0.5_{0.2}$	$2.9_{0.2}$	$0.340_{0.008}$
144.81	$2.9_{0.3}$	$2.3_{0.9}$	2_1	$1.7_{0.7}$
167.22	11_1	9_6	7_3	8_4

E

Curriculum Vitae

June 5, 1997 Born in Kozhencherry, Kerala, India

2010 – 2015 High School
DPS-MIS, Doha, Qatar
– "Best Sportsperson of the year" award for the academic year 2012-2013

2015 – 2019 B.Tech in Engineering Physics (with distinction)
National Institute of Technology Calicut (NIT Calicut), Kerala, India
– Final Project: 'Photothermal Degradation of PET and PPC'

2019 – 2021 MSc in Materials Science and Engineering
Delft University of Technology (TU Delft), Delft, The Netherlands
– Specialization: Computational Materials Science for Sustainable Development
– Thesis: 'DFT-Based Study of Hydrogen Adsorption/Desorption on Borophene Structures'

2022 – 2026 PhD in Applied Physics
Eindhoven University of Technology (TU/e), Eindhoven, The Netherlands
– Thesis: 'Absorption, Diffusion, and Reaction of Plasma Species in Aqueous Media'

List of Publications

First-author Publications

1. **T. H. G. Saji**, T. J. H. Vlugt, S. Calero, B. Bagheri, 'Predicting Absorption and Diffusion of Plasma-Generated O(^{3}P), O(^{1}D), and Other RONS in Aqueous Environments Using Molecular Simulations', *J. Phys. Chem. B*, 130, 4792 (2026).

2. **T. H. G. Saji**, T. J. H. Vlugt, S. Calero, B. Bagheri, 'Coupling Solvation Thermodynamics and Chemical Speciation: A Simulation-Based Approach to NO_x Uptake in Aqueous Environments', *J. Chem. Theory Comput.*, 22, 528 (2026).

3. **T. H. G. Saji**, T. J. H. Vlugt, S. Calero, B. Bagheri, 'Modeling Nitric Oxide and Its Dimer: Force Field Development and Thermodynamics of Dimerization', *Phys. Chem. Chem. Phys.*, 27, 13662 (2025).

4. **T. H. G. Saji**, J. M. Vicent-Luna, T. J. H. Vlugt, S. Calero, B. Bagheri, 'Computing Solubility and Thermodynamic Properties of H_2O_2 in Water', *J. Mol. Liq.*, 401, 124530 (2024).

Collaborative Publications

1. P. Habibi, **T. H. G. Saji**, T. J. H. Vlugt, O. A. Moultos, P. Dey, 'Hydrogen Dissociation in Li-Decorated Borophene and Borophene Hydride: An Ab-Initio Study', *Appl. Surf. Sci.*, 603, 154323 (2022).

Patents

1. A. Anappara, P. Parameswaran, S. John, **T. H. G. Saji**, 'A Method for the Visible Light-Induced Selective Degradation of Poly(Propylene Carbonate) to Its Monomer Propylene Carbonate', The Patent Office, Government of India. Patent No. 515351, filed 05/11/2020, issued 26/02/2024.

List of Presentations

Oral Presentations

1. **T. H. G. Saji**, T. J. H. Vlugt, S. Calero, B. Bagheri, 'Modelling Reactive Oxygen and Nitrogen Species at Plasma-Water Interfaces', NWO Physics 2026, Veldhoven, The Netherlands (2026).

2. **T. H. G. Saji**, T. J. H. Vlugt, S. Calero, B. Bagheri, 'Molecular Modelling of Reactive Oxygen and Nitrogen Species at the Plasma-Water Interface', 78^{th} Annual Gaseous Electronics Conference, Seoul, Republic of Korea (2025).

Poster Presentations

1. **T. H. G. Saji**, T. J. H. Vlugt, S. Calero, B. Bagheri, 'New All-Atom Force Field for NO-N_2O_2', Thermodynamics 2024 Conference, Delft, The Netherlands (2024).

2. **T. H. G. Saji**, T. J. H. Vlugt, S. Calero, B. Bagheri, 'A New Interaction Potential for Nitric Oxide', CTC Symposium 2024, Eindhoven, The Netherlands (2024).

3. **T. H. G. Saji**, T. J. H. Vlugt, S. Calero, B. Bagheri, 'Molecular Modelling of Hydrogen Peroxide at Gas-Water Interface', CTC Symposium 2023, Eindhoven, The Netherlands (2023).

Acknowledgements

First of all, I am deeply grateful to God for helping me complete my PhD, for picking me up when I was down and for giving me the courage to face the challenges.

I would like to express my heartfelt gratitude to **Behnaz** for her guidance and support throughout my PhD. I still remember a conversation we had when I began this journey. You said a PhD supervisor has to play many roles — manager, teacher, counsellor, motivator, and sometimes friend. You have played all these roles well for the past four years, and I can vouch for that. I cannot thank you enough for the stability you brought during the tough times. Your door was always open, whether the conversation was about a stubborn simulation or something far removed from work. I especially remember the time we spent on the nitric oxide force field. While it was frustrating not to get the results, your encouragement and your belief in me pushed me forward. I thoroughly enjoyed our conversations on so many topics, especially the ones about the Middle East. Thank you for believing in me and giving me an opportunity to prove myself.

Thijs, thank you for your excellent supervision and for the scientific rigour you introduced me to. I really enjoyed the visits to Delft and the discussions on science. Thank you for pushing me to hold my work to a higher standard. **Sofia**, I am thankful for your support throughout my PhD journey. I enjoyed our spirited conversations on science and your interesting explanations. I fondly remember how the toffees on your office table have taken different roles during my PhD - hydrogen peroxide, nitric oxide, atomic oxygen - depending on which project I was on.

I would like to extend my gratitude to my graduation committee - **Peter Bobbert**, **Alexey Lyulin**, **Poulumi Dey**, **David Dubbeldam**, and **Sjoerd Verduyn Lunel**. Thank you for your time in reading my thesis and attending

my defense in person. My gratitude extends to the chairman, **Bert Koopmans**.

I appreciate the **Materials Simulation & Modelling (MSM)** group for letting me be a part of such a vibrant group. I am grateful to **Vicent** for his collaboration on my first project. I thank **Shuxia** for allowing me to be a teaching assistant for the AM4 course. **Geert**, you always amaze me with your knowledge on a wide variety of subjects, with cricket being the one that I am most amazed by. **Dominika, Mert, Parsa, Esteban,** and **Shrinjay** - I appreciate your help at various junctures of my PhD. **Mike**, thank you for setting the bar high for your colleagues. **Konrad**, I am grateful to you for letting me be part of that amazing MSM football team last year, which you captained to third place in the tournament. **Viren**, thank you for keeping the energy levels of the group high. I thoroughly enjoyed all the conversations we had about the politics in India and nation-building. I also cherish all the wonderful time I had with my MSM colleagues - **Sofia, Marko, Susanne, Koen, Zijin, Diego, Aybuke, Samber, Parvathy, Sander,** and **Flavian**. **Marjan**, thank you for all the nice conversations and for helping me handle the non-technical aspects related to the PhD.

My sincere appreciation goes to all my pastors and spiritual mentors - **Pr. Shinoj & Angelin (Tent of Grace, Amsterdam), Pr. Sabu & Leena, Pr. Manohar & Shobha (Divine New Life Fellowship, Qatar), Pr. Premkumar & Jessy, Pr. Abraham & Blessy**. I am grateful for the prayer walks I had with **Jonathan**. I also thank **Sarika** for all the nice conversations.

I am indebted to my wife (**Sheryl**), who supported me through my highs and lows, initially as a listener to my problems remotely and later in person. Your excellent chai played a huge role in expediting my thesis writing. I owe my Appa (**Saji**) and Amma (**Minu**) heartfelt appreciation for their unconditional support. Also, I thank my siblings, **Tibin** and **Tabitha**, for lifting me up with their humour. My gratitude extends to my in-laws, Pappa (**Roni**), Mamma (**Anita**), and **Shreya**. I remember my grandparents **K. M. George (late) & Saramma (Kureekkattil)** and **T. T. Mathew & Mariamma (Thazhathu)** for their inspiration and support.

The credit for this PhD cannot be taken by me alone. It also belongs to a grandfather who had to discontinue his studies to support his family, a father who decided not to pursue a Master's because of his family's financial condition, and a mother who quit her job as a chemistry teacher to take care of her children (the eldest being me). On the day I hold that PhD certificate, it is not only my hands that deserve to be on it, but also the many invisible hands that pushed me forward.

Bibliography

[1] M. Thakrar, Lightning in ancient mythologies, 2024. URL: https://lsaclassics.com/2024/10/09/lightning-in-ancient-mythologies/, Accessed: 18 March 2026.

[2] B. Franklin, The kite experiment, 19 october 1752, 1752. URL: https://founders.archives.gov/documents/Franklin/01-04-02-0135, founders Online, National Archives. Accessed: 18 March 2026.

[3] H.-R. Metelmann, T. Von Woedtke, K.-D. Weltmann, Comprehensive clinical plasma medicine: cold physical plasma for medical application, 1st ed., Springer, Cham, Switzerland, 2018.

[4] P. J. Bruggeman, M. J. Kushner, B. R. Locke, J. G. Gardeniers, W. Graham, D. B. Graves, R. Hofman-Caris, D. Maric, J. P. Reid, E. Ceriani, D. F. Rivas, J. E. Foster, S. C. Garrick, Y. Gorbanev, S. Hamaguchi, F. Iza, H. Jablonowski, E. Klimova, J. Kolb, F. Krcma, P. Lukes, Z. Machala, I. Marinov, D. Mariotti, S. M. Thagard, D. Minakata, E. C. Neyts, J. Pawlat, Petrovic, Z. Lj, R. Pflieger, S. Reuter, D. C. Schram, S. Schröter, M. Shiraiwa, B. Tarabová, P. A. Tsai, J. R. R. Verlet, T. von Woedtke, K. R. Wilson, K. Yasui, G. Zvereva, Plasma–liquid interactions: a review and roadmap, Plasma Sources Science and Technology 25 (2016) 053002–053060.

[5] I. Adamovich, S. D. Baalrud, A. Bogaerts, P. J. Bruggeman, M. Cappelli, V. Colombo, U. Czarnetzki, U. Ebert, J. G. Eden, P. Favia, , D. B. Graves, S. Hamaguchi, G. Hieftje, M. Hori, I. D. Kaganovich, U. Kortshagen, M. J. Kushner, N. J. Mason, S. Mazouffre, S. Mededovic Thagard, H.-R. Metelmann, A. Mizuno, E. Moreau, A. B. Murphy, B. A. Niemira, G. S.

Oehrlein, Z. L. Petrovic, L. C. Pitchford, Y.-K. Pu, S. Rauf, O. Sakai, S. Samukawa, S. Starikovskaia, J. Tennyson, K. Terashima, M. M. Turner, M. C. M. van de Sanden, A. Vardelle, The 2017 plasma roadmap: Low temperature plasma science and technology, Journal of Physics D: Applied Physics 50 (2017) 323001–323046.

[6] A. L. Peratt, Physics of the Plasma Universe, 2nd ed., Springer, Los Alamos, NM, 1992.

[7] C. Da Silva, R. Sonnenfeld, H. Edens, P. Krehbiel, M. Quick, W. Koshak, The plasma nature of lightning channels and the resulting nonlinear resistance, Journal of Geophysical Research: Atmospheres 124 (2019) 9442–9463.

[8] S.-I. Akasofu, The dynamic aurora, Scientific American 260 (1989) 90–97.

[9] G. S. Oehrlein, S. Hamaguchi, Foundations of low-temperature plasma enhanced materials synthesis and etching, Plasma Sources Science and Technology 27 (2018) 023001–023021.

[10] J. F. Waymouth, F. Bitter, Analysis of the plasma of fluorescent lamps, Journal of Applied Physics 27 (1956) 122–131.

[11] M. Seeger, F. Macedo, U. Riechert, M. Bujotzek, A. Hassanpoor, J. Häfner, Trends in high voltage switchgear research and technology, IEEJ Transactions on Electrical and Electronic Engineering 20 (2025) 322–338.

[12] S. Bekeschus, T. von Woedtke, S. Emmert, A. Schmidt, Medical gas plasma-stimulated wound healing: Evidence and mechanisms, Redox Biology 46 (2021) 102116–102132.

[13] J. Schlegel, J. Köritzer, V. Boxhammer, Plasma in cancer treatment, Clinical Plasma Medicine 1 (2013) 2–7.

[14] B. Adhikari, M. Adhikari, G. Park, The effects of plasma on plant growth, development, and sustainability, Applied Sciences 10 (2020) 6045–6063.

[15] F. Chen, Introduction to Plasma Physics and Controlled Fusion, 3rd ed., Springer, Los Angeles, CA, 2015.

[16] R. Foest, M. Schmidt, K. Becker, Microplasmas, an emerging field of low-temperature plasma science and technology, International Journal of Mass Spectrometry 248 (2006) 87–102.

[17] R. Thirumdas, C. Sarangapani, U. S. Annapure, Cold plasma: a novel non-thermal technology for food processing, Food Biophysics 10 (2015) 1–11.

[18] V. M. Donnelly, A. Kornblit, Plasma etching: Yesterday, today, and tomorrow, Journal of Vacuum Science & Technology A 31 (2013) 050825–050872.

[19] J. W. Coburn, H. F. Winters, Plasma etching—a discussion of mechanisms, Journal of Vacuum Science and Technology 16 (1979) 391–403.

[20] D. B. Graves, Mechanisms of plasma medicine: Coupling plasma physics, biochemistry, and biology, IEEE Transactions on radiation and plasma medical sciences 1 (2017) 281–292.

[21] J. F. Friedrich, J. Meichsner, Nonthermal Plasmas for Materials Processing, 1st ed., John Wiley & Sons, River Street, Hoboken, 2022.

[22] Y. He, W. Sang, W. Lu, W. Zhang, C. Zhan, D. Jia, Recent advances of emerging organic pollutants degradation in environment by non-thermal plasma technology: a review, Water 14 (2022) 1351–1379.

[23] T. Desmet, R. Morent, N. De Geyter, C. Leys, E. Schacht, P. Dubruel, Nonthermal plasma technology as a versatile strategy for polymeric biomaterials surface modification: a review, Biomacromolecules 10 (2009) 2351–2378.

[24] S. Arndt, A. Schmidt, S. Karrer, T. von Woedtke, Comparing two different plasma devices kinpen and adtec steriplas regarding their molecular and cellular effects on wound healing, Clinical Plasma Medicine 9 (2018) 24–33.

[25] X. Cheng, S. R. Murthy, T. Zhuang, L. Ly, O. Jones, G. Basadonna, M. Keidar, Y. Kanaan, J. Canady, Canady helios cold plasma induces breast cancer cell death by oxidation of histone mRNA, International Journal of Molecular Sciences 22 (2021) 9578–9599.

[26] DrMediSpa, Prism plasma: Cold atmospheric plasma, 2026. URL: `https://drmedispa.com/treatments/`, Accessed: 18 March 2026.

[27] F. Rezaei, P. Vanraes, A. Nikiforov, R. Morent, N. De Geyter, Applications of plasma-liquid systems: A review, Materials 12 (2019) 2751–2819.

[28] P. Vanraes, A. Bogaerts, Plasma physics of liquids—a focused review, Applied Physics Reviews 5 (2018) 031103–031133.

[29] B. Haertel, T. Von Woedtke, K.-D. Weltmann, U. Lindequist, Non-thermal atmospheric-pressure plasma possible application in wound healing, Biomolecules & Therapeutics 22 (2014) 477–490.

[30] S. Cha, Y.-S. Park, Plasma in dentistry, Clinical Plasma Medicine 2 (2014) 4–10.

[31] A. Barjasteh, Z. Dehghani, P. Lamichhane, N. Kaushik, E. H. Choi, N. K. Kaushik, Recent progress in applications of non-thermal plasma for water purification, bio-sterilization, and decontamination, Applied Sciences 11 (2021) 3372–3393.

[32] M. Magureanu, N. B. Mandache, V. I. Parvulescu, Degradation of pharmaceutical compounds in water by non-thermal plasma treatment, Water Research 81 (2015) 124–136.

[33] Z. Machala, B. Tarabová, D. Sersenová, M. Janda, K. Hensel, Chemical and antibacterial effects of plasma activated water: correlation with gaseous and aqueous reactive oxygen and nitrogen species, plasma sources and air flow conditions, Journal of Physics D: Applied Physics 52 (2019) 034002–034018.

[34] D. B. Graves, The emerging role of reactive oxygen and nitrogen species in redox biology and some implications for plasma applications to medicine and biology, Journal of Physics D: Applied Physics 45 (2012) 263001–263042.

[35] K. Weltmann, T. Von Woedtke, Plasma medicine—current state of research and medical application, Plasma Physics and Controlled Fusion 59 (2017) 014031–014041.

[36] T. Von Woedtke, A. Schmidt, S. Bekeschus, K. Wende, K.-D. Weltmann, Plasma medicine: A field of applied redox biology, In Vivo 33 (2019) 1011–1026.

[37] M. Xie, M. G. Derks, E. H. Koch, C. B. van Boven, M. Janlad, B. Bagheri, Z. Xu, D. Kovryzhenko, C. A. van Walree, A. Sobota, M. Weingarth, J. Wong-ekkabut, M. Karttunen, E. Breukink, J. A. Killian, A. F. P. Sonnen, J. H. Lorent, Structure and pH dependence of membranolytic mechanisms by truncated oxidized phospholipids, Journal of the American Chemical Society 147 (2025) 9175–9189.

[38] B. Bagheri, P. Boonnoy, J. Wong-Ekkabut, M. Karttunen, Effect of oxidation on popc lipid bilayers: anionic carboxyl group plays a major role, Physical Chemistry Chemical Physics 25 (2023) 18310–18321.

[39] P. Boonnoy, M. Janlad, B. Bagheri, C. Dias, M. Karttunen, J. Wong-Ekkabut, Cholesterol inhibits oxygen permeation through biological membranes: mechanism against double-bond peroxidation, RSC Advances 14 (2024) 29113–29121.

[40] S.-Y. Yoon, H. Jeon, C. Yi, S. Park, S. Ryu, S. B. Kim, Mutual interaction between plasma characteristics and liquid properties in ac-driven pin-to-liquid discharge, Scientific Reports 8 (2018) 12037–12046.

[41] N. Aristova, I. Piskarev, Plasma radiation-induced electrical conductivity of water, High Energy Chemistry 53 (2019) 261–263.

[42] M. A. Lieberman, A. J. Lichtenberg, Principles of plasma discharges and materials processing, MRS Bulletin 30 (1994) 899–901.

[43] A. D. Lindsay, D. B. Graves, S. C. Shannon, Fully coupled simulation of the plasma liquid interface and interfacial coefficient effects, Journal of Physics D: Applied Physics 49 (2016) 235204–235212.

[44] K. Ikuse, S. Hamaguchi, Roles of the reaction boundary layer and long diffusion of stable reactive nitrogen species (RNS) in plasma-irradiated water as an oxidizing media—numerical simulation study, Japanese Journal of Applied Physics 61 (2022) 076002–076023.

[45] S. A. Norberg, W. Tian, E. Johnsen, M. J. Kushner, Atmospheric pressure plasma jets interacting with liquid covered tissue: touching and not-touching the liquid, Journal of Physics D: Applied Physics 47 (2014) 475203–475220.

[46] C. Verlackt, W. Van Boxem, A. Bogaerts, Transport and accumulation of plasma generated species in aqueous solution, Physical Chemistry Chemical Physics 20 (2018) 6845–6859.

[47] W. Tian, M. J. Kushner, Atmospheric pressure dielectric barrier discharges interacting with liquid covered tissue, Journal of Physics D: Applied Physics 47 (2014) 165201–165221.

[48] T. Kamidollayev, J. P. Trelles, Modeling of reactive species interphase transport in plasma jet impinging on water, Journal of Physics D: Applied Physics 56 (2023) 505203–505220.

[49] J. P. Trelles, Fluid modeling of low-temperature plasmas, Physics of Plasmas 32 (2025) 090901–090928.

[50] A. M. Lietz, M. J. Kushner, Air plasma treatment of liquid covered tissue: long timescale chemistry, Journal of Physics D: Applied Physics 49 (2016) 425204–425225.

[51] B. Bagheri, J. Teunissen, The effect of the stochasticity of photoionization on 3D streamer simulations, Plasma Sources Science and Technology 28 (2019) 045013–045024.

[52] R. Sander, Compilation of Henry's law constants (version 4.0) for water as solvent, Atmospheric Chemistry and Physics 15 (2015) 4399–4981.

[53] M. M. Turner, Uncertainty and error in complex plasma chemistry models, Plasma Sources Science and Technology 24 (2015) 035027–035058.

[54] D. Frenkel, B. Smit, Understanding molecular simulation: from algorithms to applications, 3rd ed., Elsevier, San Diego, CA, 2023.

[55] M. P. Allen, D. J. Tildesley, Computer simulation of liquids, 2nd ed., Oxford University Press, Great Clarendon Street, Oxford, 2017.

[56] I. C. Bourg, G. Sposito, Connecting the molecular scale to the continuum scale for diffusion processes in smectite-rich porous media, Environmental Science & Technology 44 (2010) 2085–2091.

[57] R. LeSar, Introduction to computational materials science: fundamentals to applications, Cambridge University Press, New York, 2013.

[58] J. Morado, P. N. Mortenson, J. W. M. Nissink, J. W. Essex, C.-K. Skylaris, Does a machine-learned potential perform better than an optimally tuned traditional force field? A case study on fluorohydrins, Journal of Chemical Information and Modeling 63 (2023) 2810–2827.

[59] J. Behler, Perspective: Machine learning potentials for atomistic simulations, Journal of Chemical Physics 145 (2016) 170901–170909.

[60] W. L. Jorgensen, J. Chandrasekhar, J. D. Madura, R. W. Impey, M. L. Klein, Comparison of simple potential functions for simulating liquid water, Journal of Chemical Physics 79 (1983) 926–935.

[61] J. L. Abascal, C. Vega, A general purpose model for the condensed phases of water: TIP4P/2005, Journal of Chemical Physics 123 (2005) 234505.

[62] S. W. Rick, A reoptimization of the five-site water potential (TIP5P) for use with Ewald sums, Journal of Chemical Physics 120 (2004) 6085–6093.

[63] M. W. Mahoney, W. L. Jorgensen, A five-site model for liquid water and the reproduction of the density anomaly by rigid, nonpolarizable potential functions, Journal of Chemical Physics 112 (2000) 8910–8922.

[64] C. Vega, J. L. Abascal, Simulating water with rigid non-polarizable models: a general perspective, Physical Chemistry Chemical Physics 13 (2011) 19663–19688.

[65] W. Smith, B. Triska, The reaction ensemble method for the computer simulation of chemical and phase equilibria. I. Theory and basic examples, Journal of Chemical Physics 100 (1994) 3019–3027.

[66] C. Heath Turner, J. K. Brennan, M. Lisal, W. R. Smith, J. Karl Johnson, K. E. Gubbins, Simulation of chemical reaction equilibria by the reaction ensemble Monte Carlo method: a review, Molecular Simulation 34 (2008) 119–146.

[67] S. C. Glotzer, D. Stauffer, N. Jan, Monte Carlo simulations of phase separation in chemically reactive binary mixtures, Physical Review Letters 72 (1994) 4109–4113.

[68] H. M. Polat, F. de Meyer, C. Houriez, O. A. Moultos, T. J. H. Vlugt, Solving chemical absorption equilibria using free energy and quantum chemistry calculations: methodology, limitations, and new open-source software, Journal of Chemical Theory and Computation 19 (2023) 2616–2629.

[69] P. W. Atkins, J. De Paula, J. Keeler, Atkins' Physical Chemistry, 11th ed., Oxford University Press, Oxford, 2023.

[70] D. McQuarrie, Statistical Mechanics, 1st ed., University Science Books, 10 East 53$^{\text{rd}}$ Street, New York, 2000.

[71] H. Hoshina, M. Slipchenko, K. Prozument, D. Verma, M. W. Schmidt, J. Ivanic, A. F. Vilesov, Infrared spectroscopy and structure of $(NO)_n$ clusters, Journal of Physical Chemistry A 120 (2016) 527–534.

[72] S. Marinakis, C. Cockrell, K. Trachenko, T. F. Headen, A. K. Soper, Microscopic structure of liquid nitric oxide, Journal of Physical Chemistry B 126 (2022) 9860–9870.

[73] R. M. Cordeiro, Reactive oxygen species at phospholipid bilayers: Distribution, mobility and permeation, Biochimica et Biophysica Acta (BBA) - Biomembranes 1838 (2014) 438–444.

[74] E. A. Orabi, A. M. English, A Simple Additive Potential Model for Simulating Hydrogen Peroxide in Chemical and Biological Systems, Journal of Chemical Theory and Computation 14 (2018) 2808–2821.

[75] E. Neria, S. Fischer, M. Karplus, Simulation of activation free energies in molecular systems, Journal of Chemical Physics 105 (1996) 1902–1921.

[76] V. Lachet, B. Creton, T. de Bruin, E. Bourasseau, N. Desbiens, Ø. Wilhelmsen, M. Hammer, Equilibrium and transport properties of CO_2+ N_2O and CO_2+ NO mixtures: Molecular simulation and equation of state modelling study, Fluid Phase Equilibria 322 (2012) 66–78.

[77] Z. Zhou, B. Todd, K. P. Travis, R. J. Sadus, A molecular dynamics study of nitric oxide in water: diffusion and structure, Journal of Chemical Physics 123 (2005) 054505–054511.

[78] M. E. Tuckerman, Statistical mechanics: theory and molecular simulation, 2nd ed., Oxford University Press, 198 Madison Avenue, New York, 2023.

[79] D. Dubbeldam, K. S. Walton, T. J. H. Vlugt, S. Calero, Design, parameterization, and implementation of atomic force fields for adsorption in nanoporous materials, Advanced Theory and Simulations 2 (2019) 1900135–1900196.

[80] D. Pan, J. Li, L. C. Voon, P. Wei, Determination of Lennard-Jones potential parameters for interfacial interaction in elemental layered crystals, Journal of Applied Physics 135 (2024) 204301–204311.

[81] H. A. Lorentz, Ueber die Anwendung des Satzes vom Virial in der kinetischen Theorie der Gase, Annalen der Physik 248 (1881) 127–136.

[82] S. E. Feller, R. W. Pastor, A. Rojnuckarin, S. Bogusz, B. R. Brooks, Effect of electrostatic force truncation on interfacial and transport properties of water, Journal of Physical Chemistry 100 (1996) 17011–17020.

[83] Y. Yonetani, A severe artifact in simulation of liquid water using a long cut-off length: Appearance of a strange layer structure, Chemical Physics Letters 406 (2005) 49–53.

[84] G. Pan, J. Ding, P. Chen, H. Yan, Y. Du, D.-J. Lee, Y. Lu, Finite-size effects on thermal property predictions of molten salts, Solar Energy Materials and Solar Cells 221 (2021) 110884–110893.

[85] I.-C. Yeh, G. Hummer, System-size dependence of diffusion coefficients and viscosities from molecular dynamics simulations with periodic boundary conditions, Journal of Physical Chemistry B 108 (2004) 15873–15879.

[86] T. Hulikal Chakrapani, H. Hajibeygi, O. A. Moultos, T. J. H. Vlugt, Impact of finite-size effects on computed transport properties: a molecular dynamics study of dilute systems, Molecular Physics 123 (2025) e2578408.

[87] A. Z. Panagiotopoulos, M. R. Stapleton, The Gibbs method for molecular-based computer simulations of phase equilibria, Fluid Phase Equilibria 53 (1989) 133–141.

[88] V. I. Manousiouthakis, M. W. Deem, Strict detailed balance is unnecessary in Monte Carlo simulation, Journal of Chemical Physics 110 (1999) 2753–2756.

[89] J. J. Potoff, J. I. Siepmann, Vapor–liquid equilibria of mixtures containing alkanes, carbon dioxide, and nitrogen, AIChE Journal 47 (2001) 1676–1682.

[90] M. G. Martin, J. I. Siepmann, Transferable potentials for phase equilibria. 1. united-atom description of n-alkanes, Journal of Physical Chemistry B 102 (1998) 2569–2577.

[91] J. Noroozi, W. R. Smith, Accurately predicting CO_2 reactive absorption properties in aqueous alkanolamine solutions by molecular simulation requiring no solvent experimental data, Industrial & Engineering Chemistry Research 59 (2020) 18254–18268.

[92] T. Heimburg, R. L. Biltonen, A Monte Carlo simulation study of protein-induced heat capacity changes and lipid-induced protein clustering, Biophysical Journal 70 (1996) 84–96.

[93] G. Kronome, T. Kristóf, J. Liszi, I. Szalai, Heat capacities of two-centre Lennard–Jones fluids from npt ensemble Monte Carlo simulations, Fluid Phase Equilibria 155 (1999) 157–166.

[94] H. C. Shi, Computational study of electronic excited states of nitric oxide monomer and nitric oxide dimer., Faculty of Graduate Studies and Research, University of Regina, 2007.

[95] W. Shi, E. J. Maginn, Continuous Fractional Component Monte Carlo: An adaptive biasing method for open system atomistic simulations, Journal of Chemical Theory and Computation 3 (2007) 1451–1463.

[96] W. Shi, E. J. Maginn, Improvement in molecule exchange efficiency in Gibbs ensemble Monte Carlo: development and implementation of the Continuous Fractional Component move, Journal of Computational Chemistry 29 (2008) 2520–2530.

[97] A. Rahbari, R. Hens, M. Ramdin, O. Moultos, D. Dubbeldam, T. J. H. Vlugt, Recent advances in the Continuous Fractional Component Monte Carlo methodology, Molecular Simulation 47 (2021) 804–823.

[98] H. M. Polat, H. S. Salehi, R. Hens, D. O. Wasik, A. Rahbari, F. de Meyer, C. Houriez, C. Coquelet, S. Calero, D. Dubbeldam, O. A. Moultos, T. J. H. Vlugt, New Features of the Open Source Monte Carlo Software Brick-CFCMC: Thermodynamic Integration and Hybrid Trial Moves, Journal of Chemical Information and Modeling 61 (2021) 3752–3757.

[99] R. Hens, A. Rahbari, S. Caro-Ortiz, N. Dawass, M. Erdös, A. Poursaeidesfahani, H. S. Salehi, A. T. Celebi, M. Ramdin, O. A. Moultos, D. Dubbeldam, T. J. H. Vlugt, Brick-CFCMC: Open source software for Monte Carlo simulations of phase and reaction equilibria using the Continuous Fractional Component Method, Journal of Chemical Information and Modeling 60 (2020) 2678–2682.

[100] A. Poursaeidesfahani, A. Torres-Knoop, D. Dubbeldam, T. J. H. Vlugt, Direct free energy calculation in the Continuous Fractional Component

Gibbs ensemble, Journal of Chemical Theory and Computation 12 (2016) 1481–1490.

[101] F. Wang, D. P. Landau, Efficient, Multiple-Range Random Walk Algorithm to Calculate the Density of States, Physical Review Letters 86 (2001) 2050–2053.

[102] F. Torrens, Aqueous coefficient calculations for chemicals and drugs, Toxicological & Environmental Chemistry 73 (1999) 177–189.

[103] L. Verlet, Computer "Experiments" on Classical Fluids. I. Thermodynamical properties of Lennard-Jones molecules, Physical Review 159 (1967) 98–103.

[104] D. C. Rapaport, The art of molecular dynamics simulation, 2nd ed., Cambridge University Press, Cambridge, UK, 2004.

[105] J.-P. Ryckaert, G. Ciccotti, H. J. Berendsen, Numerical integration of the cartesian equations of motion of a system with constraints: molecular dynamics of n-alkanes, Journal of Computational Physics 23 (1977) 327–341.

[106] B. Hess, H. Bekker, H. J. Berendsen, J. G. Fraaije, LINCS: A linear constraint solver for molecular simulations, Journal of Computational Chemistry 18 (1997) 1463–1472.

[107] H. S. Salehi, R. Hens, O. A. Moultos, T. J. H. Vlugt, Computation of gas solubilities in choline chloride urea and choline chloride ethylene glycol deep eutectic solvents using Monte Carlo simulations, Journal of Molecular Liquids 316 (2020) 113729–113738.

[108] A. T. Celebi, S. H. Jamali, A. Bardow, T. J. H. Vlugt, O. A. Moultos, Finite-size effects of diffusion coefficients computed from molecular dynamics: a review of what we have learned so far, Molecular Simulation 47 (2021) 831–845.

[109] S. H. Jamali, L. Wolff, T. M. Becker, M. De Groen, M. Ramdin, R. Hartkamp, A. Bardow, T. J. H. Vlugt, O. A. Moultos, OCTP: A tool for on-the-fly calculation of transport properties of fluids with the order-n algorithm in LAMMPS, Journal of Chemical Information and Modeling 59 (2019) 1290–1294.

[110] J. Lelieveld, P. Crutzen, Influences of cloud photochemical processes on tropospheric ozone, Nature 343 (1990) 227–233.

[111] P. J. Crutzen, M. G. Lawrence, U. Pöschl, On the background photochemistry of tropospheric ozone, Tellus B: Chemical and Physical Meteorology 51 (1999) 123–146.

[112] R. J. Lewis, G. J. Hutchings, Recent advances in the direct synthesis of H_2O_2, ChemCatChem 11 (2019) 298–308.

[113] Z. Chen, D. Yao, C. Chu, S. Mao, Photocatalytic H_2O_2 production systems: Design strategies and environmental applications, Chemical Engineering Journal 451 (2023) 138489–138511.

[114] J. Wang, Y. Zhang, E. Archibong, F. S. Ligler, Z. Gu, Leveraging H_2O_2 levels for biomedical applications, Advanced Biosystems 1 (2017) 1700084–1700098.

[115] D. Möller, Atmospheric hydrogen peroxide: Evidence for aqueous-phase formation from a historic perspective and a one-year measurement campaign, Atmospheric Environment 43 (2009) 5923–5936.

[116] D. Vione, V. Maurino, C. Minero, E. Pelizzetti, The atmospheric chemistry of hydrogen peroxide: A review, Annali di Chimica 93 (2003) 477–488.

[117] M. Lee, B. G. Heikes, D. W. O'Sullivan, Hydrogen peroxide and organic hydroperoxide in the troposphere: a review, Atmospheric Environment 34 (2000) 3475–3494.

[118] M. Hoffmann, J. Edwards, Kinetics of the oxidation of sulfite by hydrogen peroxide in acidic solution, Journal of Physical Chemistry 79 (1975) 2096–2098.

[119] S. Penkett, B. Jones, K. Brich, A. E. Eggleton, The importance of atmospheric ozone and hydrogen peroxide in oxidising sulphur dioxide in cloud and rainwater, Atmospheric Environment 13 (1979) 123–137.

[120] L. R. Martin, D. E. Damschen, Aqueous oxidation of sulfur dioxide by hydrogen peroxide at low pH, Atmospheric Environment (1967) 15 (1981) 1615–1621.

[121] D. E. Damschen, L. R. Martin, Aqueous aerosol oxidation of nitrous acid by O_2, O_3 and H_2O_2, Atmospheric Environment (1967) 17 (1983) 2005–2011.

[122] J. G. Calvert, A. Lazrus, G. L. Kok, B. G. Heikes, J. G. Walega, J. Lind, C. A. Cantrell, Chemical mechanisms of acid generation in the troposphere, Nature 317 (1985) 27–35.

[123] L. I. Kleinman, Seasonal dependence of boundary layer peroxide concentration: The low and high NO_x regimes, Journal of Geophysical Research: Atmospheres 96 (1991) 20721–20733.

[124] J. A. Logan, M. J. Prather, S. C. Wofsy, M. B. McElroy, Tropospheric chemistry: A global perspective, Journal of Geophysical Research: Oceans 86 (1981) 7210–7254.

[125] H. Levy, Normal atmosphere: Large radical and formaldehyde concentrations predicted, Science 173 (1971) 141–143.

[126] J. Fierro, J. M. Campos-Martin, G. Blanco-Brieva, Hydrogen peroxide synthesis: An outlook beyond the anthraquinone process angewandte, Angewandte Chemie-International Edition 45 (2006) 6962–6984.

[127] J. M. Campos-Martin, G. Blanco-Brieva, J. L. Fierro, Hydrogen peroxide synthesis: an outlook beyond the anthraquinone process, Angewandte Chemie International Edition 45 (2006) 6962–6984.

[128] H. Hou, X. Zeng, X. Zhang, Production of hydrogen peroxide by photocatalytic processes, Angewandte Chemie International Edition 59 (2020) 17356–17376.

[129] K. Mase, M. Yoneda, Y. Yamada, S. Fukuzumi, Seawater usable for production and consumption of hydrogen peroxide as a solar fuel, Nature Communications 7 (2016) 11470–11476.

[130] Y. Kofuji, Y. Isobe, Y. Shiraishi, H. Sakamoto, S. Tanaka, S. Ichikawa, T. Hirai, Carbon nitride–aromatic diimide–graphene nanohybrids: metal-free photocatalysts for solar-to-hydrogen peroxide energy conversion with 0.2% efficiency, Journal of the American Chemical Society 138 (2016) 10019–10025.

[131] S. Fukuzumi, Production of liquid solar fuels and their use in fuel cells, Joule 1 (2017) 689–738.

[132] E. S. Shanley, F. P. Greenspan, Highly concentrated hydrogen peroxide, Industrial & Engineering Chemistry 39 (1947) 1536–1543.

[133] S. C. Perry, S. Mavrikis, L. Wang, C. P. de León, Future perspectives for the advancement of electrochemical hydrogen peroxide production, Current Opinion in Electrochemistry 30 (2021) 100792–100801.

[134] C. Samanta, Direct synthesis of hydrogen peroxide from hydrogen and oxygen: An overview of recent developments in the process, Applied Catalysis A: General 350 (2008) 133–149.

[135] R. Burch, P. Ellis, An investigation of alternative catalytic approaches for the direct synthesis of hydrogen peroxide from hydrogen and oxygen, Applied Catalysis B: Environmental 42 (2003) 203–211.

[136] G. Genti, R. Dittmeyer, S. Perathoner, M. Reif, Tubular inorganic catalytic membrane reactors: advantages and performance in multiphase hydrogenation reactions, Catalysis Today 79 (2003) 139–149.

[137] P. Bruggeman, C. Leys, Non-thermal plasmas in and in contact with liquids, Journal of Physics D: Applied Physics 42 (2009) 053001–053028.

[138] P. J. Bruggeman, F. Iza, R. Brandenburg, Foundations of atmospheric pressure non-equilibrium plasmas, Plasma Sources Science and Technology 26 (2017) 123002.

[139] A. A. Joshi, B. R. Locke, P. Arce, W. C. Finney, Formation of hydroxyl radicals, hydrogen peroxide and aqueous electrons by pulsed streamer corona discharge in aqueous solution, Journal of Hazardous Materials 41 (1995) 3–30.

[140] B. R. Locke, K.-Y. Shih, Review of the methods to form hydrogen peroxide in electrical discharge plasma with liquid water, Plasma Sources Science and Technology 20 (2011) 034006–034020.

[141] Y. F. Yue, S. Mohades, M. Laroussi, X. Lu, Measurements of plasma-generated hydroxyl and hydrogen peroxide concentrations for plasma medicine applications, IEEE Transactions on Plasma Science 44 (2016) 2754–2758.

[142] M. Suresh, V. S. K. Kondeti, P. J. Bruggeman, Production and diffusion of H_2O_2 during the interaction of a direct current pulsed atmospheric pressure plasma jet on a hydrogel, Journal of Physics D: Applied Physics 55 (2022) 185201–185207.

[143] F. Cameli, P. Dimitrakellis, T.-Y. Chen, D. G. Vlachos, Modular plasma microreactor for intensified hydrogen peroxide production, ACS Sustainable Chemistry & Engineering 10 (2022) 1829–1838.

[144] P. A. Giguère, V. Schomaker, An electron diffraction study of hydrogen peroxide and hydrazine, Journal of the American Chemical Society 65 (1943) 2025–2029.

[145] P. Giguere, T. Srinivasan, A Raman study of H_2O_2 and D_2O_2 vapor, Journal of Raman Spectroscopy 2 (1974) 125–132.

[146] S. Abrahams, R. Collin, W. Lipscomb, The crystal structure of hydrogen peroxide, Acta Crystallographica 4 (1951) 15–20.

[147] J. M. Savariault, M. Lehmann, Experimental determination of the deformation electron density in hydrogen peroxide by combination of X-ray and neutron diffraction measurements, Journal of the American Chemical Society 102 (1980) 1298–1303.

[148] C. Fritchie, R. McMullan, Neutron diffraction study of the 1:1 urea:hydrogen peroxide complex at 81 K, Acta Crystallographica Section B: Structural Crystallography and Crystal Chemistry 37 (1981) 1086–1091.

[149] O. Maass, W. H. Hatcher, The properties of pure hydrogen peroxide. I., Journal of the American Chemical Society 42 (1920) 2548–2569.

[150] M. Phibbs, P. A. Giguère, Hydrogen peroxide and its analogues: I. density, refractive index, viscosity, and surface tension of deuterium peroxide–deuterium oxide solutions, Canadian Journal of Chemistry 29 (1951) 173–181.

[151] R. Redington, W. Olson, P. Cross, Studies of hydrogen peroxide: The infrared spectrum and the internal rotation problem, Journal of Chemical Physics 36 (1962) 1311–1326.

[152] J. Koput, On the r_0^* structure and the torsional potential function of hydrogen peroxide, Journal of Molecular Spectroscopy 115 (1986) 438–441.

[153] G. Khachkuruzov, I. Przhevalskii, Molecular constants of hydrogen peroxide. 7: Parameters of the potential energy of internal rotation, Optics and Spectroscopy 44 (1978) 112–114.

[154] R. H. Hunt, R. A. Leacock, C. W. Peters, K. T. Hecht, Internal-rotation in hydrogen peroxide: The far-infrared spectrum and the determination of the hindering potential, Journal of Chemical Physics 42 (1965) 1931–1946.

[155] O. Maass, P. Hiebert, The properties of pure hydrogen peroxide. v. vapor pressure, Journal of the American Chemical Society 46 (1924) 2693–2700.

[156] W. T. Foley, P. A. Giguère, Hydrogen peroxide and its analogues: IV. some thermal properties of hydrogen peroxide, Canadian Journal of Chemistry 29 (1951) 895–903.

[157] M. F. Easton, A. G. Mitchell, W. F. K. Wynne-Jones, The behaviour of mixtures of hydrogen peroxide and water. Part 1.—Determination of the densities of mixtures of hydrogen peroxide and water, Transactions of the Faraday Society 48 (1952) 796–801.

[158] W. T. Foley, P. A. Giguère, Hydrogen peroxide and its analogues: II. phase equilibrium in the system hydrogen peroxide–water, Canadian Journal of Chemistry 29 (1951) 123–132.

[159] G. Scatchard, G. M. Kavanagh, L. B. Ticknor, Vapor-liquid equilibrium. VIII. hydrogen peroxide—water mixtures1, Journal of the American Chemical Society 74 (1952) 3715–3720.

[160] D. Cremer, Theoretical determination of molecular structure and conformation. I. the role of basis set and correlation effects in calculations on hydrogen peroxide, Journal of Chemical Physics 69 (1978) 4440–4455.

[161] J. Koput, S. Carter, N. C. Handy, Potential energy surface and vibrational-rotational energy levels of hydrogen peroxide, Journal of Physical Chemistry A 102 (1998) 6325–6330.

[162] S. A. Kulkarni, L. J. Bartolotti, R. K. Pathak, Ab initio investigations on neutral hydrogen peroxide clusters:$(H_2O_2)_n$ (n=2–4), Chemical Physics Letters 372 (2003) 620–626.

[163] M. Elango, R. Parthasarathi, V. Subramanian, C. Ramachandran, N. Sathyamurthy, Hydrogen peroxide clusters: The role of open book motif in cage and helical structures, Journal of Physical Chemistry A 110 (2006) 6294–6300.

[164] A. D. Kulkarni, R. K. Pathak, L. J. Bartolotti, Structures, Energetics, and Vibrational Spectra of $H_2O_2 \cdots (H_2O)_n$, n=1–6 clusters: Ab Initio Quantum Chemical Investigations, Journal of Physical Chemistry A 109 (2005) 4583–4590.

[165] S. T. Moin, T. S. Hofer, B. R. Randolf, B. M. Rode, An *ab initio* quantum mechanical charge field molecular dynamics simulation of hydrogen peroxide in water, Computational and Theoretical Chemistry 980 (2012) 15–22.

[166] C. Ferreira, H. F. Martiniano, B. J. C. Cabral, V. Aquilanti, Electronic excitation and ionization of hydrogen peroxide–water clusters: Comparison with water clusters, International Journal of Quantum Chemistry 111 (2011) 1824–1835.

[167] A. Priyadarsini, B. S. Mallik, Structure and rotational dynamics of water around hydrogen peroxide, Journal of Molecular Liquids 348 (2022) 118054–118061.

[168] L. Domínguez, A. Sosa-Peinado, W. Hansberg, Catalase evolved to concentrate H_2O_2 at its active site, Archives of Biochemistry and Biophysics 500 (2010) 82–91.

[169] Y.-H. Chung, J. Xia, C. J. Margulis, Diffusion and residence time of hydrogen peroxide and water in crowded protein environments, Journal of Physical Chemistry B 111 (2007) 13336–13344.

[170] L. Domínguez, A. Sosa-Peinado, W. Hansberg, How catalase recognizes H_2O_2 in a sea of water, Proteins 82 (2014) 45–56.

[171] R. Vácha, P. Slavíček, M. Mucha, B. J. Finlayson-Pitts, P. Jungwirth, Adsorption of atmospherically relevant gases at the air/water interface: Free energy profiles of aqueous solvation of N_2, O_2, O_3, OH, H_2O, HO_2, and H_2O_2, Journal of Physical Chemistry A 108 (2004) 11573–11579.

[172] Z.-Z. Yang, C.-S. Wang, Atom- bond electronegativity equalization method. 1. calculation of the charge distribution in large molecules, Journal of Physical Chemistry A 101 (1997) 6315–6321.

[173] C.-S. Wang, Z.-Z. Yang, Atom–bond electronegativity equalization method. II. lone-pair electron model, Journal of Chemical Physics 110 (1999) 6189–6197.

[174] M. de Swart, M. Van den Bosch, H. Berendsen, G. Canters, J. Snijders, Density functional theory and molecular dynamics results for copper proteins, Journal of Inorganic Biochemistry 86 (2001) 445–445.

[175] J.-M. Flaud, C. Camy-Peyret, J. Johns, B. Carli, The far infrared spectrum of H_2O_2. First observation of the staggering of the levels and determination of the cis barrier, Journal of Chemical Physics 91 (1989) 1504–1510.

[176] A. Biswas, B. S. Mallik, Conformational dynamics of aqueous hydrogen peroxide from first principles molecular dynamics simulations, Physical Chemistry Chemical Physics 22 (2020) 28286–28296.

[177] Y. Mao, Y. Zhang, Thermal conductivity, shear viscosity and specific heat of rigid water models, Chemical Physics Letters 542 (2012) 37–41.

[178] A. Rahbari, J. Brenkman, R. Hens, M. Ramdin, L. J. Van Den Broeke, R. Schoon, R. Henkes, O. A. Moultos, T. J. H. Vlugt, Solubility of water in hydrogen at high pressures: a molecular simulation study, Journal of Chemical & Engineering Data 64 (2019) 4103–4115.

[179] P. Florová, P. Sklenovsky, P. Banas, M. Otyepka, Explicit water models affect the specific solvation and dynamics of unfolded peptides while the conformational behavior and flexibility of folded peptides remain intact, Journal of Chemical Theory and Computation 6 (2010) 3569–3579.

[180] J.-P. Ryckaert, A. Bellemans, Molecular dynamics of liquid alkanes, Faraday Discussions of the Chemical Society 66 (1978) 95–106.

[181] T. Darden, D. York, L. Pedersen, Particle mesh Ewald: An $N{\cdot}\log(N)$ method for Ewald sums in large systems, Journal of Chemical Physics 98 (1993) 10089–10092.

[182] U. Essmann, L. Perera, M. L. Berkowitz, T. Darden, H. Lee, L. G. Pedersen, A smooth particle mesh Ewald method, Journal of Chemical Physics 103 (1995) 8577–8593.

[183] M. J. Abraham, T. Murtola, R. Schulz, S. Páll, J. C. Smith, B. Hess, E. Lindahl, Gromacs: High performance molecular simulations through multi-level parallelism from laptops to supercomputers, SoftwareX 1 (2015) 19–25.

[184] E. Lindahl, B. Hess, D. Van der Spoel, Gromacs 3.0: a package for molecular simulation and trajectory analysis, Molecular Modeling Annual 7 (2001) 306–317.

[185] D. Van Der Spoel, E. Lindahl, B. Hess, G. Groenhof, A. E. Mark, H. J. Berendsen, Gromacs: fast, flexible, and free, Journal of Computational Chemistry 26 (2005) 1701–1718.

[186] B. Hess, C. Kutzner, D. Van Der Spoel, E. Lindahl, Gromacs 4: algorithms for highly efficient, load-balanced, and scalable molecular simulation, Journal of Chemical Theory and Computation 4 (2008) 435–447.

[187] S. Pronk, S. Páll, R. Schulz, P. Larsson, P. Bjelkmar, R. Apostolov, M. R. Shirts, J. C. Smith, P. M. Kasson, D. van der Spoel, B. Hess, E. Lindahl, GROMACS 4.5: a high-throughput and highly parallel open source molecular simulation toolkit., Bioinformatics 29 (2013) 845–854.

[188] W. G. Hoover, Canonical dynamics: Equilibrium phase-space distributions, Physical Review A 31 (1985) 1695–1697.

[189] M. Parrinello, A. Rahman, Polymorphic transitions in single crystals: A new molecular dynamics method, Journal of Applied Physics 52 (1981) 7182–7190.

[190] R. W. H. Eastwood, J. W., Computer Simulation Using Particles, CRC Press, Boca Raton, 2021.

[191] B. Hess, P-LINCS: A parallel linear constraint solver for molecular simulation, Journal of Chemical Theory and Computation 4 (2008) 116–122.

[192] W. Humphrey, A. Dalke, K. Schulten, VMD: Visual Molecular Dynamics, Journal of Molecular Graphics 14 (1996) 33–38.

[193] B. A. Wells, A. L. Chaffee, Ewald summation for molecular simulations, Journal of Chemical Theory and Computation 11 (2015) 3684–3695.

[194] P. A. Giguère, Molecular association and structure of hydrogen peroxide, Journal of Chemical Education 60 (1983) 399–401.

[195] C. Vega, J. Abascal, Relation between the melting temperature and the temperature of maximum density for the most common models of water, Journal of Chemical Physics 123 (2005) 144504–144511.

[196] B. Hess, Determining the shear viscosity of model liquids from molecular dynamics simulations, Journal of Chemical Physics 116 (2002) 209–217.

[197] M. A. González, J. L. Abascal, The shear viscosity of rigid water models, Journal of Chemical Physics 132 (2010) 096101–096102.

[198] P. Mark, L. Nilsson, Structure and dynamics of the TIP3P, SPC, and SPC/E water models at 298 K, Journal of Physical Chemistry A 105 (2001) 9954–9960.

[199] M. Holz, S. R. Heil, A. Sacco, Temperature-dependent self-diffusion coefficients of water and six selected molecular liquids for calibration in accurate ^{1}H NMR PFG measurements, Physical Chemistry Chemical Physics 2 (2000) 4740–4742.

[200] I. Olovsson, D. H. Templeton, The crystal structure of hydrogen peroxide dihydrate, Acta Chemica Scandinavica 14 (1960) 1325–1332.

[201] A. Luzar, D. Chandler, Structure and hydrogen bond dynamics of water–dimethyl sulfoxide mixtures by computer simulations, Journal of Chemical Physics 98 (1993) 8160–8173.

[202] D. R. Nutt, J. C. Smith, Molecular dynamics simulations of proteins: Can the explicit water model be varied?, Journal of Chemical Theory and Computation 3 (2007) 1550–1560.

[203] H. Hwang, P. K. Dasgupta, Thermodynamics of the hydrogen peroxide-water system, Environmental Science & Technology 19 (1985) 255–258.

[204] K. Yoshizumi, K. Aoki, I. Nouchi, T. Okita, T. Kobayashi, S. K. Amakura, M. Tajima, Measurements of the concentration in rainwater and of the Henry's law constant of hydrogen peroxide, Atmospheric Environment (1967) 18 (1984) 395–401.

[205] X. Zhou, Y. N. Lee, Aqueous solubility and reaction kinetics of hydroxymethyl hydroperoxide, Journal of Physical Chemistry 96 (1992) 265–272.

[206] D. Huang, Z. Chen, Reinvestigation of the Henry's law constant for hydrogen peroxide with temperature and acidity variation, Journal of Environmental Sciences 22 (2010) 570–574.

[207] E. F. Horn, F. P. Dickey, Near-infrared emission spectrum of NO, Journal of Chemical Physics 41 (1964) 1614–1620.

[208] A. R. McKellar, J. Watson, B. Howard, The NO dimer: ^{15}N isotopic infrared spectra, line-widths, and force field, Molecular Physics 86 (1995) 273–286.

[209] P. Lukes, E. Dolezalova, I. Sisrova, M. Clupek, Aqueous-phase chemistry and bactericidal effects from an air discharge plasma in contact with water: evidence for the formation of peroxynitrite through a pseudo-second-order post-discharge reaction of H_2O_2 and HNO_2, Plasma Sources Science and Technology 23 (2014) 015019–015033.

[210] M. A. Malik, Nitric oxide production by high voltage electrical discharges for medical uses: a review, Plasma Chemistry and Plasma Processing 36 (2016) 737–766.

[211] K. Tachibana, T. Nakamura, Comparative study of discharge schemes for production rates and ratios of reactive oxygen and nitrogen species in plasma activated water, Journal of Physics D: Applied Physics 52 (2019) 385202–385218.

[212] X. Lu, G. V. Naidis, M. Laroussi, S. Reuter, D. B. Graves, K. Ostrikov, Reactive species in non-equilibrium atmospheric-pressure plasmas: Generation, transport, and biological effects, Physics Reports 630 (2016) 1–84.

[213] D. B. Graves, Reactive species from cold atmospheric plasma: Implications for cancer therapy, Plasma Processes and Polymers 11 (2014) 1120–1127.

[214] D. P. Park, K. Davis, S. Gilani, C.-A. Alonzo, D. Dobrynin, G. Friedman, A. Fridman, A. Rabinovich, G. Fridman, Reactive nitrogen species produced in water by non-equilibrium plasma increase plant growth rate and nutritional yield, Current Applied Physics 13 (2013) S19–S29.

[215] N. Puač, M. Gherardi, M. Shiratani, Plasma agriculture: A rapidly emerging field, Plasma Processes and Polymers 15 (2018) 1700174–1700178.

[216] P. Ranieri, N. Sponsel, J. Kizer, M. Rojas-Pierce, R. Hernández, L. Gatiboni, A. Grunden, K. Stapelmann, Plasma agriculture: Review from the perspective of the plant and its ecosystem, Plasma Processes and Polymers 18 (2021) 2000162–2000185.

[217] C. V. Suschek, C. Opländer, The application of cold atmospheric plasma in medicine: The potential role of nitric oxide in plasma-induced effects, Clinical Plasma Medicine 4 (2016) 1–8.

[218] A. V. Butenko, A. B. Shekhter, A. V. Pekshev, A. B. Vagapov, A. L. Fayzullin, N. B. Serejnikova, N. A. Sharapov, V. A. Zaborova, V. N. Vasilets, Review of clinical applications of nitric oxide-containing air-plasma gas flow generated by plason device, Clinical Plasma Medicine 19 (2020) 100112–100120.

[219] A. Lindsay, B. Byrns, W. King, A. Andhvarapou, J. Fields, D. Knappe, W. Fonteno, S. Shannon, Fertilization of radishes, tomatoes, and marigolds using a large-volume atmospheric glow discharge, Plasma Chemistry and Plasma Processing 34 (2014) 1271–1290.

[220] C. Bradu, K. Kutasi, M. Magureanu, N. Puač, S. Živković, Reactive nitrogen species in plasma-activated water: generation, chemistry and application in agriculture, Journal of Physics D: Applied Physics 53 (2020) 223001–223021.

[221] D. Guo, H. Liu, L. Zhou, J. Xie, C. He, Plasma-activated water production and its application in agriculture, Journal of the Science of Food and Agriculture 101 (2021) 4891–4899.

[222] M. N. Hughes, Chemistry of nitric oxide and related species, Methods in Enzymology 436 (2008) 3–19.

[223] F. Kohler, H. J. Guedes, J. Revés, M. N. da Ponte, Dimerization and thermodynamic properties of nitric oxide, Journal of Molecular Liquids 67 (1995) 105–123.

[224] J. M. Walsh, H. J. Guedes, K. E. Gubbins, Physical theory for fluids of small associating molecules, Journal of Physical Chemistry 96 (1992) 10995–11004.

[225] A. L. Smith, H. L. Johnston, The magnetic susceptibility of liquid nitric oxide and the heat of dissociation of $(NO)_2$[1], Journal of the American Chemical Society 74 (1952) 4696–4698.

[226] J. K. Park, H. Sun, Relative stabilities of $(NO)_2$, Chemical Physics 263 (2001) 61–68.

[227] R. Sayós, R. Valero, J. Anglada, M. González, Theoretical investigation of the eight low-lying electronic states of the cis-and trans-nitric oxide dimers and its isomerization using multiconfigurational second-order perturbation theory (CASPT2), Journal of Chemical Physics 112 (2000) 6608–6624.

[228] F. Kohler, M. Bohn, J. Fischer, R. Zimmermann, Die exzeßeigenschaften von stickstoffoxid-mischungen, Monatshefte für Chemie/Chemical Monthly 118 (1987) 169–182.

[229] J. O. Hirschfelder, C. F. Curtiss, R. B. Bird, The molecular theory of gases and liquids, John Wiley & Sons, 1964.

[230] J. Yang, Y. Ren, A.-m. Tian, H. Sun, Compass force field for 14 inorganic molecules, He, Ne, Ar, Kr, Xe, H_2, O_2, N_2, NO, CO, CO_2, NO_2, CS_2, and SO_2, in liquid phases, Journal of Physical Chemistry B 104 (2000) 4951–4957.

[231] J. K. Johnson, A. Z. Panagiotopoulos, K. E. Gubbins, Reactive canonical Monte Carlo: a new simulation technique for reacting or associating fluids, Molecular Physics 81 (1994) 717–733.

[232] J. K. Johnson, Reactive canonical Monte Carlo, Advances in Chemical Physics: Monte Carlo Methods in Chemical Physics 105 (1999) 461–481.

[233] A. Poursaeidesfahani, R. Hens, A. Rahbari, M. Ramdin, D. Dubbeldam, T. J. H. Vlugt, Efficient application of Continuous Fractional Component Monte Carlo in the reaction ensemble, Journal of Chemical Theory and Computation 13 (2017) 4452–4466.

[234] J. Sterpenich, M.-C. Caumon, V. Lachet, B. Creton, M. El Jarmouni, A. Randi, P. Robert, NO solubility in water and brine up to 60 MPa and 373 K by combining Raman spectroscopy and molecular simulation, Journal of Raman Spectroscopy 53 (2022) 645–653.

[235] B. Creton, C. Nieto-Draghi, T. De Bruin, V. Lachet, E. El Ahmar, A. Valtz, C. Coquelet, S. Lasala, R. Privat, J.-N. Jaubert, Thermodynamic study of binary systems containing sulphur dioxide and nitric oxide: Measurements and modelling, Fluid Phase Equilibria 461 (2018) 84–100.

[236] W. Sun, L.-C. Lin, X. Peng, B. Smit, Computational screening of porous metal-organic frameworks and zeolites for the removal of SO_2 and NO_x from flue gases, AIChE Journal 60 (2014) 2314–2323.

[237] N. Qiu, X. Bai, J. Xu, N. Sun, J. S. Francisco, M. Yang, Q. Huang, S. Du, Adsorption behaviors and phase equilibria for clathrate hydrates of sulfur-and nitrogen-containing small molecules, Journal of Physical Chemistry C 123 (2018) 2691–2702.

[238] A. Z. Panagiotopoulos, N. Quirke, M. Stapleton, D. Tildesley, Phase equilibria by simulation in the Gibbs ensemble: alternative derivation, generalization and application to mixture and membrane equilibria, Molecular Physics 63 (1988) 527–545.

[239] A. Panagiotopoulos, Molecular simulation of phase equilibria: simple, ionic and polymeric fluids, Fluid Phase Equilibria 76 (1992) 97–112.

[240] A. Rahbari, A. Poursaeidesfahani, A. Torres-Knoop, D. Dubbeldam, T. J. H. Vlugt, Chemical potentials of water, methanol, carbon dioxide and hydrogen sulphide at low temperatures using Continuous Fractional Component Gibbs ensemble Monte Carlo, Molecular Simulation 44 (2018) 405–414.

[241] S. Lasala, K. Samukov, H. M. Polat, V. Lachet, O. Herbinet, R. Privat, J.-N. Jaubert, O. A. Moultos, K. De Ras, T. J. H. Vlugt, Application of thermodynamics at different scales to describe the behaviour of fast reacting binary mixtures in vapour-liquid equilibrium, Chemical Engineering Journal 483 (2024) 148961–148975.

[242] H. M. Polat, S. Lasala, F. De Meyer, C. Houriez, O. A. Moultos, T. J. H. Vlugt, Scaling towards the critical point in the combined Reaction/Gibbs ensemble, Fluid Phase Equilibria 582 (2024) 114084–114095.

[243] N. Ferrando, V. Lachet, A. Boutin, Monte Carlo simulations of mixtures involving ketones and aldehydes by a direct bubble pressure calculation, Journal of Physical Chemistry B 114 (2010) 8680–8688.

[244] J. S. Rowlinson, B. Widom, Molecular theory of capillarity, 3rd ed., Courier Corporation, Mineola, New York, 2013.

[245] A. Tamir, C. Dragoescu, A. Apelblat, J. Wisniak, Heats of vaporization and vapor-liquid equilibria in associated solutions containing formic acid, acetic acid, propionic acid and carbon tetrachloride, Fluid Phase Equilibria 10 (1983) 9–42.

[246] C. Burrus, J. Graybeal, Stark effect at 2.0 and 1.2 millimeters wavelength: nitric oxide, Physical Review 109 (1958) 1553–1557.

[247] M. W. Chase, NIST-JANAF thermochemical tables, American Chemical Society, Washington, DC; New York, 1998.

[248] B. Howard, A. McKellar, The ν_1 band of $(NO)_2$, Molecular Physics 78 (1993) 55–72.

[249] R. González-Luque, M. Merchán, B. O. Roos, A theoretical determination of the dissociation energy of the nitric oxide dimer, Theoretica Chimica Acta 88 (1994) 425–435.

[250] A. Dkhissi, P. Soulard, A. Perrin, N. Lacome, The NO dimer, Journal of Molecular Spectroscopy 183 (1997) 12–17.

[251] M. Lísal, J. K. Brennan, W. R. Smith, Chemical reaction equilibrium in nanoporous materials: NO dimerization reaction in carbon slit nanopores, Journal of Chemical Physics 124 (2006) 064712–064725.

[252] C. H. Turner, J. K. Johnson, K. E. Gubbins, Effect of confinement on chemical reaction equilibria: The reactions $2NO \leftrightarrow (NO)_2$ and $N_2 + 3H_2 \leftrightarrow 2NH_3$ in carbon micropores, Journal of Chemical Physics 114 (2001) 1851–1859.

[253] R. Rowley, W. Wilding, J. Oscarson, N. Zundel, T. Marshall, T. Daubert, R. Danner, DIPPR Data Compilation of Pure Chemical Properties, AIChE, New York, 2010.

[254] J. Pedley, Thermochemical data and structures of organic compounds, 1st ed., CRC Press, College Station, Texas, 1994.

[255] E. D. Glendening, A. M. Halpern, Ab initio calculations of nitrogen oxide reactions: Formation of N_2O_2, N_2O_3, N_2O_4, N_2O_5, and N_4O_2, from NO, NO_2, NO_3, and N_2O, Journal of Chemical Physics 127 (2007) 164307–164317.

[256] N. Taguchi, Y. Mochizuki, T. Ishikawa, K. Tanaka, Multi-reference calculations of nitric oxide dimer, Chemical Physics Letters 451 (2008) 31–36.

[257] A. Lindsay, C. Anderson, E. Slikboer, S. Shannon, D. Graves, Momentum, heat, and neutral mass transport in convective atmospheric pressure plasma-liquid systems and implications for aqueous targets, Journal of Physics D: Applied Physics 48 (2015) 424007–424020.

[258] M. Bonitz, A. Filinov, J.-W. Abraham, K. Balzer, H. Kählert, E. Pehlke, F. X. Bronold, M. Pamperin, M. Becker, D. Loffhagen, H. Fehske, Towards an integrated modeling of the plasma-solid interface, Frontiers of Chemical Science and Engineering 13 (2019) 201–237.

[259] Y. Sakiyama, D. B. Graves, H.-W. Chang, T. Shimizu, G. E. Morfill, Plasma chemistry model of surface microdischarge in humid air and dynamics of reactive neutral species, Journal of Physics D: Applied Physics 45 (2012) 425201–425219.

[260] R. Dorai, M. J. Kushner, A model for plasma modification of polypropylene using atmospheric pressure discharges, Journal of Physics D: Applied Physics 36 (2003) 666 –685.

[261] R. Atkinson, D. Baulch, R. Cox, R. Hampson Jr, J. Kerr, M. Rossi, J. Troe, Evaluated kinetic and photochemical data for atmospheric chemistry: supplement VI. IUPAC subcommittee on gas kinetic data evaluation for atmospheric chemistry, Journal of Physical and Chemical Reference Data 26 (1997) 1329–1499.

[262] G. Sathiamoorthy, S. Kalyana, W. Finney, R. Clark, B. Locke, Chemical reaction kinetics and reactor modeling of NO_x removal in a pulsed streamer corona discharge reactor, Industrial & Engineering Chemistry Research 38 (1999) 1844–1855.

[263] X. Hao, A. M. Mattson, C. M. Edelblute, M. A. Malik, L. C. Heller, J. F. Kolb, Nitric oxide generation with an air operated non-thermal plasma jet and associated microbial inactivation mechanisms, Plasma Processes and Polymers 11 (2014) 1044–1056.

[264] D. Wise, G. Houghton, Diffusion coefficients of neon, krypton, xenon, carbon monoxide and nitric oxide in water at 10–60°C, Chemical Engineering Science 23 (1968) 1211–1216.

[265] I. G. Zacharia, W. M. Deen, Diffusivity and solubility of nitric oxide in water and saline, Annals of Biomedical Engineering 33 (2005) 214–222.

[266] T. Malinski, Z. Taha, S. Grunfeld, S. Patton, M. Kapturczak, P. Tomboulian, Diffusion of nitric oxide in the aorta wall monitored in situ by porphyrinic microsensors, Biochemical and Biophysical Research Communications 193 (1993) 1076–1082.

[267] O. C. Zafiriou, M. McFarland, Determination of trace levels of nitric oxide in aqueous solution, Analytical Chemistry 52 (1980) 1662–1667.

[268] H. Komiyama, H. Inoue, Absorption of nitrogen oxides into water, Chemical Engineering Science 35 (1980) 154–161.

[269] S. E. Schwartz, W. H. White, Kinetics of reactive dissolution of nitrogen oxides into aqueous solution., Advances in Environmental Science and Technology 12 (1983) 1–116.

[270] S. P. Tan, M. Piri, Modeling the solubility of nitrogen dioxide in water using perturbed-chain statistical associating fluid theory, Industrial & Engineering Chemistry Research 52 (2013) 16032–16043.

[271] F. Menezes, G. M. Popowicz, Acid rain and flue gas: quantum chemical hydrolysis of NO_2, ChemPhysChem 23 (2022) e202200395.

[272] B. Finlayson-Pitts, L. Wingen, A. Sumner, D. Syomin, K. Ramazan, The heterogeneous hydrolysis of NO_2 in laboratory systems and in outdoor and indoor atmospheres: An integrated mechanism, Physical Chemistry Chemical Physics 5 (2003) 223–242.

[273] C. England, W. H. Corcoran, Kinetics and mechanisms of the gas-phase reaction of water vapor and nitrogen dioxide, Industrial & Engineering Chemistry Fundamentals 13 (1974) 373–384.

[274] N. Hoinkis, M. I. Litter, Mechanisms of sonochemical transformation of nitrate and nitrite under different conditions: Influence of additives and pH, Industrial & Engineering Chemistry Research 61 (2022) 16408–16417.

[275] D. M. Yost, Systematic Inorganic Chemistry, 1st ed., Read Books, 70 Fifth Avenue, New York, 2007.

[276] J. S. Levine, T. R. Augustsson, I. C. Andersont, J. M. Hoell Jr, D. A. Brewer, Tropospheric sources of NO_x: Lightning and biology, Atmospheric Environment (1967) 18 (1984) 1797–1804.

[277] S. Verma, P. K. Yadava, D. Lal, R. Mall, H. Kumar, S. Payra, Role of lightning NO_x in ozone formation: A review, Pure and Applied Geophysics 178 (2021) 1425–1443.

[278] C. D. Holmes, T. H. Bertram, K. L. Confer, K. A. Graham, A. C. Ronan, C. K. Wirks, V. Shah, The role of clouds in the tropospheric NO_x cycle: A new modeling approach for cloud chemistry and its global implications, Geophysical Research Letters 46 (2019) 4980–4990.

[279] Z. Zhu, B. Xu, Purification technologies for NO_x removal from flue gas: a review, Separations 9 (2022) 307–333.

[280] E. Bourasseau, V. Lachet, N. Desbiens, J.-B. Maillet, J.-M. Teuler, P. Ungerer, Thermodynamic Behavior of the CO_2 + NO_2/N_2O_4 Mixture: A Monte Carlo simulation study, Journal of Physical Chemistry B 112 (2008) 15783–15792.

[281] J. Noroozi, W. R. Smith, Force-Field-Based Computational Study of the Thermodynamics of a Large Set of Aqueous Alkanolamine Solvents for Post-Combustion CO_2 capture, Journal of Chemical Information and Modeling 61 (2021) 4497–4513.

[282] R. M. Cordeiro, M. Yusupov, J. Razzokov, A. Bogaerts, Parametrization and Molecular Dynamics Simulations of Nitrogen Oxyanions and Oxyacids for Applications in Atmospheric and Biomolecular Sciences, Journal of Physical Chemistry B 124 (2020) 1082–1089.

[283] A. P. Thompson, H. M. Aktulga, R. Berger, D. S. Bolintineanu, W. M. Brown, P. S. Crozier, P. J. in't Veld, A. Kohlmeyer, S. G. Moore, T. D. Nguyen, R. Shan, M. J. Stevens, J. Tranchida, C. Trott, S. J. Plimpton, LAMMPS-a flexible simulation tool for particle-based materials modeling at the atomic, meso, and continuum scales, Computer Physics Communications 271 (2022) 108171–108204.

[284] B. T. Polyak, The conjugate gradient method in extremal problems, USSR Computational Mathematics and Mathematical Physics 9 (1969) 94–112.

[285] S. Nosé, A unified formulation of the constant temperature molecular dynamics methods, Journal of Chemical Physics 81 (1984) 511–519.

[286] I. Matito-Martos, A. Rahbari, A. Martin-Calvo, D. Dubbeldam, T. J. H. Vlugt, S. Calero, Adsorption equilibrium of nitrogen dioxide in porous materials, Physical Chemistry Chemical Physics 20 (2018) 4189–4199.

[287] A. Vegh, J. Korozs, G. Kaptay, Extension of the Gibbs–Duhem equation to the partial molar surface thermodynamic properties of solutions, Langmuir 38 (2022) 4906–4912.

[288] P. J. Linstrom, W. G. Mallard, The NIST chemistry webbook: A chemical data resource on the internet, Journal of Chemical & Engineering Data 46 (2001) 1059–1063.

[289] J. Berkowitz, W. Chupka, D. Gutman, Electron affinities of O_2, O_3, NO, NO_2, NO_3 by endothermic charge transfer, Journal of Chemical Physics 55 (1971) 2733–2745.

[290] V. I. Manousiouthakis, M. W. Deem, Strict detailed balance is unnecessary in Monte Carlo simulation, Journal of Chemical Physics 110 (1999) 2753–2756.

[291] J. Cheung, Y. Li, J. Boniface, Q. Shi, P. Davidovits, D. Worsnop, J. Jayne, C. Kolb, Heterogeneous interactions of NO_2 with aqueous surfaces, Journal of Physical Chemistry A 104 (2000) 2655–2662.

[292] Y. Lee, S. Schwartz, Reaction kinetics of nitrogen dioxide with liquid water at low partial pressure, Journal of Physical Chemistry 85 (1981) 840–848.

[293] K. H. Becker, J. Kleffmann, R. M. Negri, P. Wiesen, Solubility of nitrous acid (HONO) in ammonium sulfate solutions, Journal of the Chemical Society, Faraday Transactions 94 (1998) 1583–1586.

[294] J. Y. Park, Y. N. Lee, Solubility and decomposition kinetics of nitrous acid in aqueous solution, Journal of Physical Chemistry 92 (1988) 6294–6302.

[295] H. Komiyama, H. Inoue, Reaction and transport of nitrogen oxides in nitrous acid solutions, Journal of Chemical Engineering of Japan 11 (1978) 25–32.

[296] H. Kramers, M. Blind, E. Snoeck, D2. Absorption of nitrogen tetroxide by water jets, Chemical Engineering Science 14 (1961) 115–123.

[297] P. Zheng, W. Yang, W. Wu, O. Isayev, P. O. Dral, Toward chemical accuracy in predicting enthalpies of formation with general-purpose data-driven methods, Journal of Physical Chemistry Letters 13 (2022) 3479–3491.

[298] A. Weaver, D. Arnold, S. Bradforth, D. Neumark, Examination of the $^2A_2$ and $^2E"$ states of NO_3 by ultraviolet photoelectron spectroscopy of NO_3^-, Journal of Chemical Physics 94 (1991) 1740–1751.

[299] J. E. Foster, Plasma-based water purification: Challenges and prospects for the future, Physics of Plasmas 24 (2017) 055501–055516.

[300] P. D. Ray, B.-W. Huang, Y. Tsuji, Reactive oxygen species (ROS) homeostasis and redox regulation in cellular signaling, Cellular Signalling 24 (2012) 981–990.

[301] H. Sies, D. P. Jones, Reactive oxygen species (ROS) as pleiotropic physiological signalling agents, Nature Reviews Molecular Cell Biology 21 (2020) 363–383.

[302] P. Lukes, Plasma Chemistry and Catalysis in Gases and Liquids, 1st ed., Wiley Online Library, Weinheim, Germany, 2010.

[303] W. Hoeben, P. Van Ooij, D. Schram, T. Huiskamp, A. Pemen, P. Lukeš, On the possibilities of straightforward characterization of plasma activated water, Plasma Chemistry and Plasma Processing 39 (2019) 597–626.

[304] B. Myers, A. Dogariu, B. Beeler, L. Byrom, S. Yatom, K. Stapelmann, Imaging solvated oxygen atoms with a femtosecond laser, Nature Communications 16 (2025) 11393–11402.

[305] D. B. Graves, Low temperature plasma biomedicine: A tutorial review, Physics of Plasmas 21 (2014) 080901–080912.

[306] K. Wende, P. Williams, J. Dalluge, W. Van Gaens, H. Aboubakr, J. Bischof, T. Von Woedtke, S. M. Goyal, K.-D. Weltmann, A. Bogaerts, K. Masur, P. J. Bruggeman, Identification of the biologically active liquid chemistry induced by a nonthermal atmospheric pressure plasma jet, Biointerphases 10 (2015) 029518–029533.

[307] A. Khlyustova, C. Labay, Z. Machala, M.-P. Ginebra, C. Canal, Important parameters in plasma jets for the production of RONS in liquids for plasma medicine: A brief review, Frontiers of Chemical Science and Engineering 13 (2019) 238–252.

[308] T. H. G. Saji, T. J. H. Vlugt, S. Calero, B. Bagheri, Coupling solvation thermodynamics and chemical speciation: A simulation-based approach to no_x uptake in aqueous environments, Journal of Chemical Theory and Computation 22 (2025) 528–539.

[309] T. H. G. Saji, T. J. H. Vlugt, S. Calero, B. Bagheri, Modeling nitric oxide and its dimer: force field development and thermodynamics of dimerization, Physical Chemistry Chemical Physics 27 (2025) 13662–13674.

[310] T. H. G. Saji, J. M. Vicent-Luna, T. J. H. Vlugt, S. Calero, B. Bagheri, Computing solubility and thermodynamic properties of H_2O_2 in water, Journal of Molecular Liquids 401 (2024) 124530–124540.

[311] T. Jaffke, M. Meinke, R. Hashemi, L. G. Christophorou, E. Illenberger, Dissociative electron attachment to singlet oxygen, Chemical Physics Letters 193 (1992) 62–68.

[312] R. Peyrous, The effect of relative humidity on ozone production by corona discharge in oxygen or air–a numerical simulation–part I: oxygen, Ozone: Science and Engineering 12 (1990) 41–64.

[313] S. Bekeschus, K. Wende, M. M. Hefny, K. Rödder, H. Jablonowski, A. Schmidt, T. v. Woedtke, K.-D. Weltmann, J. Benedikt, Oxygen atoms are critical in rendering THP-1 leukaemia cells susceptible to cold physical plasma-induced apoptosis, Scientific Reports 7 (2017) 2791–2802.

[314] J. Korang, I. Emahi, W. R. Grither, S. M. Baumann, D. A. Baum, R. D. McCulla, Photoinduced DNA cleavage by atomic oxygen precursors in aqueous solutions, RSC Advances 3 (2013) 12390–12397.

[315] G. Busco, F. Fasani, S. Dozias, L. Ridou, C. Douat, J.-M. Pouvesle, E. Robert, C. Grillon, Changes in oxygen level upon cold plasma treatments: consequences for rons production, IEEE Transactions on Radiation and Plasma Medical Sciences 2 (2017) 147–152.

[316] Y. Gorbanev, J. Van der Paal, W. Van Boxem, S. Dewilde, A. Bogaerts, Reaction of chloride anion with atomic oxygen in aqueous solutions: can cold plasma help in chemistry research?, Physical Chemistry Chemical Physics 21 (2019) 4117–4121.

[317] M. M. Hefny, C. Pattyn, P. Lukes, J. Benedikt, Atmospheric plasma generates oxygen atoms as oxidizing species in aqueous solutions, Journal of Physics D: Applied Physics 49 (2016) 404002–404014.

[318] J. Benedikt, M. M. Hefny, A. Shaw, B. R. Buckley, F. Iza, S. Schäkermann, J. Bandow, The fate of plasma-generated oxygen atoms in aqueous solutions: non-equilibrium atmospheric pressure plasmas as an efficient source of atomic O(aq), Physical Chemistry Chemical Physics 20 (2018) 12037–12042.

[319] B. Myers, E. Barnat, K. Stapelmann, Atomic oxygen density determination in the effluent of the cost reference source using in situ effective lifetime measurements in the presence of a liquid interface, Journal of Physics D: Applied Physics 54 (2021) 455202–455216.

[320] C. Rio, J. Brandão, W. Wang, Using the reactions O+ H_2→ OH+ H to explore the importance of the atomic quantum states on chemical kinetics and reaction dynamics, Universal Journal of Chemistry 3 (2015) 80–85.

[321] J. Gallagher, C. E. Moore, Tables of spectra of hydrogen, carbon, nitrogen, and oxygen atoms and ions, 1st ed., CRC Press, Boca Raton, Florida, 1993.

[322] W. C. Martin, V. Kaufman, A. Musgrove, A compilation of energy levels and wavelengths for the spectrum of singly-ionized oxygen (O II), Journal of Physical and Chemical Reference Data 22 (1993) 1179–1212.

[323] J. Suijker, B. Bagheri, Unraveling the interaction between singlet state atomic oxygen O(^{1}D) and water: toward the formation of oxywater and hydrogen peroxide, Physical Chemistry Chemical Physics 26 (2024) 15277–15285.

[324] M. Filatov, W. Reckien, S. D. Peyerimhoff, S. Shaik, What are the reasons for the kinetic stability of a mixture of H_2 and O_2?, Journal of Physical Chemistry A 104 (2000) 12014–12020.

[325] O. Bain, P. A. Giguère, Hydrogen peroxide and its analogues: VI. infrared spectra of H_2O_2, D_2O_2, and HDO_2, Canadian Journal of Chemistry 33 (1955) 527–545.

[326] U. Kaldor, I. Shavitt, LCAO–SCF computations for hydrogen peroxide, Journal of Chemical Physics 44 (1966) 1823–1829.

[327] J. A. Pople, K. Raghavachari, M. J. Frisch, J. S. Binkley, P. V. Schleyer, Comprehensive theoretical study of isomers and rearrangement barriers of even-electron polyatomic molecules H_mABH_n (A, B = carbon, nitrogen, oxygen, and fluorine), Journal of the American Chemical Society 105 (1983) 6389–6399.

[328] R. D. Bach, J. J. McDouall, A. L. Owensby, H. B. Schlegel, Theoretical study of oxygen atom transfer. the role of electron correlation, Journal of the American Chemical Society 112 (1990) 7065–7067.

[329] R. D. Bach, A. L. Owensby, C. Gonzalez, H. B. Schlegel, J. J. McDouall, Nature of the transition structure for oxygen atom transfer from a hydroperoxide. theoretical comparison between water oxide and ammonia oxide, Journal of the American Chemical Society 113 (1991) 6001–6011.

[330] C. Meredith, T. P. Hamilton, H. F. Schaefer III, Oxywater (water oxide): new evidence for the existence of a structural isomer of hydrogen peroxide, Journal of Physical Chemistry 96 (1992) 9250–9254.

[331] D. Schröder, C. A. Schalley, H. Schwarz, N. Goldberg, J. Hrûsák, Gas-phase experiments aimed at probing the existence of the elusive water oxide molecule, Chemistry–A European Journal 2 (1996) 1235–1242.

[332] H. H. Huang, Y. Xie, H. F. Schaefer, Can oxywater be made?, Journal of Physical Chemistry 100 (1996) 6076–6080.

[333] T. Okajima, Theoretical study on the influence of H_2O for the 1, 2-hydrogen shift from hydrogen peroxide (H_2O_2) to water oxide (O-OH_2), Canadian Journal of Chemistry 79 (2001) 22–28.

[334] T. Okajima, Ab initio MO study on the solvent effect for hydrogen shift from hydrogen peroxide (H_2O_2) to water oxide (O-OH_2), Journal of Molecular Structure: THEOCHEM 572 (2001) 45–52.

[335] S. K. Ignatov, P. G. Sennikov, H.-W. Jacobi, A. G. Razuvaev, O. Schrems, Surface species formed during UV photolysis of ozone adsorbed on water ice films at 80 K. a combined RA-FTIR and DFT study, Physical Chemistry Chemical Physics 5 (2003) 496–505.

[336] J. Franz, J. S. Francisco, S. D. Peyerimhoff, Production of singlet oxygen atoms by photodissociation of oxywater, Journal of Chemical Physics 130 (2009) 084304–084306.

[337] M. Yusupov, E. Neyts, P. Simon, G. Berdiyorov, R. Snoeckx, A. van Duin, A. Bogaerts, Reactive molecular dynamics simulations of oxygen species in a liquid water layer of interest for plasma medicine, Journal of Physics D: Applied Physics 47 (2013) 025205–025213.

[338] C. Verlackt, E. Neyts, A. Bogaerts, Atomic scale behavior of oxygen-based radicals in water, Journal of Physics D: Applied Physics 50 (2017) 11LT01.

[339] S. Xu, V. Jirasek, P. Lukes, Molecular dynamics simulations of singlet oxygen atoms reactions with water leading to hydrogen peroxide, Journal of Physics D: Applied Physics 53 (2020) 275204–275212.

[340] S. Du, J. S. Francisco, G. K. Schenter, T. D. Iordanov, B. C. Garrett, M. Dupuis, J. Li, The OH radical-H_2O molecular interaction potential, Journal of Chemical Physics 124 (2006) 224318–224332.

[341] J. M. Anglada, M. Martins-Costa, J. S. Francisco, M. F. Ruiz-Lopez, Interconnection of reactive oxygen species chemistry across the interfaces of

atmospheric, environmental, and biological processes, Accounts of Chemical Research 48 (2015) 575–583.

[342] C. Angeli, R. Cimiraglia, J.-P. Malrieu, N-electron valence state perturbation theory: a fast implementation of the strongly contracted variant, Chemical Physics Letters 350 (2001) 297–305.

[343] C. Angeli, R. Cimiraglia, S. Evangelisti, T. Leininger, J.-P. Malrieu, Introduction of n-electron valence states for multireference perturbation theory, Journal of Chemical Physics 114 (2001) 10252–10264.

[344] C. Angeli, R. Cimiraglia, J.-P. Malrieu, n-electron valence state perturbation theory: A spinless formulation and an efficient implementation of the strongly contracted and of the partially contracted variants, Journal of Chemical Physics 117 (2002) 9138–9153.

[345] T. H. Dunning Jr, Gaussian basis sets for use in correlated molecular calculations. I. the atoms boron through neon and hydrogen, Journal of Chemical Physics 90 (1989) 1007–1023.

[346] A. K. Wilson, T. van Mourik, T. H. Dunning Jr, Gaussian basis sets for use in correlated molecular calculations. VI. Sextuple zeta correlation consistent basis sets for boron through neon, Journal of Molecular Structure: THEOCHEM 388 (1996) 339–349.

[347] F. Neese, F. Wennmohs, U. Becker, C. Riplinger, The ORCA quantum chemistry program package, Journal of Chemical Physics 152 (2020) 224108–224125.

[348] F. Jensen, Introduction to Computational Chemistry, 3rd ed., John Wiley & Sons, West Sussex, England, 2017.

[349] P. Habibi, A. Rahbari, S. Blazquez, C. Vega, P. Dey, T. J. H. Vlugt, O. A. Moultos, A new force field for OH^- for computing thermodynamic and transport properties of H_2 and O_2 in aqueous NaOH and KOH solutions, Journal of Physical Chemistry B 126 (2022) 9376–9387.

[350] J. M. Carbajo, F. Maraver, Salt water and skin interactions: new lines of evidence, International Journal of Biometeorology 62 (2018) 1345–1360.

[351] E. H. Mojumdar, E. Sparr, The effect of pH and salt on the molecular structure and dynamics of the skin, Colloids and Surfaces B: Biointerfaces 198 (2021) 111476–111484.

[352] J. P. Kiss, Role of nitric oxide in the regulation of monoaminergic neurotransmission, Brain Research Bulletin 52 (2000) 459–466.

[353] N. Yan, P. Marschner, W. Cao, C. Zuo, W. Qin, Influence of salinity and water content on soil microorganisms, International Soil and Water Conservation Research 3 (2015) 316–323.

[354] A. W. Sakti, S. T. Wahyudi, F. Ahmad, N. Darmawan, H. Hardhienata, H. Alatas, Effects of salt concentration on the water and ion self-diffusion coefficients of a model aqueous sodium-ion battery electrolyte, Journal of Physical Chemistry B 126 (2022) 2256–2264.

[355] J. Peng, A. Wan, Effect of ionic strength on Henry's constants of volatile organic compound, Chemosphere 36 (1998) 2731–2740.

[356] M. Görgényi, J. Dewulf, H. Van Langenhove, K. Héberger, Aqueous salting-out effect of inorganic cations and anions on non-electrolytes, Chemosphere 65 (2006) 802–810.

[357] J. E. Hall, Guyton and hall textbook of medical physiology, Jordanian Edition E-Book, 13th ed., Elsevier Health Sciences, Amman, Jordan, 2016.

[358] H. Li, S.-r. Sun, J. Q. Yap, J.-h. Chen, Q. Qian, 0.9% saline is neither normal nor physiological, Journal of Zhejiang University-SCIENCE B 17 (2016) 181–187.

[359] I. Zeron, J. Abascal, C. Vega, A force field of Li^+, Na^+, K^+, Mg^{2+}, Ca^{2+}, Cl^-, and SO_4^{2-} in aqueous solution based on the TIP4P/2005 water model and scaled charges for the ions, Journal of Chemical Physics 151 (2019) 134504–134519.

[360] P. Habibi, P. Dey, T. J. H. Vlugt, O. A. Moultos, Effect of dissolved KOH and NaCl on the solubility of water in hydrogen: A Monte Carlo simulation study, Journal of Chemical Physics 161 (2024) 054304–054313.

[361] J. S. Kim, Z. Wu, A. R. Morrow, A. Yethiraj, A. Yethiraj, Self-diffusion and viscosity in electrolyte solutions, Journal of Physical Chemistry B 116 (2012) 12007–12013.

[362] D. O. Wasik, H. M. Polat, M. Ramdin, O. A. Moultos, S. Calero, T. J. H. Vlugt, Solubility of CO_2 in aqueous formic acid solutions and the effect of nacl addition: A molecular simulation study, Journal of Physical Chemistry C 126 (2022) 19424–19434.

[363] H. Dorrani, A. Mohebbi, A comparative study of TIP4P-2005, SPC/E, SPC, and TIP3P-Ew models for predicting water transport coefficients using EMD and NEMD simulations, Journal of Engineering Thermophysics 32 (2023) 138–161.

[364] A. East, A. McKellar, J. Watson, The intermolecular vibrations of the NO dimer, Journal of Chemical Physics 109 (1998) 4378–4383.

[365] C. M. Western, P. R. Langridge-Smith, B. J. Howard, S. E. Novick, Molecular beam electric resonance spectroscopy of the nitric oxide dimer, Molecular Physics 44 (1981) 145–160.

[366] A. Rohatgi, Webplotdigitizer: Version 4.5, `https://automeris.io/WebPlotDigitizer` 411 (2020).

[367] K. A. Persson, B. Waldwick, P. Lazic, G. Ceder, Prediction of solid-aqueous equilibria: Scheme to combine first-principles calculations of solids with experimental aqueous states, Physical Review B—Condensed Matter and Materials Physics 85 (2012) 235438–235449.

[368] P. Renders, G. Anderson, Solubility of kaolinite and beryl to 573 K, Applied Geochemistry 2 (1987) 193–203.